A Hybrid Experimental and Theoretical Investigation into the Multi-Component Gas Adsorption Properties of Selected Porous Materials

by Jan Costandius

Submitted in partial fulfilment of the requirements for the degree Doctor of Philosophy

Promotor: Professor Catharine Esterhuysen

Co-Promotor: Professor Leonard J. Barbour

Department of Chemistry and Polymer Science

Faculty of Science

Stellenbosch University

March 2021

Declaration

By submitting this dissertation electronically, I declare that the entirety of the work contained therein is my own, original work, that I am the sole author thereof (save to the extent explicitly otherwise stated), that reproduction and publication thereof by Stellenbosch University will not infringe any third-party rights and that I have not previously in its entirety or in part submitted it for obtaining any qualification.

December 2021

Abstract

The importance of advancements in multi-component gas adsorption (MGA) techniques, with respect to combating climate change, is that these methods can help treat the problem at the cause: selective capture of CO_2 from mixtures of gases. Unfortunately, new MGA techniques are rarely developed, because the experimental and theoretical methods are much more complex than the single-component gas adsorption (SGA) alternatives. Consequently, most research is focused on studying the SGA properties of novel CO_2 adsorbers, while the MGA properties of these materials are often only investigated briefly, predicted qualitatively, or overlooked entirely. This offers an opportunity to develop new experimental and theoretical MGA techniques, such as those presented in this study. Furthermore, by virtue of simply studying the MGA properties of some adsorbents comprehensively, a new predictive method for MGA was developed and new insights were gathered about the cause of ideal *vs.* non-ideal adsorption.

The development of a new volumetric MGA method is reported in the first section of this study. The design of the method is discussed and the benchmarking of the instrument against previously published SGA data is shown. The MGA equilibria of CO_2 and N_2, when adsorbed by zeolite 13X, are reported. These data are compared to the results of the predictive ideal adsorbed solution theory (IAST) method, where it is found that IAST performs well with predicting the uptake of CO_2 but fails to correctly predict the uptake of N_2. Additionally, an empirical model, namely the extended Sips isotherm, performs surprisingly well with predicting the mixed uptakes of both CO_2 and N_2 accurately around 1 bar, where IAST does not.

Using the findings of the first section as inspiration, the extended Sips is utilized alongside the non-ideal (real) case of the adsorbed solution theory (RAST), to create a new predictive MGA method named PRAST-S. This method is used to predict the mixed uptakes of CO_2 and N_2 by Cu-HKUST-1, Mg-MOF-74, MOF-14, and UiO-66. Furthermore, the MGA equilibria of CO_2 and N_2 obtained using the instrument described in the first section are also reported for Cu-HKUST-1 to confirm that PRAST-S correctly predicts the adsorbed amounts. However, what was not anticipated was that the experimental measurements and PRAST-S prediction both show that Cu-HKUST-1 exhibits ideal adsorption of CO_2 and N_2. This is in contrast with the other materials studied, which all exhibit non-ideal adsorption.

A series of *in silico* simulations of CO_2 and N_2 within the pores of 13X and Cu-HKUST-1 to probe the differences in ideal and non-ideal behavior shows that a sudden shift in the mean interaction energy upon mixing is the telltale sign of non-ideal adsorption. Furthermore, the mechanism that led to the shift in the mean interaction energy – or the lack thereof, in the ideal cases – is shown to be dependent on the mode with which the adsorbates interact with the adsorbent.

Opsomming

Klimaatsverandering kan bestry word deur multi-komponent gas adsorpsie (MGA) tegnieke te verbeter, omdat hierdie tegnieke gebruik kan word om materiale wat CO_2 selektief uit gasmengsels adsorbeer in diepte te bestudeer. Ongelukkig word nuwe tegnieke – wat gebruik kan word vir die bestudering van gasmengseladsorpsie – selde ontwikkel, omdat hierdie tegnieke meer kompleks is as die tegnieke wat gebruik word om die adsorpsie van enkele gasse te bestudeer. Meeste navorsing fokus gevolglik slegs op die ondersoek van die adsorpsie van enkele gasse, terwyl die adsorpsie van gasmengsels hoofsaaklik geïgnoreer word. Daarom word nuwe eksperimentele- and teoretiese tegnieke ontwikkel in hierdie studie. Alhoewel hierdie studie hoofsaaklik fokus op die ontwikkeling van nuwe tegnieke, is 'n nuwe voorspellingsmodel ook ontwikkel wat gelei het tot nuwe insigte ten opsigte van ideale en nie-ideale adsorpsie.

'n Nuwe volumetriese tegniek vir gasmengsels is in die eerste afdeling van hierdie studie gerapporteer. Die ontwerp van die instrument en die relavante maatstaftoetse is bespreek aan die hand van data wat voorheen gepubliseer was. Die adsorpsieëwewigte van CO_2 en N_2 is gemeet vir seoliet 13X. Die ideale adsorbeerde-oplossingsteorie kan die adsorpsie van CO_2 in die teenwoordigheid van N_2 voorspel, maar kan nie die adsorpsie van N_2 in die teenwoordigheid van CO_2 korrek voorspel nie. 'n Onverwagse ontdekking is gemaak: 'n eenvoudige empiriese model, naamlik die uitgebreide Sips isoterm, het die adsorpsie van beide CO_2 en N_2 rondom atmosferiese druk korrek voorspel.

Die ontdekkings in die eerste afdeling van hierdie studie, is gebruik as die inspirasie agter die volgende studie: om die uitgebreide Sips isoterm te kombineer met die nie-ideale adsorbeerde-oplossingteorie om 'n nuwe voorspellingsmetode te ontwikkel (PRAST-S) vir die adsorpsie van gasmengsels. PRAST-S is gebruik om die opname van mengsels van CO_2 en N_2 deur Cu-HKUST-1, Mg-MOF-74, MOF-14, en UiO-66 te voorspel. Die instrument wat in afdeling een ontwikkel is, is gebruik om te bevestig dat MGA adsorpsie van CO_2 en N_2 deur Cu-HKUST-1 akkuraat deur PRAST-S voorspel is. 'n Onverwagse ontdekking is wel gemaak: die opname van mengsels van CO_2 en N_2 is ideaal wanneer hulle deur Cu-HKUST-1 geadsorbeer is. Hierdie is in teenoorstelling met die ander stowwe bestudeer wat almal nie-ideale adsorpsie toon.

'n Reeks rekenaar-gebaseerde berekeninge van CO_2 en N_2 in die poriële van 13X en Cu-HKUST-1 is uitgevoer om die verskille tussen die ideale- en nie-idealegedrag te bestudeer. Dit is ontdek dat nie-ideale adsorpsie gepaard gaan met 'n skielike verandering in die gemiddelde interaksieënergie tussen 'n gasspesie en die adsorberende materiaal, indien die gasspesie met 'n tweede gasspesie gemeng word. 'n Verdere ontdekking is dat die meganisme wat lei tot hierdie versteuring in die gemiddelde interaksieënergie van die interaksiemodes tussen die gasspesies en die adsorberende materiaal afhang.

Acknowledgements

I would like to extend thanks to my supervisors Prof. Catharine Esterhuysen and Prof. Len Barbour who encouraged me to pursue my interests, while keeping me on the right track to success. They were always ready and willing to accommodate me, whenever I barged into their offices with research ideas. They asked the right questions, and they challenged me in all the right ways. Most importantly, they taught me the value of telling a good story.

I am grateful for the support and love that I was given freely by my father, mother, and sister. Without them, I would have not been able to complete this PhD and I would not be the person that I am today. I am especially grateful for my partner-in-crime, Jeanice Basson, for always being there for me, making me laugh, and being the most important person in my life. To my friends: thank you for carrying me.

Furthermore, to my mentors – Dr Vincent Smith, Dr Charl Bezuidenhout, and Dr Dewald van Heerden – thank you for passing on your skills, the brainstorming sessions, and being good friends. To the remainder of the Supramolecular group – thank you for tolerating me and for being a solid team of people to work with. I would also like to say a special thank you to the support team – especially Dr Leigh Loots, Dr Marike du Plessis, Debbie Isaacs, Maxwell Wakens, and Raymond Willemse – who went above and beyond to prevent the building from collapsing in on itself, while being wonderful people to spend time with.

Finally, I would like to acknowledge that this work was made possible by Stellenbosch University, with computational resources provided by the Centre for High Performance Computing in Cape Town and was funded by the National Research Foundation.

Conferences

Poster presentation ("*Mixed-gas Sorption; Method Development & Applications*") at INDABA IX, organized by the South African Crystallographic Society (SACrS) and the Structural Chemistry Commission of the International Union of Crystallography (IUCr) held in Skukuza. Kruger National Park, South Africa on 2-7 September 2018.

Publications

J. Costandius, C. Esterhuysen, L.J. Barbour, Adsorption Isotherms for Multi-Component Gases at Elevated Pressures: Measurement vs Prediction, *in preparation*, 2021.

Glossary of Terms

0D	Zero-Dimensional	MM	Molecular Mechanics
1D	One-Dimensional	MOF	Metal-Organic Framework
2D	Two-Dimensional	MPA	Mulliken Population Analysis
3D	Three-Dimensional	PBE	Perdew–Burke–Ernzerhof Functional
API	Application Programming Interface	PDF	Probability Distribution Function
AST	Adsorbed Solution Theory	PRAST-S	Predictive Real Adsorbed Solution Theory Using the Extended Sips Isotherm
CBU	Composite Building Unit	PSA	Pressure-Swing Adsorption
CCS	Carbon Capture and Storage	PXRD	Powder X-Ray Diffraction
CMC	Canonical Monte Carlo	QEq	Molecular Charge Equilibration
DFT	Density Functional Theory	RAST	Real Adsorbed Solution Theory
GCMC	Grand Canonical Monte Carlo	RDF	Radial Distribution Function
GGA	Generalized Gradient Approximation	RGA	Residual Gas Analyzer
GUI	Graphical User Interface	RMSE	Root Mean Square Error
HPA	Hirshfeld Population Analysis	SBU	Secondary Building Unit
IAST	Ideal Adsorbed Solution Theory	SGA	Single-Component Gas Adsorption
MAE	Mean Absolute Error	TGA	Thermogravimetric Analysis
MC	Monte Carlo	VDW	van der Waals Equation of State
MD	Molecular Dynamics	VDW1	van der Waals One-Fluid Model
MGA	Multi-Component Gas Adsorption		

Atomic Color Key

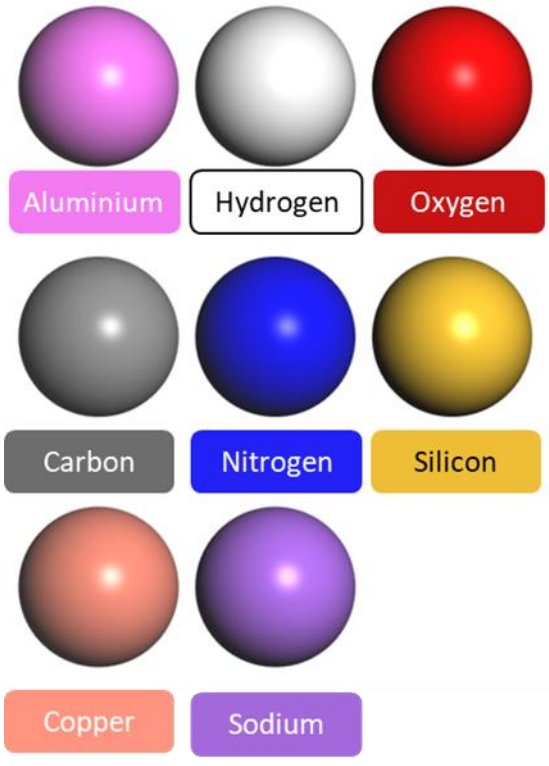

Table of Contents

Chapter 1. Introduction

1.1 CARBON CAPTURE AND STORAGE

Fossil fuel combustion as a means of electricity production was identified[1,2] as the lead contributor to climate change several years ago. Consequently, many developed countries are pursuing renewable energy resources (*i.e.* solar, wind, nuclear, and hydroelectric electricity generation) as alternatives to fossil fuels.[3,4] In terms of the available infrastructure, cost, and availability, however, fossil fuels are expected to be the dominant power source for most of the world for the foreseeable future.[4]

Bearing in mind that fossil fuels play a vital role for the economic growth of developing countries, a considerable effort has been made by the scientific community to propose solutions that mitigate the effects that continued use of fossil fuels have on the environment.[5] Researchers from several different disciplines have banded together, with each group contributing potential solutions to the climate-change problem from their own academic perspective. For example, contributions from the microbiological fields include engineered *Escherichia coli* that are capable of converting CO_2 to carbon biomass.[6] Recent advances in catalytic electrolysis technology also show increasingly promising methods and conditions for the conversion of CO_2 to usable fuels *via* electrolytic reduction.[7] New findings, regarding the sequestration of CO_2 with the aid of novel solid adsorbents and improved techniques, are also frequently published from both the chemistry and engineering frontiers.[8,9] Specifically, microporous materials such as zeolites and metal-organic frameworks (MOFs) have shown the most promise regarding the selective capture and release of CO_2 in flue gas streams.[10,11]

In this regard, post-combustion carbon capture and storage (CCS) from flue gas has become an important research topic in the fields that are focused on mitigating the effects of the current infrastructure on the environment. Many methods of post-combustion CCS have been developed, such as absorption,[12] adsorption,[13] membrane separation,[14] hydrate-based separation,[15] and cryogenic distillation processes.[16] The oldest, most widely used method of CCS is amine solvent absorption, otherwise known as amine scrubbing. The disadvantages of this technique are that large amounts of heat are required,[17] and corrosive[18] decomposition products are formed when the amine absorbent is regenerated. As an alternative, many researchers have proposed solid adsorbents as a preferred option for carbon sequestration from flue gas. Some examples of solid adsorbents include activated carbon,[19] zeolites,[20–23] molecular organic frameworks,[24–27] and metal-organic frameworks (MOF).[28] A solid adsorbent preferably demonstrates selective gas separation, high saturation capacity, thermal

robustness, chemical inertness, reproducible performance over many adsorption/desorption cycles, and commercial availability.

There are also practical challenges associated with CCS that need to be factored into the evaluation of the suitability of a solid adsorbent. First, one should consider the composition and source of the flue gas, for example, coal-fired power plants generate a flue-gas mixture of approximately 85.4% N_2 and 14.6% CO_2 by mole, along with other trace components.[15] In other words, the adsorbent should be selective for CO_2 at low partial pressures of the gas. Secondly, the adsorbent needs to have a working capacity[29] greater than 1 mmol g^{-1}. These two challenges associated with CCS are addressed in part by the development of novel adsorbent materials that show a high uptake of CO_2 and a low uptake of N_2: if the adsorbent shows a low uptake of N_2 at high pressure and a comparably high uptake of CO_2 at low pressure, then one can state, on a qualitative basis, that the material is selective for CO_2 over N_2.[30] Selectivity is also directly measured at atmospheric pressures by using the breakthrough method[31–35] where the two gases are simultaneously passed through a packed column of adsorbent and the outlet gas composition is measured over time. Breakthrough curves, however, are not representative of the adsorption equilibria at elevated pressures, which are relevant to industry practices, as in the case of pressure-swing adsorption.[36]

Although single-component gas adsorption (SGA) processes are well understood and documented, there is still much work to be done to improve multi-component gas adsorption (MGA) techniques. MGA measurements are an emerging method of adsorption analysis, with only a few publications describing experimental measurements.[37] The major reasons listed[38] for the absence of measurements involving mixed gases are (1) the lengthy experiments involved, (2) difficulty of operation, and (3) the necessity of building custom instruments. The state-of-the-art MGA theory, namely adsorbed solution theory (AST),[39] can be used to predict the outcome of an experiment, however, there are currently several limitations associated with AST as a predictive method.[40]

1.2 COMMON MOLECULAR INTERACTIONS

One of the most fundamental physicochemical processes that occur during adsorption is the formation of interactions between the adsorbates and the adsorbent. Intermolecular interactions can be defined as the non-covalent attractive and repulsive forces two chemical species experience when in close contact during adsorption, and other physicochemical processes. The following subsections on intermolecular interactions are based on information available in relevant textbook resources.[41]

1.2.1 Electrostatic Interactions

Classically, electrostatic interactions are described by Coulomb's law. The interaction between two charged atoms (ions) of opposite charges is referred to as an ionic bond. One example of an ionic compound (*i.e.*, a material that exclusively contains ions interacting electrostatically) is sodium chloride. In this material, sodium cations and chloride anions are arranged in an alternating fashion in a regular lattice. Although this is clearly a purely ionic compound, there are many bond types in chemistry that are ambiguous in their covalent or ionic character. Linus Pauling proposed an estimation of bonding character using the difference in electronegativities of both atoms. In his book, *The Nature of the Chemical Bond*, he proposed that the atoms in a fully covalent molecular bond have no difference in electronegativities, whereas those in a fully ionic bond have a large difference in electronegativity.[41] Expanding on Pauling's work, van Arkel and Ketelaar proposed a bond triangle in 1949[42], see Figure 1.1, which was developed further by Allen *et al.*[43] and Jensen[44] in the 1990s. The bond triangle proposed by Allen *et al.* shows regions of bonding character that can be unambiguously described as ionic (r_I), metallic (r_M) or covalent (r_C). Beyond the region demarcated by r_C lies the polarized covalent bond, which gives rise to permanent dipoles.

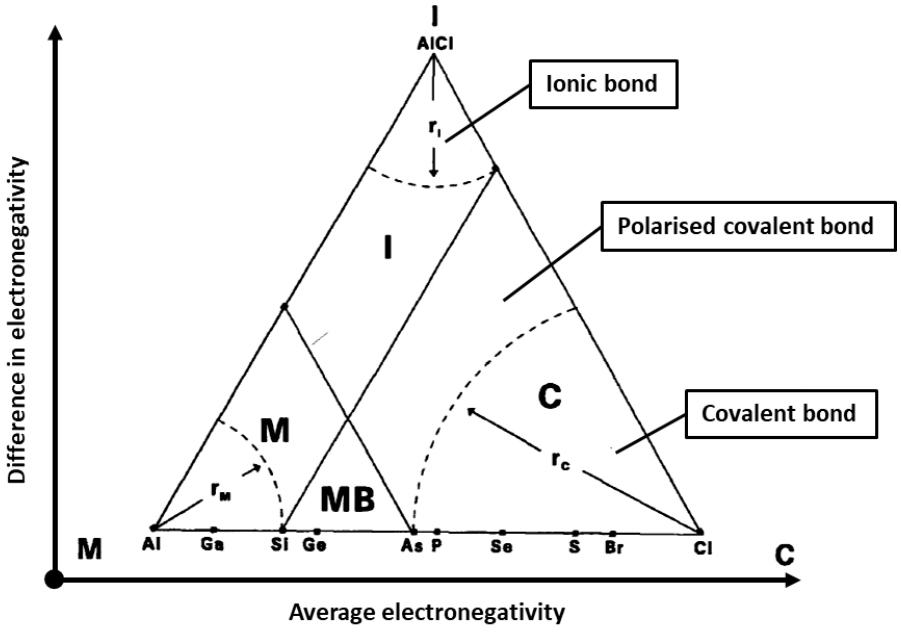

Figure 1.1. The bonding triangle proposed by Allen *et al.*[43]

1.2.2 Van der Waals Interactions

Another set of interactions present in adsorption processes, although much smaller in magnitude than ionic bonds (40-200 kcal mol^{-1}), is van der Waals interactions (<10 kcal mol^{-1}).[45] Van der Waals

interactions are related to dipole forces and the polarizability of atoms. There are two different types of dipoles that will be introduced here.

Permanent dipoles are formed when two covalently-bonded atoms have sufficiently different electronegativities, while having insufficient ionic character to form ionic bonds. Conventionally, a dipole is described as a directional vector that starts from the center of the positive charge and ends at the center of the negative charge. This is easily demonstrated with the formaldehyde molecule, as shown in Figure 1.2 A. If two molecules containing permanent dipoles are brought into proximity, they will be in a stable configuration if their respective dipoles are oriented in a collinear or antiparallel fashion. This occurs due to the repulsion of charges with equal sign, and dipole-dipole-induced torque. The name given to these particular interactions is the Keesom force.

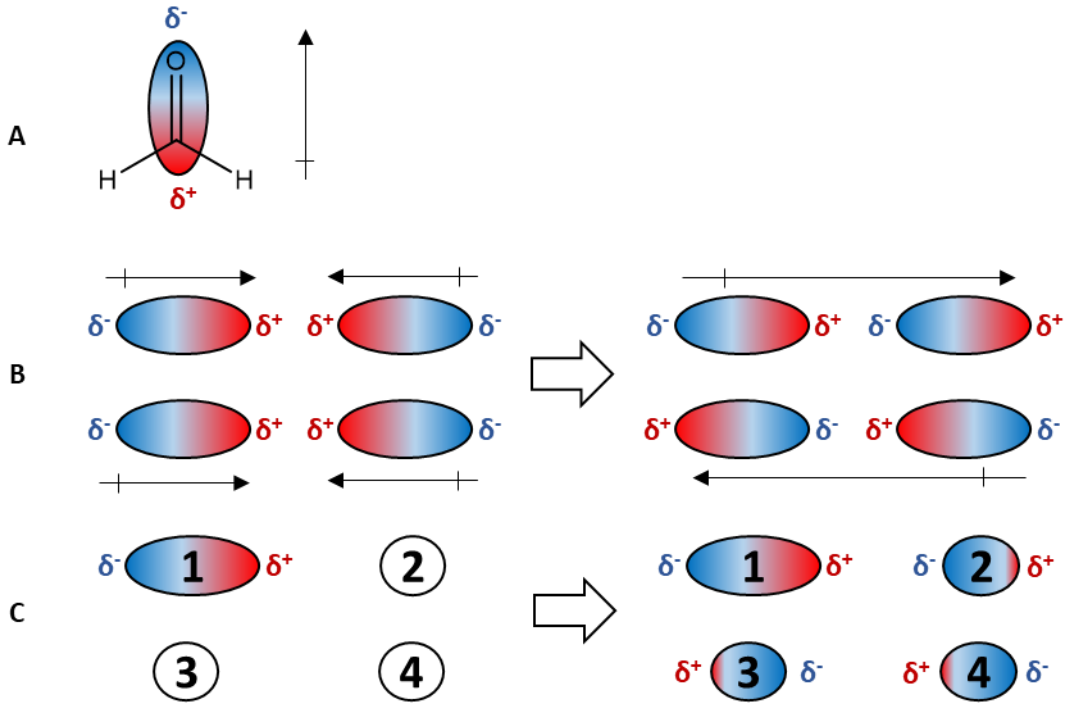

Figure 1.2. (A) Formaldehyde contains a permanently polarized bond between carbon (δ^+) and oxygen (δ^-). (B) Dipoles are at their energetic minimum when aligned in a collinear or antiparallel fashion. (C) Introduction of a permanent dipole into an environment that is normally non-polar results in the formation of induced dipoles.

Owing to the dynamic motion of electrons, momentary dipoles may occur by chance or by external perturbation. This particular behaviour of atoms is of great importance, especially in the case of condensed phases of noble gases. By definition, induced dipoles are the result of the momentary deformation of the otherwise symmetrical distribution of electron density around an atom. Induced dipoles can either be formed due to an atom being in the presence of a permanent dipole (Debye force, molecules 2 and 3 in Figure 1.2 C), or due to an atom being in the presence of another induced dipole (London dispersion forces, molecule 4 in Figure 1.2 C).

London dispersion interactions occur spontaneously, due to the momentary formation of dipoles and other types of multipoles in atoms. The ability of an atom to form and respond to momentary multipoles is referred to as an atom's polarisability, most clearly demonstrated by noble gases of increasing atomic number. Noble gases do not have a permanent dipole, nor are they charged particles in their standard state, yet at close proximities a dimer shows a favourable interaction that scales with the atomic number.[46]

In addition to dipole-based interactions, in nature, atoms and molecules often exhibit quadrupolar[47] and other higher-order multipolar noncovalent interactions with receptive molecules, for simplicity, these interactions were not discussed.

As mentioned above, van der Waals interactions techanically refer to all dipole interactions, but this text will follow the more modern convention of using *van der Waals* and *dispersion interactions* to interchangeably describe induced-dipole-induced-dipole interactions.

1.2.3 Hydrogen Bond

The hydrogen bond is one of the most common noncovalent interactions present in organic systems. Some examples of hydrogen-bonding systems can be seen in Figure 1.3. Pauling[48] described a hydrogen bond as the sharing of a hydrogen atom between two electronegative atoms, where one of the particles has a lone pair, crediting Winmill and Moore[49] for the first mention of the term in 1912. He stated that the hydrogen atom, containing only a 1*s* orbital, can only sustain one covalent bond, therefore the hydrogen-bond interaction is weakly ionic in nature.

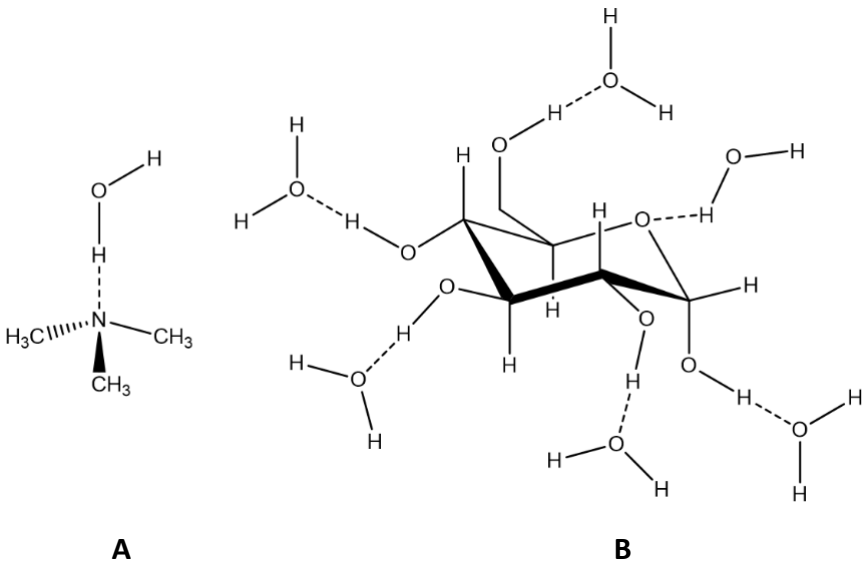

Figure 1.3. (A) Weak hydrogen-bonding complex formed between trimethylamine and water, first observed by Winmill and Moore. (B) Sugar molecules are readily soluble in water, owing to high availability of hydrogen-bonding sites.

Owing to the extensive study of hydrogen bonds over the last century, their bond strengths are well known and exist in a continuous range of approximately 1-40 kcal/mol, where moderate hydrogen bonds are in the range of 4-15 kcal/mol and strong hydrogen bonds are in the range of 15-40 kcal/mol.[50] The current IUPAC definition of the hydrogen bond is much broader than Pauling's original formulation and encompasses a wide range of D–H···A interactions, where D and A may be O, N, C, halogens, metals and more.[51]

1.3 HOST-GUEST CHEMISTRY

When a small molecule interacts with a material and is trapped within a cavity inside a larger structure, it is referred to as a guest inside a host system. The host structure can trap a guest molecule in a size-selective cavity where favorable interactions may occur. The resulting host-guest combination is called an inclusion complex. Examples of materials that can form inclusion complexes are crown ethers[52], proteins with drug-binding sites,[53] and porous materials.[54,55]

If a guest can orient itself spatially within an unfilled cavity to maximize the favorable interaction between itself and the host, a stable complex is formed. Consider, for instance, five potential guest molecules that can bind to a rigid, polarized host cavity as shown in Figure 1.4. Of the five molecules, H_2O and CO_2 would likely compete for occupation of the cavity, while the others would be excluded: H_2S has the correct charge distribution, but the host cannot accommodate the bulky sulfur atom; acetylene (C_2H_2) may be the correct size, but there is not enough space for it to reorient into a favorable configuration. Finally, nitrogen is also the correct size, but only has access to van der Waals interactions that are too weak to compete with electrostatic interactions. It would, therefore, seem logical that a cavity that is complementary in *both* size and electrostatic properties relative to a guest would be selective for that guest.[56]

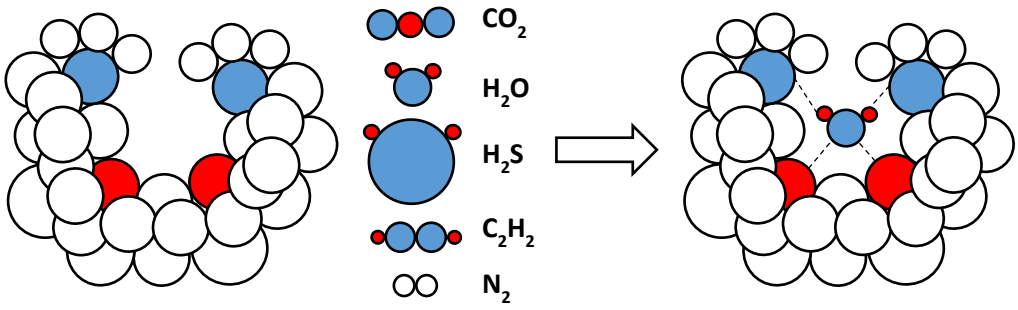

Figure 1.4. A binding cavity with partially negatively-charged sites (shown in blue) and partially positively-charged sites (shown in red). If the five molecules were to be introduced into the cavity and subsequently removed, water would bind most strongly.

All inclusion processes are reversible and exothermic. Provided with enough heat, an inclusion complex will dissociate into its host and guest fragments, in a process referred to as activation. Furthermore, if a sample is activated at reduced pressure, the process of guest removal is accelerated, and less heat is required.

1.4 POROSITY

Materials in the solid phase are conventionally thought of as impermeable lattices by the close-packing principle.[57] The solid materials in this work, however, exhibit permanent porosity and are even capable of forming host-guest complexes. Porosity is a measure of the permeability of solid materials relative to small guests, such as helium.[58] Therefore, a porous material is a solid that will have cavities and empty channels embedded into its bulk solid phase. Void volumes inside a porous material must also be large enough for gas molecules to diffuse through. Importantly, a material should retain its porosity during guest diffusion and guest removal for it to be considered truly porous.[59] An example of a class of porous materials that occur in nature is the family of zeolites, which will be discussed later in this study. Classification of the pores in porous materials rests on two descriptors: (1) pore size distribution and (2) pore dimensionality (see Figure 1.5).[60] The materials of interest in this study are microporous materials, meaning that they have pores with a diameter between 5 and 20 Å. Four types of pore dimensionalities can be found in microporous materials, ranging from zero-dimensional to three-dimensional (0D to 3D). 0D porous materials have discrete cavities in the framework, 1D porous materials have unidirectional channels that span the entire

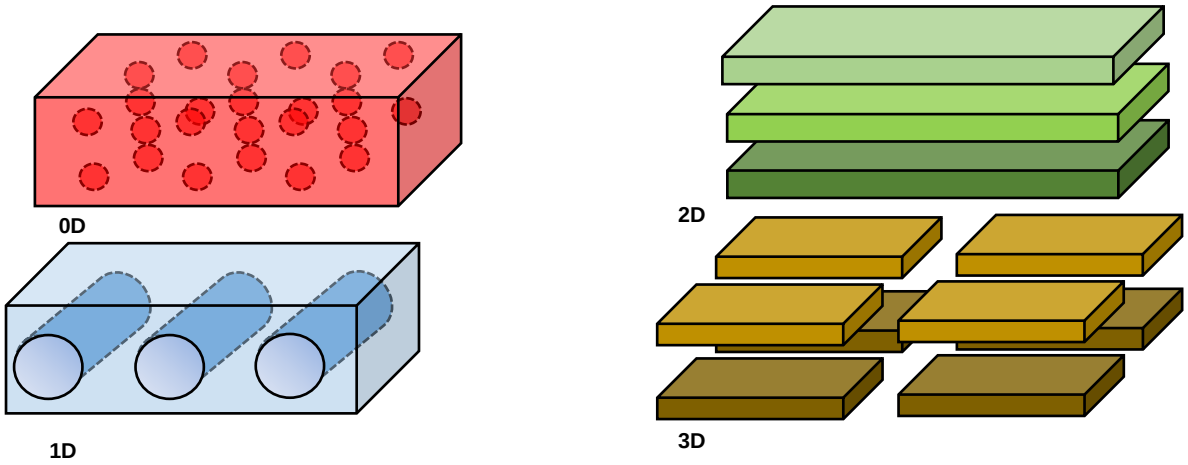

Figure 1.5. Adaptation of the description of pore dimensionality by Kitagawa *et al*.[32] 0-D porous materials contain discrete cavities. 1-D porous materials contain channels inside their structure. 2-D porous materials are layered solids containing void volumes with a planar geometry. 3-D porous materials have void volumes along all three axes.

length of the crystal, 2D porous materials are usually layered materials that have accessible void volumes between the tiers of the crystal structure, and 3D porous materials have a network of pores that are accessible from all the faces of the crystal structure.

1.5 GAS ADSORPTION

Many of the concepts of host-guest chemistry – such as inclusion, selectivity, host-guest interactions, and activation – can be directly applied to adsorption, especially when considering porous adsorbents. Adsorption, strictly defined as molecules condensing and adhering to the surface of a solid (see Figure 1.6 A), is a process that has both a pressure and temperature dependency, as described by Kayser[61] in 1881. By contrast, when a molecule, ion, or photon enters and is retained in another bulk phase, it is described as having been absorbed (see Figure 1.6 B). Owing to the ambiguous nature of the inclusion of guest molecules within porous materials (see Figure 1.6 C), neither "adsorption" nor "absorption" completely describe the processes that occur. Nevertheless, the inclusion of guest molecules into the pores of a framework is frequently referred to as "adsorption", or sometimes simply as "sorption".[62,63]

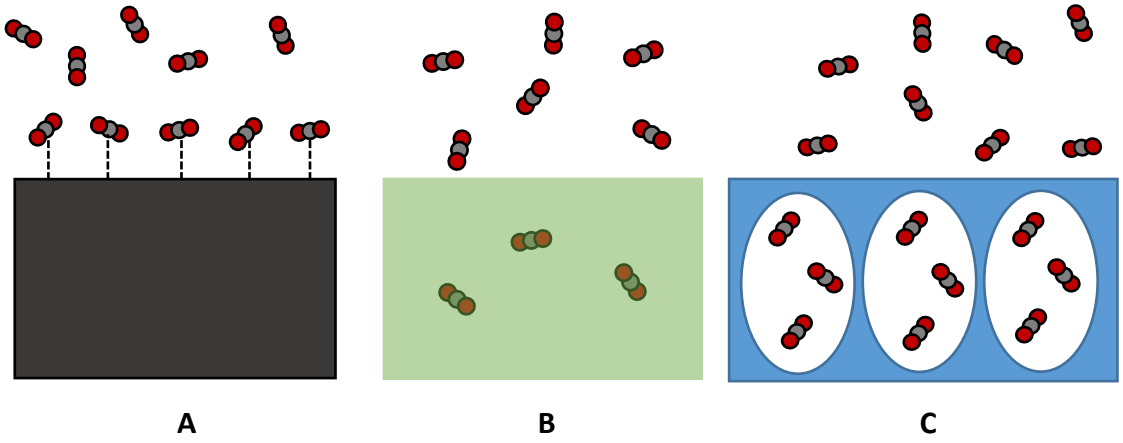

Figure 1.6. (A) Adsorption; gas molecules adhere and condense onto the surface of the adsorbent. (B) Absorption; gas molecules diffuse into the absorbent and form an absorbed solution. (C) Adsorption (sorption); gas molecules enter the porous network of a porous adsorbent material and form an inclusion complex.

At its core, adsorption is a physicochemical process that can be divided into two subcategories, namely physisorption and chemisorption. The major differences between the two types of adsorption are in the types of interactions occurring between the host (adsorbent) and the guest (adsorbate). If a guest molecule is removed from the bulk gaseous phase and enters the host system, it may eventually be locked into a localized energy minimum, inhibiting further translation. These localized energy minima are known as adsorption sites.[64] The process of chemisorption entails the formation of covalent or ionic bonds between the guest molecule and the adsorption sites.[65] Otherwise, if the guest

molecule interacts with the site through a noncovalent interaction it is known as physisorption.[66–68] A brief summary of the main types of adsorption interactions that can occur is shown in Figure 1.7. Owing to the favorable nature of the interaction between the adsorption site and the guest molecule (host-guest interaction) the process of adsorption releases energy in the form of heat, resulting in reduced uptake of guest molecules at higher temperatures. In this study, the predominant type of adsorption involved is physisorption, with the main interaction types being electrostatic and van der Waals interactions.

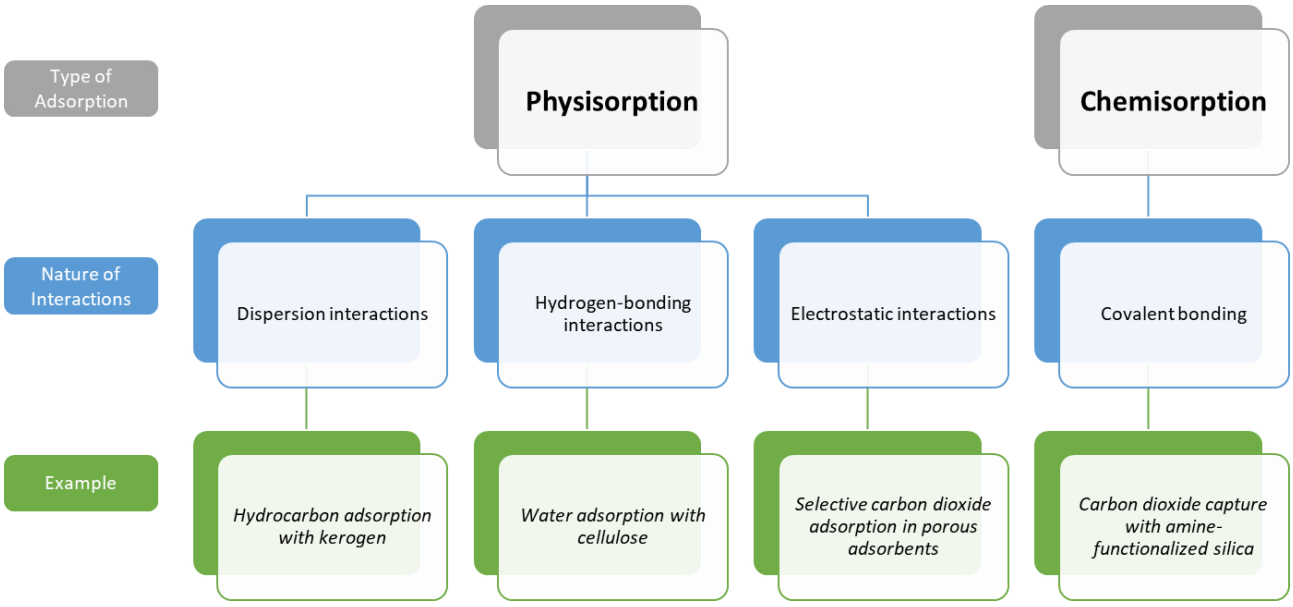

Figure 1.7. Examples of physisorption or chemisorption processes.

Adsorption can be characterized by the equilibrium state, where the rates of gas molecules being adsorbed and desorbed are equal. The uptake (loading) of guest molecules, at equilibrium, by the host can be followed by measuring the change in the density of the gas phase (volumetric adsorption) or the increase of mass in the solid phase (gravimetric adsorption). The pressure of the gas phase is used to quantify adsorption in the volumetric method, rather than the gas-phase density, since it is easier to measure the pressure, and the density is dependent on the pressure (see Section 1.6). Furthermore, the adsorbed amount, and the density of the gas phase, is dependent on the temperature; the temperature is, therefore, held constant during an adsorption experiment. For these reasons, the adsorbed amount of gas that is plotted as a function of pressure is called an adsorption isotherm.

According to the International Union of Pure and Applied Chemistry (IUPAC) classification there are six types of adsorption isotherms (Figure 1.8) that depend on the relationship between the structure of the porous material and the type of adsorption process.[60,69,70]

Type I isotherms correspond to uptake by microporous materials, Types II, III and VI show characteristic uptake paths by nonporous and microporous materials, whereas Types IV and V are seen only with mesoporous materials. Type VI isotherms are seen in stepwise multi-layer adsorption processes. The differences between Types II and III, or IV and V, are most noticeable in the low-pressure ranges. If the fluid-solid interactions are stronger than fluid-fluid interactions, then Types II and IV are observed. In the reverse scenario, Types III and V are observed.[60]

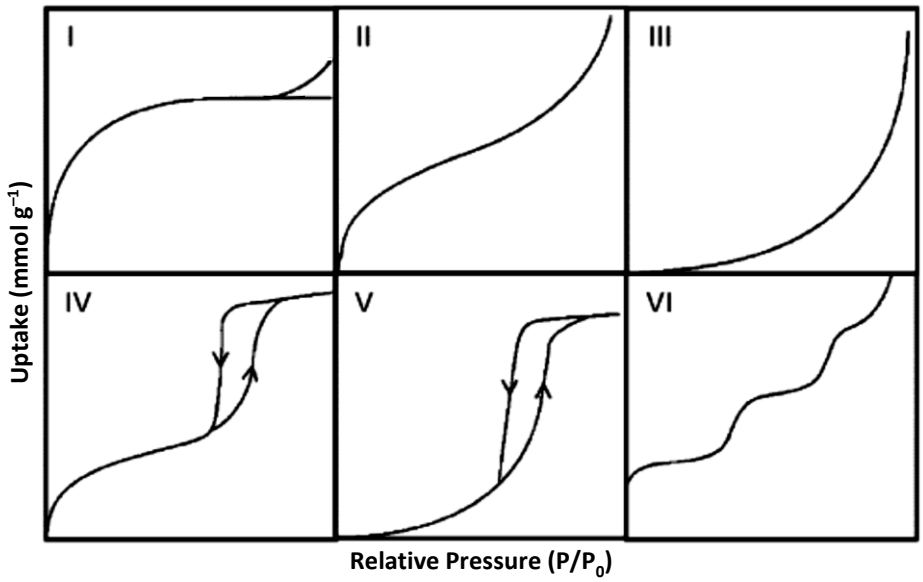

Figure 1.8. IUPAC classifications of isotherm types.

1.6 EQUATIONS OF STATE

1.6.1 Single-Component Gases

It is important to be able to relate unknown properties of the gas phase to limited, measured information in adsorption applications. The relationships between pressure, volume, temperature, and mass are referred to as equations of state (EOS).[71] The simplest EOS is the ideal gas law (Equation 1.1),

$$PV = nRT \tag{1.1}$$

where P is the pressure, V is the volume of gas, n is the number of moles of gas molecules, R is the gas constant, and T is the temperature. The ideal gas law is based on the following two assumptions: (1) gas molecules are infinitely compressible and (2) they do not interact with one another. The first assumption means that when the limit of P is taken to infinity at constant V and T, n also tends to infinity, while for the second assumption when T tends to zero at constant n and V, P also tends towards zero. Experimentally both assumptions have been shown to be false, because at low temperatures and high pressures gas molecules interact with one another and eventually condense. Furthermore, the strength of the interaction and the finite compressibility are species dependent.

To account for these non-ideal behaviors, J. D. van der Waals proposed a new equation of state (Equation 1.2) in 1873, now commonly known as the van der Waals EOS (VDW). The VDW can be written as

$$\left(P + \frac{an^2}{V^2}\right)\left(\frac{V}{n} - b\right) = RT \tag{1.2}$$

where a and b are empirical parameters. The first parameter, a, is a measure of the interaction between a binary combination of two gas molecules. The a parameter acts on the total pressure, implying that a larger a parameter indicates a stronger interaction between the gas particles. The second parameter, b, is a measure of the finite volume of gas molecules, the larger b becomes, the larger a molecule is. The ideal gas law approximates the VDW at high temperatures and low molar volumes (see Figure 1.9).

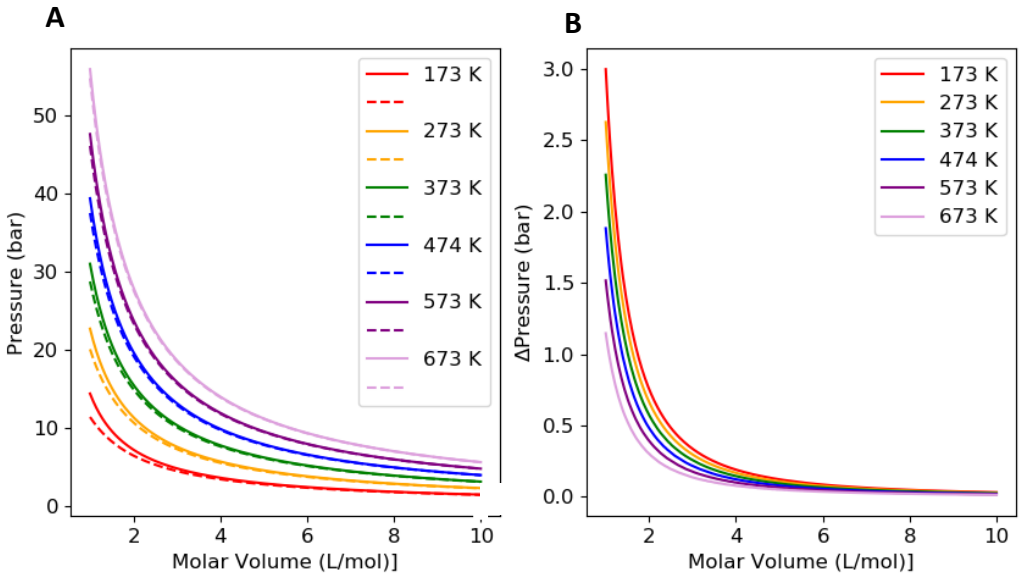

Figure 1.9. (A) Isotherms for the ideal gas law (solid lines) and VDW (dashed lines) at various temperatures. (B) Difference between VDW and the ideal gas law.

Other equations of state are available, such as the Soave-Redlich-Kwong and Peng-Robinson EOS,[72] but these are attempts to improve on the description of the isothermal phase transition from the gas-phase to the vapor-liquid phase and beyond. For this study we have assumed that the VDW is accurate enough to obtain reliable results for the pressure and temperature regions applicable to gas adsorption and separation.

1.6.2 Multi-Component Gases

The influence that each gas species has on the total observed pressure can be expressed in terms of partial pressures if the gas phase is assumed to be ideal (Equations 1.3-1.5). As formulated in the ideal gas law, each gas species contributes equally to the total pressure, regardless of the size of the particles and the interactions that may occur between particles. The expression that is commonly used to define the partial pressure can be written as

$$P_{tot} = \sum_{i}^{N} P_i \tag{1.3}$$

where P_{tot} is the total pressure, P_i is the partial pressure of component i, and N is the total number of gas species. The partial pressure is related to the total pressure *via*

$$P_i = y_i P_{tot} \tag{1.4}$$

where y_i is the mole fraction of species i in the gas phase, defined as

$$y_i = \frac{n_i}{n_{tot}} \tag{1.5}$$

where n_i is the number of particles of component i and n_{tot} is the total number of particles in the system. Partial pressures are used to qualitatively describe the thermodynamic properties of mixtures, both in the gaseous and vapor-liquid equilibrium states. In addition to the assumptions of the ideal gas law, partial pressures reasonably estimate real-gas behavior when the mole fraction of one component approaches unity.[73] However, in the case of mixed real gases, partial pressures are not well defined, owing to the nonlinear dependence of pressure with respect to number of moles of gas.

In order to apply the VDW to gas mixtures, Leland *et al.*[74] proposed the van der Waals one-fluid model (VDW1), which treats the gas mixture as an equivalent pure fluid. The equivalent pure fluid is described by the VDW1 parameters a_m and b_m, much like in the case of pure gases (see Equation 1.2).

The first mixing parameter (a_m, Equation 1.6) is written as

$$a_m = \sum_{i=1}^{N}\sum_{j=1}^{N} y_i y_j a_{ij} \tag{1.6}$$

and is related to the composition-dependent interaction between a binary combination of species i and species j. The binary a-parameter (a_{ij}, Equation 1.7) can be expressed as

$$a_{ij} = a_{ji} = \sqrt{a_{ii}a_{jj}}\left(1 - k_{ij}\right) \tag{1.7}$$

where the a_{ii} and a_{jj} parameters are equivalent to those of the single-component gas VDW EOS for each species.

The parameter k_{ij} is known as the binary interaction parameter, which is scaled by the strength of the interaction between molecules of dissimilar species. Although values of single-component gas parameters are readily available in textbooks and databases, the binary interaction parameter must be measured experimentally. It will be assumed that the binary interaction parameter has a negligible influence on the total pressure of a gas mixture in this study (i.e., $k_{ij} = 0$). The second mixing parameter (b_m, Equation 1.8),

$$b_m = \sum_{i=1}^{N} y_i b_{ii} \tag{1.8}$$

is a representation of the average size of a molecule in the gas phase, with b_{ii} being the b parameter (see Equation 1.2) for component i.

More specialized mixing rules and multi-component gas EOS are utilized for high-precision and specialist calculations, such as biphasic systems.[75,76] Nevertheless, VDW1 is used in this study for its general applicability, simplicity and close relation to the classical VDW.

1.7 ADSORPTION ISOTHERM FUNCTIONS

The gas adsorption isotherm functions that are used throughout this study are discussed in this section. An isotherm function, within the context of this study, is either an empirical or theoretical model that relates the amount of gas that is adsorbed to the total pressure of the gas phase. Measurement of adsorption isotherms lends insight into an adsorbent's capacity and, potentially, its preference for different guests. In many cases experimental results can be supplemented with computational simulations to gain insight into the processes that are occurring. Other than providing insight into phenomena, some interpolative predictions can be made about data that are not necessarily available directly from experiments by using computer simulations.

1.7.1 Single-Component Gas Adsorption

The Langmuir isotherm function[77], that was first published in 1918, describes the adsorption of gases by a uniform surface. The function (Equation 1.9) can be written as

$$n_i(P) = \frac{n_i^{\infty} K_{L,i} P}{1 + K_{L,i} P} \tag{1.9}$$

where $n_i(P)$ is the adsorbed amount, n_i^{∞} is the amount adsorbed when the uniform surface is fully covered with adsorbates, $K_{L,i}$ is the Langmuir isotherm constant that is equivalent to the equilibrium constant of the adsorption process, and P is the pressure of the gas phase. The Langmuir isotherm can be extended to adsorbents with two independent adsorption sites by use of the dual-site Langmuir function,[78] which is written as the sum of two Langmuir isotherm functions.

The Sips isotherm function,[79] published in 1948 by Robert Sips, was designed to describe the adsorption of molecules by heterogeneous catalyst surfaces. The Sips isotherm includes a heterogeneity parameter, which modifies the curvature of the Langmuir isotherm to account for deviations from the ideal uniform surface (where $c_i = 1$, see Equation 1.10). The Sips isotherm is written as

$$n_i(P) = \frac{n_i^{\infty} \left(K_{S,i} P\right)^{c_i}}{1 + \left(K_{S,i} P\right)^{c_i}} \tag{1.10}$$

where $n_i(P)$ is the amount of gas that is adsorbed, n_i^{∞} is the saturation capacity of the gas species, $K_{S,i}$ is the Sips affinity coefficient, c_i is the heterogeneity parameter and P is the pressure. The Sips affinity coefficient is related to the equilibrium constant of the adsorption process, but it should be treated as an empirical parameter. The Sips isotherm has been used to also describe the adsorption of gases by porous materials,[80] indicating that it is useful for more applications than studying catalysts.

1.7.2 Multi-Component Gas Adsorption

Extended gas adsorption isotherms are the natural extension of the single-component gas adsorption isotherms for when there are multiple gases present in the gas phase. Two of these functions are referred to within this study, namely the extended Langmuir isotherm[81] (see Equation 1.11) and the extended Sips isotherm[82] (see Equation 1.12) functions.

The extended Langmuir isotherm function can be written as

$$n_i(P,y) = \frac{n_i^{\infty} K_{L,i} P y_i}{1 + \sum_{j=1}^{N} K_{L,j} P y_j} \tag{1.11}$$

where P refers to the total pressure, and y is a vector containing the gas-phase mole fractions of each component for N components. The effect that each adsorbate species has on the adsorption of component i is expressed by the mixed terms in the denominator.

The extended Sips isotherm function can be written as

$$n_i(P,y) = \frac{n_i^{\infty} \left(K_{S,i} P y_i\right)^{c_i}}{1 + \sum_{j=1}^{N} \left(K_{S,j} P y_j\right)^{c_j}} \tag{1.12}$$

and it is like the extended Langmuir isotherm in most regards, except that the function is written in terms of the Sips isotherm (Equation 1.10).

1.8 ADSORBED SOLUTION THEORY

Adsorbed solution theory (AST) is a thermodynamic model first proposed by Myers and Prausnitz in 1965.[39] It is widely used in the industrial sector to describe and predict MGA isotherms from SGA isotherms of each component. The following section contains a discussion of the thermodynamic theories of solutions and ideal gas mixtures, which can be found in relevant physical chemistry textbooks.[73] Mathematical derivations and assumptions are based on the publications of Myers & Prausnitz,[39] Hefti *et al.*,[80] and Simons.[38] A depiction of the AST thermodynamic system is shown in Figure 1.10.

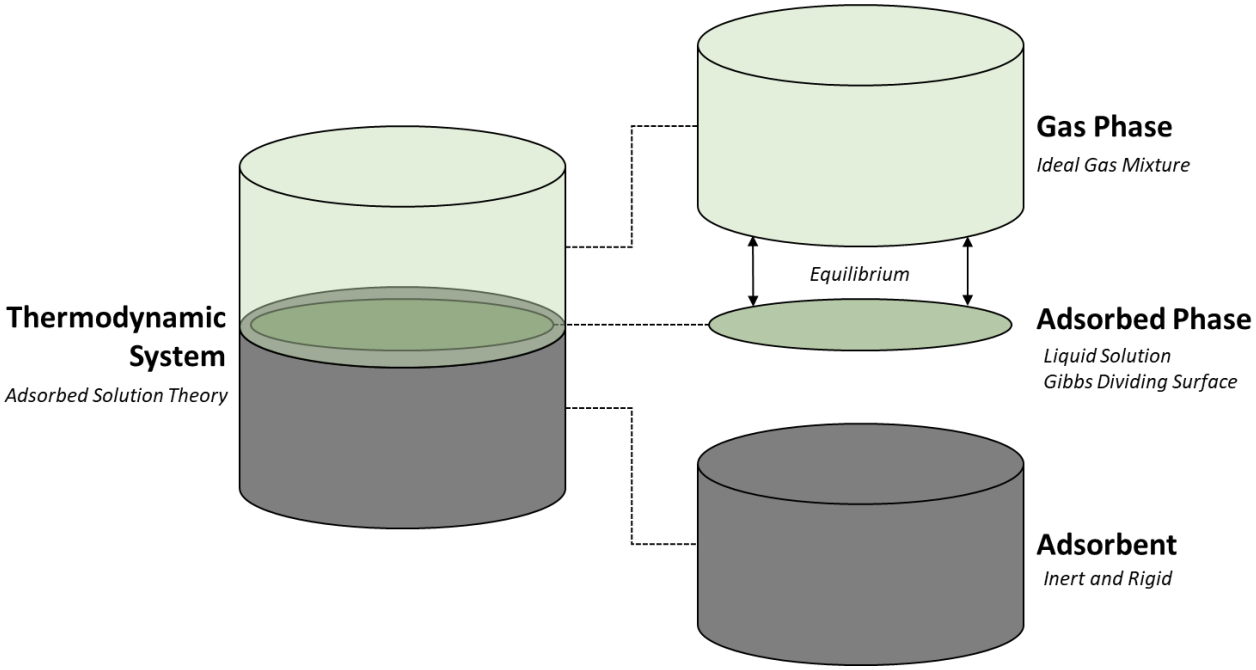

Figure 1.10. Thermodynamic system used in describing AST.

According to Myers & Prausnitz, the Gibbs free energy for the adsorbed phase (Equation 1.13) varies according to

$$dG = -SdT + Ad\pi + \sum_{i=1}^{N} \mu_i dn_i \tag{1.13}$$

where G is the Gibbs free energy, S is the entropy of the adsorbed phase, T is the temperature, A is the surface area of the Gibbs dividing surface, μ_i is the chemical potential, n_i is the quantity of component i, and π is the spreading pressure.

Within the context of surface thermodynamics, spreading pressure is equivalent to surface tension. Conceptually, spreading pressure can be described *via* the two-dimensional work term (πdA), which describes a hypothetical process in which the adsorbed species performs work to increase its surface coverage.

AST utilizes solution thermodynamics theory to describe the adsorbed phase. The changes in Gibbs free energy and entropy (Equations 1.14 and 1.15) due to mixing of two or more components are equal to

$$\Delta G_{mix} = \Delta H_{mix} - T\Delta S_{mix} \tag{1.14}$$

and

$$\Delta S_{mix} = R \sum_{i=1}^{N} n_i \ln(x_i) \tag{1.15}$$

where R is the universal gas constant, and x_i is the mole fraction of component i.

It is usually accepted that there is no enthalpy change upon mixing in AST. Therefore, the change in Gibbs free energy of the multi-component adsorbed phase is solely described by the entropy term (Equation 1.16). Using the single-component adsorbed phase Gibbs free energy (G_i^o) at the same spreading pressure and temperature as a reference state, the total Gibbs free energy of mixing can also be calculated (Equation 1.17). The change in the Gibbs free energy upon mixing can be written as

$$\Delta G_{mix} = RT \sum_{i=1}^{N} n_i \ln(x_i \gamma_i) \tag{1.16}$$

with the total Gibbs free energy of mixing being

$$G_{mix} = \sum_{i=1}^{N} (G_i^o + RT n_i \ln(x_i \gamma_i)) \tag{1.17}$$

owing to the exclusion of the enthalpy of mixing term. Non-ideal behavior (*i.e.*, the excess Gibbs free energy) is accounted for through the incorporation of an activity coefficient (γ_i).

The chemical potential of a system is defined as the partial dependence of the Gibbs free energy on the composition of the system at constant temperature and pressure (Equation 1.18). The chemical potential reduces to the molar Gibbs free energy for a system consisting of only one species and phase. The chemical potential is used when a second phase or chemical species is introduced, as in the case of a solution or multi-component adsorbed phase. The chemical potential of component i in the adsorbed phase is shown in Equation 1.19. The total chemical potential is defined as

$$\mu = \left(\frac{\partial G}{\partial n}\right)_{T,\pi} = \sum_{i=1}^{N} \left(\frac{\partial G}{\partial n_i}\right)_{T,\pi,n_j\,(j \neq i)} = \sum_{i=1}^{N} \mu_i \tag{1.18}$$

with

$$\mu_i = \mu_i^o + RT \ln(x_i \gamma_i) \tag{1.19}$$

where the "reference-state" chemical potential (μ_i^o) is that of the single-component adsorption of species i onto the surface at the same temperature and spreading pressure of the mixture. This

chemical potential is usually denoted as μ_i^* in solution thermodynamics, but this symbol is typically not used in AST literature.

The chemical potentials of the adsorbed and gas phases are equal at equilibrium; therefore, μ_i can be related to the chemical potential of the gas phase (μ_i^g, see Equation 1.20) to relate the composition of the adsorbed phase to the pressure and composition of the gas phase. The chemical potential of component i in an ideal gas mixture with partial pressure P_i and temperature T is

$$\mu_i^g = \mu_i^{o,g} + RT\, ln\left(\frac{P_i}{P_0}\right) \tag{1.20}$$

with $\mu_i^{o,g}$ being the reference-state chemical potential, and P_0 being the standard pressure of the gas species. The reference-state chemical potential of a gas species is conventionally defined as the chemical potential of gas i at $P_0 = 1$ bar.

The chemical potential of the gas phase is equal to the chemical potential of the adsorbed phase at equilibrium. Therefore, Equations 1.19 and 1.20 can be equated and algebraically manipulated to yield (Equation 1.21)

$$\mu_i^{o,g} + RT \ln\left(\frac{P_i}{P_0}\right) = \mu_i^o + RT \ln(x_i\gamma_i) \tag{1.21}$$

which can be rewritten (Equation 1.22) as

$$\frac{P_i}{P_0} = x_i\gamma_i e^{\frac{\mu_i^o - \mu_i^{o,g}}{RT}} \tag{1.22}$$

resulting in one of the core expressions of adsorbed solution thermodynamics.

Considering the scenario where x_i approaches unity, and γ_i reaches unity by default – since the activity of the pure component is simply the concentration, (see Equation 1.23) results in the expression

$$P_i^o = P_0 e^{\frac{\mu_i^o - \mu_i^{o,g}}{RT}} \tag{1.23}$$

that can be substituted into Equation 1.22, leading to Equation 1.24, written as

$$P_i = P_i^o x_i\gamma_i \tag{1.24}$$

which is a relation analogous to Raoult's Law for multi-component vapor-liquid equilibria.

The new quantity, P_i^o, is defined as the pressure at which the single-component adsorption of component i would have the same spreading pressure (see Equation 1.13) as the mixture. This

definition can be extended to each component in the mixture to yield N P_i^o terms that are all at the same spreading pressure π (see Equation 1.25). The spreading pressure of each component and the mixture is, therefore, written as

$$\pi = \pi_1(P_1^o) = \pi_2(P_2^o) = \cdots = \pi_N(P_N^o) \tag{1.25}$$

and is a core constraint that is used to solve AST equations.

Spreading pressure can be determined by manipulation of the Gibbs isotherm for surfaces. The Gibbs free energy of the adsorbed phase at constant spreading pressure, temperature, and composition (Equation 1.26) can be written as

$$G = \sum_{i=1}^{N} \mu_i n_i \tag{1.26}$$

which is the integral of Equation 1.13 at constant temperature, spreading pressure, and adsorbed-phase composition.

However, if the composition and the chemical potentials were to be changed infinitesimally (see Equation 1.27), then the Gibbs free energy is expected to change according to

$$dG = \sum_{i=1}^{N} \mu_i dn_i + \sum_{i=1}^{N} n_i d\mu_i \tag{1.27}$$

which is the total differential of Equation 1.26.

The Gibbs-Duhem equation for the adsorbed phase at constant temperature, or Gibbs isotherm, (Equation 1.28 and Equation 1.29) is obtained by subtraction of Equation 1.27 from Equation 1.13 and rearrangement of the terms. The Gibbs isotherm for a mixture of species can be written as

$$Ad\pi = \sum_{i=1}^{N} n_i d\mu_i \tag{1.28}$$

with n_i being the adsorbed quantity of component i. Equation 1.28 reduces to

$$Ad\pi_i = n_i d\mu_i^o \tag{1.29}$$

when there is only one component present in the adsorbed phase.

The dependence of the chemical potential of the adsorbed phase consisting of only one component (*i.e.*, μ_i^o) on the pressure can be shown to be

$$\frac{d\mu_i^o}{dP} = RT\frac{1}{P} \tag{1.30}$$

from Equation 1.21. The reference-state chemical potential of the gas phase ($\mu_i^{o,g}$) is a constant value and the entropy term (*i.e.*, $RT\ln(x_i\gamma_i)$) is pressure independent; therefore, these terms are not present in the derivative of Equation 1.21. Equation 1.30 can then be resubstituted into Equation 1.29 to yield

$$\frac{Ad\pi_i}{RT} = \frac{n_i(P)}{P}dP \tag{1.31}$$

where $n_i(P)$ is given by the SGA isotherm of component i. The relationship shown in Equation 1.31 can be integrated to calculate the spreading pressure for component i. A core assumption of AST is that the surface area of the adsorbed phase (A) is proportional to only the spreading pressure – regardless of the composition of the adsorbed phase (see Equation 1.32). It is, therefore, useful to rewrite Equation 1.25 as

$$\Pi = \frac{A\pi}{RT} = \frac{A\pi_1}{RT} = \cdots = \frac{A\pi_N}{RT} \tag{1.32}$$

with Π referred to as the reduced surface potential. Consequently, the constraint shown in Equation 1.32 can be employed to equate the reduced surface potential for each gas species *via* the integral of Equation 1.31. Equation 1.33, the result of this substitution, can be written as

$$\Pi = \int_0^{P_1^o} \frac{n_1(P)}{P}dP = \int_0^{P_2^o} \frac{n_2(P)}{P}dP = \cdots = \int_0^{P_N^o} \frac{n_N(P)}{P}dP \tag{1.33}$$

and it is used to calculate the P_i^o terms used in Equation 1.24.

Talu[83] derived an expression (Equation 1.34) that can be used to calculate the total amount adsorbed which can be written as

$$\frac{1}{n_{tot}} = \sum_{i=1}^{N} x_i \left[\frac{1}{n_i(P_i^o)} + \frac{\partial \ln(\gamma_i)}{\partial \Pi}\right] \tag{1.34}$$

and is an extension of the expression used by Myers and Prausnitz for non-ideal mixtures of adsorbates.

In the ideal case of AST (referred to as IAST), where the activity coefficients are equal to 1 for all species, one needs to solve for four parameters (P_1^o, P_2^o, x_1, x_2) if there are two adsorbate species present in the system. This is achieved by using Equation 1.24 (one equation for each species), Equation 1.33, and the mass balance (*i.e.*, $\sum x_i = 1$). This means that there are four equations and four parameters, and IAST can be solved exactly – provided that the partial pressure of each gas species is specified and that the isotherm for each gas species in isolation has been fitted to an isotherm function. However, in the non-ideal (real) case of AST (referred to as RAST), the activity coefficients

(γ_1 and γ_2) must be calculated and, consequently, additional equations are required. A popular activity coefficient model that is used for this purpose is the Wilson equation that was developed for non-ideal solutions.[84–87]

1.9 COMPUTATIONAL METHODS

In addition to the thermodynamic theories that are used in this study, a variety of computational simulations and methods are also employed. These techniques can be used to study the finer aspects of adsorption that are difficult to measure experimentally, such as the locations and the interaction energies of guest molecules in crystalline porous adsorbents too small to study with single-crystal X-ray diffraction. Dynamic processes that occur within the adsorbent can be studied on the molecular[88] and even the electronic[89] time scale. The value of these computational techniques lies within the unique insights that these methods provide, and the rate at which *in silico* experiments can be completed. Modern molecular mechanics and electronic structure theory calculations approximate experimental observations with staggering accuracy at a fraction of the cost of materials and instrumentation.[90,91] Nevertheless, these methods are defined by the experiments that precede them – one cannot exist without the other; the computational methods used in this study supplement and, potentially, explain the interesting phenomena that will be observed in the later chapters.

1.9.1 Molecular Mechanics

Molecular mechanics (MM) is a classical approach to describe the energy of a spatial configuration of atoms and bonds. According to Bowen and Allinger,[92] in MM all atoms are treated as charged and weighted spheres bound together by near-harmonic oscillators. The near-harmonic oscillator equations describe bond, angle, torsion, and out-of-plane distortions along with cross terms. In addition, intermolecular interactions (see Section 1.2) can also be incorporated into the total energy summation of the system. Electrons are not explicitly included within the calculation of the total energy, by the Born-Oppenheimer approximation,[93] which states that electronic motions occur many orders of magnitude faster than nuclear motion. Therefore, throughout an MM simulation, electrons are assumed to adopt their most stable distribution faster than any perturbation of nuclear geometry can take place.

The total potential energy of a system, based on MM theory, is a sum across all contributions of intramolecular and intermolecular interactions.[92] The parameters that can be used to calculate the potential energy of atoms and bonds in MM are contained in a specialized list of definitions, commonly referred to as a forcefield. Forcefields contain equilibrium bond lengths, angles, torsion

angles with corresponding force constants describing their distortions, as well as atomic masses, atomic charges, and Lennard-Jones[94,95] parameters. Most well-defined forcefields, with the exception of the Universal Forcefield,[96] only contain a highly specialized set of potential energy parameters with a particular application in mind, such as drug molecule docking, vibrational analysis, conformational analysis and various adsorption simulations.[97]

Although MM theory cannot describe more fine-grained quantum mechanical phenomena,[98] MM simulations are preferred over *ab initio* simulations in situations where large-scale calculations (10^2-10^8 atoms)[99] are performed in rapid succession, such as in the case where adsorption by porous materials is studied.

1.9.2 Metropolis Monte Carlo Simulations

The adsorbed phase can be thought of as a statistical distribution of adsorbate molecules that frequent favorable positions (*i.e.*, adsorption sites) of the adsorbent framework. Locating the adsorption sites by hand or by conventional MM simulations would be a time-consuming and a non-trivial task. Instead, if one were to distribute guest molecules randomly throughout the framework over an immensely large number of iterations and calculate the energy of the configurations, then one would have a greater success rate with describing the adsorbed phase completely. This type of methodology can be found in the Metropolis algorithm[100] for Monte Carlo simulations. Monte Carlo (MC) simulations are massive-scale uniform samplings of statistical configurations used to approximate the true distributions of probabilistic outcomes.[101] Owing to the scale of the MC simulations, the MM level of theory will be used.

In terms of statistical thermodynamics and chemistry, the distributions sampled by MC are referred to as ensembles of the Boltzmann distribution.[71] Three state parameters are fixed in a thermodynamic ensemble, while others are allowed to vary. Two thermodynamic ensembles are utilized in this study, namely the canonical ensemble (NVT) and the grand canonical ensemble (μVT). The canonical ensemble describes a system that has a fixed number of particles (N) that are confined in fixed volume (V) at constant temperature (T). The grand canonical ensemble, on the other hand, describes a system with a fixed volume (V) that is in equilibrium with an infinitely large reservoir of particles at a specified temperature (T) and pressure (μ, see Equation 1.20).

MC simulations are compatible with both the canonical ensemble and the grand canonical ensemble.[102] Functionally, MC simulations of the canonical ensemble (CMC) are used to describe the spatial and energetic distributions of particles in the adsorbed phase. Grand canonical MC

simulations (GCMC), on the other hand, are used to calculate the uptake of gas molecules at a specified pressure. Although these simulations are inherently similar, the outcomes of the calculations will be used for different purposes. GCMC simulations will be used to determine whether an appropriate description (*i.e.*, forcefield parameters and atomic charges) is being used for the adsorbent and adsorbates. This will be achieved by comparing the SGA isotherms that were obtained by GCMC simulations to the experimental SGA isotherms. CMC simulations, on the other hand, will be used to investigate the interaction strengths and adsorption sites of different gas molecules in SGA and MGA.

1.9.3 Density Functional Theory

Density functional theory (DFT)[103–105] is an approximate solution to the many-electron Schrödinger equation. As opposed to the classical Hartree-Fock[106] method where the electronic wavefunction is used to calculate the electronic ground-state energy of a system, DFT utilizes the electron density to do the same. Furthermore, DFT can account for electron correlation, which is not considered in the Hartree-Fock theory. Electron density, by the Born interpretation, is the square of the absolute value of the quantum mechanical wavefunction. However, where the wavefunction is effectively an immeasurable probability distribution, electron density is an experimental observable – such as in the case of X-ray diffraction. Notably, the true value of DFT lies in the price-to-performance ratio[107] of the method, relative to its quantum mechanical counterparts. Although the method can be used to calculate the outcome of several physicochemical phenomena (such as electronic excitations, chemical reactions, and so forth), it will be used in this study specifically to calculate the partial charges and optimize the spatial coordinates of framework atoms in solid adsorbents.

1.10 OBJECTIVES

Multi-component gas adsorption (MGA) is still in its nascent phase of development, both in terms of the experimental techniques and the thermodynamic treatment of the non-ideal adsorption of gases. Furthermore, the study of the adsorption of mixtures of CO_2 and N_2 are of cardinal importance so that better, more efficient, and economical processes can be developed to counteract climate change by treating the problem at its source.

This study will, therefore, be focused on developing methods of MGA analysis from both the theoretical and experimental frontiers. An MGA analyzer will be developed, from the ground up, to study the uptake of CO_2 and N_2 by different adsorbent materials at elevated pressures. These

experimental data will be used as an impetus to make improvements on predictive AST, if necessary. Lastly, the modes of adsorption of the two gas species by a series of adsorbent materials will be studied *in silico*, so that a more intuitive understanding can be gained of the actual adsorptive processes described by the theory.

1.11 THESIS OUTLINE

Chapter 2 includes information about the thermal, X-ray diffraction, and adsorption analyses. The software used to perform multivariate optimizations, curve-fitting, and make graphics are also discussed. Lastly, the software that were used to perform molecular mechanics, density functional theory, and Metropolis Monte Carlo simulations or calculations are outlined.

The development of an MGA analyzer and the measurement of the SGA and MGA isotherms of CO_2 and N_2 into zeolite 13X[108] with this instrument are discussed in Chapter 3. The results from the multi-component gas adsorption isotherms are compared to two predictive models, namely the extended Sips isotherm and the IAST.

Using the findings from Chapter 3, a new predictive AST method (PRAST-S) and activity coefficient model (virial activity coefficient model) are introduced in Chapter 4. PRAST-S, like IAST, can be used to predict MGA isotherms from SGA isotherms, but it allows for non-ideal adsorption behavior *via* activity coefficients that are also calculated from SGA isotherms. The PRAST-S method is benchmarked against experimental MGA data of 13X. The MGA isotherms of CO_2 and N_2 uptake by Cu-HKUST-1,[109] MOF-14,[110] Mg-MOF-74,[111] and UiO-66[112] are predicted up to 10 bar using the PRAST-S method. The MGA isotherms of mixtures of CO_2 and N_2 by Cu-HKUST-1 are also measured up to 3 bar and compared to the PRAST-S method's results.

It is shown in Chapter 4 that the simultaneous adsorption of CO_2 and N_2 is ideal for Cu-HKUST-1 and non-ideal for 13X in the same pressure and gas-phase composition range. Specifically, the MGA isotherms of Cu-HKUST-1 match IAST results, while the MGA isotherms of 13X must be described using activity coefficients. A series of canonical Monte Carlo and molecular mechanics simulations are used to study the interaction of gas mixtures with the frameworks of Cu-HKUST-1 and 13X in Chapter 5. It is shown that ideality is linked to the adsorption of guest molecules in spatially and energetically independent adsorption sites, while non-ideal behavior is caused by one species of guest molecules forcing the other species into more favorable adsorption sites.

Chapter 6 contains the summary and conclusions of the findings of this study. Unexplored research routes are highlighted, and recommendations for improvements on theoretical methods and experimental MGA techniques are made.

Chapter 2. Materials and Methods

2.1 ABSTRACT

The experimental methodologies and the software that are used throughout this study are outlined in this chapter. The thermal and characterization techniques that were used to investigate the physical properties of adsorbent materials in this work are discussed. An overview of the development of the multi-component gas adsorption instrument, and accompanying software, is given. Lastly, the software packages that were used to perform data analysis, multivariate calculations, and computational simulations are introduced.

2.2 EXPERIMENTAL METHODS

2.2.1 Materials and Analytical Gases

Adsorbents, starting materials, solvents, and analytical gases were used as purchased and without further purification. Specific experimental and sourcing details regarding adsorbent materials and analytical gases can be found in the appendices of Chapters 3 and 4.

2.2.2 Thermogravimetric Analysis

Thermogravimetric analysis (TGA) was performed on a *TA Instruments Q500*. Samples of 5-7 mg were weighed on a high-precision ($\pm 1 \times 10^{-5}$ g) scale and transferred to an aluminum crucible. The aluminum crucible was then transferred to a sealed furnace. The sample was heated from room temperature up to 600 °C at a rate of 10 °C min^{-1} under a constant flow of nitrogen at 50 mL min^{-1} and the loss of weight was recorded over time. These thermogram data were converted to a numerical form using the *TA Universal Analysis 2000* software.

2.2.3 Powder X-Ray Diffraction

Powdered adsorbent samples were placed on a zero-background sample plate and inserted into a *Bruker D2 Phaser* for powder X-ray diffraction (PXRD) analysis. The diffractometer is equipped with a Cu-K_α X-Ray source ($\lambda = 1.54184$ Å) and *Lynxeye* 1-D detector. PXRD data were collected in the angular scanning range of 5-40°, with a step size of 0.01617°, at atmospheric pressure and operating temperatures ($T \approx 40\ ^\circ C$).

2.2.4 Sample Activation

Adsorbent samples that were intended for adsorption experiments were activated at elevated temperatures and under dynamic vacuum (~1.8×10^{-3} mbar) for 24-48 hours in a *Büchi* furnace. The temperature of the furnace and the duration of the activation procedure required is dependent on the adsorbent material and is specified in Appendices A and B.

2.2.5 Volumetric Adsorption Analysis

2.2.5.1 Single-Component Gas Adsorption

Volumetric adsorption analysis is a technique for measuring adsorption indirectly by determining the change in the pressure, which is equivalent to the density, of the gas phase (see Section 1.6). The Gibbs' phase-rule for gas adsorption on an inert adsorbent[39] is described by Equation 2.1. The phase rule can be written as

$$F = C - P + 3 \tag{2.1}$$

where F is the degrees of freedom, C is the number of components in the gas phase and P is the number of phases present. There is one component and two phases (adsorbed and gas phase) in single-component gas adsorption (SGA), implying that two intrinsic state parameters need to be measured to fully describe the system. The two parameters most easily measured are temperature, kept constant by default, and pressure, which is varied over the adsorption process.

The phase rule is useful for determining the amount of information necessary to describe all the intrinsic parameters of the gas phase. In practice, however, two other quantities are measured to scale the adsorption experiment, namely the activated mass of adsorbent and the "dead" volume.[58] The activated mass is the mass of adsorbent material left after all adsorbate molecules have been removed; the dead volume is the volume of the sample chamber less the volume taken up by the activated material. For porous materials, the dead volume is determined using a gas that is assumed to not interact with the host framework, such as helium. By expanding a known amount of helium gas at sub-atmospheric pressures into an adsorption vessel containing the sample, the dead volume is readily measured (see Section 2.2.5.4 for more details).

A depiction of a volumetric single-component gas adsorption (SGA) experiment is shown in Figure 2.1. The number of particles present in the gas phase can be calculated at both the initial and equilibrium pressures using the van der Waals equation of state (see Section 1.6.2). The dead volume and temperature are known, and the pressure change between the initial and equilibrium states can be measured to quantify the adsorbed amount.

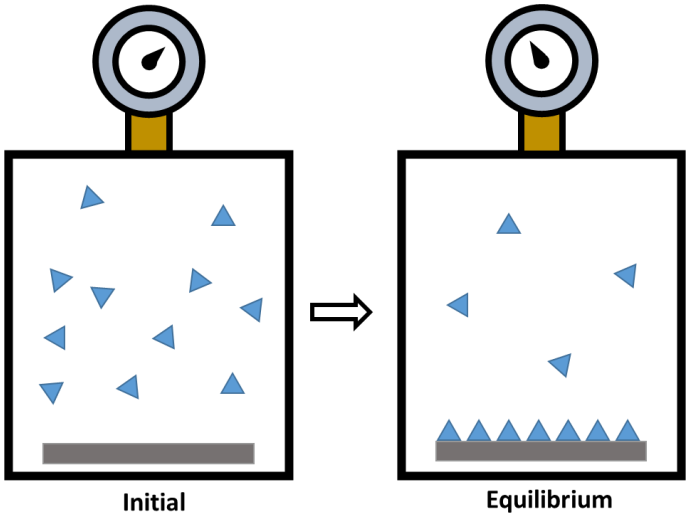

Figure 2.1. Depiction of a volumetric SGA experiment.

For practical efficiency, volumetric adsorption is generally performed as a series of pressure ramps – commonly known as doses. Each equilibrium is treated as the initial condition for the next adsorption step, with loading measured cumulatively.

2.2.5.2 Multi-Component Gas Adsorption

Volumetric multi-component gas adsorption (MGA) measurements have three degrees of freedom, owing to an increase in the number of components in the system (see Figure 2.2). In other words, an additional parameter must be measured to quantify the adsorbed amount of each gas species. Although the change in pressure can be used to determine the total amount of gas adsorbed (*i.e.*, if the gas mixture is assumed to be ideal), the amount of each gas species that is adsorbed cannot be determined from this data alone. It is, therefore, necessary to measure the change in the composition of the gas phase between the initial and equilibrium states to fully describe the content of the adsorbed phase at equilibrium.

The removal of gas molecules from the headspace, for the purposes of compositional analysis (*e.g.*, mass spectrometry or gas chromatography), would perturb the system, considering that the amount adsorbed is dependent on the total pressure and the gas-phase composition. This implies that additional experimental steps need to be introduced to perform MGA measurements correctly. Specifically, the headspace volume needs to be split so that the gas-phase composition can be determined without disrupting the equilibrium that has been established.

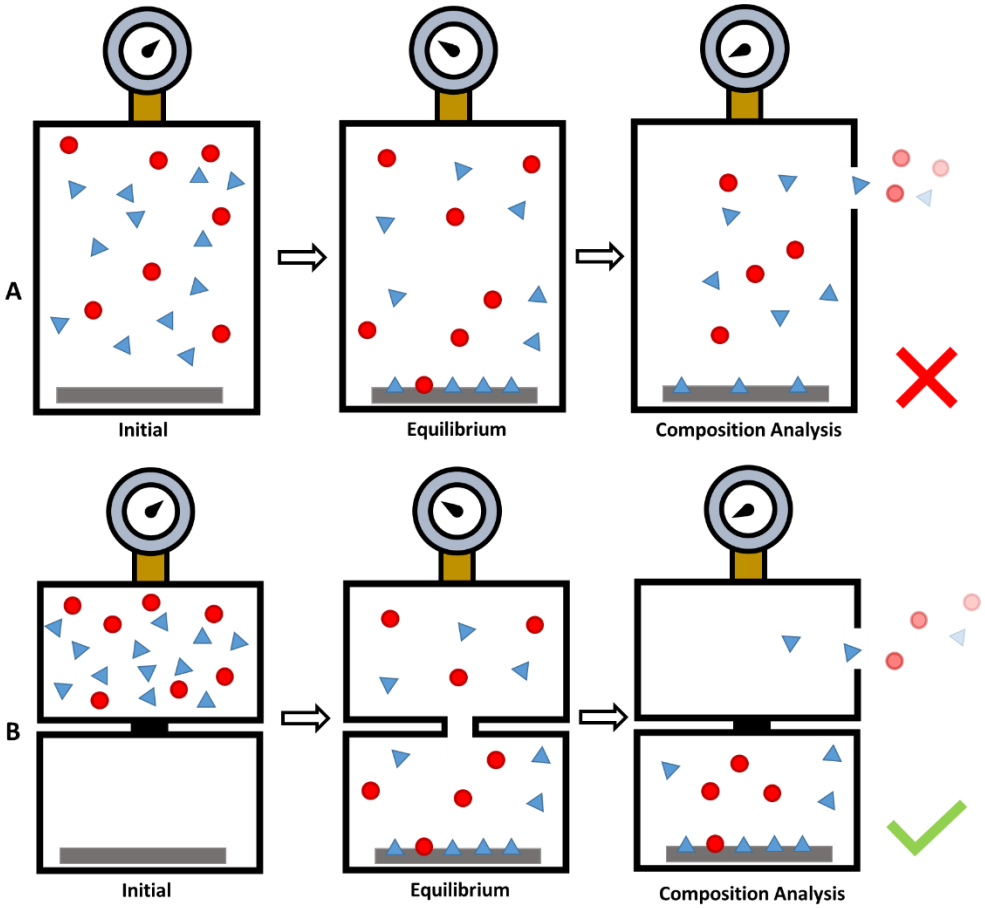

Figure 2.2. Depiction of a volumetric MGA experiment performed (A) incorrectly and (B) correctly.

2.2.5.3 *Adsorption Apparatus*

MGA experiments were performed on a purpose-built instrument (see Figure 2.3) that was developed from the ground up by the author, in collaboration with Professor Leonard J. Barbour of Stellenbosch University. This automated instrument can be used to measure the adsorption equilibria of gas mixtures between vacuum and 3 bar and the adsorption equilibria of single-component gases between vacuum and 10 bar.

The instrument consists of three parts: (1) a gas-supply rig, (2) a volumetric adsorption analyzer, and (3) a *Setaram RGAPro 200* residual gas analyzer (RGA). The instrument is controlled by software (*MULTIDOSER*) that was developed, alongside the instrument.

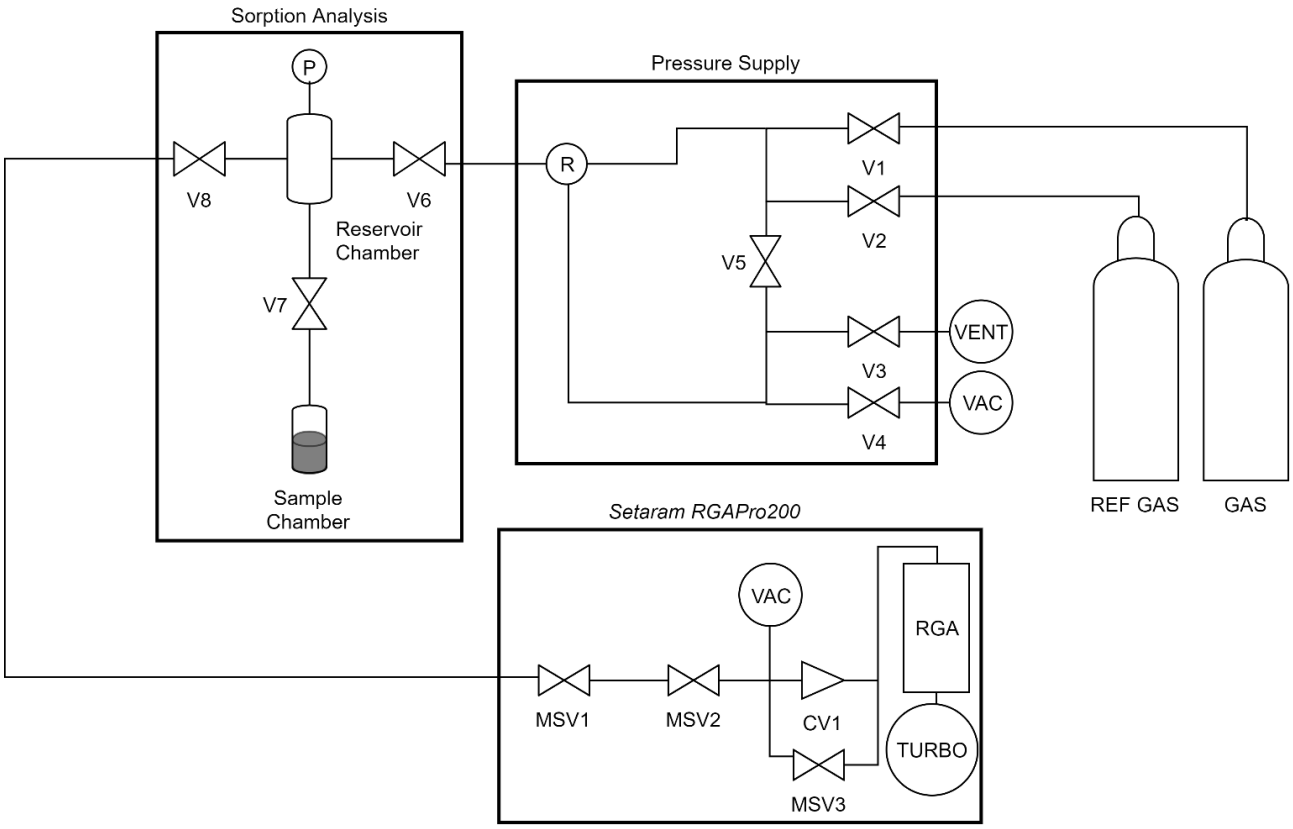

Figure 2.3. Components of the adsorption instrument, including the pressure-supply manifold, the adsorption-analysis manifold, and the *Setaram RGAPro* 200. (Symbols. P = Pressure sensor, R = Pressure regulator, V = Valve, MSV = Valve located in RGA manifold, CV = Pressure-regulating aperture, VAC = vacuum pump, TURBO = Turbomolecular pump, RGA = RGA probe, VENT = Vent pipe, GAS = Analytical gas or gas mixture cylinder, REF GAS = Helium gas cylinder.

Some of the algorithms used in the instrument software (*MULTIDOSER*) are outlined in Figure 2.4. Subroutines are introduced as green-colored headings. Called subroutines are shown in black, and the logical tests are shown as diamonds. Some of the steps in these algorithms, such as waiting a set period, are omitted.

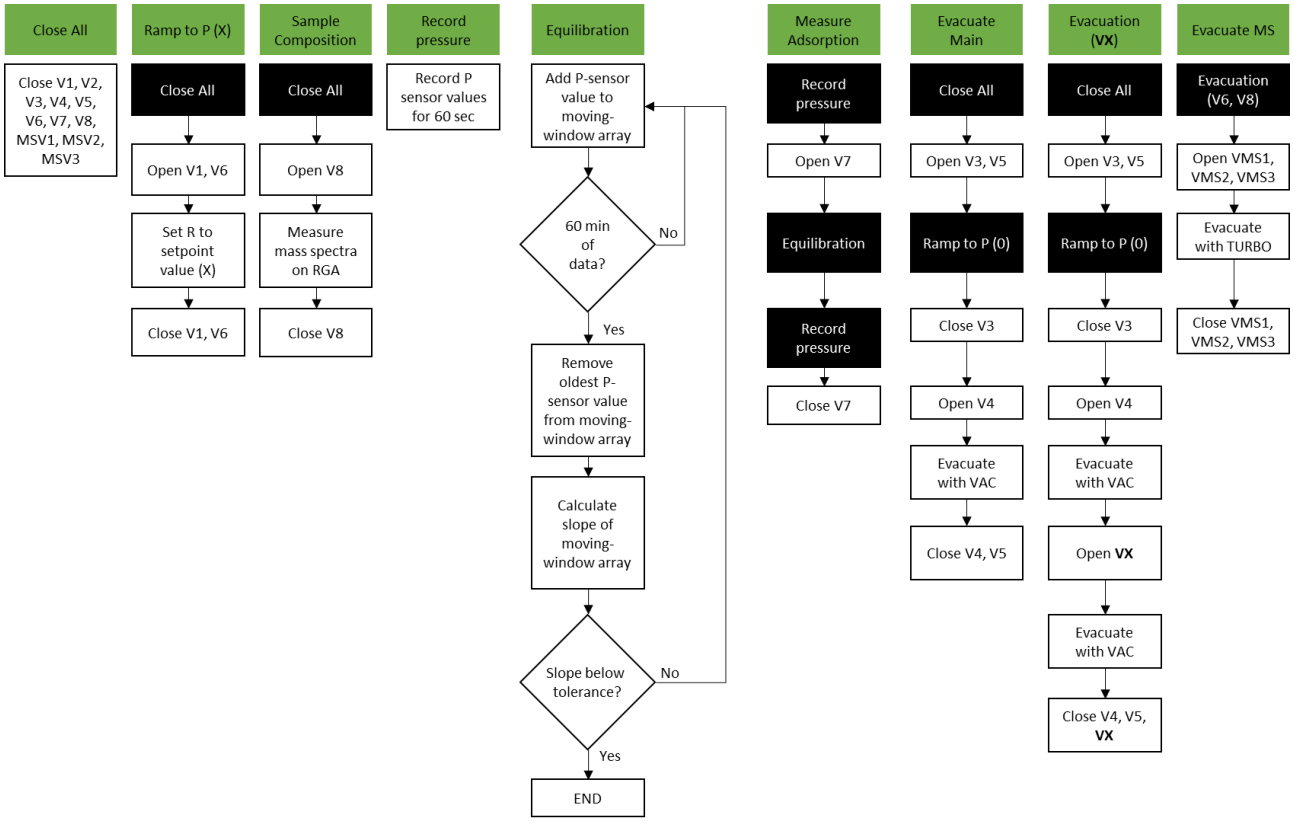

Figure 2.4. Some of the main algorithms that are used by the *MULTIDOSER* software to perform an MGA or SGA experiment.

The main loop of the adsorption analysis program of *MULTIDOSER* is shown in Figure 2.5. Given an array of dosing pressures (P), the instrument will follow a predetermined procedure until all the values in P have been completed. The procedure is started once the weighed activated adsorbent sample is loaded into the sample chamber of the instrument. The sample is evacuated *in situ* on the instrument in the *Evacuation (V6, V7)* step of the experiment to ensure that all moisture captured by the adsorbent during transfer is removed. During an SGA experiment, the system simply ramps to each pressure specified in P and measures the adsorbed amount. MGA experiments require a few extra steps: the composition of the supply-gas is measured, then the adsorbed amount is measured, and, finally, the composition of the headspace post-adsorption is measured in the manner discussed in Section 2.2.5.2. This procedure is used to measure many MGA equilibria in a sequence without having to reactivate the adsorbent sample. On completion of the experiment, the pressure-supply rig and RGA are brought to vacuum, but the equilibrium within the sample chamber is maintained in case another pressure dose is desired.

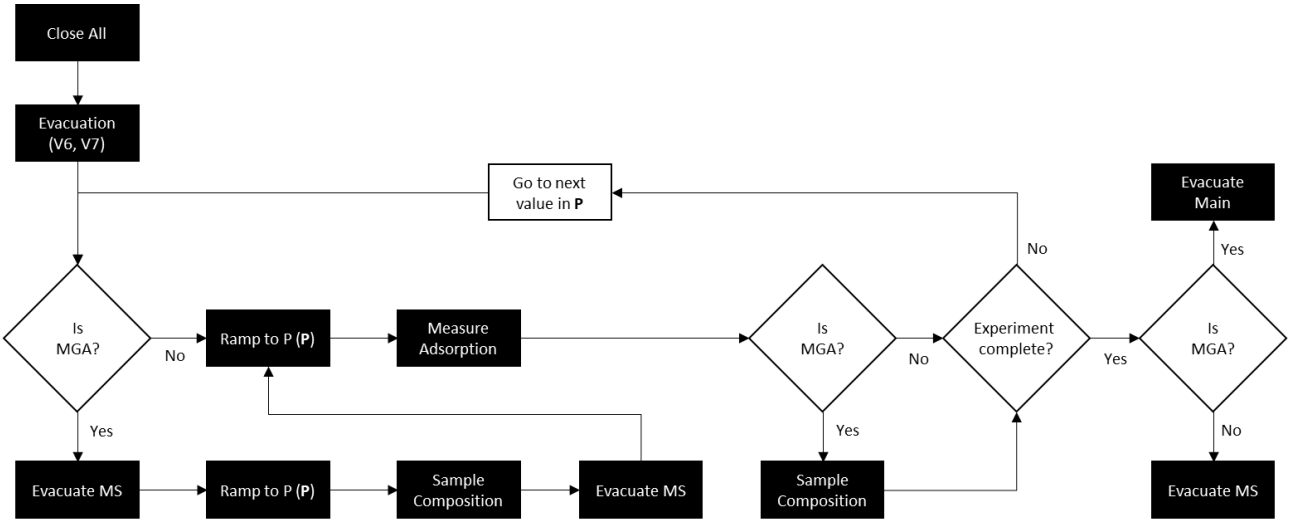

Figure 2.5. Main loop of an SGA or MGA adsorption experiment.

2.2.5.4 Calibration

Pressure sensors and electronic regulators were calibrated against a *WIKA* high-precision pressure gauge. Thermocouples were calibrated against a *Signstek* 6802 II dual channel digital thermometer within the range of 10 °C to 50 °C.

The volumes of the reservoir chamber and sample chamber were measured *via* a helium expansion (see Figure 2.6). In the first expansion (1→2 in Figure 2.6), the sample chamber is initially at vacuum. In the second expansion (3→4 in Figure 2.6), a reference stainless-steel cylinder (V = 0.848 mL @ 25 °C) is included within the sample chamber. The reservoir chamber and sample chamber volumes are determined by solving the ideal gas law (see Section 1.6.1) for both helium expansions simultaneously. The dead volume (see Section 2.2.5.1) was measured using a single expansion of helium from the reservoir chamber into the sample chamber containing the adsorbent material.

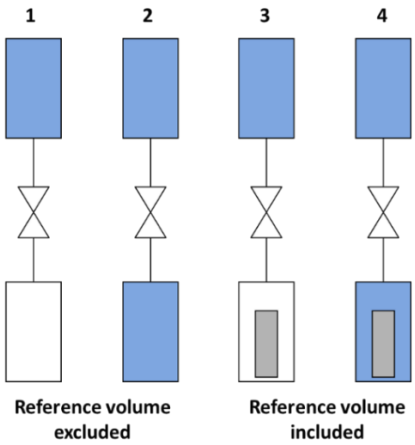

Figure 2.6. Volume calibration of the sample chamber and the reservoir chamber in the volumetric adsorption analyzer. Blue colored volumes indicate the presence of helium gas, while white colored volumes indicate a vacuum.

Calibration of the mass spectrometer was achieved by measuring mass spectra of gas-mixture standards (0%, 20%, 40%, 60%, 80%, 100% CO_2 with the balance being N_2) at various pressures (see Appendix A).

2.3 COMPUTATIONAL METHODS

2.3.1 BIOVIA Materials Studio

2.3.1.1 Materials Visualizer

The *Materials Visualizer* is the graphical user interface (GUI) that allows for the creation and visualization of molecular and periodic structures in *Materials Studio 2018*.[113] The visualizer is used to generate input documents for simulation modules. Properties, such as atomic coordinates, element types, atomic charges, forcefield definitions, positional constraints, and more, are stored in a single document, which can be transferred to a module for a computational task to be performed.

2.3.1.2 Forcite Plus

Forcite Plus is a collection of molecular mechanics (see Section 1.9.1) simulation tools available in *Materials Studio 2018* and *Materials Studio 2019*. The forcefield of choice throughout this study is COMPASSII,[97] as it contains all the necessary parameters for the systems used. *Forcite Plus* can perform a variety of tasks, such as single-point energy calculations (*Energy* task), geometry optimizations (*Geometry Optimization* task), and molecular dynamics (*Dynamics* task). The user has the option to use predetermined forcefield atomic partial charges, quantum mechanical partial atomic charges, or partial charge estimation using the Molecular Charge Equilibration[114] (QEq) method.

2.3.1.3 Sorption

The *Sorption* module allows for the simulation of pure-gas and mixed-gas adsorption inside a compatible porous periodic framework. The *Fixed loading* (canonical Metropolis Monte Carlo simulation, see Section 1.9.2) task was performed to determine the minimum energy adsorbate positions in the porous material. The *Fixed pressure* and *Adsorption isotherm* (Metropolis grand canonical Monte Carlo simulation, see Section 1.9.2) tasks simulates the porous adsorbent framework (treated as an open system) in equilibrium with an infinitely large adsorbate source, or reservoir, at fixed pressure.

2.3.1.4 CASTEP

CASTEP[115] is a density functional theory-based (see Section 1.9.3) program that was designed with solid-state materials is mind. *CASTEP* uses plane-wave basis sets, as opposed to the classical atom-centered basis sets, that are better suited to calculate the electronic properties of a periodic system. The GGA-PBE functional,[103–105] alongside Grimme's DFT-D3[116,117] dispersion correction, was used to optimize the description of the electron density of periodic (i.e., adsorbent) systems and to calculate the partial charges of atoms using either the Mulliken or Hirshfeld population analysis schemes. A k-point sampling of 1x1x1 was chosen with a separation of 0.04 $Å^{-1}$. The SCF tolerance was set at 1×10^{-6} eV $atom^{-1}$.

2.3.1.5 MaterialsScript application programming interface

The *MaterialsScript* application programming interface (API) was used to rapidly perform vast numbers of tasks in succession. The *MaterialsScript* API can perform any task that a standard user can accomplish using the GUI. *Materials Studio 2018* has a built-in code editor for writing and debugging programs written in Perl. Any function that is available in the base version of Perl is also included, such as general mathematical, numerical, and string manipulation functions.

2.3.2 Python

Experimental data (pressure, temperature, and mass spectral data) that were obtained from the adsorption instrument (see Section 2.2.5.3) were processed using the *numpy*[118] (numerical methods), *pandas*[119] (data structures and management), *thermo* (physicochemical properties and functions, see https://github.com/CalebBell/thermo), and *matplotlib*[120] (data visualization) modules.

2.3.3 MATLAB

MATLAB R2019b was used to perform multivariate optimization calculations to solve adsorbed solution theory calculations (see Section 1.8). The *fmincon*, *GlobalSearch*, and *MultiStart* algorithms were used extensively to find minima of systems of equations.

Chapter 3.

Adsorption Isotherms for Multi-Component Gases at Elevated Pressures: Measurement *vs* Prediction

The following chapter is an adapted version of a submitted publication manuscript. (*Chemical Science*)

Contributions by the Author

- Design of the project with Prof. Leonard J. Barbour and Prof. Catharine Esterhuysen.
- Thermal and PXRD analyses of zeolite 13X.
- Development of MGA instrument in collaboration with Prof. Leonard J. Barbour.
- Calibration of MGA instrument sensors and detectors.
- SGA and MGA analyses of CO_2 and N_2 with 13X.
- IAST calculations and curve-fitting procedures.
- Interpretation of the results with Prof. Catharine Esterhuysen.
- Writing the first draft of the article.

3.1 ABSTRACT

Experimental results for the binary adsorption of CO_2 and N_2 on zeolite 13X, over a moderate range of pressures and compositions, obtained using an in-house built volumetric adsorption apparatus combined with mass spectrometry confirm that zeolite 13X selectively adsorbs CO_2 in comparison to N_2. Although selectivity diagrams indicate that 13X selectively adsorbs CO_2 over N_2 at low pressures, the selectivity for CO_2 decreases significantly as the total pressure is increased. The experimental adsorption results allow us to make recommendations regarding the use of theoretical models for predicting multi-component gas adsorption based on pure-gas adsorption data. Although the commonly used Ideal Adsorbed Solution Theory (IAST) correctly predicts individual gas uptake under low-pressure mixed-gas conditions, large deviations from theory are observed beyond 1 bar and at higher concentrations of N_2. Consequently, IAST should only be used to predict selectivity at low pressures since it overestimates CO_2 selectivity by 13X in the presence of N_2 at pressures above 1 bar. Instead, the extended Sips isotherm should be used at higher pressures since it yields a more accurate representation of selectivity under these conditions.

3.2 INTRODUCTION

Adsorption is the process whereby a guest molecule (sorbate) is included into the bulk of a porous host material (adsorbent) from the surroundings. It is a vital step in many important multi-step processes involving porous materials, such as heterogenous catalysis,[121] drug binding and delivery,[122,123] water capture[124] and gas separations. Gas separation by means of selective adsorption is critically important for a number of applications, including the generation of affordable medical-grade oxygen[125] and on-site generation of liquid nitrogen,[126] and it is also considered a potential alternative[127] to amine scrubbing for carbon capture and storage. Some examples of porous materials that are used as gas-separation media include zeolites[128] and metal-organic frameworks (MOFs).[129,130] Although much research has been carried out in this regard, especially for MOFs in recent years, there is still a profound lack of information on adsorptive capabilities under mixed-gas conditions, despite the wide use of adsorption as a means of separating gases.

Of the various industrial approaches to gas purification, few are as versatile as pressure swing adsorption (PSA).[36] Gas separation by PSA is conceptually a two-step process. Ideally, the target component of a gas mixture is selectively trapped by an adsorbent at relatively high pressures during the first step, while the remainder of the components are excluded and subsequently vented from the system. In the second step, the pressure is reduced, and the trapped components are released from the adsorbent as an enriched gas mixture. Much of the crucial information needed to optimize such a PSA

system is obtained by measuring adsorption equilibria. One of the most important parameters is the pressure range at which the PSA system operates, while the composition of the supply-gas stream is usually invariant. For example, the recommended pressure is typically greater than 6 bar[131,132] for the separation of flue gases (15% CO_2 by mole, with the balance being N_2) using zeolite 13X.

Multi-component gas adsorption (MGA) quantifies the amount of each component that is captured by an adsorbent from a gas mixture of two or more compounds at equilibrium. From these MGA equilibria we can determine selectivity,[133] working capacity[29] and relevant thermodynamic parameters[134] of an adsorbent material under mixed-gas conditions. One of the main concerns in MGA is that there are insufficient data for generating and testing the theoretical models that describe the process.[135] MGA is also considered to be a difficult experimental technique to perform,[37] since custom instruments need to be designed, and headspace composition analysis must be undertaken without perturbing the equilibrium conditions.[38] Two popular approaches of MGA analyses are either measuring or predicting the adsorbed amounts of the gas species *via* the breakthrough method[136] or the widely-used Ideal Adsorbed Solution Theory (IAST),[39] respectively. Breakthrough columns are used to study the adsorption kinetics and adsorbed amounts of fluid mixtures. Shortcomings of this method are that only one adsorption equilibrium can be measured before the adsorbent needs to be regenerated, and that MGA equilibria are rarely studied at pressures well above or below 1 bar total pressure.[35] Considering that PSA cycles often reach and even exceed 6 bar, an alternative method must be used to measure the adsorption of gas mixtures at these pressures. IAST, on the other hand, is often used to predict MGA equilibria from single-component adsorption isotherms.

Credible volumetric MGA data were first recorded over a wide pressure range by Richardson and Woodhouse[137] in 1923 using their volumetric apparatus, although such measurements had been attempted as early as 1868.[138,139] The general design of volumetric MGA instruments has not changed significantly over time.[63,84,85,139–144] However, the quality of the results has improved markedly over the last century, owing to advances in sensor and detector technology. Instruments typically consist of a sample chamber, a quantitative composition analyzer, and an intermediate reservoir chamber connected to the sample chamber and the detector (see Figure 3.1). The greatest advances in MGA are due almost entirely to the use of more sophisticated detection methods; early MGA research was hampered by complicated and frequently unreliable composition analysis protocols that were designed with specific mixtures of gases in mind. Moreover, the individual components of gas mixtures needed to have significantly different physical characteristics to be distinguishable in composition analyses (*i.e.*, a flammable gas and a non-flammable gas). Modern detection methods,

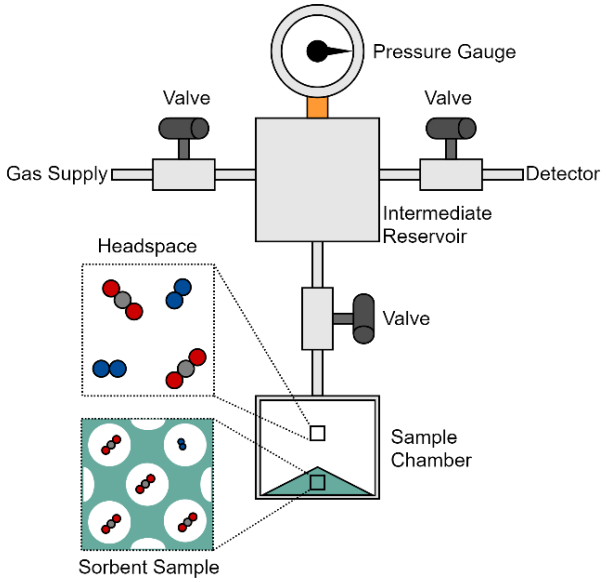

Figure 3.1. Schematic representation of a typical volumetric multi-component gas adsorption analyzer.

such as gas chromatography and mass spectrometry, have allowed for an enormous variety of gas mixtures to be analyzed post-adsorption, and at significantly low detection limits.

Here we report detailed multi-component gas adsorption results obtained with a simple purpose-built volumetric instrument for measuring pure and multi-component gas adsorption equilibria at various pressures and gas-phase compositions. The instrument (see Figure 3.1) consists of three components, namely a gas supply rig, a volumetric adsorption analyzer, and a mass spectrometer. A more comprehensive description of the instrument can be found in Section A.2.5 of Appendix A. The gas supplier employs a software-controlled electronic pressure regulator to introduce gas into the adsorption analyzer by means of a series of doses. The volumetric adsorption analyzer is housed within a commercial refrigerator for thermoregulation (heat is provided by a 60 W incandescent light bulb and cooling by the refrigerator). This simple, "dry" and affordable thermoregulation system is suitable for measuring adsorption equilibria between 4 and 50 °C. Software was developed in-house to control the pressure regulator and the refrigerator temperature, actuate the valves, monitor pressure and mass spectrometric data, and to control dosing according to a desired program.

3.3 RESULTS AND DISCUSSION

To validate the accuracy of the instrument, single-component gas adsorption (SGA) isotherms for CO_2 and N_2 adsorbed onto zeolite 13X were recorded. These show good agreement with previously reported data[11,109,145–147] (see Figure 3.2 for the CO_2 adsorption data, and Figure A.6 in Appendix A for the N_2 adsorption data). The uptake of CO_2 and N_2 by 13X follows a type I[60] profile, which is characteristic of rigid microporous materials. It is usually appropriate to use a Langmuir[77] or Langmuir-type[148] isotherm to describe type I adsorption data. The Sips[79] isotherm is an example of a Langmuir-type treatment, and it will play an important role in our discussions below that relate to the uptake of mixed gases. The SGA isotherm for N_2 can be modelled using either the Langmuir or the Sips isotherm. However, the SGA isotherm for CO_2 can be modelled using the dual-site Langmuir[78] or the Sips isotherm (see Table A.1 and Figure A.6 in Appendix A for more information regarding

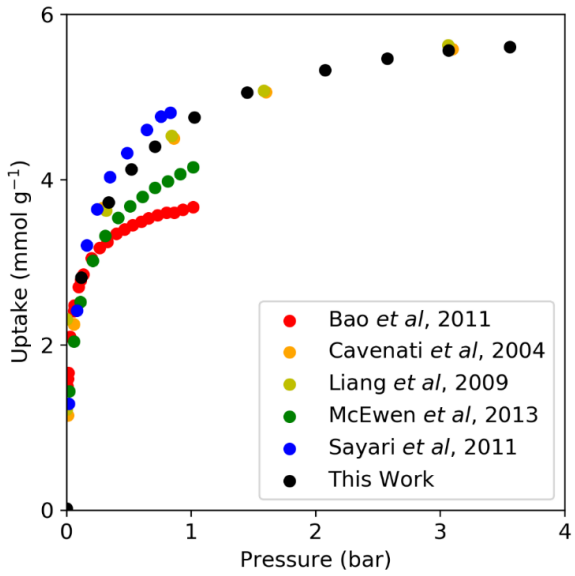

Figure 3.2. Literature isotherms for CO_2 adsorbed into 13X.

the isotherm functions and the fitting parameters). For each isotherm the goodness of fit (i.e., relative to experimental data) was evaluated by calculating the mean absolute error (MAE)[149] and root mean square error (RMSE)[149] values. The MAE is the averaged sum of the absolute deviations between predicted and observed values, while the RMSE is the square root of the averaged sum of the squared deviations between predicted and observed values. The MAE values are reported here, but the RMSE values are given in Table A.2 in Appendix A.

The Langmuir (MAE = 8.25×10^{-3} mmol g^{-1}) and Sips (MAE = 8.25×10^{-3} mmol g^{-1}) isotherms both describe the uptake of pure N_2 accurately, which is to be expected since the fitted Sips heterogeneity parameter is equal to 1. The isotherm for CO_2 is best described by both the dual-site Langmuir (MAE = 1.10×10^{-2} mmol g^{-1}) and the Sips (MAE = 2.47×10^{-2} mmol g^{-1}) isotherms. The heterogeneity parameter for CO_2 is equal to 0.508, indicating that the curvature of the CO_2 isotherm cannot be described adequately by the Langmuir isotherm. The SGA isotherms suggest that 13X interacts more favorably with CO_2 than with N_2 at similar pressures. The apparent selectivity for CO_2 over N_2 can be attributed to the favorable electrostatic interaction between the partially negatively charged CO_2 oxygen atoms and the extra-framework cations, whereas N_2 experiences relatively weak van der Waals dispersion interactions with the entire 13X framework in a nonspecific fashion.[150] However, it is not clear from the SGA isotherms how the selectivity would be affected by varying the relative concentrations of N_2 and CO_2 if 13X were exposed to a mixture of these gases.

For a pure gas, the two-dimensional isotherm plots the concentration (c) of an adsorbed species as a function of the equilibrium pressure (P) at a constant temperature. However, for binary gas mixture the presence of an additional component increases the degrees of freedom by one,[39] and a complete description of binary MGA thus requires the introduction of a third dimension (i.e. the gas-phase composition at equilibrium, y) into the adsorption isotherm. For convenience, the composition is expressed as the molar percentage of one of the components in the gas mixture. Since it would be challenging to carry out MGA measurements across a broad range of composition and pressure in a single experiment, we performed several MGA experiments in the range 0 to 3 bar using different

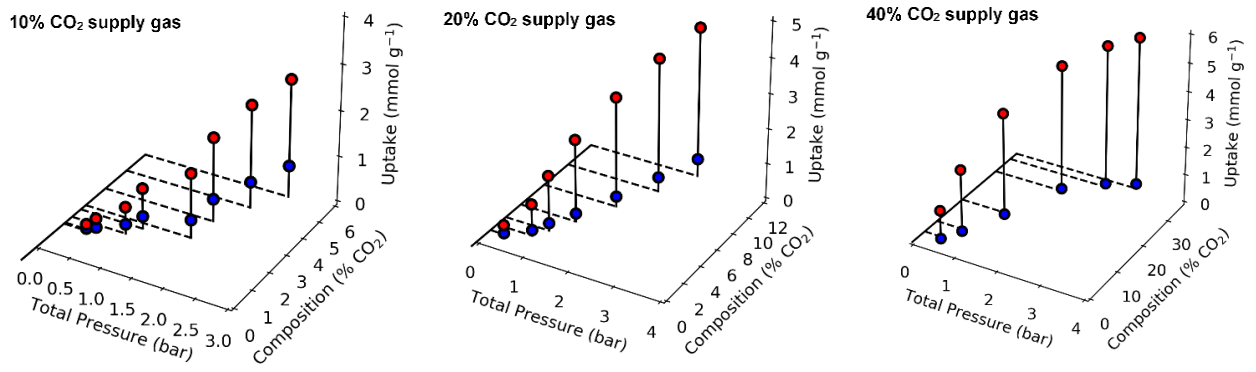

Figure 3.3. Measured MGA equilibria for CO_2 (red) and N_2 (blue) on 13X.

supply-gas compositions (10%, 20%, 40% CO_2, with the balance being N_2, see Figures 3.3 and A.8). The numerical excess[151] MGA isotherm data and error margins can be found in the supplementary information (Table A.3). Figure 3.3 shows that N_2 uptake increases proportionally with the total pressure if there is a significant proportion of N_2 (>90% N_2 by mole) in the gas phase. Nevertheless, the N_2 uptake is generally lower than that of CO_2 for all the adsorption equilibria measured, confirming that 13X is indeed selective for CO_2 over N_2.

The MGA isotherm is best expressed as a surface in a three-dimensional plot. The simplest way to generate MGA isotherm surfaces is to use interpolation. In addition to the appropriate boundary conditions (*i.e.*, $n_i(0, y_i) = 0$ and $n_i(P, 0) = 0$ for any species i in the gas phase), the SGA data can be plotted on the pressure and equilibrium gas-phase composition axes. Following this, the features of the MGA isotherm are obtained by systematically adding the measured MGA equilibrium data and then interpolating in all directions by means of Delaunay triangulation[152] (see Figure 3.4).

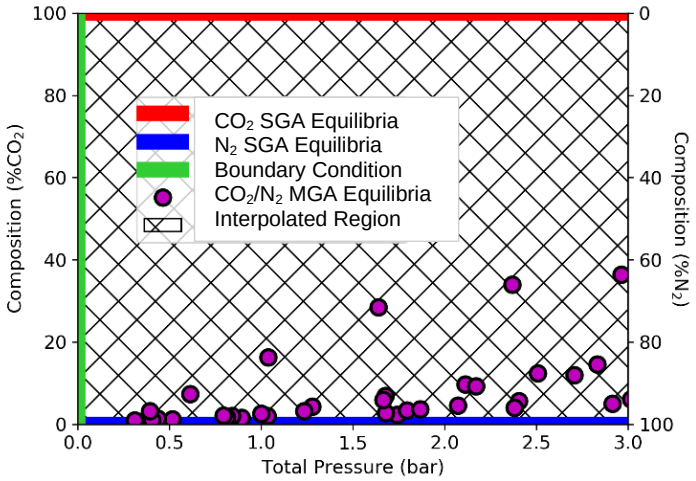

Figure 3.4. Visual description of the method used to generate MGA isotherm surfaces numerically. The boundary condition shown here is zero uptake as the total pressure approaches zero.

This process yields the interpolated MGA isotherms for both gas species, as shown in Figure 3.5. The contour lines indicate that the surface representing CO_2 uptake is convex, which implies that its uptake is high even when its proportion in the gas phase is low, thus

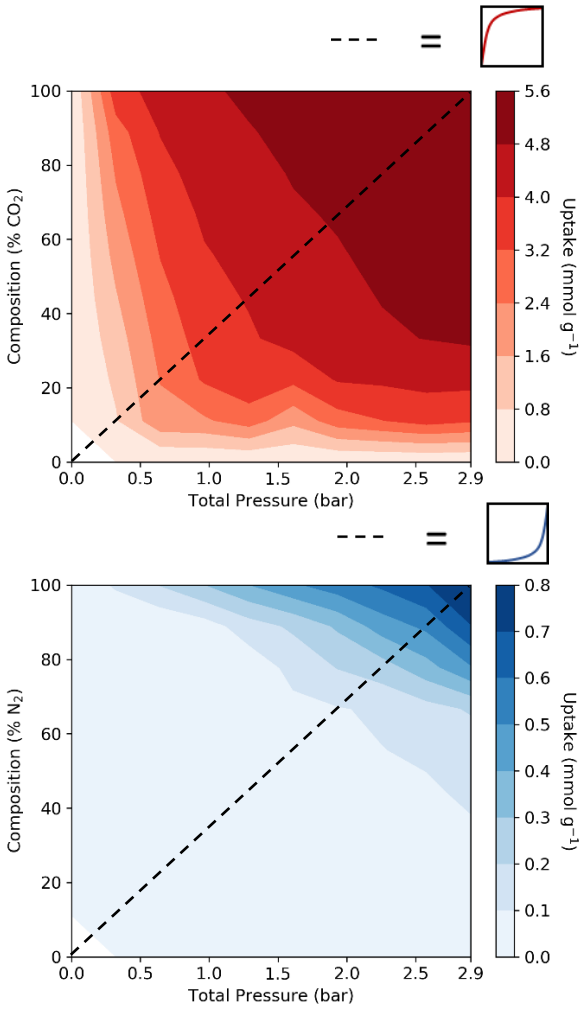

Figure 3.5. Interpolated experimental MGA isotherm contour plots of CO2 (red) and N2 (blue) on zeolite 13X. Traces of the isotherm surfaces are also shown as dashed lines.

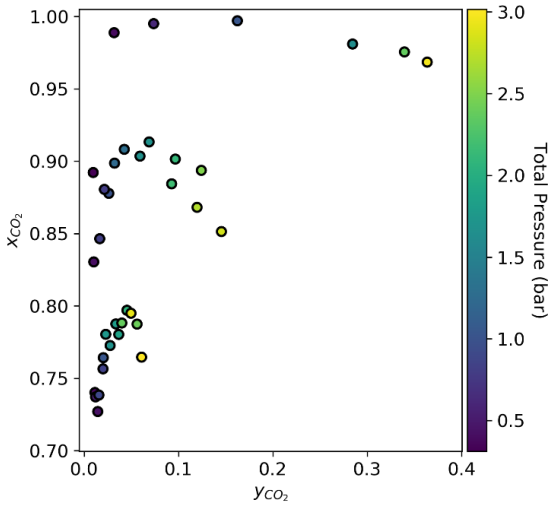

Figure 3.6. Selectivity diagram for CO_2 at experimental equilibria. x_{CO2} is the adsorbed-phase mole fraction and y_{CO2} is the gas-phase mole fraction of CO_2. Equilibria are color coded according to pressure.

illustrating the high selectivity towards CO_2 over a broad range of gas-phase compositions. In contrast the N_2 surface is concave and its uptake only becomes significant when the total pressure and proportion of N_2 in the gas phase are high.

To illustrate selectivity more intuitively, selectivity plots[153] can be used to describe the fractions of the different adsorbate molecules that are present in the gas and adsorbed phases. Figure 3.6 relates the gas-phase composition (y_{CO2}) to the adsorbed-phase composition (x_{CO2}) for each measurement. The data are also color coded according to the magnitude of the pressure.

At low pressures, the selectivity for CO_2 is very high, with an adsorbed-phase CO_2 fraction of more than 95% when the gas-phase composition consists of ≥ 5% CO_2. However, CO_2 is adsorbed considerably less selectively at higher pressures. For example, to capture CO_2 from anhydrous flue gas (15% CO_2) under ambient conditions, we could expect a maximum CO_2 uptake in the range of 2.4 – 3.2 mmol g^{-1}, with the adsorbed phase consisting of more than 95% CO_2. In contrast, at approximately 3 bar CO_2 uptake from the same gas-phase composition only increases to 3.2 – 4 mmol g^{-1}, while the purity of the adsorbed-phase composition decreases to 85% CO_2. From these data we can infer that merely increasing the pressure will not lead to improved separation; we must consider that the selectivity also changes with pressure, which is

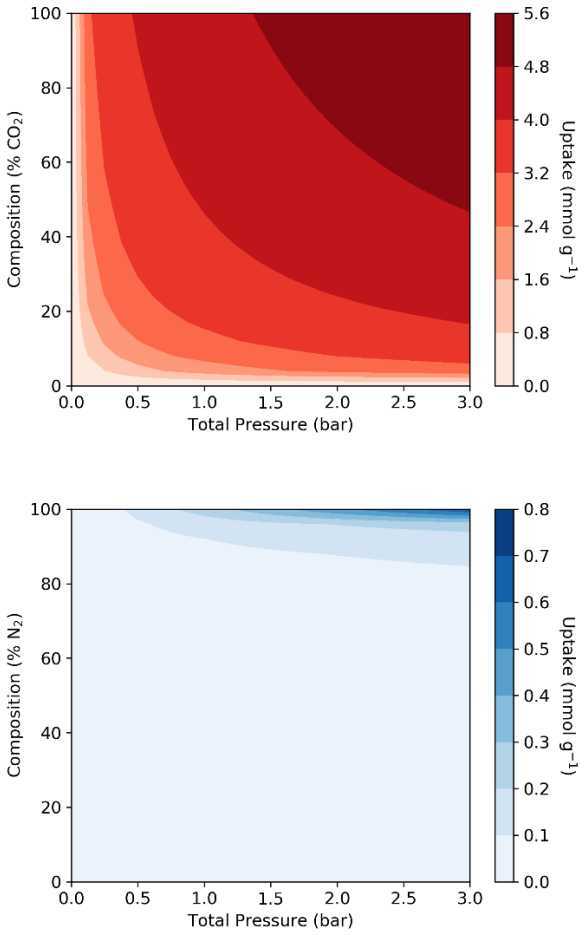

Figure 3.7. IAST-predicted MGA isotherm contour plots of CO_2 (red) and N_2 (blue) on zeolite 13X.

not accounted for by IAST. It is therefore clear that there is a trade-off between purity in the adsorbed phase and the amount of gas that is adsorbed.

A consequence of obtaining such detailed MGA data using our method is that we can compare experimental data to those predicted from measured SGA isotherms using standard theoretical models such as IAST.[39] However, caution is advised when using IAST to predict MGA isotherms, since IAST was derived using a very specific set of assumptions (*viz.* ideal mixing of adsorbates, chemically inert and structurally rigid adsorbents, low surface coverage). Previous studies[37] have shown that IAST produces erroneous results when the SGA isotherms are integrated beyond the limits of Henry's law (*e.g.* as would be the case for the data reported here). Additionally, the theoretical basis of IAST is limited by the assumptions made in its derivation (*i.e.*, ideal gases and ideal solutions), some of which may not be valid in the pressure ranges typically used for MGA experiments. Furthermore, IAST may not be well suited for predicting the mixed adsorption of two or more gas species with significantly different physical characteristics.[37,154] Similar to the experimental MGA isotherms, Figure 3.7 shows the IAST isotherms calculated across the composition range and between 0 and 3 bar; the IAST-predicted MGA isotherm for CO_2 compares well to the experimental CO_2 MGA isotherm. However, a stark difference between experiment and IAST is apparent for the adsorption of N_2: according to IAST, N_2 uptake is essentially zero, whereas the experimental data show that this is not the case. Even at pressures as low as 2 bar, and for gas mixtures containing 20% CO_2 in the gas phase, the adsorbed phase consists of approximately 10% N_2 at equilibrium.

As an alternative to IAST, Real Adsorbed Solution Theory (RAST)[39,80] treats deviations from ideality by incorporating the activity coefficients of each gas species into the model. Remarkably, the gas

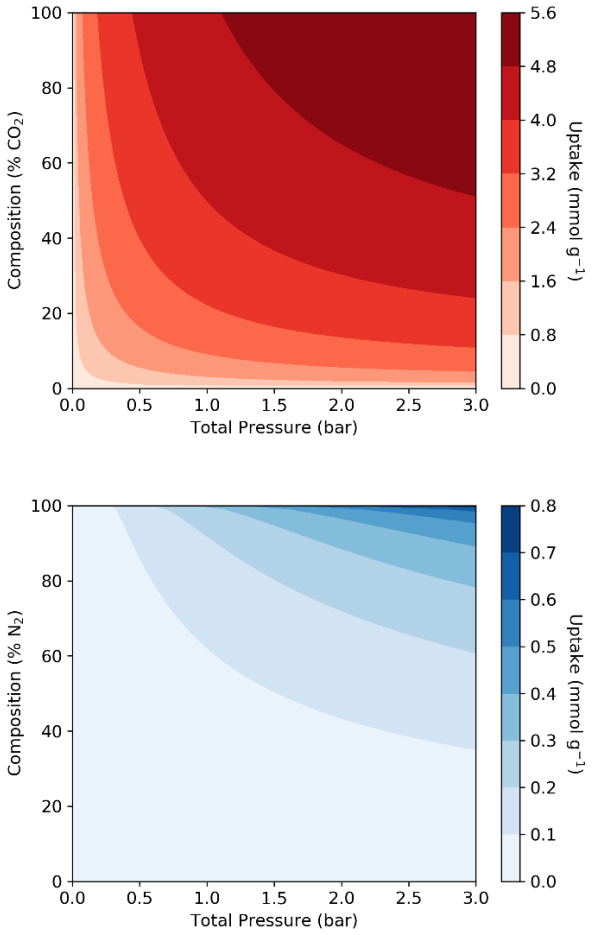

Figure 3.8. Predicted MGA isotherms for CO2 (red) and N2 (blue) by the extended Sips isotherm.

phase is almost always treated as ideal in RAST, indicating that the major shortcoming of using IAST at elevated pressure lies in the thermodynamic description of the adsorbed phase. One might consider employing RAST to correctly describe the adsorbed phase, but experimental MGA data are required in order to parameterize the Wilson[80] or UNIQUAC[155] activity coefficient functions that are typically used for solving the RAST equations. If MGA equilibrium data are not unavailable, RAST is usually disqualified for predictive purposes.

Another, albeit seemingly primitive, method for generating *ad hoc* MGA isotherms is by utilizing the extended adsorption isotherms.[81] These extended isotherms function in a similar manner to IAST in that SGA isotherm functions are fitted to experimental SGA data, and that the MGA isotherms are calculated without the need for any further experimental measurements. A potential caveat of using this approach is that there are many extended adsorption isotherm functions, and it may not be obvious which is most suited to describing MGA isotherms in the absence of experimental validation.

It has been shown[80] that the pure- and mixed-gas uptake of CO_2 and N_2 on zeolite 13X can be modelled accurately using the extended Sips isotherm (see Section A.3.8 of Appendix A) in the pressure range relevant to this work. Indeed, the extended Sips isotherms for CO_2 and N_2 shown in Figure 3.8 describe both the CO_2 and N_2 MGA isotherms well, and they even outperform IAST in this instance despite being more simplistic.

This is confirmed by calculating the MAE values for the results predicted by both models: the MAE values for the predicted CO_2 isotherms are similar for both IAST (3.60×10^{-1} mmol g^{-1}) and the extended Sips isotherm (4.28×10^{-1} mmol g^{-1}). However, the MAE values for the predicted N_2 isotherms are 1.94×10^{-1} mmol g^{-1} for IAST and 9.42×10^{-2} mmol g^{-1} for the extended Sips isotherm. As might be expected, the MAE values for the MGA measurements are much larger than those for

SGA, which can be attributed to errors introduced by the mass spectrometry measurements (see Table A.4 in Appendix A), and by the fact that these are predictive models that were not fitted to experimental MGA data. Nevertheless, the extended Sips isotherm is a clear improvement on IAST in this instance, considering that an MAE of approximately 0.2 mmol g^{-1} is relatively large for data that range between 0 and 0.8 mmol g^{-1}. It has also been shown[80] that the extended Sips isotherm becomes inaccurate at higher pressures (> 3 bar) when predicting the mixed uptake of CO_2 and N_2 by 13X. This can be directly attributed to the selectivity function[133] of the extended Sips isotherm, (Equation 3.1):

$$S_{1,2} = \frac{x_1 y_2}{x_2 y_1} = \frac{y_2 n_1^{\infty} \left(K_{S,1} y_1 P\right)^{c_1}}{y_1 n_2^{\infty} \left(K_{S,2} y_2 P\right)^{c_2}} \tag{3.1}$$

where x_i is the adsorbed mole fraction, n_1^{∞} is the saturation capacity, $K_{s,i}$ is the Sips affinity constant, y_i is the gas-phase mole fraction, and c_i is the heterogeneity factor for species i. It is important to note that a_i is limited to the range 0 to 1. If the system contains only two gas species, and the gas-phase composition is held constant, then the selectivity for species 1 will mathematically decay, or be amplified, (Equation 3.2) as the pressure is increased according to

$$\left(S_{1,2}\right)_y \propto \frac{P^{c_1}}{P^{c_2}} \tag{3.2}$$

Therefore, selectivity for species 1 will approach zero if its heterogeneity factor is smaller than that of species 2, or infinity if its heterogeneity factor is larger. Given that the heterogeneity parameters for CO_2 and N_2 are approximately 0.5 and 1 (see Table A.1 in Appendix A), respectively, the extended Sips isotherm predicts that the selectivity for CO_2 will decrease as the pressure is increased. As was previously shown, the selectivity will continue to decrease unrealistically beyond 3 bar, until the extended Sips isotherm eventually overpredicts N_2 uptake and underpredicts CO_2 uptake under MGA conditions. Although there are several theoretical models that can be used to elucidate the MGA performance of a material (be they AST-based or extended isotherms), the most reliable method is to measure the MGA equilibria experimentally. Nevertheless, the extended Sips isotherm predicts some form of selectivity decay for uptake of CO_2 by 13X as a function of pressure, which is also apparent from our experimental data.

3.4 CONCLUSIONS

In the very specific case of CO_2 adsorption by 13X in the presence of N_2 we have shown that high pressure has the effect of increased uptake by an adsorbent, but at the cost of selectivity. Obtaining MGA equilibria at pressures beyond atmospheric pressure is therefore important for optimizing

conditions for PSA systems. IAST performs well in predicting the CO_2 MGA isotherm, but it fails to produce useful results regarding the uptake of N_2 at higher pressures. On the other hand, the extended Sips isotherm performed better than IAST to predict the mixed-gas uptake of CO_2 and N_2 by 13X. We recommend that the extended Sips isotherm be used instead of IAST for predicting MGA equilibria in 13X, at least in the pressure ranges considered in this work. Since both IAST and the extended Sips isotherm are *ad hoc* methods that can be used to predict MGA isotherms, if MGA equilibria at intermediate pressures (> 1 bar) were to be predicted from SGA equilibria, then it is imperative that extended adsorption isotherm results should be included alongside IAST results in the absence of experimental MGA equilibria. The MGA experiments that were carried out in this study simulate adsorption by a PSA unit. Further research is under way to study the MGA equilibria of CO_2 and N_2 by other porous materials, and to further test the validity of the extended Sips isotherm.

Chapter 4.

Predicting Binary Multi-Component Gas Adsorption Equilibria at High Pressure by Utilizing the Real Adsorbed Solution Theory and the Extended Sips Isotherm

The following chapter is an adapted version of a prepared publication manuscript.

Contributions by the Author

- Design of the project with Prof. Catharine Esterhuysen.
- Preparation of Cu-HKUST-1.
- Thermal and PXRD analyses of Cu-HKUST-1.
- SGA and MGA analyses of CO_2 and N_2 with Cu-HKUST-1.
- Development of PRAST-S.
- MGA predictions with PRAST-S.
- Interpretation of the results with Prof. Catharine Esterhuysen and Prof. Leonard J. Barbour.
- Writing the first draft of the article.

4.1 ABSTRACT

This study introduces a method to predict the outcome of a multi-component gas adsorption experiment at elevated pressures by using the extended Sips isotherm alongside real adsorbed solution theory (RAST) equations, PRAST-S. The method incorporates a new activity coefficient model, analogous to the virial equation of state, that improves on the ideal adsorbed solution theory (IAST) model. The PRAST-S method was verified by benchmarking against the measured multi-component gas adsorption data of zeolite 13X in the range 1 to 10 bar. The high-pressure multi-component gas adsorption isotherms of CO_2 mixed with N_2 were then predicted from single-component gas adsorption data for Cu-HKUST-1, MOF-14, Mg-MOF-74, and UiO-66. To test the predictions, the multi-component gas adsorption equilibria of CO_2 and N_2 with Cu-HKUST-1 were measured in the range 0 to 3 bar and found to agree well with the predicted data. Finally, the PRAST-S results were used to compare the selectivities and working capacities for CO_2 for the four potential adsorbents, with Cu-HKUST-1 being the most suitable for pressure swing adsorption applications.

4.2 INTRODUCTION

Anthropogenic carbon emissions have been isolated as one of the root-cause problems of climate change; therefore, interest in carbon capture and conversion technologies has soared within the scientific community. New findings regarding the sequestration of CO_2 with the aid of novel solid adsorbents and improved techniques are frequently published at the frontiers of both chemistry and engineering.[8,9] Specifically, microporous materials such as zeolites and metal-organic frameworks (MOFs) have shown the most promise regarding the selective capture and release of CO_2 in flue gas streams.[10,11] New porous materials are being synthesized *via* several simple methods and their physical properties can be measured to determine whether they are suitable for industrial adsorption processes.[156–158] To this end, the uptake of single gas species as a function of pressure is measured using either the volumetric or gravimetric adsorption methods,[159] both of which ultimately provide a profile of uptake *vs* pressure known as an adsorption isotherm.[160] These single-component gas adsorption (SGA) isotherms can be used, in conjunction with the Ideal Adsorbed Solution Theory (IAST),[39] to accurately predict the low-pressure ($P < 1$ bar) multi-component gas adsorption (MGA) isotherms for mixtures of gases without the need for any additional information.[37] However, for industrial gas-separation processes that require higher gas pressures, such as pressure-swing adsorption (PSA) technology,[36] high-pressure adsorption isotherms need to be obtained. Although multiple-component gas adsorption experiments can be performed, most standard gravimetric and volumetric instruments are typically not equipped to also measure the change in the gas-phase

composition due to selective adsorption. Most research groups opt to construct their own instruments for MGA analyses to overcome this issue; however, this is beyond the scope of most research groups.[161] An alternative approach is to employ the extended Sips isotherm or the Real Adsorbed Solution Theory (RAST).[80,162] The extended Sips isotherm can provide reasonably accurate MGA data in the intermediate range (1 to 3 bar),[80] while RAST yields very accurate results over the full range of pressures and gas-phase compositions. RAST, however, requires some MGA data for fitting purposes,[39] while the extended Sips isotherm does not.

In this study, we present the PRAST-S method, which bypasses the need to perform any experimental MGA analyses for binary gas mixtures of CO_2 and N_2 by using a simple combination of RAST with the extended Sips isotherm to predict high-pressure (1 to 10 bar) MGA isotherms from only SGA data.

4.3 RESULTS AND DISCUSSION

The single-component (SGA) and multi-component gas adsorption (MGA) equilibria for CO_2 and N_2 by 13X up to 10 bar at 298 K published by Hefti et al[80] were used as a starting point for verifying the predictive RAST methodology described in Appendix B. The SGA CO_2 and N_2 equilibrium adsorption data were fitted to the Sips isotherm (see Equation B1); the optimized Sips isotherm parameters are shown in Table 4.1. The resulting SGA isotherms are shown in Figure 4.1.

Table 4.1. Sips isotherm parameters fitted to experimental SGA isotherms of 13X for CO_2 and N_2.

Framework	Gas	n_i^{∞} (mmol g^{-1})	$K_{S,i}$ (bar^{-1})	c_i
Zeolite 13X	CO_2	7.073	13.607	0.442
	N_2	3.894	0.106	0.990

The Sips affinity coefficient ($K_{S,i}$) and saturation capacity (n_i^{∞}) for the adsorption of CO_2 by 13X are much greater than those for N_2. This indicates that CO_2 interacts strongly with 13X, while N_2 interacts less favorably. On the other hand, the heterogeneity parameter (c_i) is lower for the adsorption of CO_2, as compared to near unity for N_2. This implies that the adsorbent surface is uniform for N_2, but heterogeneous for CO_2, which adversely affects the potential uptake of CO_2 by 13X. These deductions are in line with previous findings by Khoramzadeh *et al*.[108]

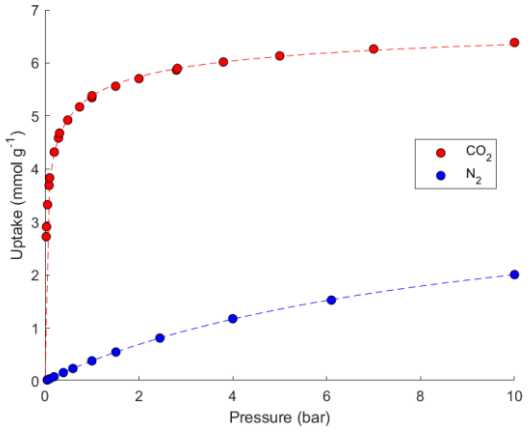

Figure 4.1. Fitted SGA isotherms for CO_2 and N_2 onto 13X. Dashed lines indicate the single-component Sips isotherm fit.

It has been shown that the extended Sips isotherm (see Equation B2) provides a very accurate prediction of the mixed uptake of CO_2 and N_2 by Zeolite 13X around 1 bar.[163] This property of the extended Sips isotherm offers a unique opportunity to calculate the activity coefficients for CO_2 and N_2 in the adsorbed phase directly across the full gas-phase composition range (0.05% to 99% CO_2). The activity coefficients are calculated by using a combination of Equations B6, B7, and B9, along with the extended Sips adsorbed quantities and adsorbed-phase compositions at 1 bar. It is assumed that the activity coefficients are independent of the reduced surface potential (Π, see Equation B3) in this study.

The calculated activity coefficients for CO_2 and N_2 in the adsorbed phase are shown in Figure 4.2. An interesting feature of these activity coefficient plots are that the CO_2 activity appears to remain almost invariant as the fraction of CO_2 is decreased. N_2, on the other hand, shows activity coefficients almost exclusively lower than 1. Furthermore, the N_2 activity coefficients have a much larger dependence on the adsorbed-phase composition than those of CO_2. Consequently, the adsorption of CO_2 is significantly more ideal than that of N_2 which is highly non-ideal within the context of adsorbed solutions.

The cubic virial function (see Equation B12) was fitted to these activity coefficient data. It was found that the activity coefficients at infinite dilution are 20.62 for CO_2 and 1.14×10^{-3} for N_2. Although the CO_2 activity coefficient at infinite dilution is probably inaccurate, it is unlikely that one would ever need to consider CO_2 gas-phase mole fractions lower than 0.05% in this type of study, and therefore the quantity does not need to be described accurately.

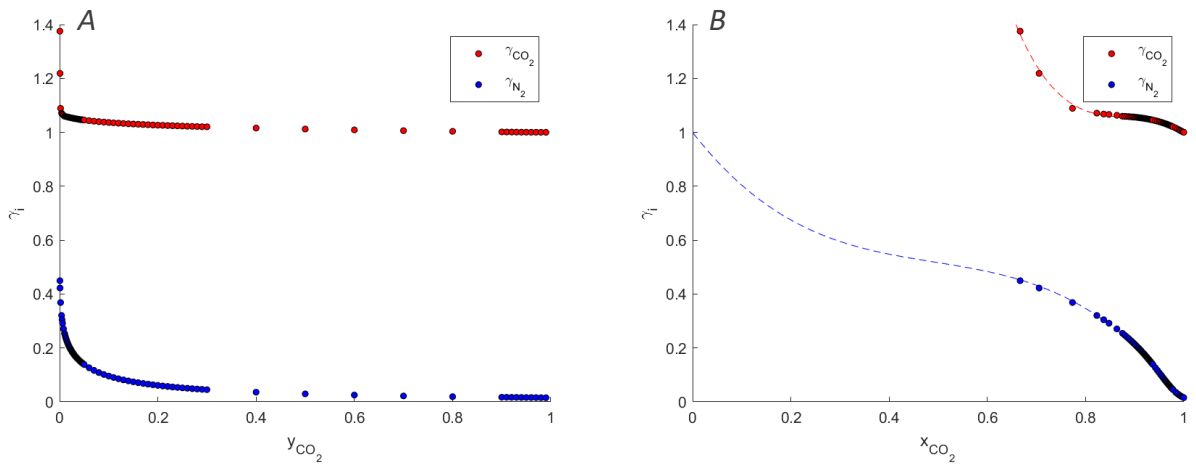

Figure 4.2. Activity coefficients of CO_2 and N_2 when adsorbed by 13X at 1 bar expressed relative to the (A) gas-phase composition and (B) adsorbed-phase composition. The fitted virial activity coefficient functions are shown as dashed lines.

It is possible, with the fitted pure-component adsorption data (Figure 4.2), to predict the mixed uptake of CO_2 and N_2 at virtually any pressure and gas-phase composition using IAST or the extended Sips isotherm. The results of these calculations can be seen in Figure 4.3, along with the experimental MGA equilibria that were measured by Hefti *et al.*[80] Using IAST, uptake is generally overestimated for CO_2 and underestimated for N_2. On the other hand, the extended Sips isotherm performs very well in predicting the CO_2 and N_2 uptake at 1.2 bar. From 3 bar onwards, however, the extended Sips isotherm diverges from the experimental data. Finally, at 10 bar, neither of the models predict the uptake of the two gases accurately.

The RAST MGA equilibria for CO_2 and N_2 can be calculated at these pressures, assuming that the fitted virial activity coefficient functions at 1 bar are independent of the reduced surface potential. This assumption proves to be valid between 1 and 3 bar in that the predictive RAST method presented here (PRAST-S) yields the best results of the three models. Although better than the IAST prediction, PRAST-S still suffers from inaccuracies at 10 bar, when the gas-phase consists mainly of N_2. Nevertheless, PRAST-S may prove useful for predicting the MGA uptake of CO_2 and N_2 by other rigid frameworks at elevated pressures, although some additional parameterization will be necessary to correctly account for the dependence of the activity coefficients on the reduced surface potential.

PRAST-S can also be applied to other porous materials; however, the assumptions of the method must first be discussed. It is assumed that the extended Sips isotherm accurately describes the mixed uptake of CO_2 and N_2 by rigid porous frameworks that show selectivity for CO_2 based on the pure-component adsorption isotherms around 1 bar. It is also assumed that the activity coefficient functions

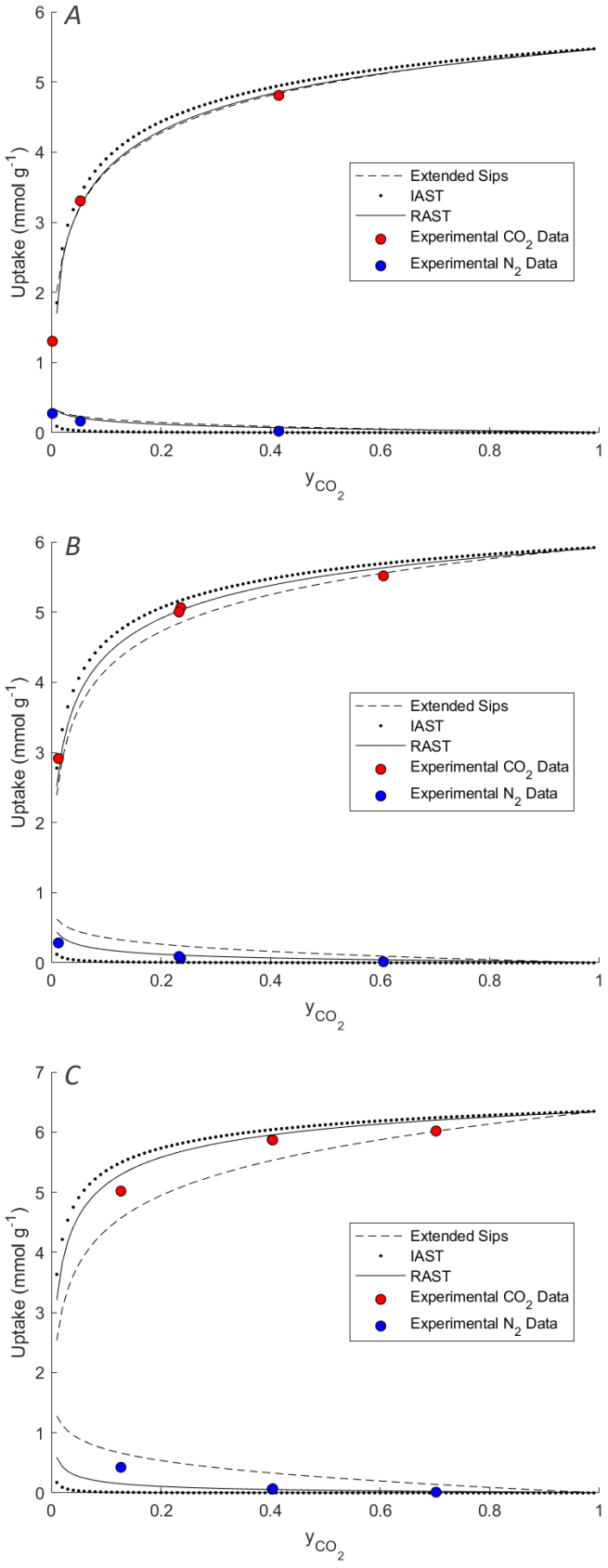

Figure 4.3. MGA isotherms for CO_2 and N_2 adsorbed onto 13X at (A) 1.2, (B) 3, and (C) 10 bar.

that are obtained by fitting RAST equations to the extended Sips isotherm are independent of the reduced surface potential – since the dependence of the virial activity coefficients (see Equation B12) on the reduced surface potential is not known. The SGA adsorption isotherm data at 298 K for the four porous materials UiO-66,[112] Cu-HKUST-1,[109] Mg-MOF-74,[111] and MOF-14[110] were obtained from previously published studies. These isotherms were fitted to the Sips isotherm and the results are shown in Table 4.2. There is a consistent trend in the Sips affinity coefficients ($K_{S,i}$) for each gas species, where $K_{S,CO_2} > K_{S,N_2}$, indicating that CO_2 interacts most strongly with these frameworks, as would be expected, considering the electrostatic environment within the pores of these frameworks. Generally, the heterogeneity factor associated with the adsorption of CO_2 is larger than that of N_2, except in the case of Cu-HKUST-1. It is not clear from only these data why Cu-HKUST-1 behaves differently to the other frameworks, but it could be that the adsorption sites of Cu-HKUST-1 may have some unknown special properties absent from the other frameworks (including 13X).[164]

Table 4.2. Fitted Sips parameters for the respective pure-component adsorption isotherms of the selected porous materials.

Framework	Gas	n_i^{∞} (mmol g^{-1})	$K_{S,i}$ (bar^{-1})	c_i
Cu-HKUST-1	CO_2	14.486	0.507	1.000
MOF-14		20.986	0.056	0.719
Mg-MOF-74		11.980	0.605	0.771
UiO-66		11.025	0.109	0.746
Cu-HKUST-1	N_2	7.945	0.028	0.932
MOF-14		7.749	0.024	1.000
Mg-MOF-74		7.657	0.092	1.000
UiO-66		3.945	0.026	0.874

The Sips isotherm fits are plotted alongside the experimental SGA data in Figure 4.4. There appears to be good agreement between the isotherm model and the experimental data for the pressure region below 10 bar. Cu-HKUST-1 shows the greatest amount of CO_2 taken up, followed by Mg-MOF-74, MOF-14, and UiO-66. Mg-MOF-74 adsorbs the largest amount of N_2, followed by Cu-HKUST-1, MOF-14, and UiO-66 in the same region.

The extended Sips isotherms at 1 bar were calculated for each of the frameworks using the pure-component adsorption isotherms. The same procedure was followed as for 13X, where Equations B6, B7, and B9 were solved simultaneously to obtain the activity coefficients for each gas in the various frameworks (Figure 4.5). The activity coefficients of CO_2 and N_2 are generally well described by Equation B12, with the exception being the N_2 activity coefficients for Cu-HKUST-1. Closer inspection of the IAST and extended Sips results for Cu-HKUST-1 (Figure B.1 in Appendix B)

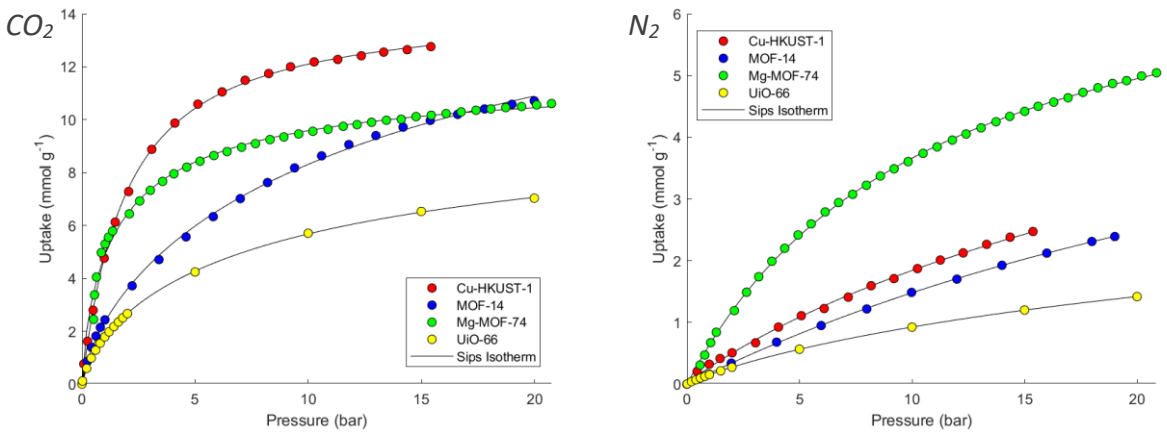

Figure 4.4. SGA isotherms for CO_2 and N_2 adsorbed into the selected frameworks.

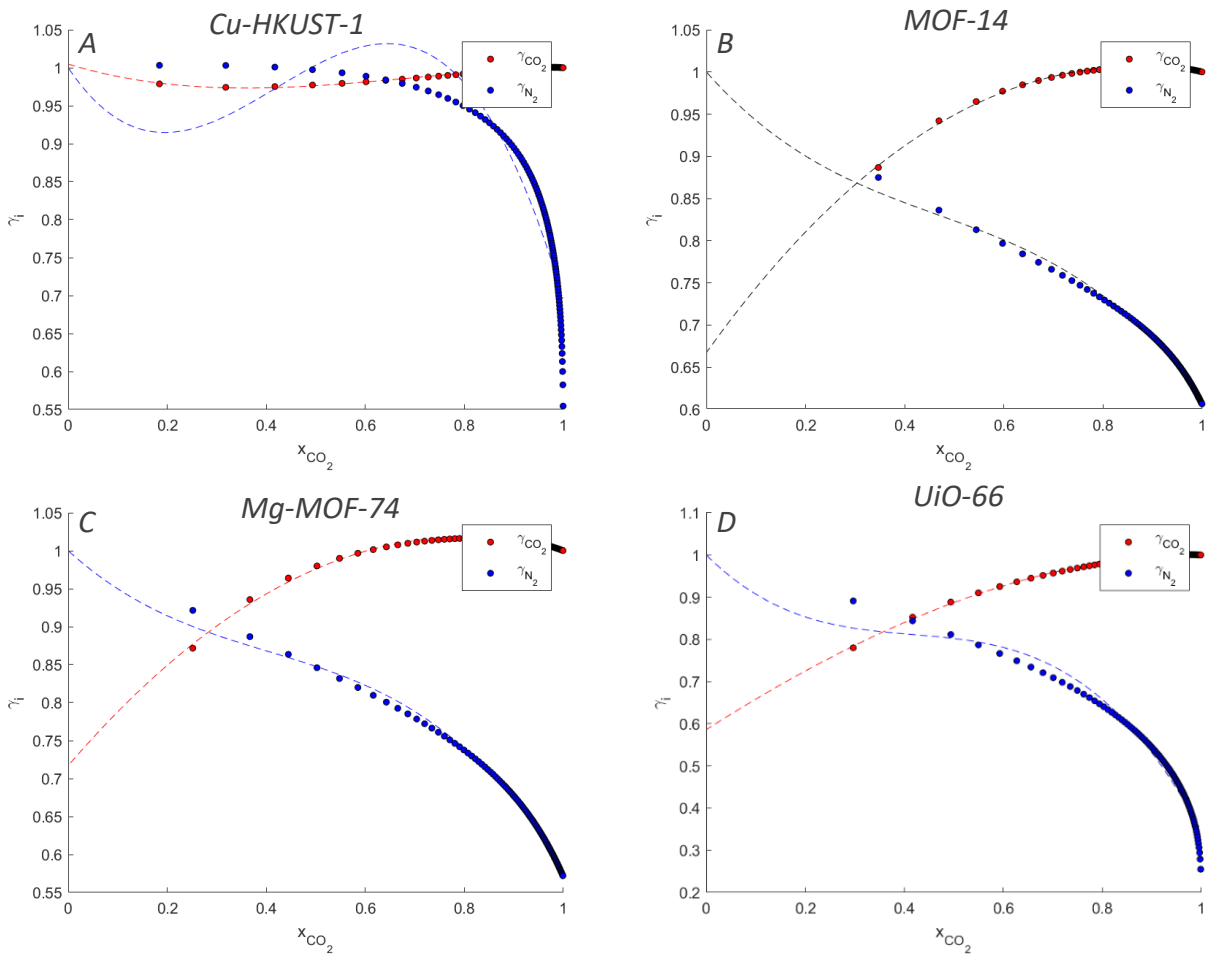

Figure 4.5. Activity coefficient plots at 1 bar for the selected frameworks.

suggest that there is little to no difference between the two models. All the frameworks other than Cu-HKUST-1 have heterogeneity parameters below 0.8 for the adsorption of CO_2. Most of the frameworks, excluding UiO-66 (c = 0.874), have heterogeneity parameters that are close to 1 for the adsorption of N_2, indicating idealized Langmuir surfaces. However, other than Cu-HKUST-1, each of the frameworks shows a difference (Figures B.4, B.7, B.10) between the extended Langmuir isotherm and IAST. This could mean that the presence of heterogeneity in the adsorption sites of either species may be one of the main causes for IAST deviating from the experimental data.

The fitted virial activity coefficient functions can be used to calculate the multiple-component uptakes of CO_2 and N_2 for all the frameworks within the range of 1 to 10 bar. Isobaric traces were taken from the multiple-component isotherms at 1, 5 and 10 bar (Figure 4.6) to determine the evolution of the MGA isotherms as the pressure is increased. Both Cu-HKUST-1 and Mg-MOF-74 display a reasonably large amount of CO_2 adsorbed under mixed-gas conditions, followed by MOF-14 and, finally, UiO-66. Mg-MOF-74 adsorbs the largest amount of N_2 at all the pressures, followed by Cu-

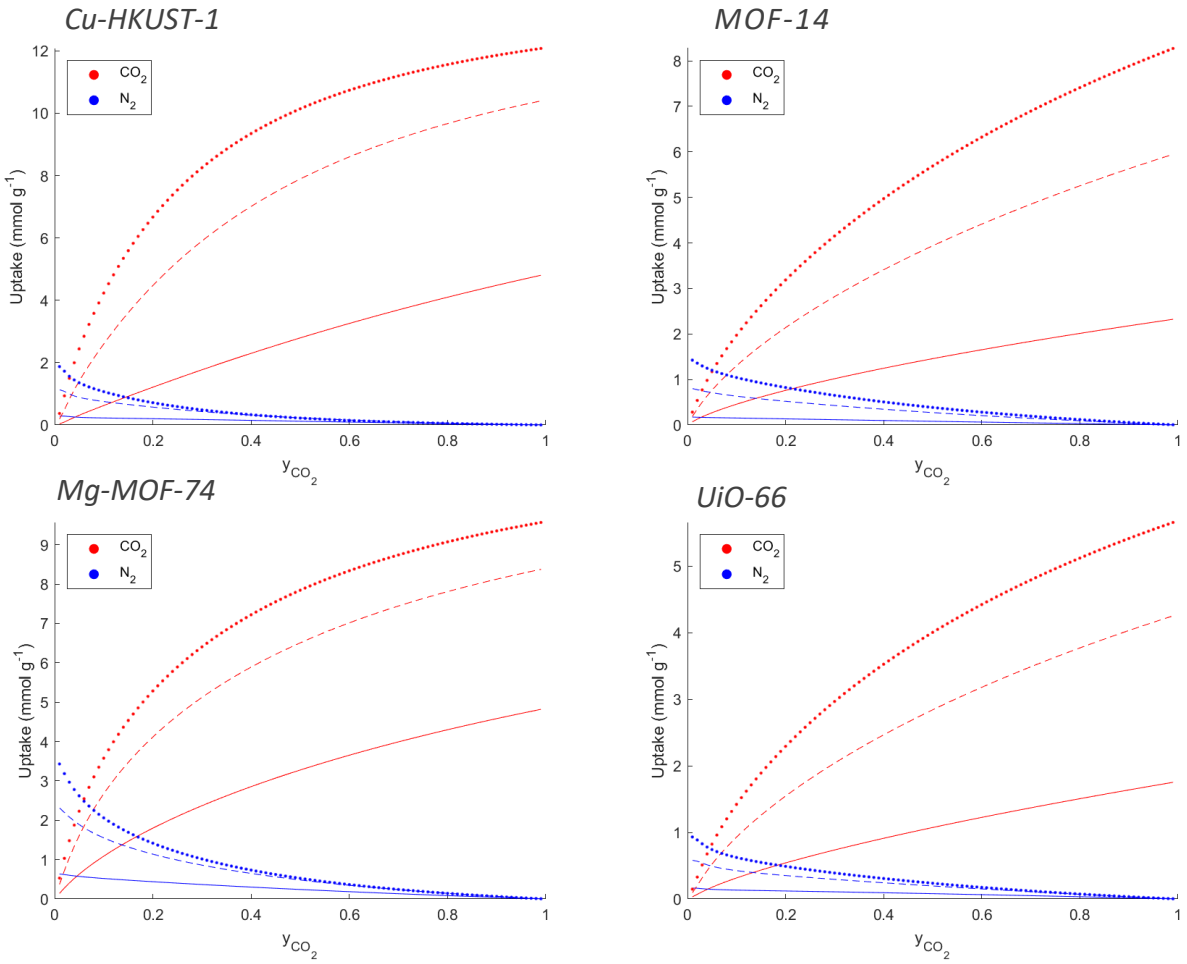

Figure 4.6. MGA isotherms for CO_2 and N_2 adsorbed into the selected frameworks at 1 (–), 5 (--) and 10 (●) bar.

HKUST-1, MOF-14 and UiO-66. The large amount of N_2 adsorbed by Mg-MOF-74 under mixed-gas condition is unsurprising considering its large pure-component N_2 uptake (Figure 4.4).

This information can be used to rank the four materials for their applicability as CO_2 adsorbers in terms of their MGA equilibria. There are three main measures that are used in grading a material for a pressure swing adsorption (PSA) operation: the working capacity (Equation B15), selectivity (Equation B16), and heat of adsorption.[165] A framework is considered a good candidate for PSA if it has a comparably high selectivity and working capacity (> 1 mmol g^{-1}) for the target gas species, and if the amount of heat that is released by the adsorption process is low. The working capacity of each material will be considered at three fixed gas-phase compositions that are relevant for carbon capture and conversion, namely 5%, 15%, 25% CO_2 (with the balance being N_2, see Figure 4.7). The standard reference pressure used in pressure-swing adsorption (PSA) technology is 1 bar,[36] and we will therefore define our working capacity accordingly. The data in the working capacity plots show that Cu-HKUST-1 outshines the other materials in terms of having a high working capacity for CO_2 and a comparably low working capacity for N_2. MOF-14 has a substantially lower working capacity for

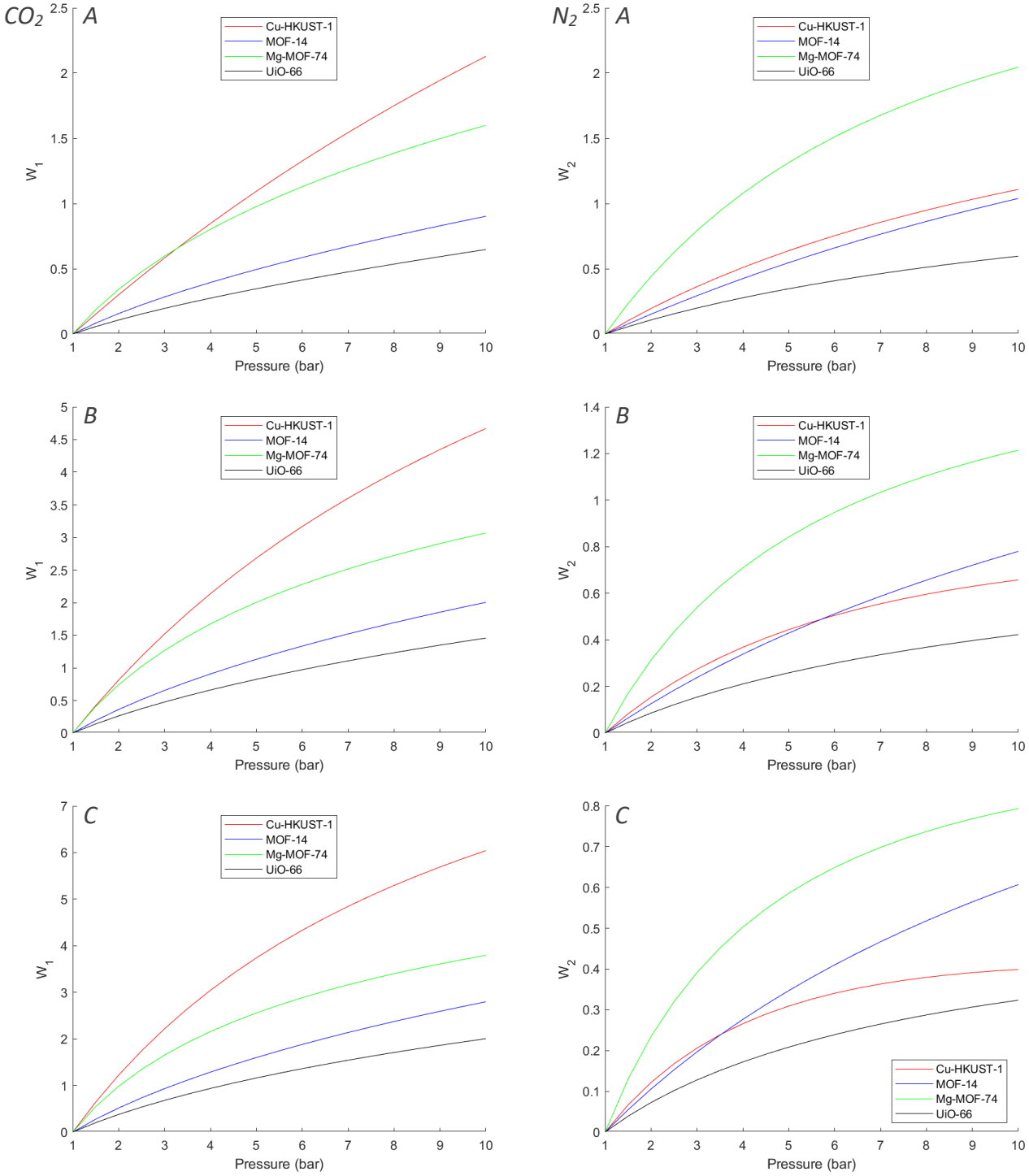

Figure 4.7. Multi-component working capacity (P_{ref} = 1 bar) of CO_2 for the selected frameworks at (A) 5%, (B) 15%, and (C) 25% CO_2 in the gas phase, with the balance being N_2.

CO_2 than Cu-HKUST-1, but it has a similar N_2 working capacity to Cu-HKUST-1. Although Mg-MOF-74 has an impressive working capacity for CO_2, it also has the largest working capacity for N_2. UiO-66 has the lowest working capacities for both CO_2 and N_2.

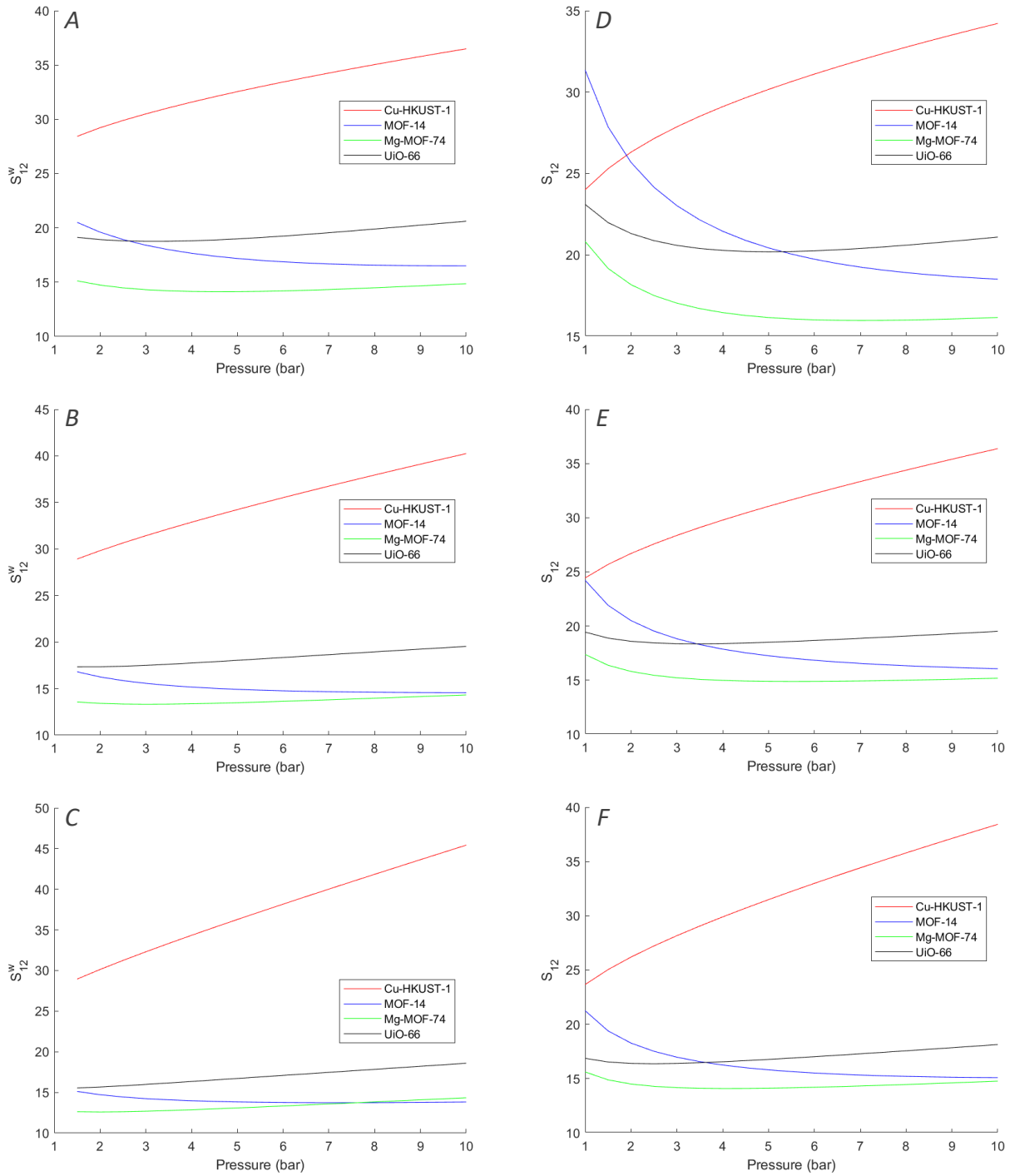

Figure 4.8. Working selectivity plots (1 = CO_2, 2 = N_2) at (A) $y_1 = 5\%$, (B) $y_1 = 15\%$, and (C) $y_1 = 25\%$, and selectivity plots at (D) $y_1 = 5\%$, (E) $y_1 = 15\%$, and (F) $y_1 = 25\%$ for the four frameworks.

The working selectivity (Equation B17) plots in Figure 4.8 show that Cu-HKUST-1 is generally the most selective for CO_2, followed by UiO-66, then MOF-14, and lastly Mg-MOF-74. These selectivity data, combined with the working capacity data, allow us to make our final rankings for each material. It is important to emphasize that the ranking of these four materials is only based on their selectivity for CO_2 and their working capacities at 298 K. Other important factors such as cost,[166] stability,[167]

and heats of adsorption[62] were not considered. Cu-HKUST-1 has both the best selectivity and working capacity for CO_2; therefore, it is the best of the four materials studied for CO_2 adsorption using PSA. MOF-14 has both a lower capacity for CO_2 than Mg-MOF-74 and a lower selectivity for CO_2 than UiO-66, but it also has a better selectivity for CO_2 than Mg-MOF-74 and a better working capacity for CO_2 than UiO-66. Therefore, MOF-14 is our choice for the second-best material. Although quite selective, UiO-66 has a very low working capacity for CO_2 that only reaches the required 1 mmol g^{-1} at pressures much larger than the other candidates. Mg-MOF-74 has an excellent working capacity for CO_2. However, owing to its poor selectivity for CO_2 (relative to N_2) it is a weak candidate for CO_2 capture using PSA, alongside UiO-66. Furthermore, selectivity plots (Equation B16) of the same data have been included for comparison. Working selectivity provides a different perspective of the selectivity that a material shows for a gas species when the system is close to the reference state (see Equation B15). Notably, the ranking of MOF-14 and UiO-66 would have been more difficult because UiO-66 is more selective at high pressures, while MOF-14 is more selective at low pressures according to the normal treatment of selectivity.

The fact that the extended Sips isotherm and IAST predictions are quite close to one another in the case of Cu-HKUST-1 (see Figures B.1-B.3) raises some questions regarding the origin of the non-idealities that are seen in the other isotherms. The close agreement between IAST and the extended Sips isotherm in the case of Cu-HKUST-1 might even be an indication of a shortcoming in our own approach in that not all non-idealities can be represented accurately by the extended Sips isotherm. These issues could be resolved by performing an extensive MGA analysis (CO_2/N_2) of Cu-HKUST-1 in the range 1 to 3 bar to ascertain the validity of the extended Sips isotherm as a general input for RAST calculations. Fortunately, we have access to a MGA instrument,[163] and it is thus possible to perform the necessary experiments to test the validity of the predictive RAST method. Specifically, the SGA equilibria of Cu-HKUST-1 would need to be measured to obtain the correct fitted parameters of the predictive RAST method for our instrument and the Cu-HKUST-1 that was synthesized on site. Moreover, the MGA equilibria of mixtures of CO_2 and N_2 with Cu-HKUST-1 would need to be measured for direct comparison to the predicted RAST results.

To this end, Cu-HKUST-1 was synthesized as previously described.[168] Experimental details and results regarding the characterization of the physical properties (*i.e.* thermogravimetric analysis and powder X-Ray diffraction data) of Cu-HKUST-1 can be found in Appendix B (see Figure B.13 and Figure B.14). The SGA isotherms of CO_2 and N_2 with Cu-HKUST-1 were measured in duplicate (see Figure 4.9).

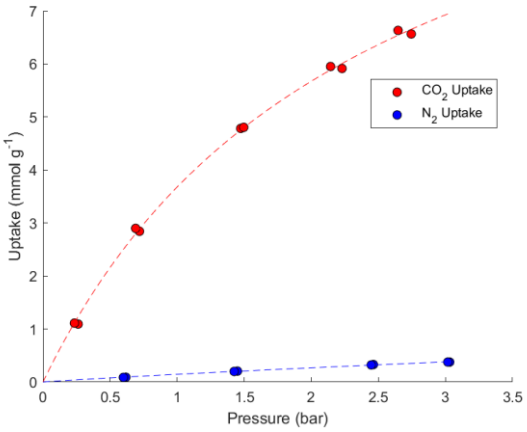

Figure 4.9. Fitted SGA isotherms for CO_2 and N_2 into Cu-HKUST-1 measured on the in-house adsorption instrument. Dashed lines indicate the single-component Sips isotherm fit.

The Sips isotherm was fitted to the measured adsorption data (see Table 4.3), and though there is a difference in terms of the values of the fit parameters between the previously published (see Table 4.2) and current data sets for Cu-HKUST-1, the relative magnitudes of the fit parameters are maintained. Furthermore, the experimental CO_2 uptake values for Cu-HKUST-1 are well within the margins given by Park *et al.*[169]

Table 4.3. Sips isotherm parameters fitted to experimental SGA isotherms for CO_2 and N_2 adsorption by Cu-HKUST-1.

Framework	Gas	n_i^{∞} (mmol g^{-1})	$K_{S,i}$ (bar^{-1})	c_i
Cu-HKUST-1	CO_2	12.404	0.422	1.000
	N_2	5.025	0.022	0.914

The same procedure as before was followed to calculate the activity coefficients for CO_2 and N_2 as a function of adsorbed-phase composition. There is an almost exact agreement between the activity coefficient plots above (Figure 4.5 A) and the activity coefficient plots for the experimental data (Figure B.15). The multicomponent adsorption isotherms for Cu-HKUST-1 predicted from these data (see Figures B.16-B.18) bear a striking resemblance to those calculated from literature data (see Figures B.1-B.3) in that the uptakes predicted by the extended Sips isotherm and IAST are very close to one another. Consequently, the RAST and IAST isotherm surfaces are effectively equal.

The MGA isotherm was measured in duplicate for Cu-HKUST-1 using four different mixtures of CO_2 and N_2 (20%, 40%, 60%, 80% CO_2) in the range of 0 to 3 bar to directly compare experimental measurements with the predicted results. The measured MGA data can be seen in Figure B.19 in

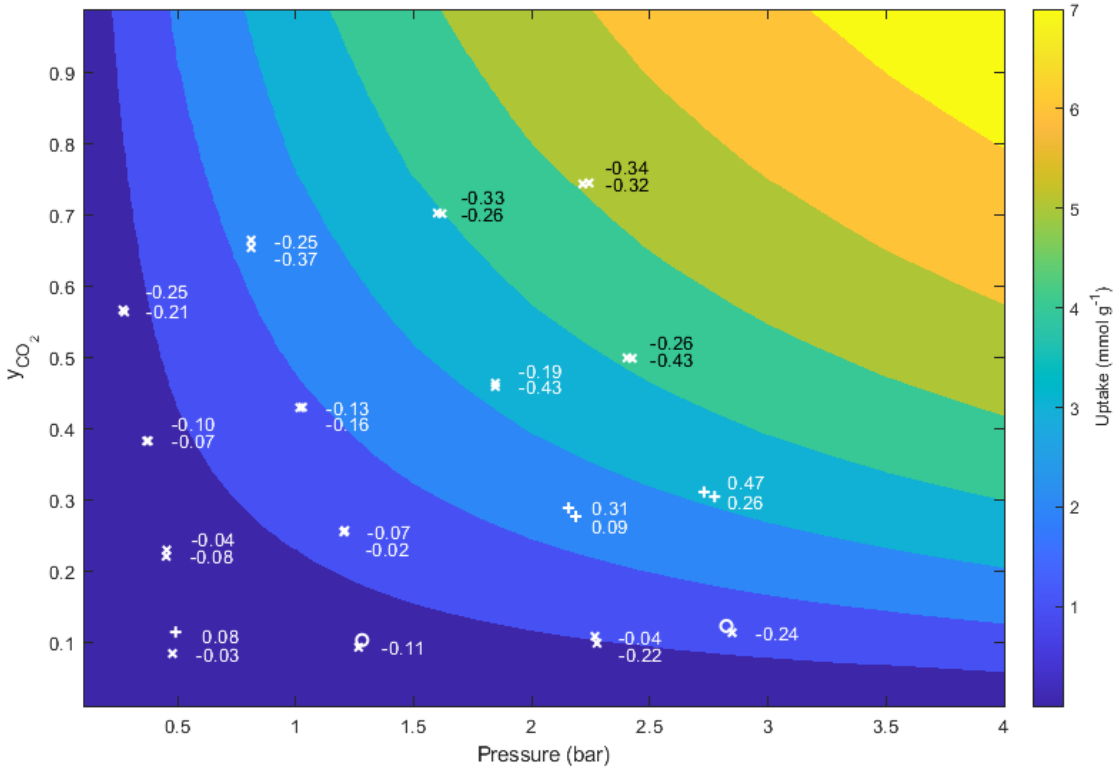

Figure 4.10. Comparison between the predicted (contour map) and measured multiple-component uptake of CO_2 by Cu-HKUST. A positive deviation is indicated by a "+" symbol, a negative deviation by an "×" symbol, and a negligible deviation by an "o" symbol.

Appendix B. A comparison between the two datasets for CO_2 is shown in Figure 4.10. The predicted isotherm surface is shown as a contour map, while the measured data are shown as markers. The numerical values associated with the markers are the magnitudes of the measured CO_2 uptakes relative to the predicted isotherm surface ($c_i^{predicted} - c_i^{measured}$).

The results in Figure 4.10 indicate that the predicted isotherm produced by the RAST method is a good description of the experimental data, because the distribution of deviations is relatively small and somewhat random. The range of errors observed between the predicted and measured amounts of CO_2 uptake are between 0.02 and 0.47 mmol g^{-1}. The same analysis as above was performed for the multi-component uptake of N_2 (see Figure 4.11). It is more difficult to make an accurate assessment of how well the RAST method predicts the N_2 uptake. Specifically, the associated range is 0.01 to 0.17 mmol g^{-1}, which is large in comparison to the amount of N_2 adsorbed, but small relative to the total amount adsorbed. The experimental errors associated with the N_2 equilibrium uptakes can be attributed to the interdependence of the measured CO_2 and N_2 uptakes (they are derived from the single set of pressure and the single set of gas-phase composition data), their magnitudes relative to

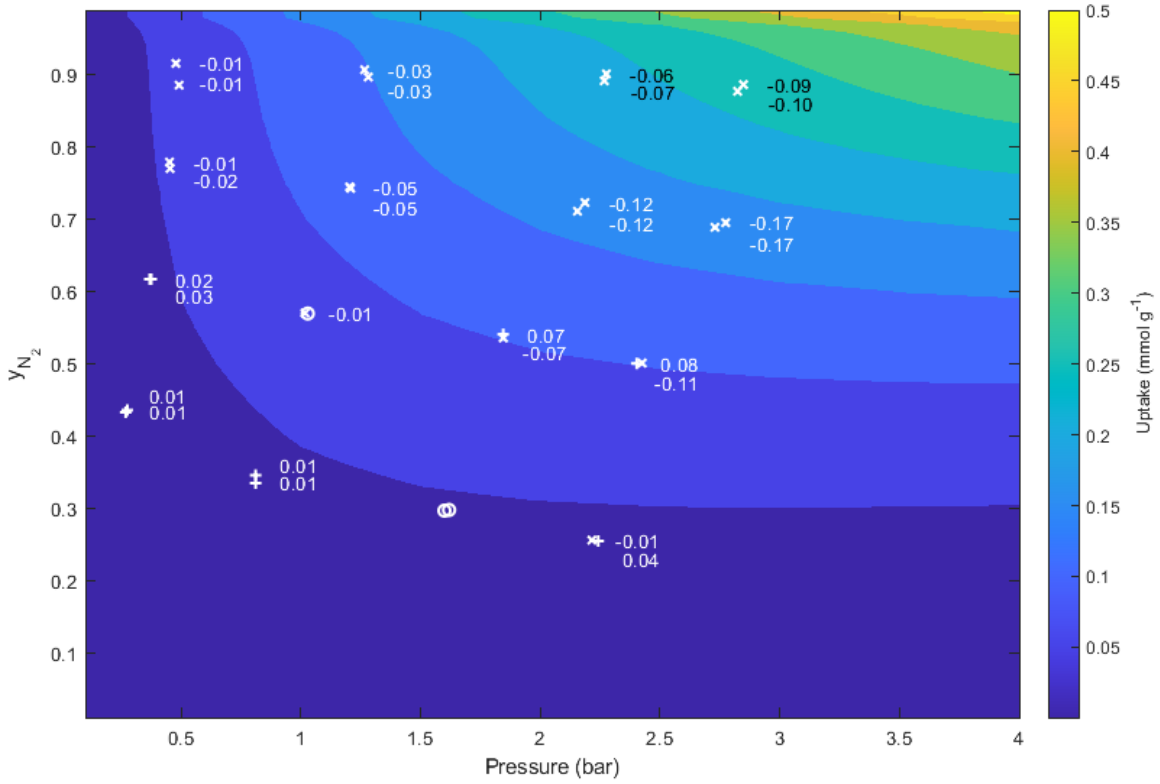

Figure 4.11. Comparison of the predicted (contour map) and measured multiple-component uptake of N_2 by Cu-HKUST-1. A positive deviation is indicated by a "+" symbol, a negative deviation by an "×" symbol, and a negligible deviation by an "o" symbol.

the total uptake, and the propagation of errors. It is also worth noting that the curvature present in the predicted N_2 isotherm in the region where y_{N_2} is greater than 0.9 is an artifact of the virial activity model (see Figures 4.5 and B.15).

Since the RAST CO_2 isotherm is effectively equal to the IAST and extended Sips isotherms, the information contained in Figure 4.10 reinforces the notion that there is some link between the lack of heterogeneity in the isotherm surface (*i.e.*, an idealized Langmuir surface) and ideal behavior in RAST. The N_2 results in Figure 4.11, although mostly inconclusive, do not necessarily contradict this.

4.4 CONCLUSIONS

We have shown that the RAST method presented in this study can be useful for evaluating porous materials for their ability to capture CO_2 selectively at higher pressures. Although it is tempting to apply the method to other mixtures of gases such as CO_2 and CH_4, it will first be necessary to

determine whether the extended Sips isotherm would provide an adequate description of the MGA in such cases. Additionally, the relationship between the activity coefficients and the reduced surface potential was not considered in this study; this may have played a role in the difference between the experimental and predicted results at higher pressures (Figure 4.3). Nevertheless, we believe that the method presented here is a step in the right direction for the prediction of MGA equilibria at high pressures, especially in that it provides a middle-ground between IAST and the extended Sips isotherm. Admittedly, the method is more complex than the extended Sips isotherm and IAST, but it can be automated. This implies that it could serve as a powerful and inexpensive tool to screen new porous materials for carbon capture with PSA. It has, furthermore, allowed us to predict that Cu-HKUST-1 is likely the best material for separating CO_2 and N_2 at elevated pressures, in comparison to MOF-14, Mg-MOF-74, and UiO-66. In contrast to the other compounds studied, Cu-HKUST-1 exhibits ideal adsorption behavior, as confirmed by the real adsorption model yielding almost identical results to the ideal adsorption model (Figures B.1-B.3). Since this is somewhat unexpected in the context of a real compound, we sought confirmation of this result by measuring the single-component and MGA isotherms of CO_2 and N_2. These measurements verified that the PRAST-S method provides the correct MGA isotherm for CO_2, and possibly also N_2, when these gases are adsorbed by Cu-HKUST-1 and confirm the method's general utility even when the adsorption behavior is ideal. Our findings indicate that there may be a link between the heterogeneity of the adsorption sites and the expression of non-idealities in AST. This, however, needs to be investigated further.

Chapter 5.

Exploring the Origin of Ideal and Non-Ideal Adsorption in Porous Frameworks

The following chapter is an adapted version of a prepared publication manuscript.

Contributions by the Author

- Design of the project with Prof. Catharine Esterhuysen.
- Predictions with PRAST-S.
- MM, MD, and MC simulations.
- Interpretation of the results with Prof. Catharine Esterhuysen.
- Writing the first draft of the article.

5.1 ABSTRACT

The origin of non-ideal behavior of zeolite 13X during adsorption of mixtures of CO_2 and N_2 is investigated in this study and contrasted to the ideal behavior of Cu-HKUST-1. Cu-HKUST-1 provides both spatially and energetically independent adsorption sites for CO_2 and N_2, respectively, which leads to the adsorption of the mixture being ideal. In contrast, CO_2 and N_2 interact with each other within 13X when adsorbed simultaneously: CO_2 effectively modifies the surface of 13X so that N_2 bonds more favorably, leading to an increased uptake of N_2.

5.2 INTRODUCTION

Ideal vs. non-ideal behavior is a concept that is present in virtually all major thermodynamic theories.[73] The notion of ideality is tied to the extent to which the thermodynamic system conforms to the underlying assumptions of a thermodynamic model within specified ranges of state parameters. Conversely, non-ideality frequently manifests as an experimentally measured deviation from the idealized thermodynamic model's description of the system and indicates that a systematic invalidation of the assumptions of the model is occurring.

One such thermodynamic model where non-ideal behavior is a common occurrence, is Adsorbed Solution Theory (AST).[39] AST is used to describe, and, in special cases, predict the simultaneous adsorption of multi-component gases by an adsorbent. Non-ideal adsorption in the context of AST refers to a positive, or negative, deviation from the ideal thermodynamic description of the adsorbed phase. This deviation in non-ideal AST (often referred to as the Real Adsorbed Solution Theory or RAST) is mathematically accounted for by using activity coefficients, much like the non-ideal treatment of Raoult's Law. However, where solution thermodynamics has access to several theories that relate activity coefficients to physically meaningful concepts,[87] no such activity coefficient models have been developed specifically for AST. Furthermore, the adsorption of gas mixtures within the same pressure and gas-phase composition range is also affected by the adsorbent material. Specifically, the mixed uptake of N_2 is significantly higher and the mixed uptake of CO_2 is marginally lower for 13X than predicted by the ideal case of AST (often referred to as IAST), even at total pressures as low as 1 bar, indicating that it is a non-ideal process.[80] IAST, on the other hand, accurately predicts the adsorption of mixtures of CO_2 and N_2 by Cu-HKUST-1,[170] which is, therefore, a seemingly ideal process.

The non-ideal behavior of zeolite 13X has previously been ascribed to an inhomogeneous distribution of adsorbate molecules due to strong interactions between CO_2 and extra-framework cations that are

also inhomogeneously distributed.[162] We, therefore, decided to investigate whether the modes of interaction between the guest molecules (CO_2 and N_2) and the host frameworks at the extremes of ideal adsorption (Cu-HKUST-1) and non-ideal adsorption (13X) differ to the extent that they can cause the differences in ideality. These will be studied *in silico* to identify the factors that contribute to ideality, or the lack thereof, in adsorption.

5.3 RESULTS AND DISCUSSION

Crystallographic data for zeolite 13X[171] and Cu-HKUST-1[172] were obtained from the International Zeolite Association and the Cambridge Structural Database, respectively. Both the materials crystallize in face-centered cubic space groups: $Fd\bar{3}m$ for 13X and $Fm\bar{3}m$ for Cu-HKUST-1. Beyond this shared symmetrical relationship, however, there are several differences between these materials. Zeolite 13X is an aluminosilicate material, meaning that it consists of alternating interconnected tetrahedra of SiO_4 and AlO_4. These tetrahedra form regular substructures within the overall zeolite crystal structure that are called composite building units (CBU).[171] Two of these CBUs are present in the 13X structure: sodalite cages and hexagonal prism moieties. Sodalite cages are connected to one another in a tetrahedral fashion with hexagonal prism moieties located at the junction between the cages. Furthermore, there are Na atoms located in key positions of the 13X framework to balance the negative charge of the $[Al_mSi_nO_{2(m+n)}]^{m-}$ backbone.

Cu-HKUST-1 is classified as a porous metal-organic framework (MOF). Metal-organic frameworks are a class of coordination compounds that form 2D and 3D structures[60] consisting of metal nodes and carbon-containing linker units. Cu-HKUST-1 consists of copper clusters that are joined by trimesic acid linkers. The substructures within the overall MOF crystal structure are classified according to their appearance, like CBUs for zeolites, however, the accepted nomenclature for these in MOFs is secondary building units (SBUs).[173] Cu-HKUST-1 displays a paddle wheel SBU, in which four carboxylate moieties originating from four separate trimesic acid linkers coordinate to two opposing copper atoms, each with square pyramidal geometry.

Representations of Cu-HKUST-1 and 13X are shown in Figure 5.1. Both materials are 3D porous materials, however, where Cu-HKUST-1 has a well-defined “grid” of channels, 13X has an intricate network of interconnected channels. Furthermore, Cu-HKUST-1 can be subdivided into two parts,

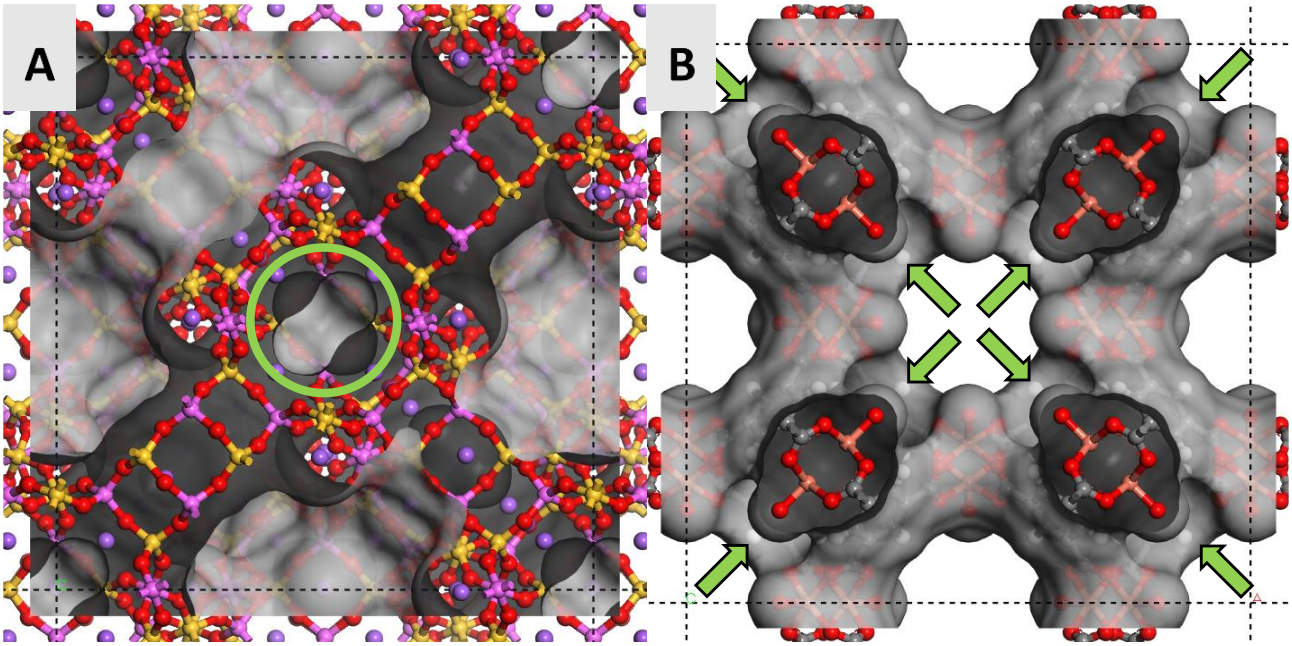

Figure 5.1.(A) Zeolite 13X and (B) Cu-HKUST-1 crystal structures viewed from the [0 0 1] face. A discrete cavity within the 13X framework is encircled in green, and the inner cavities of Cu-HKUST-1 are labelled with green arrows.

which will be referred to as the outer porous network and the inner cavities. 13X, on the other hand, has discrete cavities located inside of the sodalite cages that are enclosed by the framework atoms.

An important feature of 13X is the Na extra-framework cations that are found in key positions of the framework. There are, in total, three types of positions where these atoms may be found, namely the Sites I, II, and III (see Figure 5.2). Site I cations can be found in the hexagonal prism CBUs, and do not contribute to the interactions between 13X and guest molecules. Site II cations are located on the open faces of the sodalite cages and are partially exposed. Site III cations are the most exposed of the three cation types and are nested in the junctions between the sodalite cages and hexagonal prism moieties.

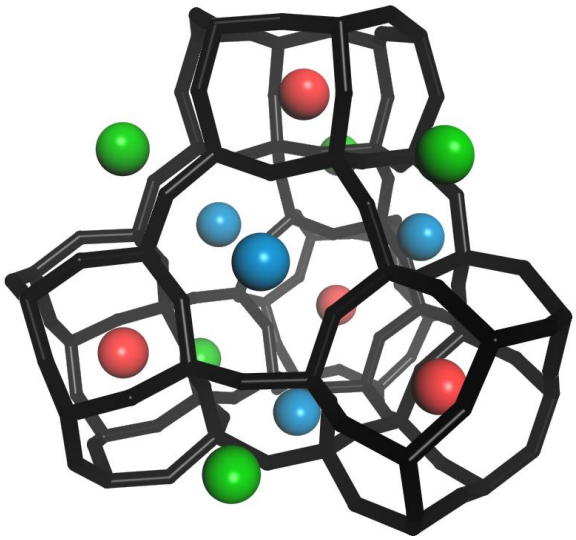

Figure 5.2. 13X sodalite cage including four hexagonal prism moieties that are tetrahedrally oriented. The positions of the three types of extra-framework cations are shown in red (Site I), blue (Site II) and green (Site III).

Terms, such as “framework backbone” and “accessible volumes”, amongst others, have very specific meanings when discussing porous materials.[60] Virtually all porous frameworks can be subdivided into three parts: the backbone,

accessible void volumes, and inaccessible void volumes. The part of the framework that is occupied by the atoms that make up the crystal structure is referred to as the backbone, the volume of which can be calculated using computational methods. One such computational method is called the Connolly surface,[174] where a spherical probe is used to map out the van der Waals surface of the framework. The size of the spherical probe is chosen according to the size of the molecules that are intended to be placed inside of the porous framework. CO_2, a molecule of interest in this study, has a kinetic diameter (*i.e.*, the average spherical diameter of the molecule in the gas phase) of 3.3 Å,[175] which indicates that a probe radius of at least 1.65 Å must be used to define the volume of the backbone. Accessible void volumes are the parts of the crystal structure that are permanently accessible and traversable by guest molecules, and inaccessible void volumes are the unfilled volumes of the framework that are enclosed by the backbone. The guest-accessible regions of the optimized structures defined by Connolly surfaces are shown for each material in Figure 5.3.

A computational model for each framework was generated using a combination of density functional theory methods and forcefield definitions (see Appendix C for more information). To test the quality of the computational models, the adsorption of CO_2 and N_2 with 13X and Cu-HKUST-1 were investigated using Metropolis Monte Carlo[176] simulations of the grand canonical ensemble (μVT, shortened to GCMC).[73] GCMC simulations are useful for benchmarking computational parameters (*i.e.*, atomic partial charges and forcefield definitions, and accessible volumes definitions, see

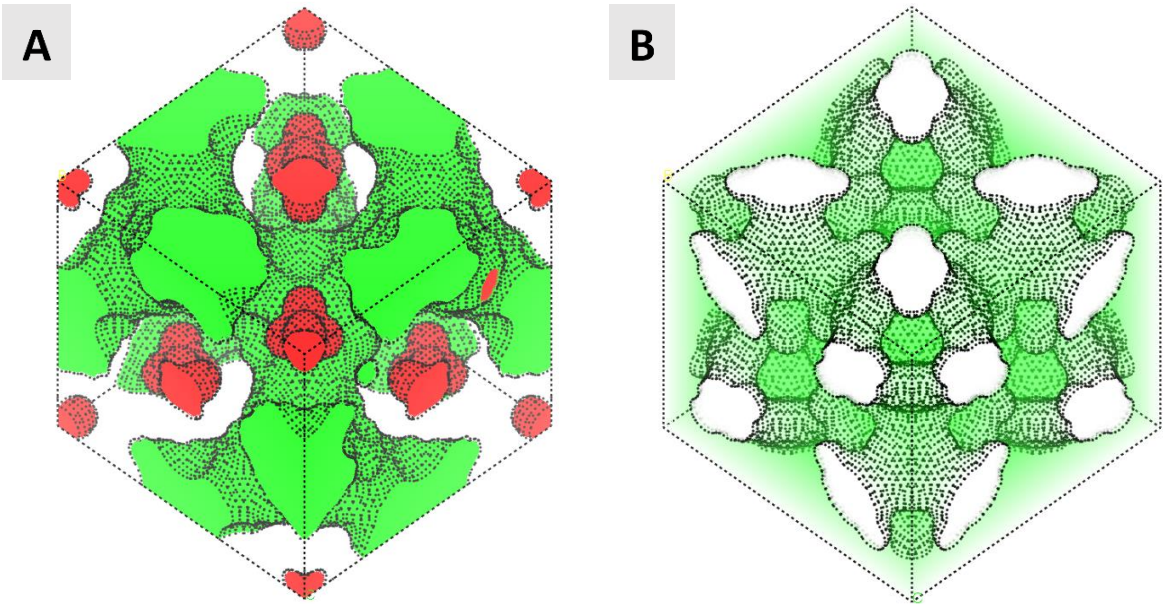

Figure 5.3. Representation of the portions of the porous frameworks that are accessible to guest molecules viewed from the [-1 1 1] face of (A) 13X and (B) Cu-HKUST-1. Accessible void spaces are indicated by a green color, inaccessible void spaces are indicated by a red color, and the framework backbone is either transparent (A) or shown in a white color (B).

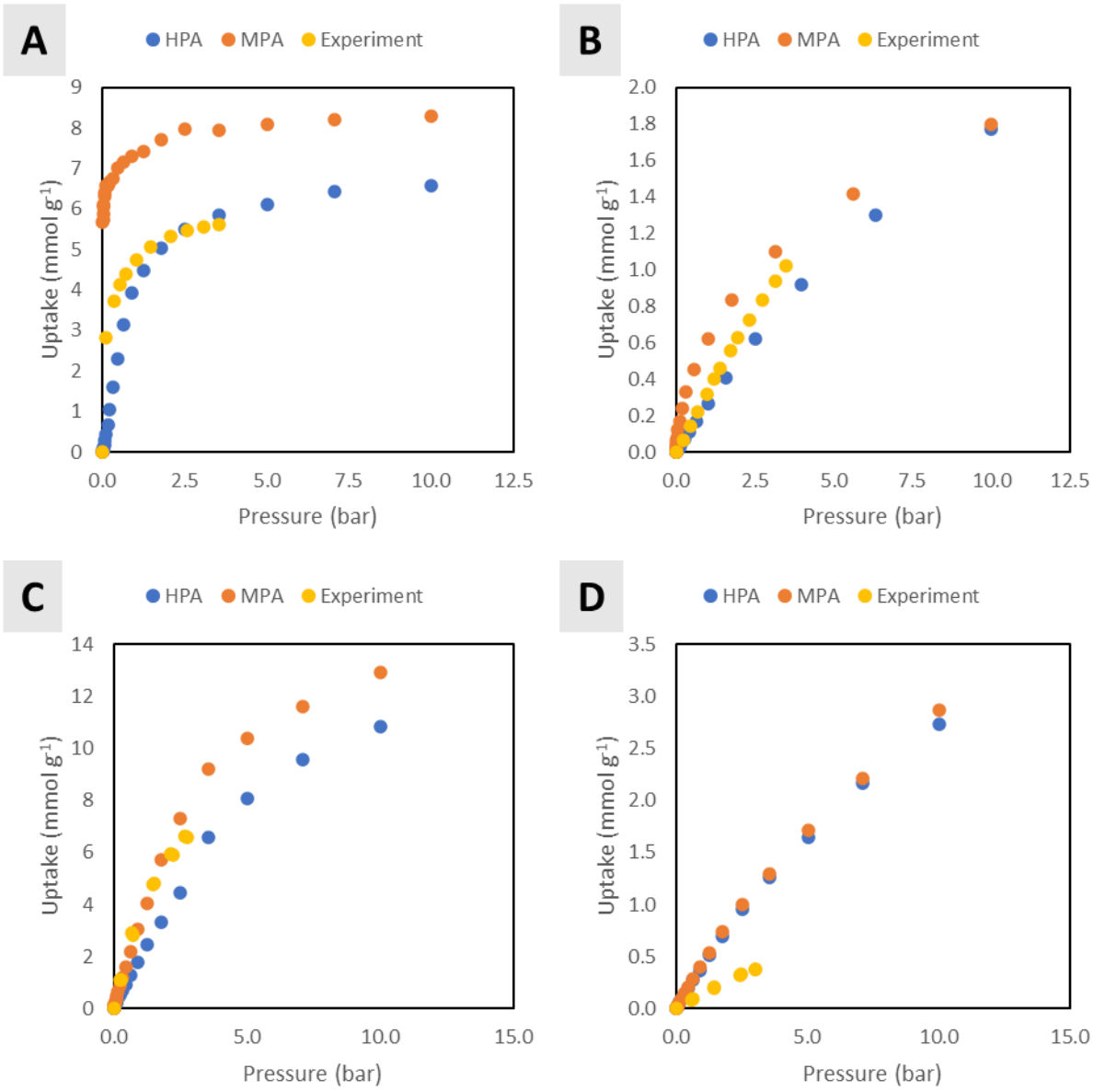

Figure 5.4. Results of the GCMC simulations. (A) CO_2 isotherms and (B) N_2 isotherms of 13X; (C) CO_2 isotherms and (D) N_2 isotherms of Cu-HKUST-1.

Appendix C) against experimental adsorption data. GCMC adsorption simulations can be thought of as a representation of a gravimetric[22] adsorption experiment where the adsorbent material is immersed into an infinitely large reservoir of a gas at a specified temperature and pressure. The goal of the GCMC simulation is to predict how much gas would be adsorbed once the porous material and the reservoir have reached equilibrium. GCMC simulations will be used, in this case, to determine whether the Mulliken (MPA)[177] or Hirshfeld (HPA)[178] population analysis must be used to describe the partial charges of the atoms in the frameworks, in addition to benchmarking the computational models against experimental data.[163,170] The results of the GCMC simulations are shown in Figure 5.4.

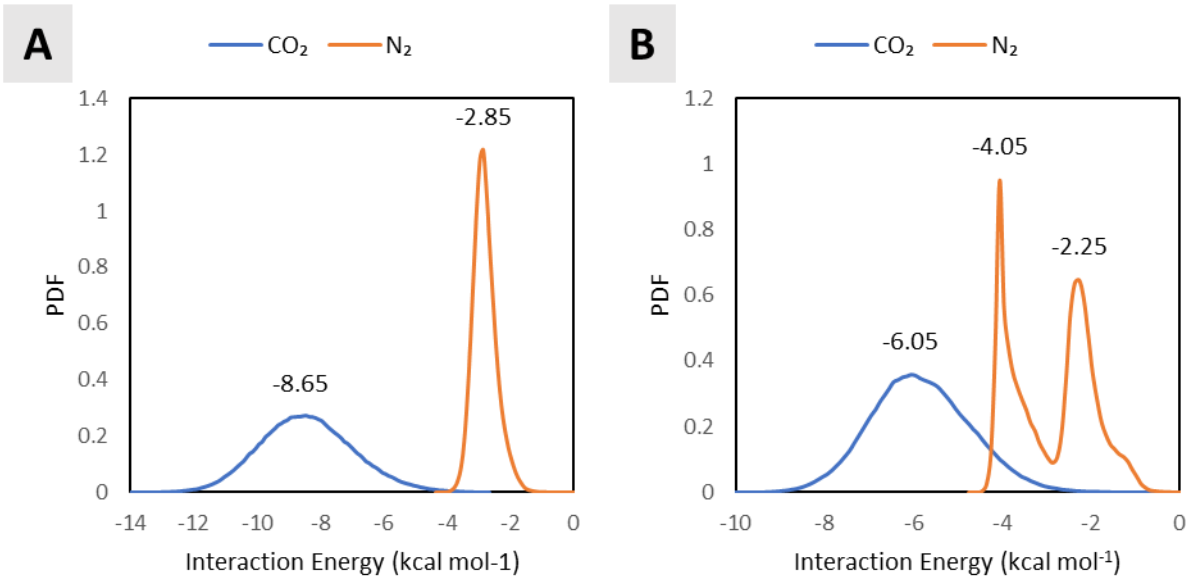

Figure 5.5. Interaction energy distribution plots of CO_2 and N_2 when adsorbed into (A) 13X and (B) Cu-HKUST-1 at 10 bar.

The GCMC results indicate that the HPA charge scheme must be used for 13X and the MPA charge scheme should be used for Cu-HKUST-1. CO_2 interacts more favorably with 13X than Cu-HKUST-1 with an interaction energy that is approximately 2.4 kcal mol^{-1} lower (see Figure 5.5). These findings are in line with isotherm fits of the experimental CO_2 adsorption data,[170] which show that CO_2 has a greater affinity for 13X than Cu-HKUST-1. The GCMC N_2 isotherm for Cu-HKUST-1, however, is not well described by any of the Cu-HKUST-1 models (*i.e.*, the HPA and MPA variants). Considering that charge schemes would not have a major impact on the description of N_2, which is uncharged within the context of our choice of forcefield (COMPASSII),[97] it is likely that the reason for the poor description of the N_2 uptake lies elsewhere. Therefore, the probability distribution functions (PDF) of the interaction energies (henceforth interaction energy distribution, see Figure 5.5) from the GCMC calculations were examined to pinpoint the cause of the unrealistic description of the N_2 uptake.

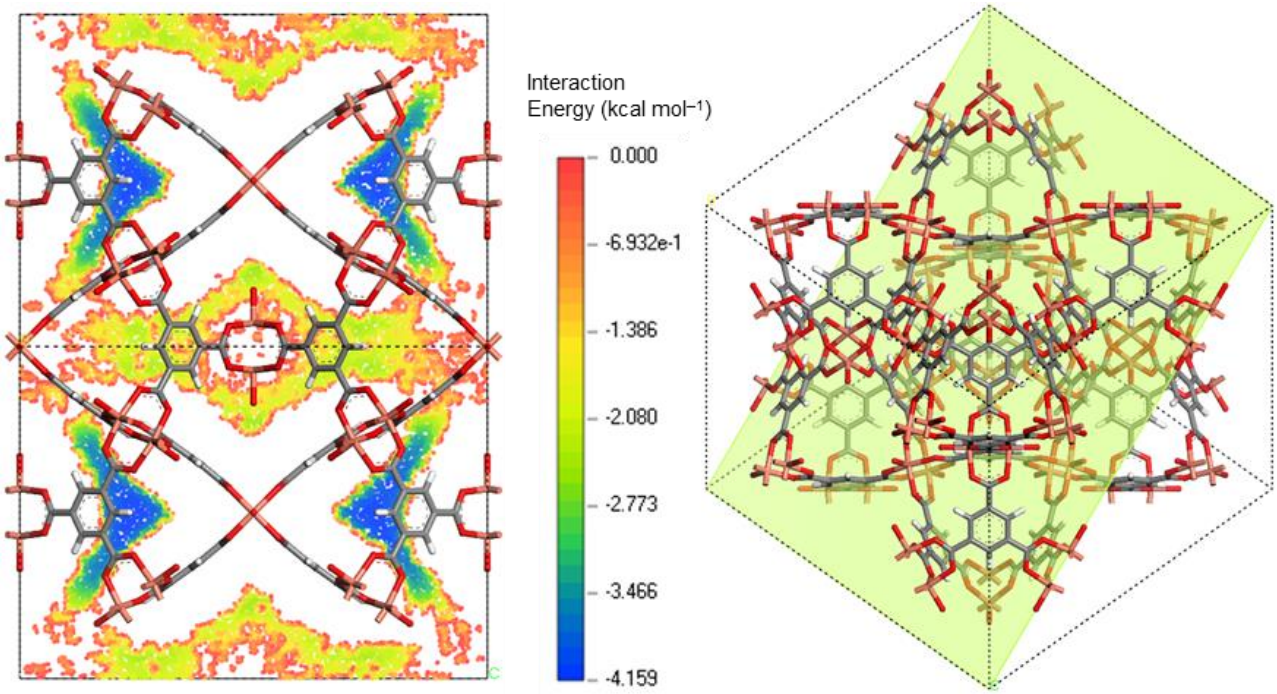

Figure 5.6. Plane sample of the interaction energy field of N_2 when it is adsorbed by Cu-HKUST-1. The position of the plane sample within the framework is indicated in lime.

The interaction energy distribution plot associated with the adsorption of N_2 in Cu-HKUST-1 shows that there is a secondary interaction peak centered around approximately –4 kcal mol^{-1}. It was found, upon integration of the PDF, that nearly half of the N_2 molecules interact with the Cu-HKUST-1

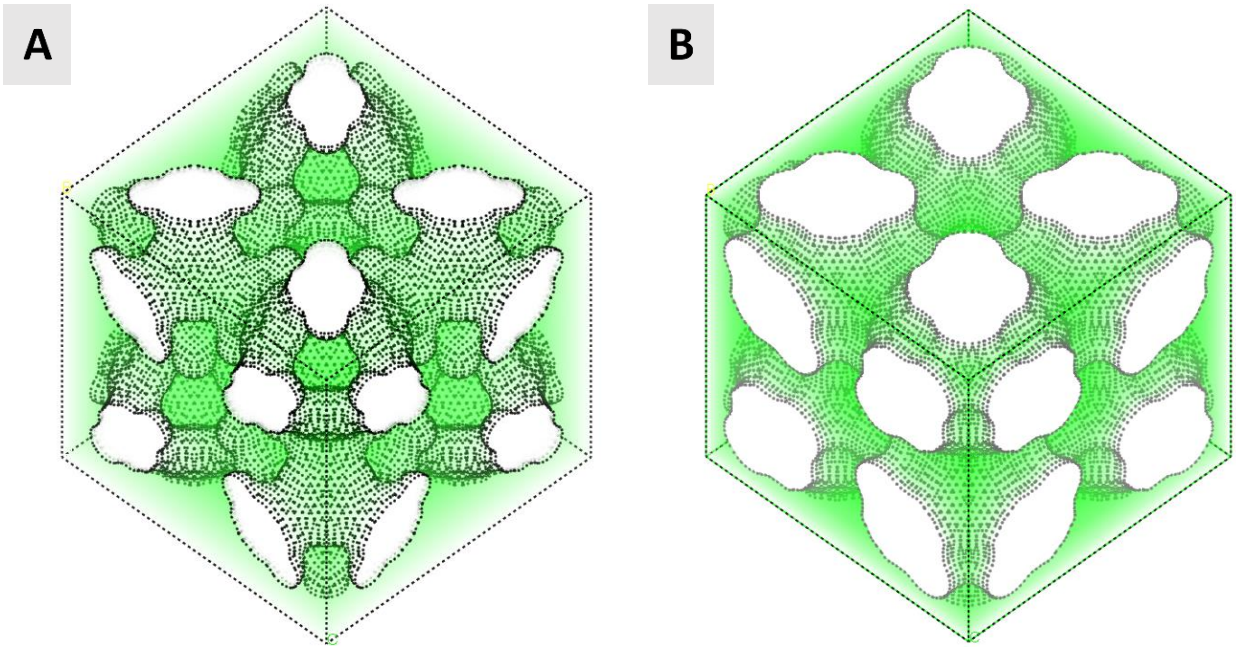

Figure 5.7. Representation of the accessible void space of Cu-HKUST-1 with a van der Waals scale factor of (A) 1 and (B) 1.65. Accessible regions are shown in green, and the inaccessible regions are shown in white. A probe radius of 1.65 was used to create the Connolly surfaces.

framework in this extremely favorable mode. The interaction energy field (see Figure 5.6) that corresponds to the interaction energy distribution plot of N_2 (Figure 5.5 B) shows that this highly favorable mode of interaction is, in fact, the adsorption of N_2 into the inner cavities found in the Cu-HKUST-1 structure (see Figures 5.1 B and 5.3 B). It is highly unlikely that N_2 would have an interaction mode with an associated energy that is only 2 kcal mol^{-1} higher than the mean interaction energy of CO_2 with Cu-HKUST-1, given that the measured uptake of N_2 is much smaller than that of CO_2. This suggests that there is an error with our Cu-HKUST-1 model.

One possibility is that N_2 does not access the smaller cavities of Cu-HKUST-1: this can be tested by altering the region where adsorption can take place. Specifically, an artificial adjustment can be made to the van der Waals radii of the backbone atoms of the Cu-HKUST-1 framework to effectively seal the smaller cavities when the Connolly surface of the framework is calculated with the same probe radius. To this end, the van der Waals radii of the backbone atoms were multiplied by a factor of 1.65 which was the smallest value that would cause the smaller cavities to be blocked. The original and recalculated Connolly surface for Cu-HKUST-1 is shown in Figure 5.7. It is worth noting, however, that this method of altering the backbone volume will likely affect the uptake of N_2 by all sites in Cu-HKUST-1 due to an overall reduction in the accessible volume.

The CO_2 and N_2 isotherms were simulated again with the blocked framework of Cu-HKUST-1. The interaction energy distribution plots of the two cases of N_2 adsorption were calculated, and it was found that blocking the access to the smaller cavities of the Cu-HKUST-1 framework effectively removed the strong interaction (see Figure 5.8) that contributed to the high uptake of N_2 in the earlier GCMC simulations (see Figure 5.4 D). The interaction between N_2 and Cu-HKUST-1 is isolated to a distribution with a slight shoulder centered around –2.3 kcal mol^{-1} when using the blocked framework. The subsequent results (Figure 5.9) agree with the experimental results, suggesting that, although CO_2

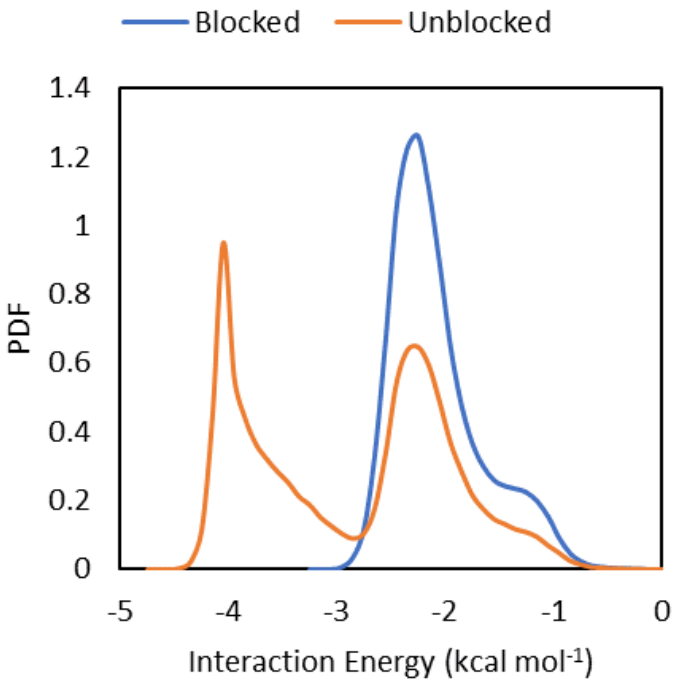

Figure 5.8. Energy distributions of N_2 adsorption into Cu-HKUST-1 with smaller cavities blocked and unblocked at 10 bar of N_2.

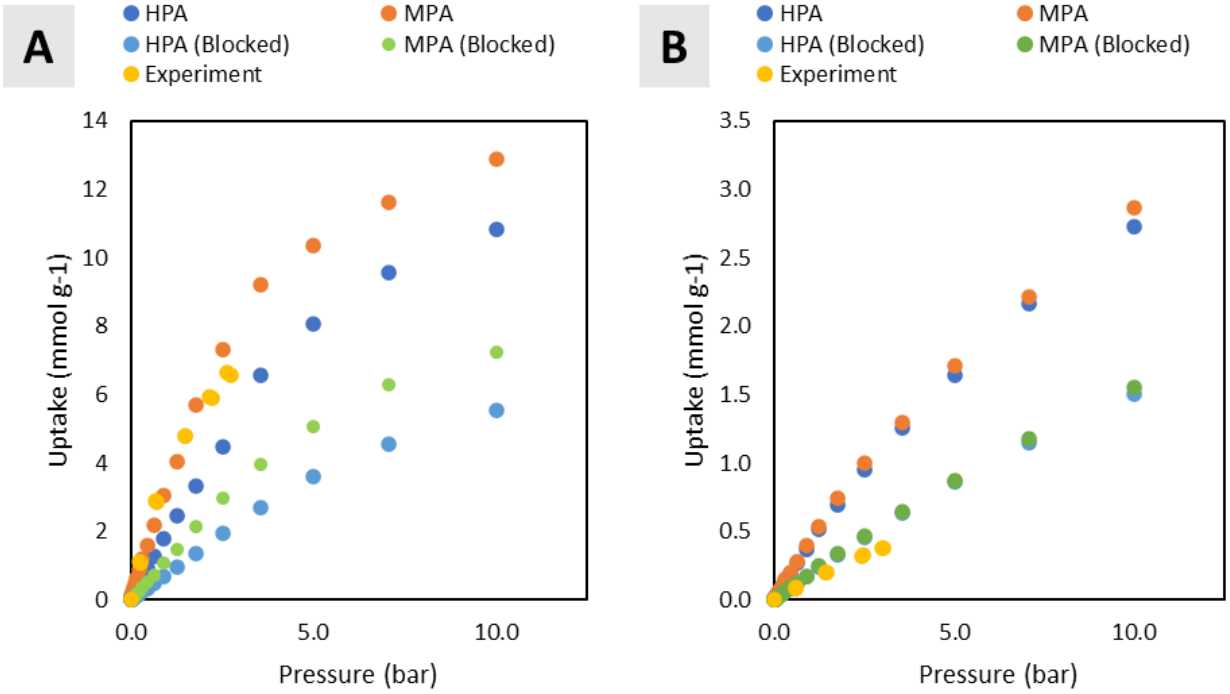

Figure 5.9. Adsorption isotherms of (A) CO_2 and (B) N_2 into Cu-HKUST in the conventional representation and sealed (blocked) representation.

does appear to enter the smaller cavities of Cu-HKUST-1, N_2 might not. It is not clear what mechanism could prevent N_2 from entering the smaller cavities, considering that Cu-HKUST-1 is a rigid framework and that CO_2 and N_2 are roughly the same size.[179] Nevertheless, this peculiar mode of N_2 adsorption will be assumed to be valid for this study.

When compared to the adsorption of N_2 in 13X, with an interaction energy distribution centered around –2.9 kcal mol^{-1} (see Figure 5.5), N_2 is slightly less favored by Cu-HKUST-1. It should be expected that 13X would interact more strongly with N_2, since it has a higher abundance of heavier elements, which results in a stronger dispersion interaction than with Cu-HKUST-1. This is confirmed by the fact that 13X displays a higher uptake of N_2 than Cu-HKUST-1 (see Figures 5.4 B and 5.4 D) even though 13X has a smaller calculated accessible volume (0.235 mL g^{-1}) than Cu-HKUST-1 (0.671 mL g^{-1}).

Benchmarked models for 13X and Cu-HKUST-1 can now be used in a series of Metropolis Monte Carlo simulations of the canonical ensemble (*NVT*, shortened to CMC)[73] with mixtures of CO_2 and N_2 to determine the interaction energies and the distribution of guest molecules in the framework. However, CMC simulations require that a predefined number of molecules of each adsorbate be loaded into the model, therefore, the adsorbed amounts, especially those that are obtained when multiple gases are adsorbed simultaneously, must be known. Our predictive RAST method (PRAST-S)[170] allows us to calculate the adsorbed amounts of multi-component gases, much like IAST, using

single-component adsorbed amounts. PRAST-S is set apart from IAST in that activity coefficients are included in the calculation of multi-component adsorbed amounts. The inner workings of PRAST-S are detailed briefly in Appendix C (see Figure C.1 and C.2), and it has previously been benchmarked against experimentally-determined adsorbed amounts for mixtures of CO_2 and N_2 with 13X and Cu-HKUST-1.[170]

The calculated single- and multi-component adsorbed quantities, obtained using PRAST-S, of CO_2 and N_2 at 1, 3 and 5 bar are shown in Table 5.1 for each adsorbent material. The full multi-component gas adsorption isotherms at these pressures can be found in Appendix C.

Table 5.4. Calculated adsorbed amounts (predictive RAST method) of CO_2 and N_2 per unit cell at various pressures and gas-phase compositions.

		Zeolite 13X		Cu-HKUST-1	
Pressure (bar)	y_{CO_2}	N_{CO_2}	N_{N_2}	N_{CO_2}	N_{N_2}
1	0.0	0	4	0	2
	0.1	34	3	5	1
	0.2	43	2	9	1
	0.3	48	2	14	1
	1.0	63	0	38	0
3	0.0	0	12	0	4
	0.1	46	5	13	3
	0.2	55	3	25	2
	0.3	60	3	34	2
	1.0	74	0	72	0
5	0.0	0	18	0	6
	0.1	52	6	21	4
	0.2	61	4	36	3
	0.3	66	3	48	2
	1.0	79	0	88	0

CMC simulations were performed for each of these loadings with the benchmarked models. The guest-accessible void spaces (see Figures 5.3 and 5.7 B) were used as defined for the GCMC simulations. The interaction energy distribution plots of the CMC simulations for 13X are shown in Figure 5.10. CO_2 appears to be unaffected by the presence of N_2 (Figure 5.10 A-C), except for a small

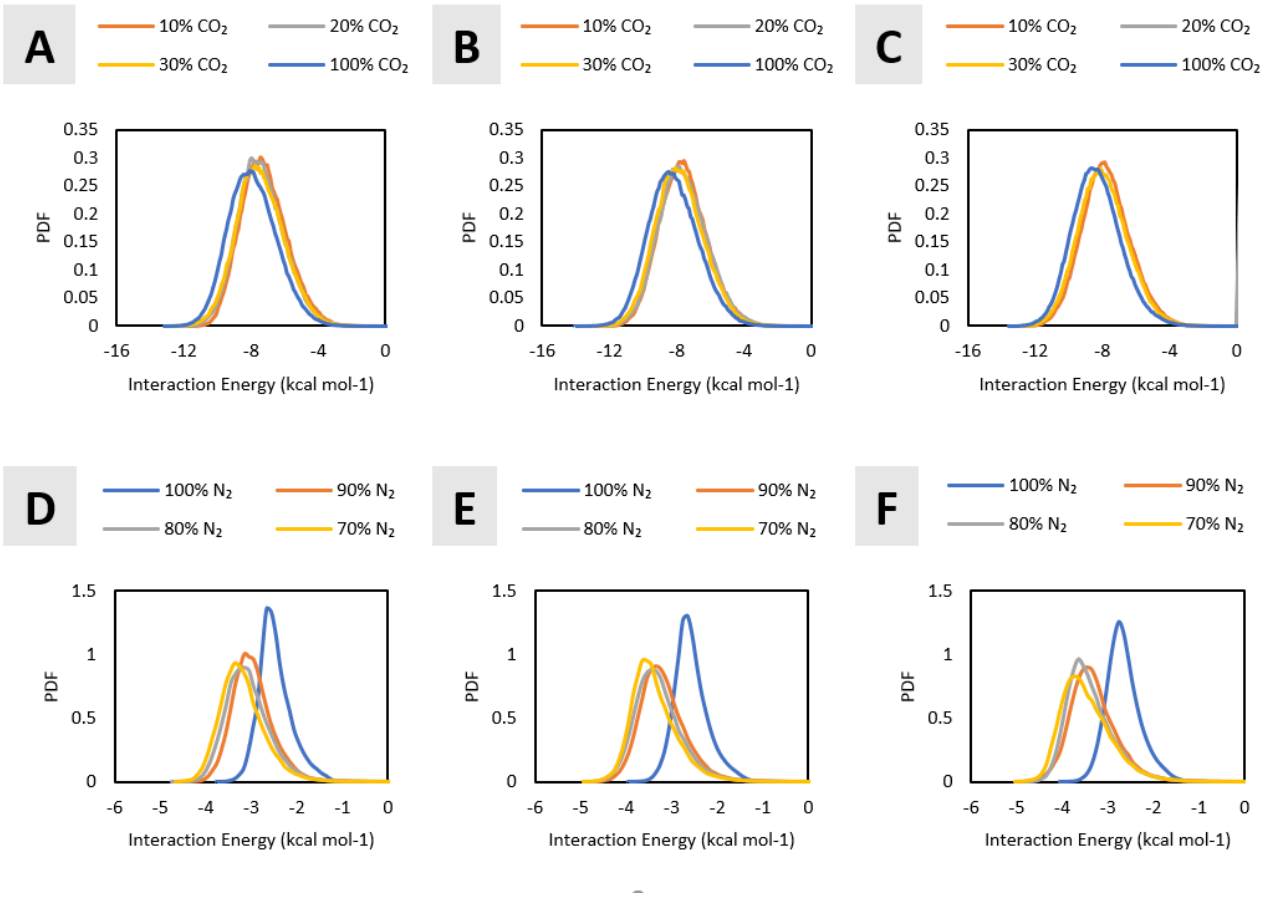

Figure 5.10. Single- and multi-component adsorption interaction energies for CO_2 at (A) 1 bar, (B) 3 bar, and (C) 5 bar; N_2 at (D) 1 bar, (E) 3 bar, and (F) 5 bar when they are adsorbed into 13X.

destabilization as the concentration of N_2 is increased in the pores. A striking feature of these interaction energy distribution plots is the sudden shift to a more favorable interaction energy between N_2 and 13X (Figure 5.10 D-F) for multi-component adsorption (90% N_2) compared to the single-component adsorption (100% N_2). CO_2, thus, appears to influence the adsorption of N_2 in 13X so that it becomes more favorable.

If it is assumed that these interaction energy distribution plots consist of only one distribution, as opposed to several overlapping distributions, then the mean interaction energy and standard deviation of the interaction energy can be calculated by integrating the probability distributions shown in Figure 5.10. The result of this process (see Figure 5.11) indicates that the interaction between N_2 and 13X strengthens significantly in the presence of CO_2. However, only the change from pure N_2 to 90% N_2 in the gas phase yielded a large change in the interaction energy; further changes (*e.g.*, 90% N_2 *vs.* 80% N_2 in the gas phase) did not alter the interaction energy significantly. In contrast, the interaction between CO_2 and the framework only weakens slightly as N_2 is introduced.

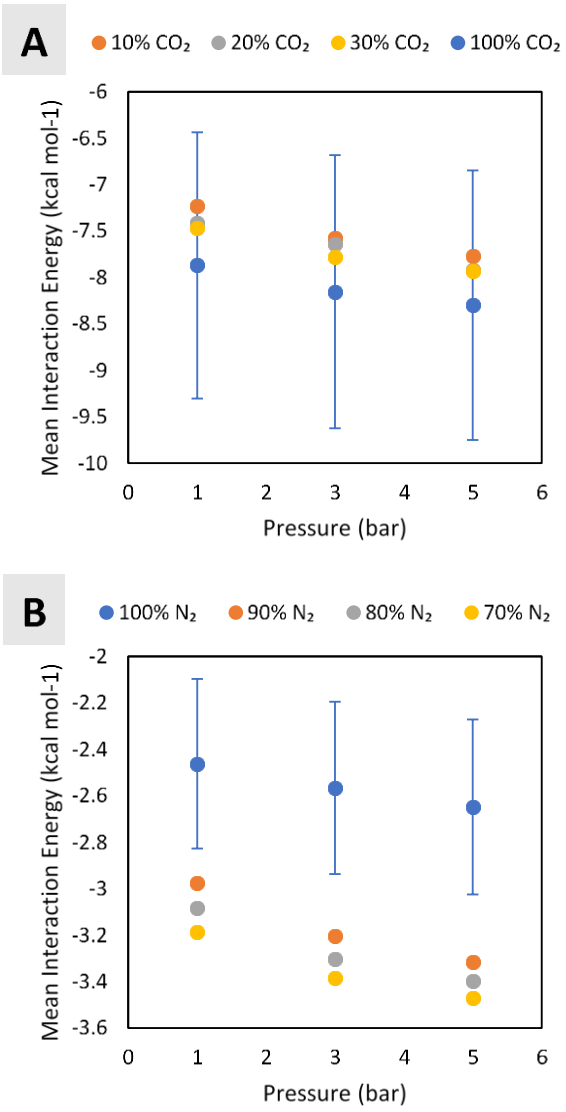

Figure 5.11. Mean interactions energies of (A) CO_2 and (B) N_2 at various pressures and compositions. The standard deviation of the interaction energy distribution of the pure component is also shown.

A different treatment was required for the CMC simulations of Cu-HKUST-1: the different species of adsorbates had to be loaded into the framework sequentially due to their accessible volumes being different. Therefore, the simulation was broken up into parts. In the first simulation, (1) CO_2 was loaded into the empty framework, then (2) the lowest-energy configuration from (1) was selected and used as the input for the N_2 CMC simulation. In the second simulation, (3) N_2 was loaded into the empty framework and then (4) CO_2 was loaded into the lowest-energy configuration of the N_2 CMC simulation in (3). The data from (2) was used as a representation of the N_2 adsorption (in the presence of CO_2), while the data from (4) was used as a representation of the CO_2 adsorption (in the presence of N_2) by Cu-HKUST-1.

The results of these CMC simulations for Cu-HKUST-1 are shown in Figure 5.12. These interaction energy distribution plots are far more complex than those of 13X, since they consist of several overlapping interaction peaks that cannot be deconvoluted easily. Therefore, the approach previously used to interpret the interaction energy distribution plots of 13X (see Figure 5.11) cannot be applied to those of Cu-HKUST-1. The interaction energy distributions of CO_2 clearly tend towards a single distribution centered around –6 to –5 kcal mol^{-1} as the amount of CO_2 in the pores is increased. The N_2 interaction energy distribution plots (see Figure 5.12 D-F) appear to consist of fewer overlapping distributions than the CO_2 interaction energy distribution plots. Interestingly, at 1 bar total pressure, the N_2 interaction energy distribution remains virtually unchanged as the mole fraction of CO_2 is increased in the gas phase. At

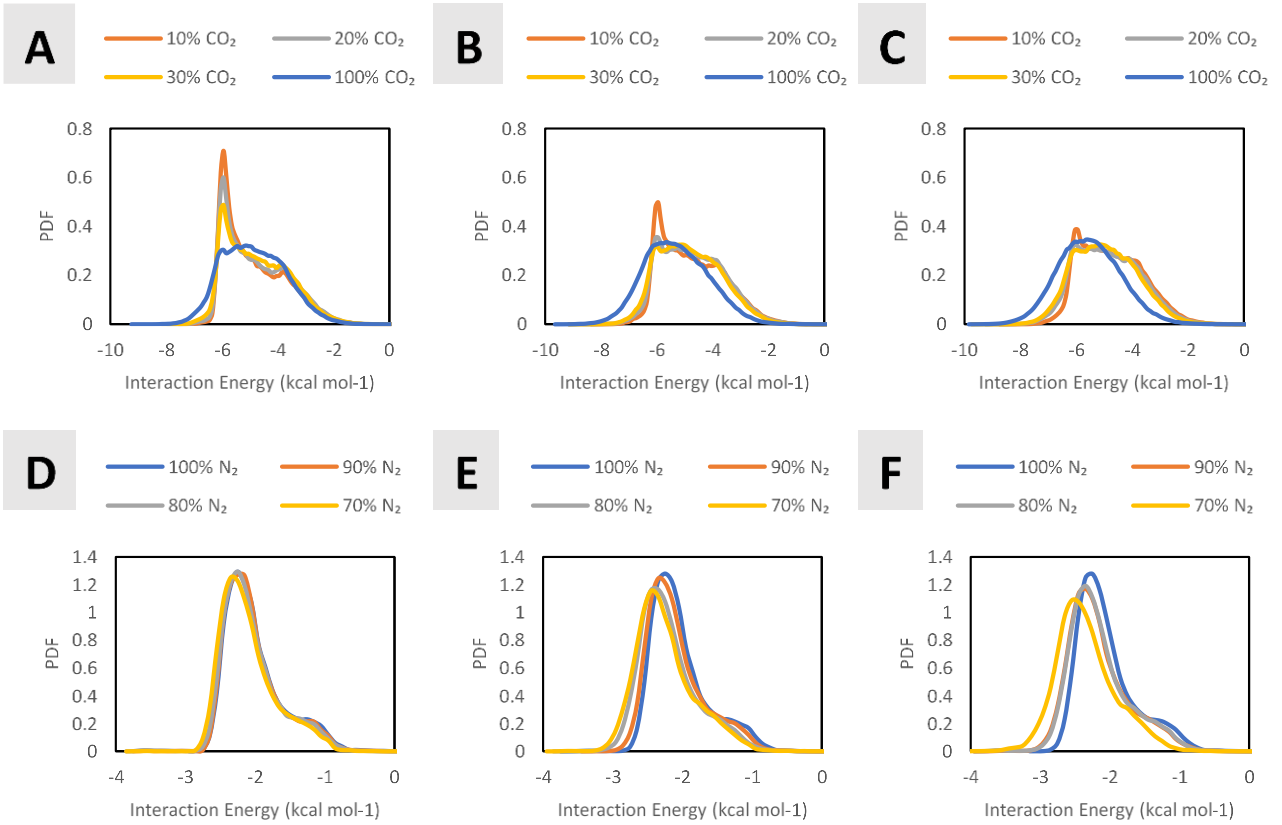

Figure 5.12. Single- and multi-component adsorption interaction energies for CO_2 at (A) 1 bar, (B) 3 bar and (C) 5 bar total pressure and N_2 at (D) 1 bar, (E) 3 bar and (F) 5 bar total pressure, when they are adsorbed by Cu-HKUST-1.

higher pressure, however, a shift in the N_2 interaction energy distribution becomes visible as the proportion of CO_2 is increased.

These data (in Figures 5.10 and 5.12) can be reconciled to the notion of ideality, in terms of AST. It has been shown previously[170] that 13X and Cu-HKUST-1 have different outcomes when adsorbing mixtures containing only CO_2 and N_2. In the case of zeolite 13X, the mixed adsorption of CO_2 is essentially always ideal, which means that IAST gives a good description of the measured adsorption, whereas in the mixed adsorption, N_2 displays the non-ideal behavior (*i.e.*, there are significant deviations between the measured uptake and IAST). Furthermore, the mixed adsorption of both CO_2 and N_2 are ideal for Cu-HKUST-1. It was not clear, before the calculations presented in the current study were performed, why this was the case. However, the data in this study indicate that a drastic shift in the interaction energy of an adsorbed species when adsorbed in isolation compared to it being adsorbed in the presence of another gas species may be a telltale sign of non-ideal adsorption.

Closer investigation of the distribution of the guest molecules within the host structures is warranted to gain a better understanding of what physical phenomenon may be leading to the ideal, and non-

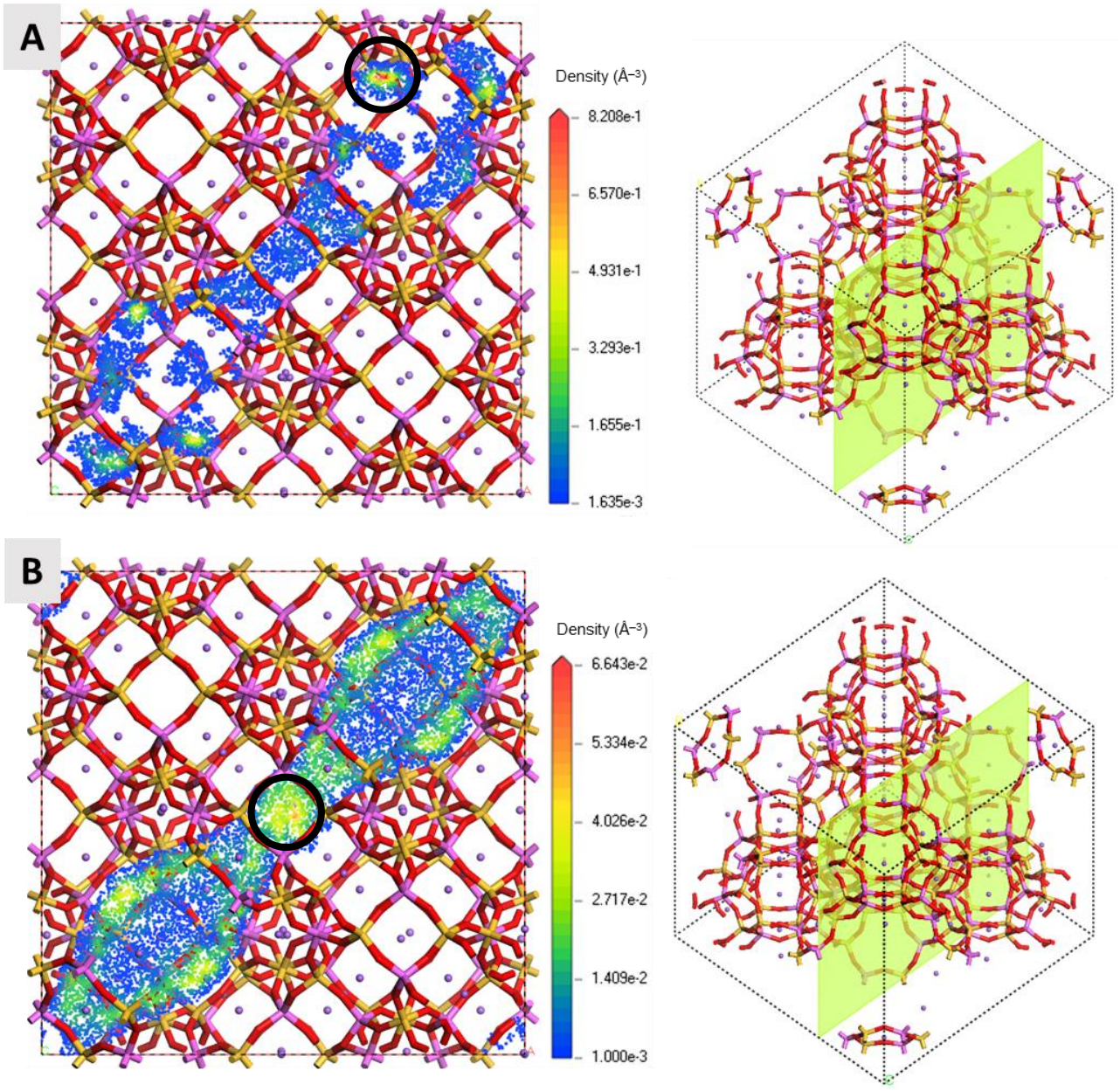

Figure 5.13. Plane samples of the number density fields of (A) CO_2 and (B) N_2 when they are adsorbed in isolation by 13X. The locations of the planes relative to the framework coordinates are shown in lime. Zones with a higher density are highlighted with a black circle.

ideal, adsorption of these molecules. The strategy employed is to calculate the local density of guest molecules around key locations within the porous frameworks. In a CMC simulation, the local density of molecules in the adsorbent is calculated alongside the interaction energy distribution. Representations of the local densities of the guest molecules in 13X are shown in Figure 5.13. The average densities of CO_2 and N_2, relative to the unit cell volume of 13X, in these simulations are 5.75×10^{-3} Å^{-3} and 2.11×10^{-3} Å^{-3}, respectively. These density profiles indicate that CO_2 tends to be localized around certain parts of the framework, while N_2 is diffusely distributed throughout the framework at an almost fixed distance from the framework that likely corresponds to the minima of

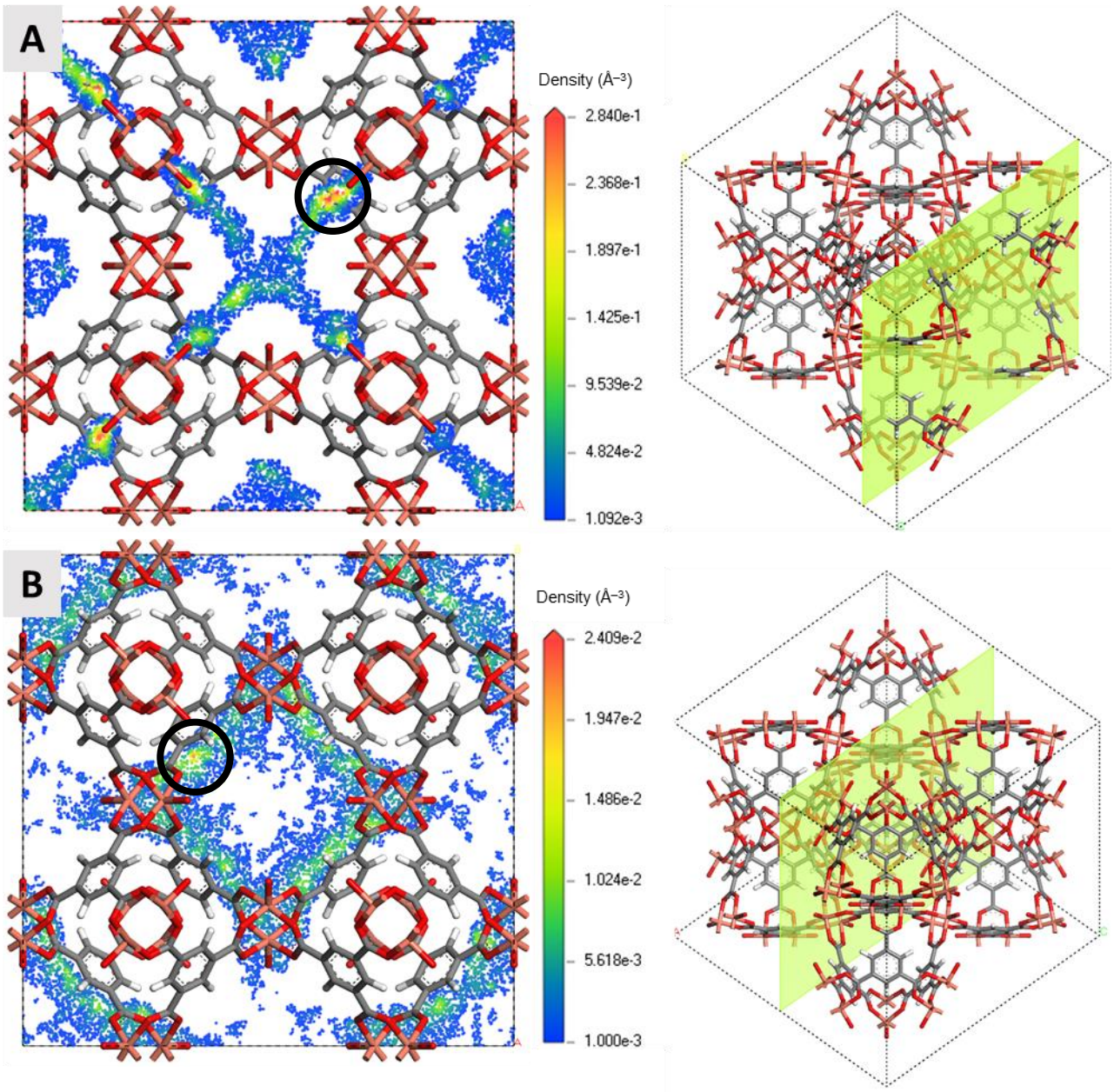

Figure 5.14. Plane samples of the number density fields of (A) CO_2 and (B) N_2 when they are adsorbed in isolation by Cu-HKUST-1. The locations of the planes relative to the framework coordinates are shown in lime. Zones with a higher density are highlighted with a black circle.

the Lennard-Jones[94,95] potential. The highest local density of N_2 is located around a special site in the 13X framework – a Site III position (see Figure 5.2) that is unfilled by an Na cation (there are not as many Al atoms as Si atoms in the 13X framework and, consequently, some of the Site III positions are unfilled).[180] Specifically, there are a 10 of these special sites per unit cell in the 13X model that is used in this study.

The local densities of CO_2 and N_2 were also investigated in Cu-HKUST-1. The average densities of CO_2 and N_2 were 5.77×10^{-3} Å^{-3} and 5.69×10^{-4} Å^{-3}, respectively. CO_2 tends to adsorb into the inner cavities of Cu-HKUST-1, although there are several other sites where the CO_2 molecules can also

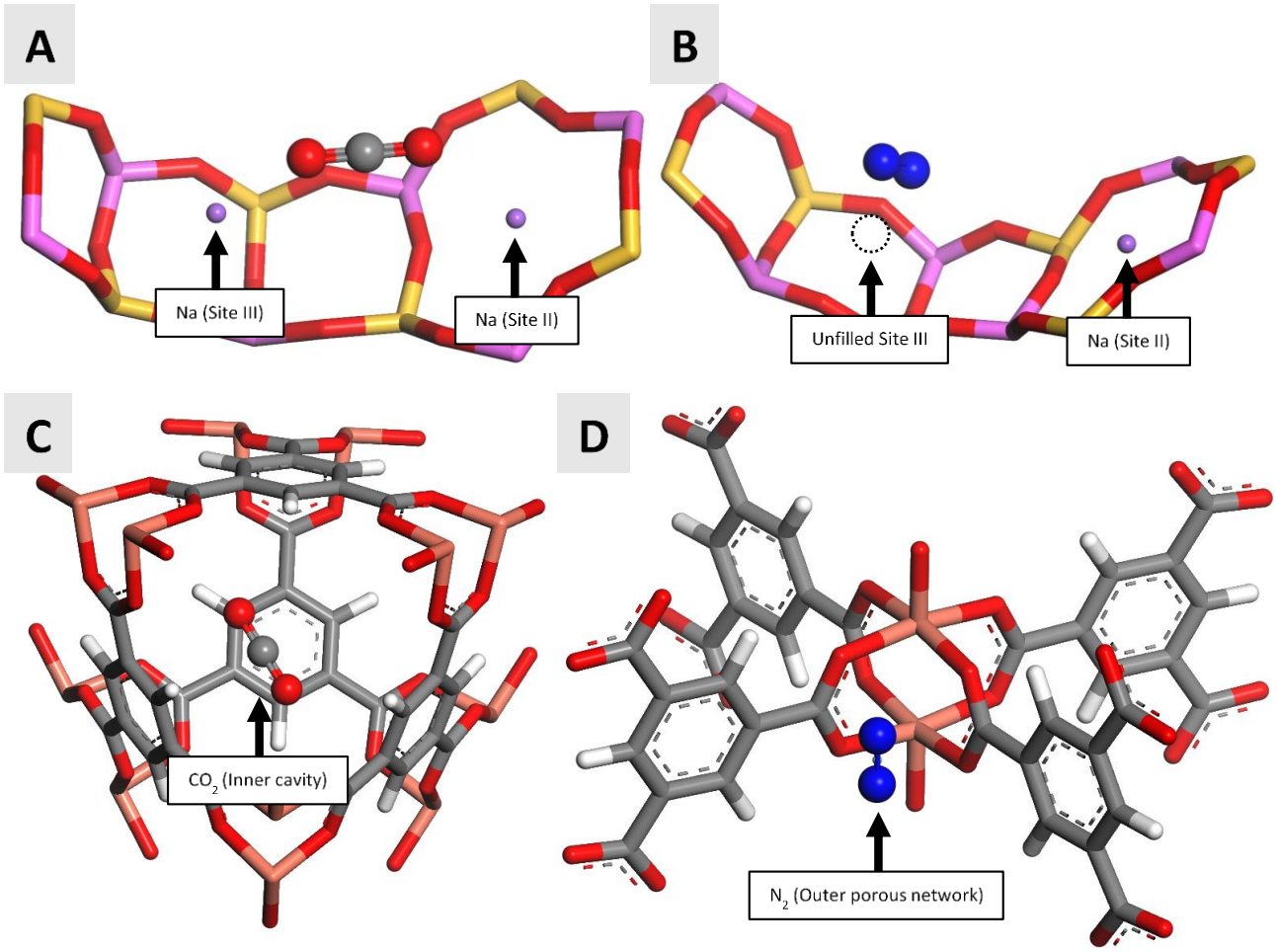

Figure 5.15. Most favorable interaction modes of (A) CO_2 and (B) N_2 when adsorbed by 13X and the most favorable interaction modes of (C) CO_2 and (D) N_2 when adsorbed by Cu-HKUST-1.

interact favorably with the framework (see Figure 5.14). Consequently, the local density of CO_2 in Cu-HKUST-1 is much less localized when compared to 13X. N_2 is spread diffusely throughout the framework – excluding the inner cavities, because these parts of the framework were blocked for N_2 – but its local density is slightly higher around the paddle-wheel motif.

These local density fields provide clues as to the parts of the frameworks that need to be monitored for each gas species, to gain some understanding as to what interactions are leading to ideal or non-ideal behavior during adsorption. The simplest method to quantify these interactions is to calculate the radial distribution function (RDF) for the guest molecules relative to these adsorption sites. An RDF, in the context of periodic systems, is a function that relates the local density of a species (CO_2 or N_2) around reference particles, such as the adsorption sites, to the overall density of the species in the periodic system.[181]

The low-energy configurations of the CMC simulations used in Figures 5.13 and 5.14 indicate that each guest species has a preferred interaction mode with the frameworks (see Figure 5.15). CO_2 is

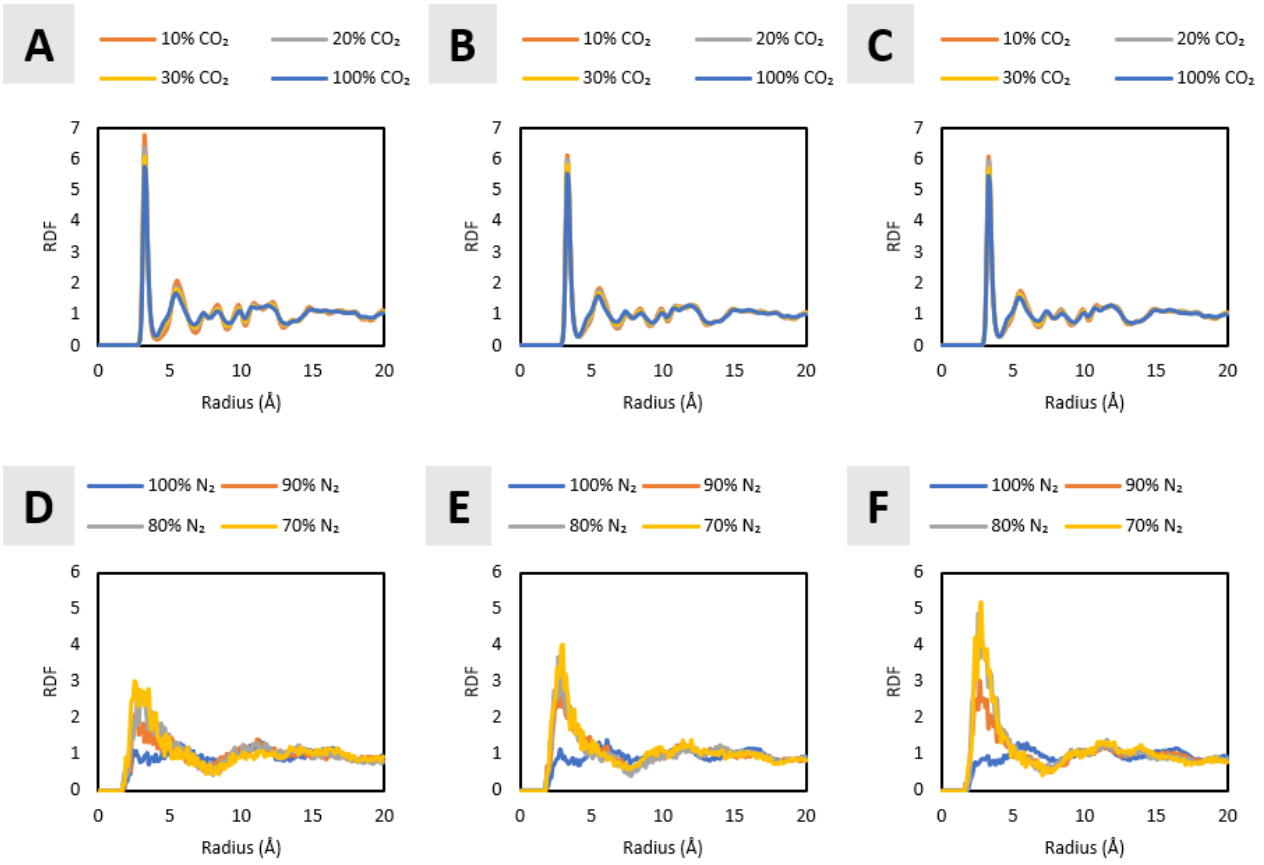

Figure 5.16. Radial distribution functions of CO_2 around the Site III Na atoms at (A) 1 bar, (B) 3 bar and (C) 5 bar total pressure and N_2 around the unfilled Site III positions at (C) 1 bar, (D) 3 bar and (E) 5 bar.

generally found around the Site III Na cations of 13X. Closer inspection shows that a favorable electrostatic interaction between the negatively-charged oxygen atoms of CO_2 and the positively-charged Site III Na atoms of 13X occurs. Additionally, the positively-charged carbon atom of CO_2 also interacts favorably with the negatively-charged oxygen atoms of 13X. As stated earlier, N_2 atoms are distributed diffusely throughout the 13X pores, but the data (see Figure 5.13) do show that there is a higher density of N_2 around the unfilled Site III positions. It is difficult to specify particles in the Cu-HKUST-1 framework with which CO_2 and N_2 interact favorably, therefore, the most "central" atomic species (Cu) was used as the reference particle for RDF calculations involving both CO_2 and N_2.

Molecular dynamics (MD) simulations of the canonical ensemble (*NVT*) of the guest-loaded zeolite 13X structures (taken from the same CMC simulations used in Figure 5.10) were performed to obtain an unbiased representation of the distribution of guest molecules over time. Following this, RDF calculations were performed on the results of these MD simulations. The reference particles that were used for the RDF calculations concerning 13X are the Site III Na cations and the unfilled Site III

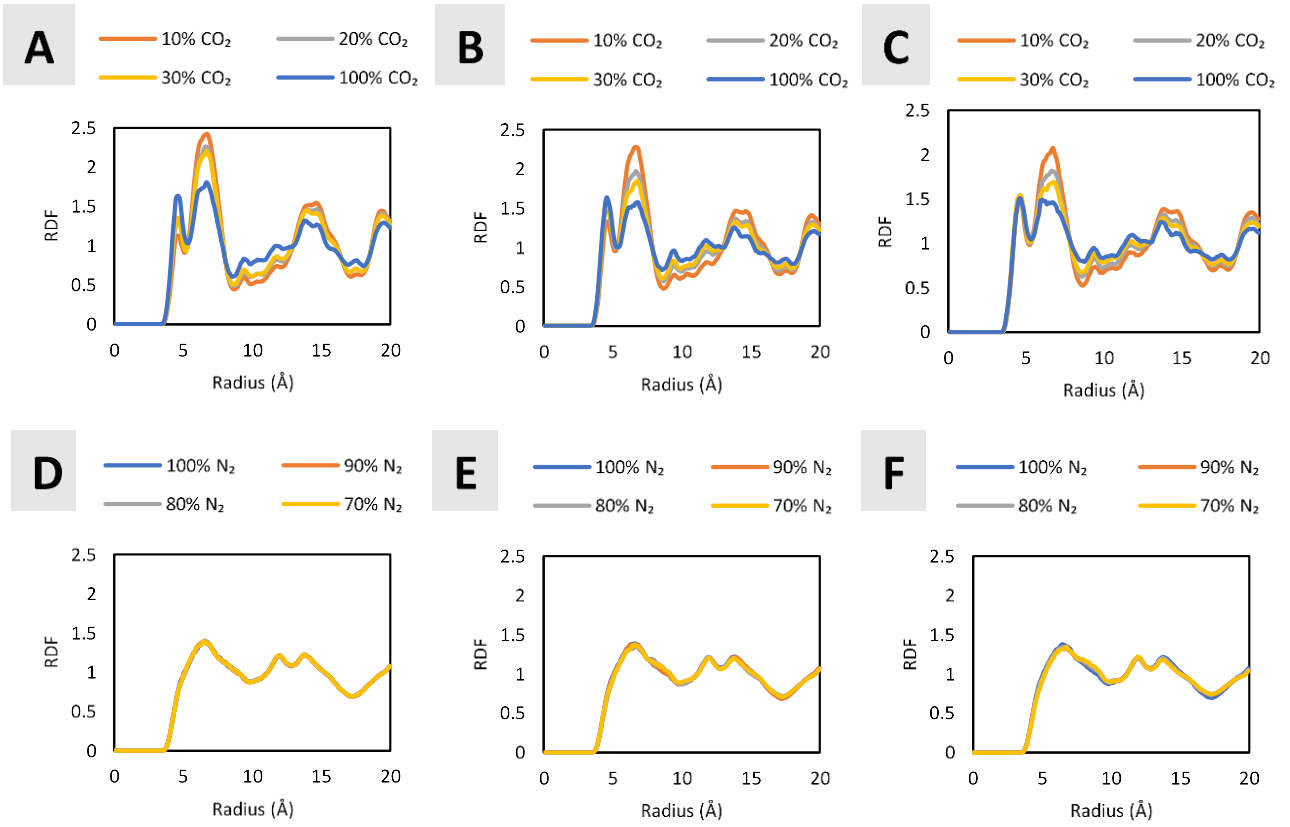

Figure 5.17. Radial distribution functions of CO_2 around the Cu atoms at (A) 1 bar, (B) 3 bar, and (C) 5 bar total pressure and N_2 around the Cu atoms at (C) 1 bar, (D) 3 bar, and (E) 5 bar.

positions. The RDFs of CO_2 and N_2 were calculated around these reference particles in 13X, yielding the data shown in Figure 5.16, and Figure C.13 in Appendix C.

The data shown in Figure 5.16 demonstrate that the presence of N_2 has very little influence on the density of CO_2 around the Site III Na cations, however the density of N_2 around the unfilled Site III positions increases sharply as CO_2 is introduced into the system. The CO_2 molecules do not interact as favorably with the unfilled Site III positions as with the Site III Na atoms (given the low density of CO_2 around the unfilled Site III positions, see Figure C.13 in Appendix C), therefore, it is shown that CO_2 effectively modulates the surface of 13X so that N_2 molecules bind to more favorable sites by blocking the areas of 13X that are less favorable for N_2 to interact with. The sudden shift to a more favorable interaction energy for N_2 seen in Figure 5.10 D-F and Figure 5.11 B, can likely be attributed to this "shepherding" effect. This effect could also be the reason for which the multi-component N_2 uptake is measured to be higher than the ideal case of AST – the single-component adsorption isotherm of N_2 is based on a lower interaction energy than that which is seen in the multi-component adsorption isotherm for N_2 in the presence of CO_2.

Owing to the definitions used for the accessible space of each guest molecule in Cu-HKUST-1 (see Figure 5.7), it was not possible to perform MD simulations for Cu-HKUST-1, since the available

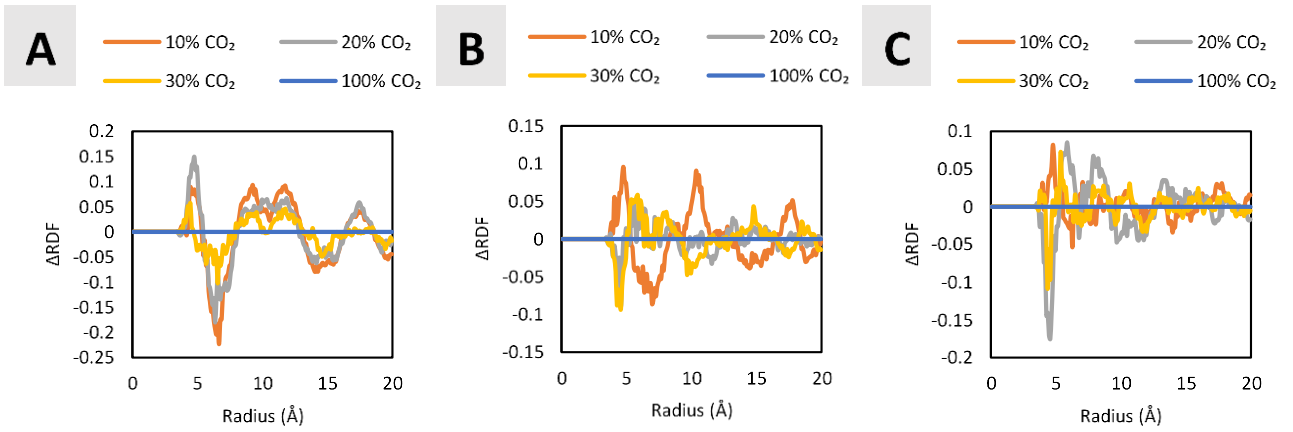

Figure 5.18. Difference radial distribution functions of Cu-HKUST-1 loaded with only CO_2 and Cu-HKUST-1 loaded with both CO_2 and N_2.

software does not allow the user to constrain two different guest species to two different void space domains in the unit cell simultaneously. Therefore, the results of the CMC simulation must be used instead for the RDF calculations; the results of these RDF calculations are shown in Figure 5.17. The CO_2 molecules, N_2 molecules, and Cu atoms were used as the sets of interest for the Cu-HKUST-1 RDF calculations.

Considering that CO_2 and N_2 bind to two independent parts of the framework, it is unsurprising that the RDF data for N_2 does not vary as CO_2 is introduced into the system at constant total pressure. It does appear, however, as if the CO_2 RDF data vary with the total pressure and the composition. It can be tested whether the presence of N_2 has any effect on the interaction of CO_2 with Cu-HKUST-1 by performing the same CMC simulations as before (see Figure 5.12) with the exception that only CO_2 is loaded into the empty framework. Once completed, the resulting RDF data from these simulations were then subtracted from the CO_2 RDF data shown in Figure 5.17 A-C to determine the whether the interaction between CO_2 and Cu-HKUST-1 was influenced by N_2 (see Figure 5.18).

Since the difference between the radial distributions, shown in Figure 5.18, is less than 0.2 as compared to the RDF values of 2.5 (Figure 5.17), it can be concluded that N_2 has little to no effect on the interaction between CO_2 and Cu-HKUST-1. Furthermore, this implies that interference by N_2 molecules was not the cause of the change in the shape of the interaction energy distributions for CO_2 seen in Figure 5.12 A-C. Instead, it could be that CO_2 molecules influence the binding of other CO_2 molecules to Cu-HKUST-1 as the loading of CO_2 is increased. It can be shown, for example, that CO_2 molecules are less likely to form localized clusters in the framework as the amount of CO_2 is increased in the framework (Figure 5.19). The RDF curves for CO_2 flatten at higher loadings of CO_2, which indicates that the local density of CO_2 around the Cu atoms and the average density of CO_2 within the framework becomes indistinguishable. This means that CO_2 is distributed more evenly

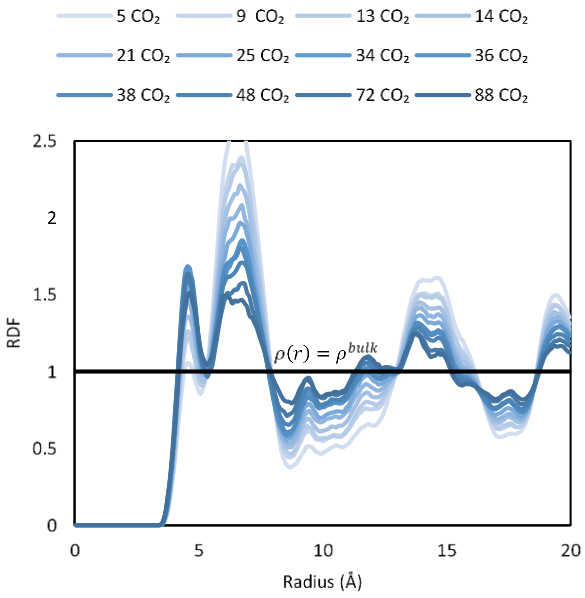

Figure 5.19. Radial distribution functions of CO_2 around the Cu atoms of Cu-HKUST-1 at various loadings. The value for the RDF at which the local density ($\rho(r)$) of CO_2 around the Cu atoms is equal to the average density (ρ^{bulk}) of CO_2 in the framework is shown as a black line.

throughout the framework at higher loadings and would likely explain why the CO_2 interaction energy distribution coalesces into a broad single distribution (at 100% CO_2 in the gas phase) as seen in Figure 5.12 A-C.

The combination of the interaction energy distributions and local density distributions provide the necessary insights as to what the cause of ideal or non-ideal behavior may be in the adsorption processes that involve CO_2 and N_2, and these two frameworks. Mean interaction energies, specifically the difference between the mean interaction energy of the guest molecule in isolation and the mean interaction energy of the guest molecule in the presence of another gas species, define whether the adsorption process was ideal or not. If there is an excess energy of "mixing" in the adsorbed phase between the adsorption of the pure component and the mixed component, such as in the case of N_2 adsorbing into 13X in the presence of CO_2, then the system is likely non-ideal. Conversely, like ideal solutions, if the change in energy due to mixing is zero then the adsorption of the mixture is ideal.

Qualitative energy diagrams describing the adsorption of CO_2 and N_2 in these two frameworks are shown in Figure 5.20. The change in energy of guest molecules during a multi-component gas adsorption process is described in three steps: (1) the mean interaction energy of a guest species in isolation at P_{total}; (2) the mean interaction energy of the guest species at partial pressure P_{CO_2} or P_{N_2}; and (3) the mean interaction energy of a guest molecule when mixed with another gas species at $P_{CO_2} + P_{N_2} = P_{total}$. Any energy changes prior to (3) are unrelated to the adsorption of the mixture, because they are part of the shifts in energy that occur naturally during the single-component gas adsorption of a species. If there is a significant change in energy between (2) and (3), however, then the adsorption is likely non-ideal, otherwise the adsorption is ideal. Once it has been established that the adsorption of a gas species in a mixture is either ideal or non-ideal, then analysis of the local

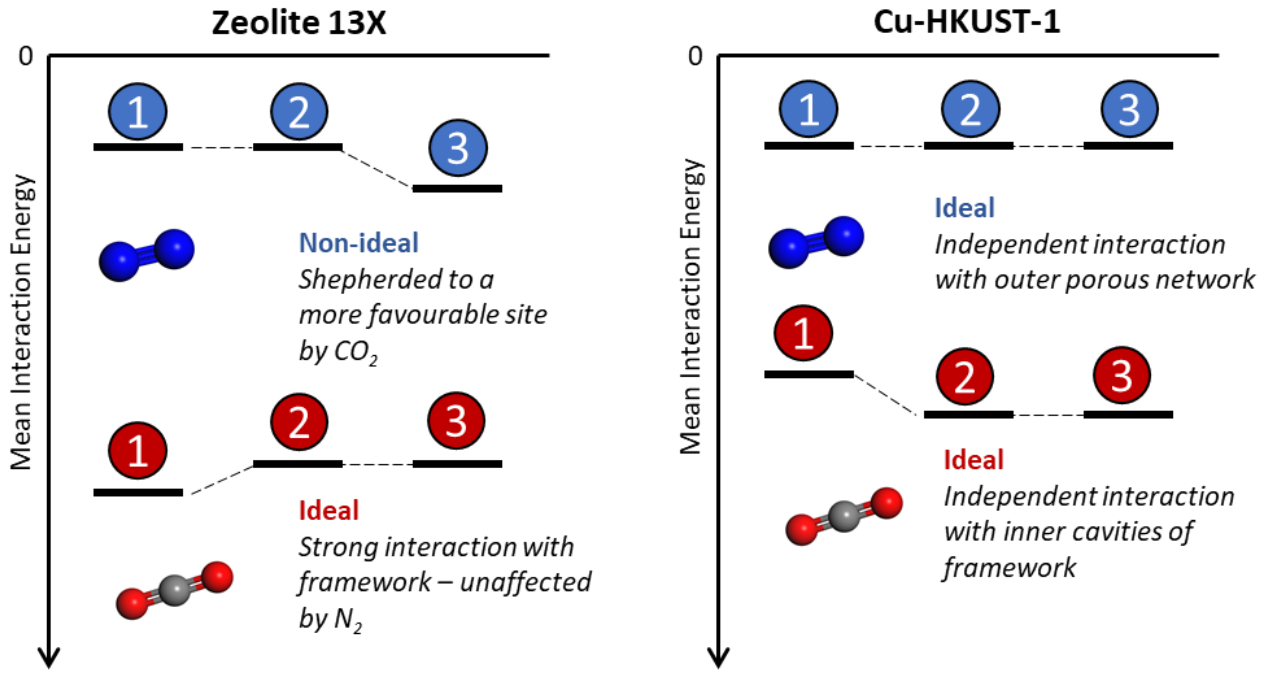

Figure 5.20. Energy diagrams for the adsorption of CO_2 and N_2 into 13X and Cu-HKUST-1. (1) Pure component interaction energy at total pressure P. (2) Pure component interaction energy at partial pressure P_{CO_2} or P_{N_2}. ($P_{CO_2} + P_{N_2} = P$). (3) Interaction energy of the component under mixed adsorption conditions.

density (*via* RDF analysis) provides the necessary insights into the mechanism causing the type of adsorption.

5.4 CONCLUSION

Multi-component gas adsorption processes are nuanced phenomena that require more attention than a simple selectivity calculation. This notion is demonstrated in this study, in that similar mixtures of guest molecules behave radically differently in porous materials. The main difference between the adsorption of these gas mixtures is that some gases are adsorbed ideally, while others are not. The analyses that were performed in this study allowed us to gain insight into the driving force behind ideal or non-ideal adsorption. For example, one mode of non-ideal behavior was discovered in this work where one gas species (CO_2) was optimizing the surface of the adsorbent (13X) so that another gas species (N_2) would interact more favorably. Ideal adsorption thus manifests as the independent adsorption of gas species, where the gas is either experiencing a strong interaction with the framework (*e.g.*, CO_2 in 13X) or the gases interact with different parts of the framework (CO_2 and N_2 in Cu-HKUST-1). This is not to say that all multi-component adsorptive processes, with varying degrees of ideality, would adhere to the modes discussed above. It is likely that much more work needs to be done before a comprehensive understanding of the forces that lead to ideal or non-ideal adsorption can be obtained.

Chapter 6. Future Work and Conclusions

6.1 ABSTRACT

Many of the facets of capturing multiple-component gases, specifically mixtures of CO_2 and N_2, using solid porous adsorbents were addressed in this study. Experimental multi-component gas adsorption techniques were furthered by the development of a volumetric adsorption instrument that can measure the uptake of individual gases from a gas mixture. Theoretical techniques were improved by the introduction of a new predictive adsorbed solution theory method (PRAST-S), a new activity coefficient model (the virial activity coefficient model), a new multiple-component gas adsorption metric (working selectivity), and various new insights into the origin of ideal and non-ideal adsorption through molecular modeling.

6.2 EXPERIMENTAL METHODS

The multi-component gas adsorption (MGA) experiments that were performed with mixtures of CO_2 and N_2 with zeolite 13X and Cu-HKUST-1 were largely successful. These successes can be attributed to the quality of the materials and gas mixtures that were used, the continued development of the instrument since its inception, the design philosophies that were followed, and the development of rapid data-analysis software to test the quality of an adsorption experiment.

6.2.1 Materials

Zeolite 13X and Cu-HKUST-1 are both well-known adsorbent materials that show great promise to capture CO_2 from N_2, but their MGA characteristics had only been studied to a limited extent. The MGA data measured in this study (Chapter 3 and 4) show that both materials are, without question, excellent adsorbers with respect to selectively capturing CO_2 from N_2. 13X, the current industry standard for CO_2 capture, is more selective for CO_2 than Cu-HKUST-1, but it requires much more heat to activate the material and it has an overall lower capacity for CO_2 than Cu-HKUST-1. Regardless, it was shown that both materials are viable candidates for large-scale industrial applications. It is suggested that the MGA characteristics of more adsorbent materials (especially flexible microporous materials),[182,183] and different binary mixtures of gases (*e.g.*, CO_2/CH_4,[184] CH_4/N_2,[185] NO_2/N_2,[186] and CO_2/C_2H_2),[187] should be studied so that more data can be obtained regarding the usefulness of novel microporous adsorbers in these important gas separations.

6.2.2 Multi-Component Gas Adsorption Instrument

The MGA instrument was in a continuous state of development until the measurement of the Cu-HKUST-1 MGA isotherms, which were the final MGA isotherms measured for this study. The design philosophy that was followed for the development of the MGA instrument was that (1) running experiments should require as little human input as possible and (2) the user should be able to define their own experiments on the instrument and be able to run them safely. To this end, many of the features of the instrument were automated, using the *MULTIDOSER* application, so that human error could be eliminated. Several overhauls of the adsorption analyzer (see Section 2.2.5.3 in Chapter 2) were needed, especially with regard to the choice of valves that were used and the size of the reservoir and the sample chamber volumes.

It was found that ball valves were the best choice for the adsorption analyzer, compared to bellows-sealed pneumatic valves and needle values, owing to their reliability and the quality of the gas-tight seal. However, owing to the availability of components, only manual ball valves were available and, consequently, some human input was required during experiments. It is recommended that these ball valves be motorized in future work involving the MGA instrument.

Regarding the choice of reservoir and sample chamber volumes: the final volumes of the sample chamber and reservoir chamber were 3.84 mL and 3.91 mL, which was sufficient for 100 mg adsorbent samples. Larger reservoir chamber volumes of up to 16 mL were used, but it was found that the change in the gas phase composition was more difficult to detect in these cases.

6.2.3 Composition Analysis

The quality of the data that are obtained from the instrument is ensured by the benchmarking against single-component gas adsorption (SGA) data, as seen in Chapter 3. However, the quality of the multiple-component gas adsorption (MGA) data obtained is largely dependent on the quality of the gas-phase composition analysis that is done on the residual gas analyzer (RGA), as can be seen in Section A.3.3 and Table A.4 in Appendix A, and Table B.1 in Appendix B. This means that the volumetric MGA technique that was introduced in this study should yield more accurate results if the method of composition analysis was to be upgraded. Finally, if higher-pressure MGA data (upwards of 3 bar) is desired, then it is important that a leak-proof pressure-reduction system is installed between the adsorption analyzer and the RGA.

6.3 THEORETICAL METHODS

6.3.1 PRAST-S

The predictive real adsorbed solution theory using the extended Sips (PRAST-S) method, demonstrated in Chapter 4, shows great promise as the next generation of predictive adsorbed solution theory methods. PRAST-S was developed as a response to the quality of the prediction of the CO_2/N_2 MGA equilibria for 13X made using the extended Sips isotherm. In fact, the extended Sips isotherm vastly outperformed the ideal adsorbed solution theory (IAST) prediction of the same MGA equilibria. It was hypothesized that the extended Sips isotherm contains information regarding the non-ideal adsorption of CO_2/N_2 (*i.e.*, those observed in experimental measurements) that are not described in IAST. It was also hypothesized that the extended Sips isotherm could be used as a general-purpose predictor of the mixed adsorption of CO_2 and N_2 by other microporous adsorbents at 1 bar.

These ideas were tested in Chapter 4, where the extended Sips isotherm was used to calculate the activity coefficients of gas species in the mixed adsorbed phase. It was found that the activity coefficients when plotted as a function of the adsorbed phase composition (see Figure 4.2 in Chapter 4) did not resemble the curves seen in solution mixtures. Therefore, we designed our own activity coefficient model, namely the virial activity coefficient model (see Appendix B). Unfortunately, the dependence of the virial parameters (B, C, D, and so forth) on the reduced surface potential (Π, see Section 1.8 of Chapter 1) is not known. This means that the virial activity coefficient model is incomplete, and that a potential avenue for future work would be to study this dependence. Alternatively, a non-empirical activity coefficient model could be derived for multi-component adsorption – however this would likely be very challenging. Nonetheless, the results obtained from the virial activity coefficient model were useful for predicting the adsorbed amounts of mixtures of CO_2 and N_2 in various frameworks.

It was found, however, that PRAST-S becomes less accurate at high pressures, meaning that the dependence of the activity coefficients on the reduced surface potential likely becomes much more significant as the pressure is increased. Still, the PRAST-S results were quite accurate when compared to the measured adsorbed amounts of CO_2 and N_2 with Cu-HKUST-1 and 13X. The PRAST-S results were, however, not validated for Mg-MOF-74, UiO-66, and MOF-14 against experimental data. This presents an opportunity for more benchmarking experiments, alongside testing the usefulness of PRAST-S with other rigid porous frameworks and different mixtures of gases, such as CO_2/CH_4 and CO_2/C_2H_2.

6.3.2 Ideality in Adsorption

Experimental MGA isotherms of mixtures of CO_2 and N_2 with 13X and Cu-HKUST-1 showed that both the choice of framework and the mixture of gases determined whether the adsorption was ideal. Specifically, the mixed adsorption of N_2 in 13X was non-ideal, while the mixed adsorption of CO_2 in 13X was ideal. Furthermore, the mixed adsorptions of both CO_2 and N_2 in Cu-HKUST-1 were ideal.

Ideal and non-ideal adsorption may appear to be a somewhat abstract concept, with the thermodynamic definition forming part of the Gibbs free energy of mixing in the adsorbed phase (see Equation 1.17 in Section 1.8). Specifically, if the Gibbs free energy of mixing is equal to the entropy term multiplied by the temperature (see Equation 1.15 in Section 1.8), then the adsorption of the mixture is ideal, otherwise it is non-ideal. We sought to gain an intuitive understanding of what the reasons for ideality are with respect to the microscopic behavior of the guests within the adsorbents.

The strategy that was employed was to simulate MGA equilibria of mixtures of guest molecules within the pores of the two frameworks (*i.e.*, 13X and Cu-HKUST-1) *in silico*. A series of canonical Metropolis Monte Carlo (CMC) simulations were performed using the benchmarked PRAST-S MGA data for 13X and Cu-HKUST-1. It was found, in these simulations, that non-ideal adsorption was paired with a drastic shift in the mean interaction energy from when the gas species is adsorbed in isolation to when it is adsorbed alongside another gas species. These findings are in line with the thermodynamic formulation of ideality: if there is an excess energy associated with a thermodynamic process, then the process is non-ideal.

The energetic argument provided clues as to how non-ideality (excess energy) can be measured using simulations; however, it was found that the local density of guests within the framework provided the remainder of the information necessary to better understand ideality and its manifestations. The local densities of the guests within the frameworks were studied using a series of radial distribution function (RDF) calculations that accompany the CMC simulations. These calculations allowed us to study how molecules of a particular species were grouped around key positions (*i.e.*, adsorption sites) in the frameworks. It was found that CO_2 grouped around exposed Na cations in the 13X framework and that N_2 was spread diffusely throughout the 13X framework when in isolation. Upon mixing, however, CO_2 retained its density distribution, but N_2 had been effectively guided by CO_2 to take up more favorable positions in the 13X framework. In contrast, CO_2 and N_2 bound to independent parts of the Cu-HKUST-1 framework, even when mixed. We believe that the types of interactions leading to ideal or non-ideal adsorption are likely not limited to those that were observed in this study. It is, therefore, important that the type of analysis that was performed to study the ideality of adsorption

be undertaken for other porous materials and gas mixtures, so that the interactions leading to the outcome of ideal or non-ideal adsorption can be categorized and fully understood.

6.4 CONCLUDING REMARKS

Although this study was mainly focused on developing methods for MGA, many new findings were made along the way. The question, however, remains as to whether this study would contribute to the scientific community's continued fight against climate change. Retrospectively, only a small part of the problem was truly addressed – providing more analytical tools that are necessary to carve out the solution for climate change from the adsorption research frontier. Therefore, we hope that, *at least*, this study will inspire future researchers to use the methods that were developed here to make accurate and realistic conclusions about the value of their novel adsorbents, relative to what already exists.

References

1 D. J. Wuebbles and A. K. Jain, *Fuel Process. Technol.*, 2001, **71**, 99–119.

2 R. R. Judkins, W. Fulkerson and M. K. Sanghvi, *Energy Fuels*, 1993, **7**, 14–22.

3 K. Saidi and M. Ben Mbarek, *Prog. Nucl. Energy*, 2016, **88**, 364–374.

4 R. Waheed, S. Sarwar and C. Wei, *Energy Reports*, 2019, **5**, 1103–1115.

5 S. Fawzy, A. I. Osman, J. Doran and D. W. Rooney, *Environ. Chem. Lett.*, 2020, **1**, 3.

6 S. Gleizer, R. Ben-Nissan, Y. M. Bar-On, N. Antonovsky, E. Noor, Y. Zohar, G. Jona, E. Krieger, M. Shamshoum, A. Bar-Even and R. Milo, *Cell*, 2019, **179**, 1255–1263.

7 H. Xu, D. Rebollar, H. He, L. Chong, Y. Liu, C. Liu, C. J. Sun, T. Li, J. V. Muntean, R. E. Winans, D. J. Liu and T. Xu, *Nat. Energy*, 2020, **5**, 623–632.

8 F. M. Baena-Moreno, M. Rodríguez-Galán, F. Vega, B. Alonso-Fariñas, L. F. Vilches Arenas and B. Navarrete, *Energy Sources, Part A Recover. Util. Environ. Eff.*, 2019, **41**, 1403–1433.

9 A. Foley, B. M. Smyth, T. Pukšec, N. Markovska and N. Duić, *Renew. Sustain. Energy Rev.*, 2017, **68**, 835–839.

10 G. Singh, J. Lee, A. Karakoti, R. Bahadur, J. Yi, D. Zhao, K. Albahily and A. Vinu, *Chem. Soc. Rev.*, 2020, **49**, 4360–4404.

11 S. Cavenati, C. A. Grande and A. E. Rodrigues, *J. Chem. Eng. Data*, 2004, **49**, 1095–1101.

12 M. Wang, A. Lawal, P. Stephenson, J. Sidders and C. Ramshaw, *Chem. Eng. Res. Des.*, 2011, **89**, 1609–1624.

13 J. A. A. Gibson, E. Mangano, E. Shiko, A. G. Greenaway, A. V. Gromov, M. M. Lozinska, D. Friedrich, E. E. B. Campbell, P. A. Wright and S. Brandani, *Ind. Eng. Chem. Res.*, 2016, **55**, 3840–3851.

14 A. Brunetti, F. Scura, G. Barbieri and E. Drioli, *J. Membr. Sci.*, 2010, **359**, 115–125.

15 A. Hassanpouryouzband, J. Yang, B. Tohidi, E. Chuvilin, V. Istomin, B. Bukhanov and A. Cheremisin, *Environ. Sci. Technol.*, 2018, **52**, 4324–4330.

16 D. Berstad, P. Nekså and R. Anantharaman, in *Energy Procedia*, Elsevier, 2012, vol. 26, pp. 41–48.

17 A. S. Bhown and B. C. Freeman, *Environ. Sci. Technol.*, 2011, **45**, 8624–8632.

18 D. Y. C. Leung, G. Caramanna and M. M. Maroto-Valer, *Renew. Sustain. Energy Rev.*, 2014, **39**, 426–443.

19 B. Guo, L. Chang and K. Xie, *J. Nat. Gas Chem.*, 2006, **15**, 223–229.

20 R. V. Siriwardane, M.-S. Shen, E. P. Fisher and J. Losch, *Energy Fuels*, 2005, **19**, 1153–1159.

21 M. R. Hudson, W. L. Queen, J. A. Mason, D. W. Fickel, R. F. Lobo and C. M. Brown, *J. Am. Chem. Soc.*, 2012, **134**, 1970–1973.

22 D. P. Bezerra, F. W. M. D. Silva, P. A. S. D. Moura, A. G. S. Sousa, R. S. Vieira, E. Rodriguez-Castellon and D. C. S. Azevedo, *Appl. Surf. Sci.*, 2014, **314**, 314–321.

23 M. Mofarahi and F. Gholipour, *Microporous Mesoporous Mater.*, 2014, **200**, 1–10.

24 J. Lü, C. Perez-Krap, M. Suyetin, N. H. Alsmail, Y. Yan, S. Yang, W. Lewis, E. Bichoutskaia, C. C. Tang, A. J. Blake, R. Cao and M. Schröder, *J. Am. Chem. Soc.*, 2014, **136**, 12828–12831.

25 J. Lü, C. Perez-Krap, F. Trousselet, Y. Yan, N. H. Alsmail, B. Karadeniz, N. M. Jacques, W. Lewis, A. J. Blake, F. X. Coudert, R. Cao and M. Schröder, *Cryst. Growth Des.*, 2018, **18**, 2555–2562.

26 W. Yang, A. Greenaway, X. Lin, R. Matsuda, A. J. Blake, C. Wilson, W. Lewis, P. Hubberstey, S. Kitagawa, N. R. Champness and M. Schröder, *J. Am. Chem. Soc.*, 2010, **132**, 14457–14469.

27 H. Kim, Y. Kim, M. Yoon, S. Lim, S. M. Park, G. Seo and K. Kim, *J. Am. Chem. Soc.*, 2010, **132**, 12200–12202.

28 K. Sumida, D. L. Rogow, J. A. Mason, T. M. McDonald, E. D. Bloch, Z. R. Herm, T. H. Bae and J. R. Long, *Chem. Rev.*, 2012, **112**, 724–781.

29 J. H. Park and R. T. Yang, *Ind. Eng. Chem. Res.*, 2005, **44**, 1914–1921.

30 P. Nugent, E. G. Giannopoulou, S. D. Burd, O. Elemento, E. G. Giannopoulou, K. Forrest, T. Pham, S. Ma, B. Space, L. Wojtas, M. Eddaoudi and M. J. Zaworotko, *Nature*, 2013, **495**, 80–84.

31 Q. Al-Naddaf, A. A. Rownaghi and F. Rezaei, *Chem. Eng. J.*, 2020, **384**, 123251.

32 Y. Belmabkhout, G. Pirngruber, E. Jolimaitre and A. Methivier, in *Adsorption*, Springer US, 2007, vol. 13, pp. 341–349.

33 F. Luo, C. Yan, L. Dang, R. Krishna, W. Zhou, H. Wu, X. Dong, Y. Han, T. L. Hu, M. O'Keeffe, L. Wang, M. Luo, R. B. Lin and B. Chen, *J. Am. Chem. Soc.*, 2016, **138**, 5678–5684.

34 S. Yang, A. J. Ramirez-Cuesta, R. Newby, V. Garcia-Sakai, P. Manuel, S. K. Callear, S. I. Campbell, C. C. Tang and M. Schröder, *Nat. Chem.*, 2015, **7**, 121–129.

35 T. Saleman, G. Xiao, G. Li and E. F. May, *Adsorption*, 2017, **23**, 671–684.

36 S. Sircar, *Ind. Eng. Chem. Res.*, 2002, **41**, 1389–1392.

37 K. S. Walton and D. S. Sholl, *AIChE J.*, 2015, **61**, 2757–2762.

38 C. M. Simon, B. Smit and M. Haranczyk, *Comput. Phys. Commun.*, 2016, **200**, 364–380.

39 A. L. Myers and J. M. Prausnitz, *AIChE J.*, 1965, **11**, 121–127.

40 S. Bartholdy, M. G. Bjørner, E. Solbraa, A. Shapiro and G. M. Kontogeorgis, *Ind. Eng. Chem. Res.*, 2013, **52**, 11552–11563.

41 P. Atkins and J. De Paula, *Atkins' Physical Chemistry*, W.H. Freeman and Company, 10th edn., 2014.

42 T. L. Meek and L. D. Garner, *J. Chem. Educ.*, 2005, **82**, 325.

43 L. C. Allen, J. F. Capitani, G. A. Kolks and G. D. Sproul, *J. Mol. Struct.*, 1993, **300**, 647–655.

44 W. B. Jensen, *J. Chem. Educ.*, 1995, **72**, 395.

45 W. Soboyejo, *Mechanical Properties of Engineered Materials*, CRC Press, 1st edn., 2002.

46 J. Hermann, R. A. DiStasio and A. Tkatchenko, *Chem. Rev.*, 2017, 117, 4714–4758.

47 M. Kocman, M. Pykal and P. Jurečka, *Phys. Chem. Chem. Phys.*, 2014, **16**, 3144.

48 L. Pauling, *The Nature of the Chemical Bond*, Cornell University Press, 1931.

49 T. S. Moore and T. F. Winmill, *J. Chem. Soc., Trans.*, 1912, **101**, 1635–1676.

50 R. Parthasarathi, V. Subramanian and N. Sathyamurthy, *J. Phys. Chem. A*, 2006, **110**, 3349–3351.

51 E. Arunan, G. R. Desiraju, R. A. Klein, J. Sadlej, S. Scheiner, I. Alkorta, D. C. Clary, R. H. Crabtree, J. J. Dannenber, P. Hobza, H. G. Kjaergaard, A. C. Legon, B. Mennucci and D. J. Nesbitt, *Pure Appl. Chem.*, 2011, **83**, 1637–1641.

52 C. J. Pedersen, *Angew. Chemie Int. Ed. in Eng.*, 1988, 27, 1021–1027.

53 I. Tabushi, *Acc. Chem. Res.*, 1982, **15**, 66–72.

54 S. Stepanow, M. Lingenfelder, A. Dmitriev, H. Spillmann, E. Delvigne, N. Lin, X. Deng, C. Cai, J. V. Barth and K. Kern, *Nat. Mater.*, 2004, **3**, 229–233.

55 O. M. Yaghi, H. Li, C. Davis, D. Richardson and T. L. Groy, *Acc. Chem. Res.*, 1998, **31**, 474–484.

56 E. P. Kyba, R. C. Helgeson, K. Madan, G. W. Gokel, T. L. Tarnowski, S. S. Moore and D. J. Cram, .

57 A. I. Kitaigorodskii, *Acta Crystallogr.*, 1965, **18**, 585–590.

58 A. L. Myers, *AIChE J.*, 2002, **48**, 145–160.

59 L. J. Barbour, *Chem. Commun.*, 2006, **0**, 1163–1168.

60 S. Kitagawa, R. Kitaura and S. I. Noro, *Angew. Chem. Int. Ed.*, 2004, **43**, 2334–2375.

61 H. Kayser, *Ann. Phys.*, 1881, **248**, 526–537.

62 W. K. Feldmann, K. A. White, C. X. Bezuidenhout, V. J. Smith, C. Esterhuysen and L. J. Barbour, *ChemSusChem*, 2020, **13**, 102–105.

63 B. P. Bering and V. V. Serpinsky, *Bull. Acad. Sci. USSR Div. Chem. Sci.*, 1953, **2**, 851–859.

64 F. Hans-Cur, *Water Sci. Technol.*, 1995, **32**, 27–33.

65 M. W. Hahn, J. Jelic, E. Berger, K. Reuter, A. Jentys and J. A. Lercher, *J. Phys. Chem. B*, 2016, **120**, 1988–1995.

66 H. Zhao, Z. Lai and A. Firoozabadi, *Sci. Rep.*, 2017, **7**, 16209.

67 X. Guo, Y. Wu and X. Xie, *Sci. Rep.*, 2017, **7**, 14207.

68 C. X. Bezuidenhout, V. J. Smith, P. M. Bhatt, C. Esterhuysen and L. J. Barbour, *Angew. Chem. Int. Ed.*, 2015, **54**, 2079–2083.

69 S. J. Gregg, K. S. W. Sing and H. W. Salzberg, *J. Electrochem. Soc.*, 1967, 114, 279C.

70 S. Brunauer, L. S. Deming, W. E. Deming and E. Teller, *J. Am. Chem. Soc.*, 1940, **62**, 1723–1732.

71 L. Vinet and A. Zhedanov, *J. Phys. A Math. Theor.*, , DOI:10.1088/1751-8113/44/8/085201.

72 C. H. Twu, J. E. Coon and D. Bluck, *Ind. Eng. Chem. Res.*, 1998, **37**, 1580–1585.

73 T. Engel and P. Reid, *Thermodynamics, Statistical Thermodynamics, & Kinetics*, Pearson, 2012.

74 T. W. Leland, P. S. Chappelear and B. W. Gamson, *AIChE J.*, 1962, **8**, 482–489.

75 L. H. Wang, C. M. Hsieh and S. T. Lin, *Ind. Eng. Chem. Res.*, 2018, **57**, 10628–10639.

76 L. Chen, J. Meyer, T. Campbell, J. Canas, S. S. Betancourt, H. Dumont, J. C. Forsythe, S. Mehay, S. Kimball, D. L. Hall, J. Nighswander, K. E. Peters, J. Y. Zuo and O. C. Mullins, *Fuel*, 2018, **221**, 216–232.

77 I. Langmuir, *J. Am. Chem. Soc.*, 1918, 1361–1368.

78 P. M. Mathias, R. Kumar, J. D. Moyer, J. M. Schork, S. R. Srinivasan, S. R. Auvil and O. Talu, *Ind. Eng. Chem. Res.*, 1996, **35**, 2477–2483.

79 R. Sips, *J. Chem. Phys.*, 1948, **16**, 490–495.

80 M. Hefti, D. Marx, L. Joss and M. Mazzotti, *Microporous Mesoporous Mater.*, 2015, **215**, 215–228.

81 S. Al-Asheh, F. Banat, R. Al-Omari and Z. Duvnjak, *Chemosphere*, 2000, **41**, 659–665.

82 J. Tantet, M. Eić and R. Desai, *Gas Sep. Purif.*, 1995, **9**, 213–220.

83 O. Talu and I. Zwiebel, *AIChE J.*, 1986, **32**, 1263–1276.

84 J. Möllmer, M. Lange, A. Möller, C. Patzschke, K. Stein, D. Lässig, J. Lincke, R. Gläser, H. Krautscheid and R. Staudt, *J. Mater. Chem.*, 2012, **22**, 10274–10286.

85 R. Van Der Vaart, C. Huiskes, H. Bosch and T. Reith, *Adsorption*, 2000, **6**, 311–323.

86 R. V Orye and J. M. Prausimitz, *Ind. Eng. Chem.*, 1965, **57**, 18–26.

87 S. K. Ghosh and S. J. Chopra, *Ind. Eng. Chem. Process Des. Dev.*, 1975, **14**, 304–308.

88 S. A. Adcock and J. A. McCammon, *Chem. Rev.*, 2006, **106**, 1589–1615.

89 A. D. Laurent and D. Jacquemin, *Int. J. Quantum Chem.*, 2013, **113**, 2019–2039.

90 S. Grimme and P. R. Schreiner, *Angew. Chem. Int. Ed.*, 2018, **57**, 4170–4176.

91 T. Sperger, I. A. Sanhueza and F. Schoenebeck, *Acc. Chem. Res.*, 2016, **49**, 1311–1319.

92 J. P. Bowen and N. L. Allinger, *Rev. Comput. Chem.*, 2007, **2**, 81–97.

93 M. Born and R. Oppenheimer, *Ann. Phys.*, 1927, **389**, 457–484.

94 J. E. Lennard-Jones, *Proc. R. Soc. London A*, 1924, **106**, 441–462.

95 J. E. Lennard-Jones, *Proc. R. Soc. London A*, 1924, **106**, 463–477.

96 A. K. Rappe, C. J. Casewit, K. S. Colwell, W. A. Goddard and W. M. Skiff, *J. Am. Chem. Soc.*, 1992, **114**, 10024–10035.

97 H. Sun, Z. Jin, C. Yang, R. L. C. Akkermans, S. H. Robertson, N. A. Spenley, S. Miller and S. M. Todd, *J. Mol. Model.*, 2016, **22**, 1–10.

98 T. Engel, *Quantum Chemistry and Spectroscopy*, Pearson Education, 3rd edn., 2006.

99 M. L. Klein and W. Shinoda, *Science*, 2008, 321, 798–800.

100 N. Metropolis and S. Ulam, *J. Am. Stat. Assoc.*, 1949, **44**, 335–341.

101 W. K. Hastings, *Biometrika*, 1970, **57**, 97–109.

102 D. Frenkel and B. Smit, *Understanding Molecular Simulation: From Algorithms to Applications*, 1996.

103 K. Burke, *J. Chem. Phys.*, 2012, **136**, 150901-1-150901–8.

104 W. Kohn and L. J. Sham, *Phys. Rev.*, 1965, **140**, A1133–A1138.

105 P. Hohenberg and W. Kohn, *Phys. Rev.*, 1964, **136**, B864–B871.

106 P. Echenique and J. L. Alonso, *Mol. Phys.*, 2007, **105**, 3057–3098.

107 T. Van Mourik, M. Bühl and M. P. Gaigeot, *Philos. Trans. R. Soc. A*, 2014, **372**, 20120488–1–20120488–5.

108 E. Khoramzadeh, M. Mofarahi and C. H. Lee, *J. Chem. Eng. Data*, 2019, **64**, 5648–5664.

109 Z. Liang, M. Marshall and A. L. Chaffee, *Energy Fuels*, 2009, **23**, 2785–2789.

110 J. R. Karra, B. E. Grabicka, Y. G. Huang and K. S. Walton, *J. Colloid Interface Sci.*, 2013, **392**, 331–336.

111 X. Wu, Z. Bao, B. Yuan, J. Wang, Y. Sun, H. Luo and S. Deng, *Microporous Mesoporous Mater.*, 2013, **180**, 114–122.

112 G. E. Cmarik, M. Kim, S. M. Cohen and K. S. Walton, *Langmuir*, 2012, **28**, 15606–15613.

113 Dassault Systèmes BIOVIA, 2018.

114 A. K. Rappé and W. A. I. Goddard, *J. Phys. Chem.*, 1991, **95**, 3358–3363.

115 S. J. Clark, M. D. Segall, C. J. Pickard, P. J. Hasnip, M. I. J. Probert, K. Refson and M. C. Payne, *Z. Kristallogr. Cryst. Mater*, 2005, **220**, 567–570.

116 S. Grimme, *J. Comput. Chem.*, 2006, **27**, 1787–1799.

117 S. Grimme, J. Antony, S. Ehrlich and H. Krieg, *J. Chem. Phys.*, 2010, **132**, 154104–01–154104–19.

118 C. R. Harris, K. J. Millman, S. J. van der Walt, R. Gommers, P. Virtanen, D. Cournapeau, E. Wieser, J. Taylor, S. Berg, N. J. Smith, R. Kern, M. Picus, S. Hoyer, M. H. van Kerkwijk, M. Brett, A. Haldane, J. F. del Río, M. Wiebe, P. Peterson, P. Gérard-Marchant, K. Sheppard, T. Reddy, W. Weckesser, H. Abbasi, C. Gohlke and T. E. Oliphant, *Nature*, 2020, **585**, 357–362.

119 W. McKinney, in *Proceedings of the 9th Python in Science Conference*, eds. S. van der Walt and J. Millman, 2010, vol. 9, pp. 56–61.

120 J. D. Hunter, *Comput. Sci. Eng.*, 2007, **9**, 90–95.

121 I. H. Hwang, J. M. Bae, W. S. Kim, Y. D. Jo, C. Kim, Y. Kim, S. J. Kim and S. Huh, *Dalton Trans.*, 2012, **41**, 12759–12765.

122 P. K. Thallapally, L. Dobrzańska, T. R. Gingrich, T. B. Wirsig, L. J. Barbour and J. L. Atwood, *Angew. Chem. Int. Ed.*, 2006, **45**, 6506–6509.

123 D. Y. Ma, J. Xie, Z. Zhu, H. Huang, Y. Chen, R. Su and H. Zhu, *Inorg. Chem. Commun.*, 2017, **86**, 128–132.

124 H. Kim, S. Yang, S. R. Rao, S. Narayanan, E. A. Kapustin, H. Furukawa, A. S. Umans, O. M. Yaghi and E. N. Wang, *Science*, 2017, **356**, 430–434.

125 J. G. Jee, M. B. Kim and C. H. Lee, *Chem. Eng. Sci.*, 2005, **60**, 869–882.

126 A. Schulte-Schulze-Berndt and K. Krabiell, *Gas Sep. Purif.*, 1993, **7**, 253–257.

127 J. M. Huck, L. C. Lin, A. H. Berger, M. N. Shahrak, R. L. Martin, A. S. Bhown, M. Haranczyk, K. Reuter and B. Smit, *Energy Environ. Sci.*, 2014, **7**, 4132–4146.

128 S. Sircar and A. L. Myers, in *Handbook of Zeolite Science and Technology*, eds. S. M. Auerbach, K. A. Carrado and P. K. Dutta, CRC Press, Basel, New York, New York, 1st edn., 2003, pp. 1063–1105.

129 H. Li, M. Eddaoudi, T. L. Groy and O. M. Yaghi, *J. Am. Chem. Soc.*, 1998, **120**, 8571–8572.

130 K. Adil, Y. Belmabkhout, R. S. Pillai, A. Cadiau, P. M. Bhatt, A. H. Assen, G. Maurin and M. Eddaoudi, *Chem. Soc. Rev.*, 2017, **46**, 3402–3430.

131 M. T. Ho, G. W. Allinson and D. E. Wiley, *Ind. Eng. Chem. Res.*, 2008, **47**, 4883–4890.

132 G. D. Pirngruber and D. Leinekugel-Le-Cocq, *Ind. Eng. Chem. Res.*, 2013, **52**, 5985–5996.

133 C. W. Wu and S. Sircar, *Sep. Purif. Technol.*, 2016, **170**, 453–461.

134 S. Sircar, *Ind. Eng. Chem. Res.*, 1999, **38**, 3670–3682.

135 F. R. Siperstein and A. L. Myers, *AIChE J.*, 2001, **47**, 1141–1159.

136 V. Finsy, L. Ma, L. Alaerts, D. E. De Vos, G. V. Baron and J. F. M. Denayer, *Microporous Mesoporous Mater.*, 2009, **120**, 221–227.

137 L. B. Richardson and J. C. Woodhouse, *J. Am. Chem. Soc.*, 1923, **45**, 2638–2653.

138 A. Smith, *Proc. R. Soc. London*, 1863, **12**, 424–426.

139 F. C. Tompkins and D. M. Young, *Trans. Faraday Soc.*, 1951, **47**, 88–96.

140 B. P. Burtt, J. D. Kurbatov and B. P. Burtt, *J. Am. Chem. Soc.*, 1948, **70**, 2278–2282.

141 J. A. Ritter and R. T. Yang, *Ind. Eng. Chem. Res.*, 1987, **26**, 1679–1686.

142 J. A. Dunne, M. Rao, S. Sircar, R. J. Gorte and A. L. Myers, *Langmuir*, 1997, **13**, 4333–4341.

143 A. Busch, Y. Gensterblum, B. M. Krooss and N. Siemons, *Int. J. Coal Geol.*, 2006, **66**, 53–68.

144 A. Ghoufi, L. Gaberova, J. Rouquerol, D. Vincent, P. L. Llewellyn and G. Maurin, *Microporous Mesoporous Mater.*, 2009, **119**, 117–128.

145 Z. Bao, L. Yu, Q. Ren, X. Lu and S. Deng, *J. Colloid Interface Sci.*, 2011, **353**, 549–556.

146 J. McEwen, J. D. Hayman and A. Ozgur Yazaydin, *Chem. Phys.*, 2013, **412**, 72–76.

147 A. Sayari, Y. Belmabkhout and R. Serna-Guerrero, *Chem. Eng. J.*, 2011, **171**, 760–774.

148 N. Ayawei, A. N. Ebelegi and D. Wankasi, *J. Chem.*, , DOI:10.1155/2017/3039817.

149 C. J. Willmott and K. Matsuura, *Clim. Res.*, 2005, **30**, 79–82.

150 K. Yang, J. Wu, C. Li, Y. Xiang and G. Yang, *J. Phys. Chem. C*, 2019, **124**, 544–556.

151 S. Brandani, E. Mangano and L. Sarkisov, *Adsorption*, 2016, **22**, 261–276.

152 B. Delaunay, *Bull. l'Académie des Sci. l'URSS*, 1934, **6**, 793–800.

153 L. R. Nassimbeni, S. Marivel, H. Su and E. Weber, *RSC Adv.*, 2013, **3**, 25758–25764.

154 J. C. Crittenden, S. W. Loper, M. Ari, P. Luft, D. W. Hand and J. L. Oravltz, *Environ. Sci. Technol.*, 1985, **19**, 1037–1043.

155 E. Costa, J. L. Sotelo, G. Calleja and C. Marrón, *AIChE J.*, 1981, **27**, 5–12.

156 Y. R. Lee, J. Kim and W. S. Ahn, *Korean J. Chem. Eng.*, 2013, **30**, 1667–1680.

157 A. J. Howarth, Y. Liu, P. Li, Z. Li, T. C. Wang, J. T. Hupp and O. K. Farha, *Nat. Rev. Mater.*, 2016, **1**, 1–15.

158 Y. S. Bae and R. Q. Snurr, *Angew. Chem. Int. Ed.*, 2011, **50**, 11586–11596.

159 Y. Belmabkhout, M. Frère and G. De Weireld, *Meas. Sci. Technol.*, 2004, **15**, 848–858.

160 K. Y. Foo and B. H. Hameed, *Chem. Eng. J.*, 2010, **156**, 2–10.

161 J. A. Mason, T. M. McDonald, T. H. Bae, J. E. Bachman, K. Sumida, J. J. Dutton, S. S. Kaye and J. R. Long, *J. Am. Chem. Soc.*, 2015, **137**, 4787–4803.

162 R. Krishna and J. M. van Baten, *Sep. Purif. Technol.*, 2018, **206**, 208–217.

163 J. Costandius, C. Esterhuysen and L. J. Barbour, *Multi-Component Adsorption Isotherms of Gases at Elevated Pressures: Measurement vs Prediction (Manuscript Submitted)*, 2021.

164 J. Costandius and C. Esterhuysen, *Exploring the Origin of Ideal and Non-Ideal Adsorption in Porous Frameworks (Manuscript in Preparation)*, 2021.

165 A. D. Wiersum, J. S. Chang, C. Serre and P. L. Llewellyn, *Langmuir*, 2013, **29**, 3301–3309.

166 D. DeSantis, J. A. Mason, B. D. James, C. Houchins, J. R. Long and M. Veenstra, *Energy Fuels*, 2017, **31**, 2024–2032.

167 M. Ding, X. Cai and H. L. Jiang, *Chem. Sci.*, 2019, 10, 10209–10230.

168 M. K. Bhunia, J. T. Hughes, J. C. Fettinger and A. Navrotsky, *Langmuir*, 2013, **29**, 8140–8145.

169 J. Park, J. D. Howe and D. S. Sholl, *Chem. Mater.*, 2017, **29**, 10487–10495.

170 J. Costandius, L. J. Barbour and C. Esterhuysen, *Predicting binary multiple-component adsorption equilibria at high pressure by utilizing the Real Adsorbed Solution Theory and the extended Sips isotherm (Manuscript in preparation)*, 2021.

171 L. B. McCusker, D. H. Olson and C. Baerlocher, *Atlas of Zeolite Framework Types*, 2007.

172 Y. Chen, L. Wojtas, S. Ma, M. J. Zaworotko and Z. Zhang, *Chem. Commun.*, 2017, **53**, 8866–8869.

173 J. Ha, J. H. Lee and H. R. Moon, *Inorg. Chem. Front.*, 2019, **7**, 12–27.

174 M. L. Connolly, *Science*, 1983, **221**, 709–713.

175 N. Mehio, S. Dai and D. E. Jiang, *J. Phys. Chem. A*, 2014, **118**, 1150–1154.

176 N. Metropolis, A. W. Rosenbluth, M. N. Rosenbluth, A. H. Teller and E. Teller, *J. Chem. Phys.*, 1953, **21**, 1087–1092.

177 R. S. Mulliken, *J. Chem. Phys.*, 1955, **23**, 1833–1840.

178 F. L. Hirshfeld, *Isr. J. Chem.*, 1977, **16**, 168–174.

179 G. Aguilar-Armenta, M. E. Patino-Iglesias and R. Leyva-Ramos, *Adsorpt. Sci. Technol.*, 2003, **21**, 81–92.

180 S. Chen, Y. Fu, Y. Huang and Z. Tao, *J. Porous Mater.*, 2016, **23**, 713–723.

181 A. K. Soper, *ISRN Phys. Chem.*, 2013, **2013**, 1–67.

182 A. Boutin, F.-X. Coundert, M.-A. S. Huet, A. V. Neimark, G. Férey and A. H. Fuchs, *J. Phys. Chem. C*, 2010, **114**, 22237–22244.

183 P. Mishra, H. P. Uppara, B. Mandal and S. Gumma, *Ind. Eng. Chem. Res.*, 2014, **53**, 19747–19753.

184 Y. Zhang, J. Sunarso, S. Liu and R. Wang, *Int. J. Greenh. Gas Control*, 2013, **12**, 84–107.

185 J. Hu, T. Sun, X. Liu, Y. Guo and S. Wang, *RSC Adv.*, 2016, **6**, 64039–64046.

186 T. Chokbunpiam, R. Chanajaree, J. Caro, W. Janke, T. Remsungnen, S. Hannongbua and S. Fritzsche, *Comput. Mater. Sci.*, 2019, **168**, 246–252.

187 L. Zhang, K. Jiang, L. Li, Y. P. Xia, T. L. Hu, Y. Yang, Y. Cui, B. Li, B. Chen and G. Qian, *Chem. Commun.*, 2018, **54**, 4846–4849.

188 J. D. van der Waals, Dover Publications, 1988.

189 T. Y. Kwak and G. A. Mansoori, *Chem. Eng. Sci.*, 1986, **41**, 1303–1309.

190 T. E. Oliphant, *Comput. Sci. Eng.*, 2007, **9**, 10–20.

191 P. Virtanen, R. Gommers, T. E. Oliphant, M. Haberland, T. Reddy, D. Cournapeau, E. Burovski, P. Peterson, W. Weckesser, J. Bright, S. J. van der Walt, M. Brett, J. Wilson, K. J. Millman, N. Mayorov, A. R. J. Nelson, E. Jones, R. Kern, E. Larson, C. J. Carey, İ. Polat, Y. Feng, E. W. Moore, J. VanderPlas, D. Laxalde, J. Perktold, R. Cimrman, I. Henriksen, E. A. Quintero, C. R. Harris, A. M. Archibald, A. H. Ribeiro, F. Pedregosa, P. van Mulbregt and SciPy 1.0 Contributors, *Nat. Methods*, 2020, 1–12.

192 K. Levenberg, *Q. Appl. Math.*, 1944, **2**, 164–168.

193 D. W. Marquardt, *J. Soc. Ind. Appl. Math.*, 1963, **11**, 431–441.

194 I. Langmuir, *J. Am. Chem. Soc.*, 1918, **40**, 1361–1403.

195 D. G. Kinniburgh, *Environ. Sci. Technol.*, 1986, **20**, 895–904.

196 H. C. Van Ness, *Ind. Eng. Chem. Fundam.*, 1969, **8**, 464–473.

197 S. Gebreyohannes, B. J. Neely and K. A. M. Gasem, *Ind. Eng. Chem. Res.*, 2014, **53**, 12445–12454.

198 S. Sochard, N. Fernandes and J. M. Reneaume, *AIChE J.*, 2010, **56**, 3109–3119.

199 C. S. Schacht, L. Zubeir, T. W. De Loos and J. Gross, *Ind. Eng. Chem. Res.*, 2010, **49**, 7646–7653.

200 H. J. Monkhorst and J. D. Pack, *Phys. Rev. B*, 1976, **13**, 5188–5192.

201 M. C. Payne, M. P. Teter, D. C. Allan, T. A. Arias and J. D. Joannopoulos, *Rev. Mod. Phys.*, 1992, **64**, 1045–1097.

202 A. Tkatchenko and M. Scheffler, *Phys. Rev. Lett.*, 2009, **102**, 73005.

Appendix A. Supporting Information for Chapter 3

A.1 MATERIALS

A.1.1 Zeolite 13X

Zeolite 13X (13X) was obtained as a powder from *Alfa Aesar* and used as purchased. A sample of 200-250 mg of 13X was activated in vacuo (2 × 10–2 mbar) at 453 K for periods of 8-12 hours before it was used in further analyses.

A.1.2 Analytical gases

Analytical gases (He, CO_2, and N_2) with a minimum purity grade of 99.999% were purchased from *Afrox*.

A.2 METHODS

A.2.1 Thermogravimetric Analysis

Thermogravimetric analysis (TGA) was performed on a TA Instruments Q500 instrument. The sample was heated from room temperature up to 873 K at a rate of 10 K min^{-1}, and weight loss was recorded under a constant flow of a nitrogen purge stream at 50 mL min^{-1}. Thermogravimetric data were processed using the Universal Analysis 2000 software.

A.2.2 Powder X-Ray Diffraction

Powder X-Ray diffraction (PXRD) was performed on the Bruker D2 Phaser. PXRD analyses were undertaken using a zero-background sample holder. The diffractometer is equipped with a Cu-K_α X-Ray source (λ = 1.54184 Å) and a *Lynxeye* 1-D detector. Powder-diffraction data were recorded at atmospheric pressure and operational temperature (T = 310 K) with an angular increment of 0.01617° in the scanning range of 5 - 40°.

A.2.3 Gas Mixtures

Gas mixtures were prepared on site from high-purity single-component gases (<10 ppm impurities) with a custom-made gas mixing system.

A.2.4 Equation of State for Gas Mixtures

The van der Waals Equation of State[188] (Equation A1) was used to describe pure gases at elevated pressures,

$$\left(P + \frac{an^2}{V^2}\right)\left(P - \frac{bV}{n}\right) = nRT \tag{A1}$$

where P is the pressure, n is the number of moles of gas, V is the volume, R is the gas constant, T is the temperature, a is the interaction parameter, and b is the finite volume parameter of the gas species. Equation A1 does not inherently describe gas mixtures, and an adapted version of the van der Waals one-fluid mixing rules[189] (Equations A2.1-2.3) was therefore used to describe van der Waals parameters (a, b) of the gas mixture (a_m, b_m):

$$a_m = \sum_{i=1}^{N}\sum_{j=1}^{N} y_i y_j a_{ij} \tag{A2.1}$$

$$a_{ji} = a_{ij} = \sqrt{a_i a_j} \tag{A2.2}$$

$$b_m = \sum_{i=1}^{N} y_i\, b_i \tag{A2.3}$$

where a_i and b_i are the van der Waals a and b parameters for pure components, a_{ij} is the van der Waals mixed a parameter for components i and j, and y_i is the gas-phase mole fraction of component i. Finally, the resulting one-fluid mixture parameters a_m and b_m were used to calculate the other state parameters of the gas mixture using Equation A1.

A.2.5 Volumetric Gas Adsorption Analysis

Volumetric single-component and multi-component gas adsorption analyses (SGA, MGA) were performed using a custom-built instrument (Figure A.1). The adsorption instrument consists of an automated pressure/vacuum supply manifold, an adsorption analysis manifold, and a mass spectrometer. Pressure data were recorded with a high-precision (± 0.5%) *WIKA A-10* absolute pressure transmitter with a range of 0 to 4 bar. Headspace composition analyses were performed using a *Setaram RGAPro 200* mass spectrometer. The *RGAPro* is equipped with a *Stanford Research Systems RGA200* residual gas analyzer (single quadrupole mass spectrometer fitted with a Faraday cup detector) and a *Pfeiffer* hybrid turbomolecular drag pump with an operational minimum vacuum pressure of 1.7×10^{-3} mbar. Adsorption experiments and data acquisition are controlled entirely by software (*MULTIDOSER*) developed by the authors.

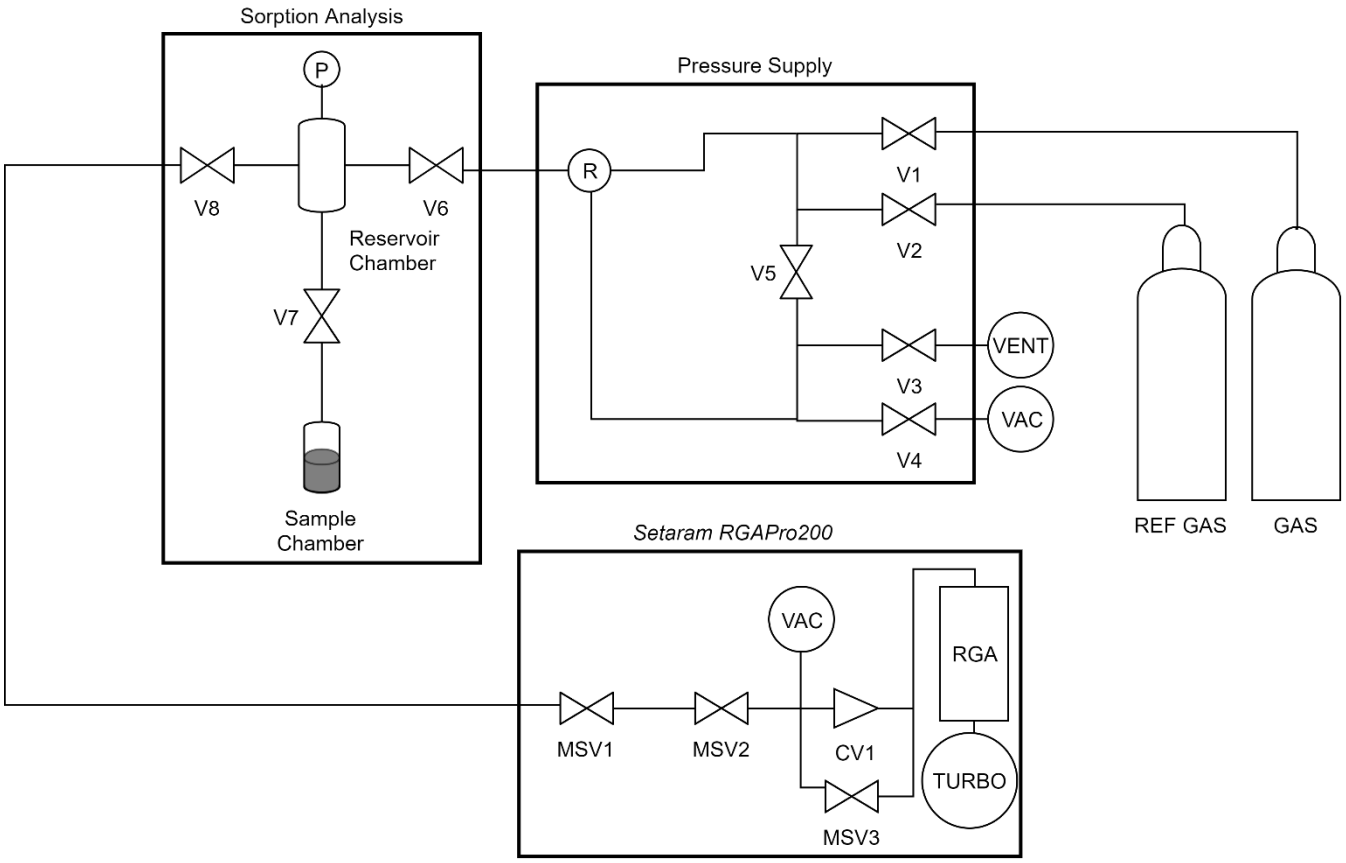

Figure A.1. Components of the adsorption instrument, including the pressure-supply manifold, the adsorption-analysis manifold, and the *RGAPro 200*. (Symbols. P = Pressure sensor, R = Pressure regulator, V = Valve, MSV = Valve located in RGA manifold, CV = Pressure-regulating aperture, VAC = vacuum pump, TURBO = Turbomolecular pump, RGA = RGA probe, VENT = Vent pipe, GAS = Analytical gas or gas mixture cylinder, REF GAS = Helium gas cylinder.

The main principle of the technique is that the equilibrium between the adsorbent material and the gas phase cannot be altered by removing some of the gas-phase volume at constant pressure and composition. In other words, if a portion of the headspace volume that is in equilibrium with the adsorbent were to be partitioned off, then the state parameters (*i.e.* pressure and composition) of the partitioned volume (reservoir chamber, see Figure A.1) can be altered without perturbing the sample. Therefore, the composition of the gas mixture can be analyzed using some analytical method, while the equilibrium in the sample chamber remains undisturbed. The combination of volume, pressure and composition data can then be used to calculate the uptake of the components of the gas by the adsorbent material. The mixed-gas volumetric method that is proposed in this study is employed in the adsorption uptake analyzer. The adsorption instrument always provides pressure and temperature data, and mass spectrometry measurements are performed at initial conditions and at equilibrium. Mass spectrometry allows for determination of the composition of mixtures of relatively inert gases, such as N_2 and CO_2, and it was therefore chosen as the method of analysis in this study.

A.2.6 Ideal Adsorbed Solution Theory

At thermodynamic equilibrium, the single component adsorbed phase is related to the multicomponent adsorbed phase by the equivalence of their spreading pressures. The main equation that describes IAST is shown in Equation A3.1.

$$P_i = x_i P_i^o(\pi), \qquad \pi = \pi_i = \cdots = \pi_j \tag{A3.1}$$

where P_i is the partial pressure, x_i is the adsorbed mole fraction, and $P_i^o(\pi)$ is the equilibrium single-component pressure at the mixture spreading pressure (π) for component i. In IAST, the mixture spreading pressure is equal to all the single-component spreading pressures ($\pi_i \ldots \pi_j$) at equilibrium. The spreading pressures of the components can be calculated by integrating the single-component SGA isotherms ($n_i^o(P)$, Equation A3.2).

$$\pi_i(P_i^*) = \int_0^{P_i^o} \frac{n_i^o(P)}{P} dP \tag{A3.2}$$

The total uptake of gas by the adsorbent is defined in IAST by the relationship that is shown in Equation A3.3.

$$c_{tot} = \sum_i \frac{x_i}{n_i^o\left(P_i^o(\pi)\right)} \tag{A3.3}$$

where n_{tot} is the total uptake.

Ideal Adsorbed Solution Theory[39] (IAST) calculations were performed using the *PyIAST* module (Python 3.x) written by Cory Simon.[38] The module was slightly modified to prevent extrapolation of the single-component adsorption isotherms if desired.

A.2.7 Data Processing and Images

SGA and MGA data were processed in Python 3.7 using the *Pandas*,[119] *NumPy*,[190] and *SciPy*[191] libraries. Plots were generated with the aid of the *Matplotlib*[120] library.

A.2.8 Statistical Analyses

Whenever SGA data are fitted to curves, or MGA data are predicted by a thermodynamic model, the Mean Absolute Error (MAE, Equation A4.1) and the Root Mean Squared Error (RMSE, Equation A4.2) are used as metrics to evaluate the goodness of fit. The MAE is defined as

$$MAE = \frac{1}{n}\sum_i |y_i - \hat{y}_i| \tag{A4.1}$$

where n is the number of data points, y_i is the observed value, and $\hat{y}_i$ is the predicted (or fitted value). The RMSE is defined as

$$RMSE = \sqrt{\frac{1}{n}\sum_{i}(y_i - \hat{y}_i)^2} \qquad (A4.2)$$

where n is the number of data points, y_i is the observed value, and $\hat{y}_i$ is the predicted (or fitted value).

A.3 ADDITIONAL INFORMATION

A.3.1 Thermogravimetric analysis

The thermogram of as-purchased zeolite 13X (Figure A.2) shows that 13X expels most of its guest content by 580 K under ambient pressures. No mass-loss events were detected between 580 K and 873 K. Owing to instrumental limitations, the decomposition of 13X could not be observed.

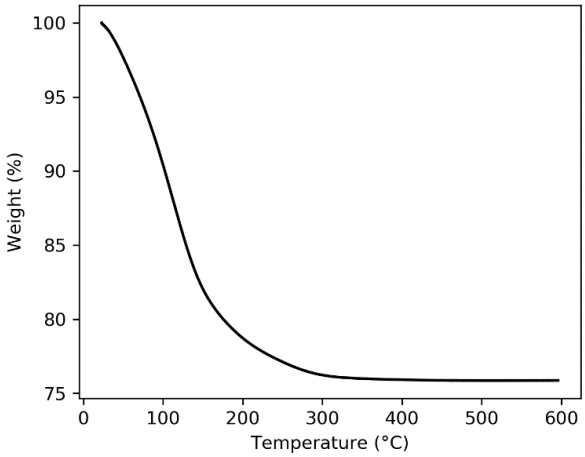

Figure A.2. Thermogram for as-purchased zeolite 13X.

A.3.2 Powder X-Ray Diffraction

PXRD data were recorded to investigate the thermal stability of 13X after TGA. The as-purchased 13X PXRD data are shown, along with the PXRD data of 13X after TGA in Figure A.3. 13X retains its crystallinity at temperatures exceeding 580 K, but the material had become slightly brown after being exposed to such heat. Therefore, it was decided to activate 13X under milder temperatures; 13X was therefore activated at 453 K *in vacuo* for 8-12 hours.

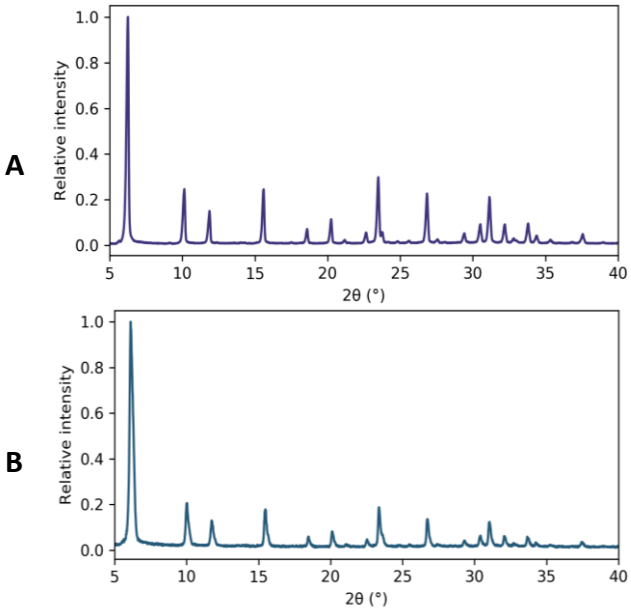

Figure A.3. (A) PXRD pattern of as-purchased zeolite 13X and (B) post-TGA (up to 873 K) zeolite 13X.

A.3.3 Calibration of the Mass Spectrometer

The residual gas analyzer (RGA) was calibrated by means of a series of standard mixtures of CO_2 and N_2. Seven sets of calibration experiments were performed (Figure A.4) with 0%, 10%, 20%, 40%, 60%, 80%, and 100% CO_2 with a balance of N_2. The *m/z* 12 and *m/z* 14 peaks were monitored to quantify the composition of CO_2 and N_2, respectively. The calibration plot is also supplemented with the confidence interval (95%) that indicate the relative intensity range in which a specific composition must occur. The confidence interval upper limit is shown as a red dashed line and the lower limit is shown as a blue dashed line.

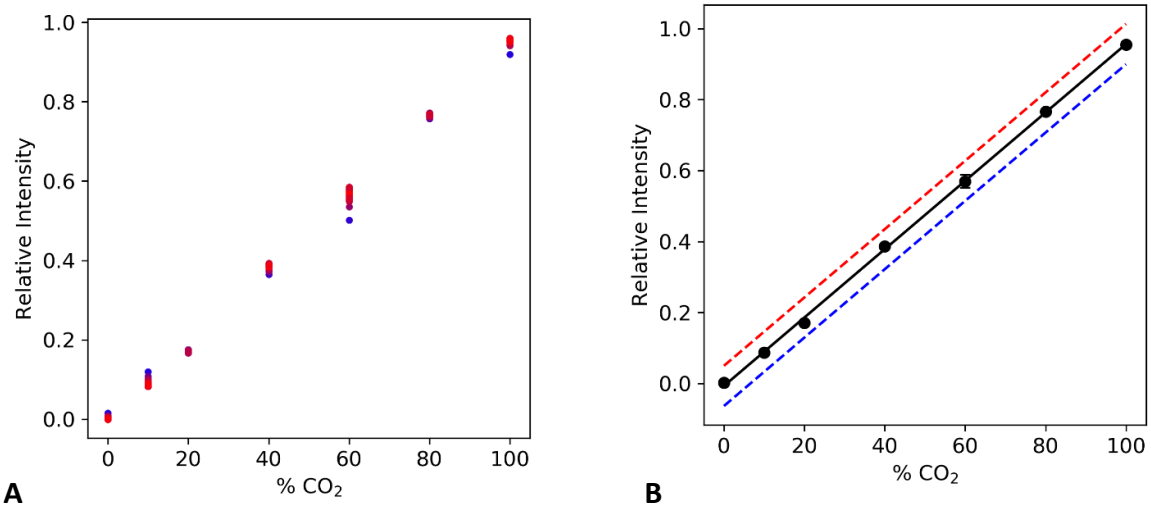

Figure A.4. RGA calibration for binary mixtures of CO_2 and N_2. (A) Measured relative intensities of CO_2/N_2 calibration standards, red regions show the location of the mean relative intensity of a standard. (B) Calibration plot shown with regression line (RI = 0.963 y_{CO2} – 0.007, R^2 = 0.999).

A.3.4 Single-component gas adsorption benchmarking

The CO_2 isotherm that was measured on the adsorption instrument was compared to several sources.[11,109,145–147] It can be seen, in Figure A.5, that there is a very good agreement between the literature sources and our data.

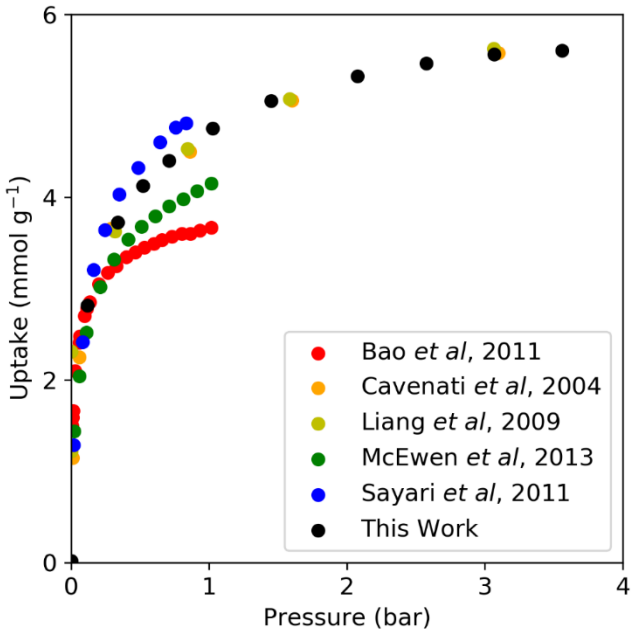

Figure A.5. Benchmarked CO_2 adsorption results.

A.3.5 Curve fitting method and results

Curve fitting was performed using the Python module Scipy.[191] Specifically, the *scipy curve_fit* method was used as it contains the simplest-to-use implementation of the Levenberg-Marquardt[192,193] algorithm that can be used for nonlinear least-squares regression. The Langmuir,[194] Dual-Site Langmuir,[78] and Sips[79] isotherms were used in this work. The Langmuir isotherm (Equation A5.1) is defined as

$$n_i(P) = \frac{n_i^{\infty} K_{L,i} P}{1 + K_{L,i} P} \qquad (A5.1)$$

where $n_i(P)$ is the adsorbed amount, n_i^{∞} is the saturation concentration of adsorbate, $K_{L,i}$ is the Langmuir constant, and P is the pressure. The Dual-Site Langmuir (Equation A5.2) is defined as

$$n_i(P) = n_{i,\alpha}(P) + n_{i,\beta}(P) = \frac{n_{i,\alpha}^{\infty} K_{L,i,\alpha} P}{1 + K_{L,i,\alpha} P} + \frac{n_{i,\beta}^{\infty} K_{L,i,\beta} P}{1 + K_{L,i,\beta} P} \qquad (A5.2)$$

where α and β refer to the two independent adsorption sites that each follow a Langmuir-type uptake. The Sips isotherm (Equation A5.3) is defined as

$$n_i(P) = \frac{n_i^{\infty}(K_{S,i}P)^{c_i}}{1 + (K_{S,i}P)^{c_i}} \qquad (A5.3)$$

where $K_{S,i}$ is the Sips constant, and c_i is the heterogeneity factor. The heterogeneity factor must lie between 0 and 1. The Sips isotherm reduces to the Langmuir isotherm if the heterogeneity factor is equal to 1.

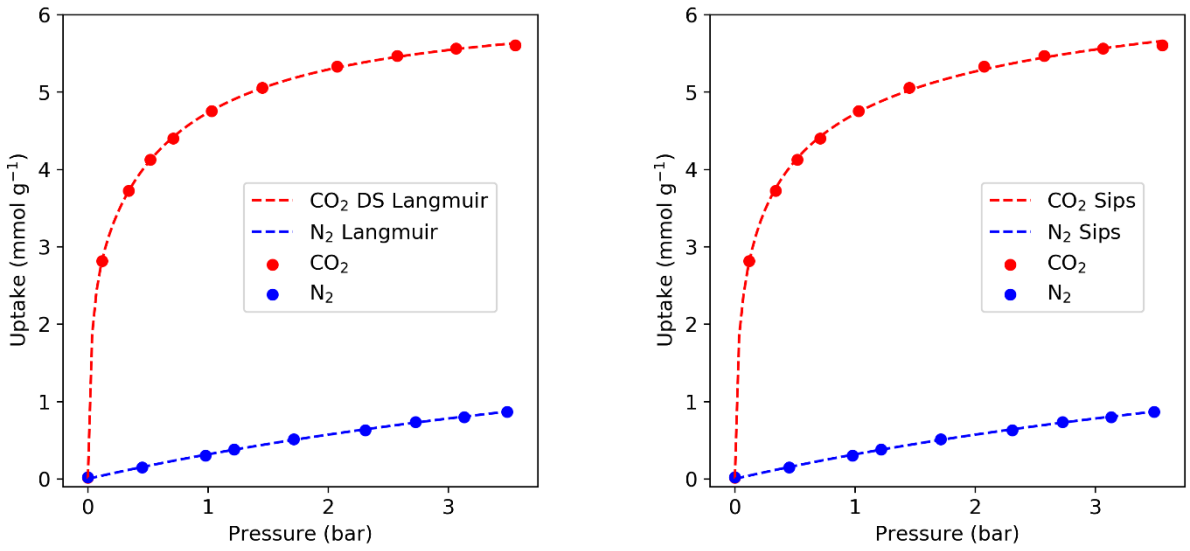

Figure A.6. Isotherms fitted to experimental data.

The results and relevant statistics of the isotherm fits to experimental data are shown in Figure A.6, Table A.1 and Table A.2. The CO_2 experimental adsorption data were fitted separately to both the Dual-Site Langmuir (DS Langmuir) and Sips isotherms. The N_2 experimental adsorption data were fitted separately to the Langmuir and Sips isotherms.

Table A.1. Nonlinear Least-Squares Regression Parameters

Gas Species	Dual-Site Langmuir Isotherm			Langmuir Isotherm			Sips Isotherm		
	Parameter	Value	Std Deviation	Parameter	Value	Std Deviation	Parameter	Value	Std Deviation
CO_2	$n_{i,\alpha}^{\infty}$ (mmol g^{-1})	2.761	4.55E-02				n_i^{∞} (mmol g^{-1})	7.259	4.62E-02
	$K_{L,\alpha}$ (bar^{-1})	44.70	1.84E+02				$K_{S,i}$ (bar^{-1})	3.375	1.65E-01
	$n_{i,\beta}^{\infty}$ (mmol g^{-1})	3.453	3.27E-02				c_i (unitless)	0.508	6.67E-04
	$K_{L,\beta}$ (bar^{-1})	1.431	2.53E-02						
N_2				n_i^{∞} (mmol g^{-1})	2.887	7.48E-02	n_i^{∞} (mmol g^{-1})	2.887	1.52E+00
				K_L (bar^{-1})	0.123	2.39E-04	$K_{S,i}$ (bar^{-1})	0.123	7.15E-03
							c_i (unitless)	1	1.08E-02

Table A.2. Nonlinear Least-Squares Regression Parameters

Gas Species	Isotherm	Mean Absolute Error (mmol g^{-1})	Root Mean Squared Error (mmol g^{-1})
CO2	Dual-Site Langmuir	1.10E-02	1.29E-02
	Sips	2.47E-02	2.81E-02
N2	Langmuir	8.25E-03	1.06E-02
	Sips	8.25E-03	1.06E-02

A.3.6 Multicomponent Adsorption Experiments

A sample of 13X was activated within a stainless-steel 316 sample chamber that fits onto the adsorption instrument. The still-hot sample chamber was attached to the adsorption system and evacuated until it reached room temperature by means of natural cooling. Then, the sample chamber dead volume was determined by means of helium gas expansions. The adsorption instrument was then primed for multicomponent-gas adsorption (MGA) experiments. Five MGA experiments are reported in this paper (Table A.3). In these five experiments, the supply-gas compositions were 10%, 20%, and 40% CO_2, by mole fraction, with a balance of N_2. The naming convention used for these experiments were 13XKCO_2N_2, where K signifies the supply-gas composition. The MGA isotherm data are described by five parameters, namely the temperature, pressure, composition, N_2 uptake, and CO_2 uptake. Each of these parameters have an associated mean value, standard deviation value. Each of the different experiments are listed by their key (see Table A.1). Although the errors associated with the measured uptake and pressure are relatively low, the confidence interval associated with the measured gas-phase composition that was calculated at the 5% significance level is approximately ±

5% CO_2. These large errors originate from the CO_2-N_2 gas standard calibrations (Figure A.4) that were performed on the mass spectrometer.

Table A.3. Adsorption experiment key and details

Experiment			Supply Gas			
Name	Sample	Sample Mass (mg)	Analytical Gas	%	Balance Gas	%
13X10CO2N2		204.6		10		90
13X10CO2N2-2		204.6		10		90
13X20CO2N2	13X	208.6	CO_2	20	N_2	80
13X20CO2N2-2		208.6		20		80
13X40CO2N2		208.6		40		60

Table A.4. Numerical excess MGA isotherm results.

	Step	T (K)		P (bar)		y (% CO_2)		c_{CO2} (mmol g^{-1})		c_{N2} (mmol g^{-1})	
		Mean	Std. Deviation	Mean	Std. Deviation	Mean	Std. Deviation	Mean	Std. Deviation	Mean	Std. Deviation
13X10CO2N2	1	299.0	0.21	0.375	0.001	1.15	0.43	0.13	0.01	0.05	0.01
	2	298.7	0.21	0.517	0.001	1.22	0.42	0.29	0.01	0.10	0.01
	3	298.7	0.22	0.893	0.001	1.57	0.42	0.55	0.02	0.19	0.02
	4	298.7	0.16	1.034	0.001	2.04	0.42	0.83	0.03	0.26	0.03
	5	299.3	0.20	1.741	0.001	2.30	0.42	1.32	0.05	0.37	0.05
	6	298.7	0.16	1.794	0.001	3.37	0.42	1.72	0.06	0.46	0.06
	7	298.6	0.19	2.072	0.001	4.54	0.41	2.11	0.07	0.54	0.07
	8	299.2	0.20	2.406	0.001	5.61	0.41	2.42	0.09	0.65	0.09
13X10CO2N2-2	1	298.7	0.16	0.436	0.001	1.45	0.42	0.15	0.01	0.05	0.01
	2	299.2	0.21	0.841	0.001	2.01	0.42	0.39	0.02	0.13	0.02
	3	299.0	0.20	1.679	0.001	2.76	0.42	0.85	0.04	0.25	0.04
	4	299.1	0.21	1.867	0.001	3.68	0.42	1.24	0.06	0.35	0.06
	5	298.6	0.20	2.381	0.001	4.00	0.42	1.71	0.07	0.46	0.07
	6	299.2	0.19	2.916	0.001	4.97	0.41	2.13	0.09	0.55	0.10
	7	298.6	0.23	3.016	0.001	6.10	0.41	2.41	0.11	0.74	0.11
13X20CO2N2	1	298.5	0.23	0.311	0.001	0.97	0.43	0.25	0.01	0.03	0.01
	2	298.5	0.17	0.813	0.001	1.66	0.42	0.84	0.02	0.15	0.02
	3	298.6	0.21	1.001	0.001	2.62	0.42	1.47	0.03	0.20	0.03
	4	298.8	0.21	1.278	0.001	4.26	0.42	2.18	0.04	0.22	0.04
	5	299.0	0.22	1.677	0.001	6.89	0.41	2.92	0.05	0.28	0.05
	6	298.6	0.18	2.113	0.001	9.67	0.40	3.55	0.07	0.39	0.07
	7	298.5	0.20	2.509	0.001	12.43	0.39	3.99	0.08	0.47	0.08
13X20CO2N2-2	1	298.5	0.17	0.406	0.001	1.03	0.43	0.32	0.01	0.06	0.01
	2	298.5	0.19	0.794	0.001	2.15	0.42	0.90	0.02	0.12	0.02
	3	298.5	0.18	1.233	0.001	3.23	0.42	1.68	0.03	0.19	0.03
	4	298.4	0.14	1.666	0.001	5.93	0.41	2.51	0.05	0.27	0.05
	5	298.5	0.21	2.172	0.001	9.28	0.40	3.21	0.06	0.42	0.07
	6	298.5	0.17	2.708	0.001	11.97	0.39	3.70	0.08	0.56	0.08
	7	298.3	0.19	2.832	0.001	14.56	0.39	3.93	0.10	0.69	0.10
13X40CO2N2	1	298.6	0.16	0.392	0.001	3.18	0.42	0.81	0.01	0.00	0.01
	2	298.5	0.19	0.612	0.001	7.37	0.41	1.93	0.02	0.00	0.02
	3	298.8	0.19	1.037	0.001	16.24	0.38	3.28	0.03	0.02	0.03
	4	299.2	0.20	1.639	0.001	28.45	0.36	4.17	0.04	0.16	0.04
	5	299.2	0.20	2.370	0.001	33.95	0.35	4.71	0.06	0.20	0.06
	6	298.6	0.14	2.964	0.001	36.36	0.35	5.03	0.08	0.24	0.08

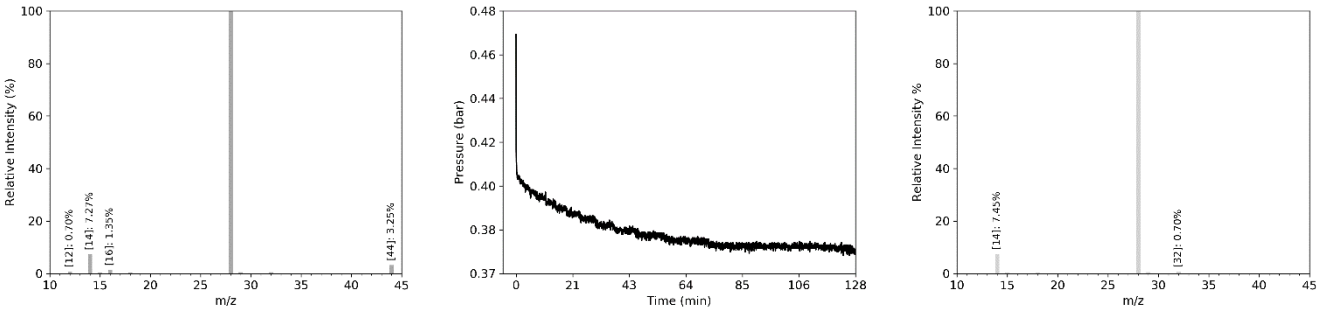

Figure A.7.1. 13X10CO2N2 Step 1.

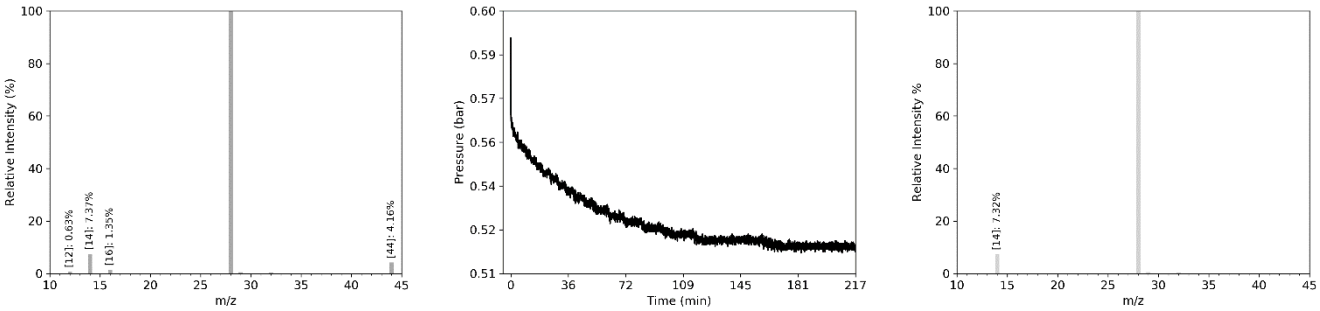

Figure A.7.2. 13X10CO2N2 Step 2.

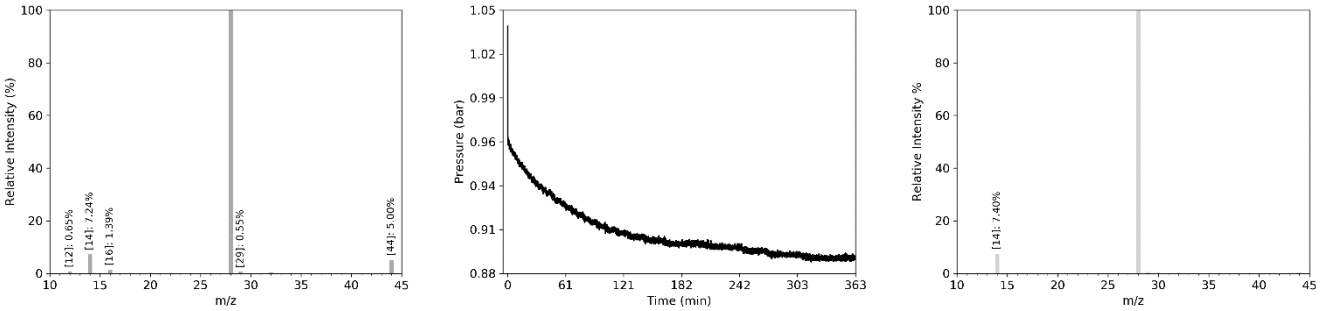

Figure A.7.3. 13X10CO2N2 Step 3.

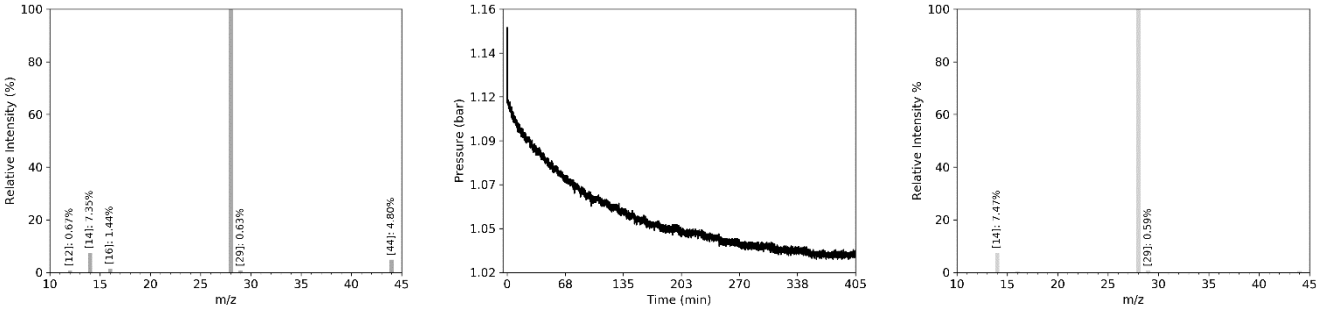

Figure A.7.4. 13X10CO2N2 Step 4.

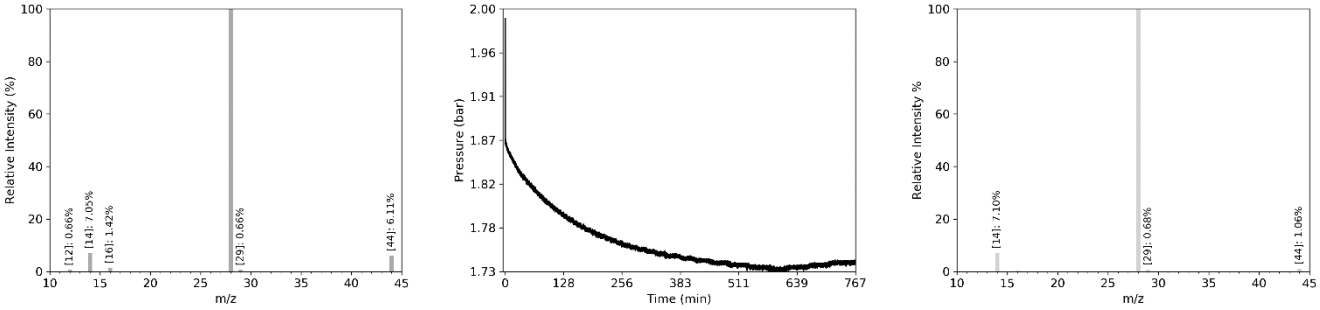

Figure A.7.5. 13X10CO2N2 Step 5.

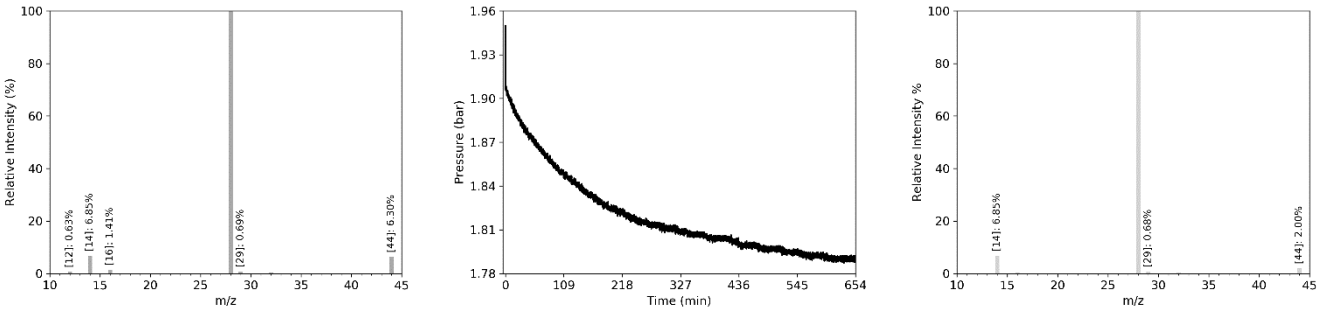

Figure A.7.6. 13X10CO2N2 Step 6.

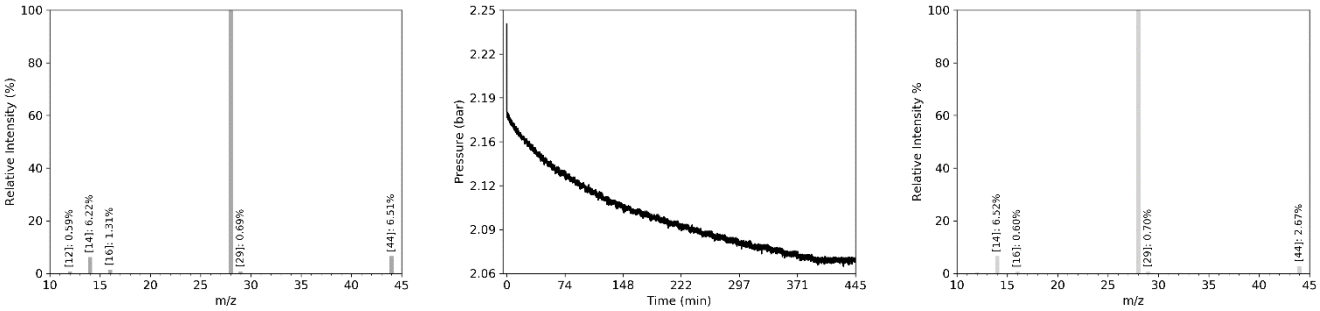

Figure A.7.7. 13X10CO2N2 Step 7.

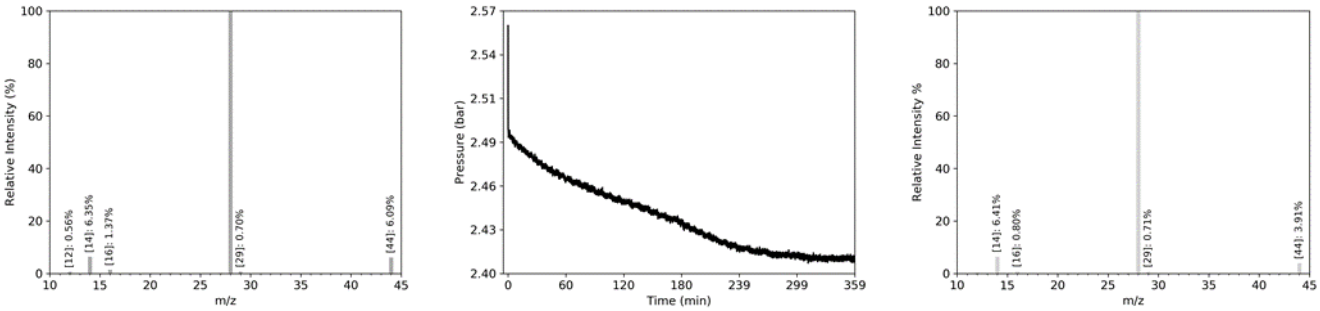

Figure A.7.8. 13X10CO2N2 Step 8.

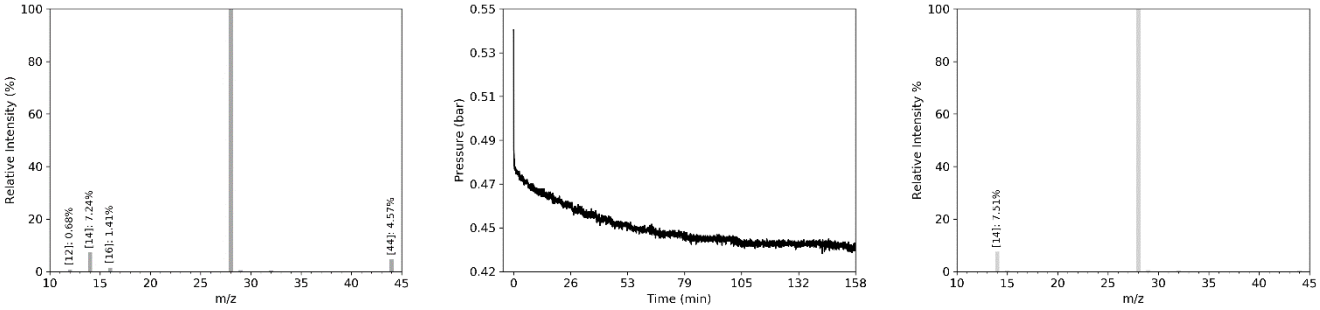

Figure A.7.9. 13X10CO2N2-2 Step 1.

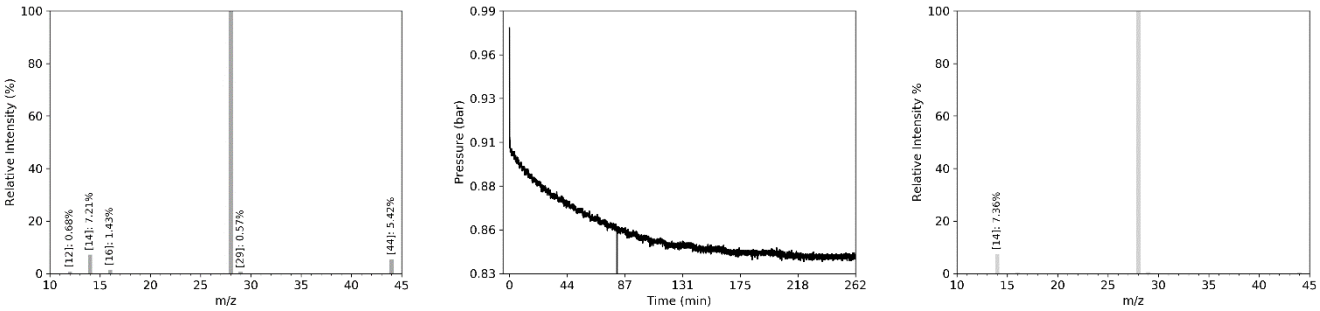

Figure A.7.10. 13X10CO2N2-2 Step 2.

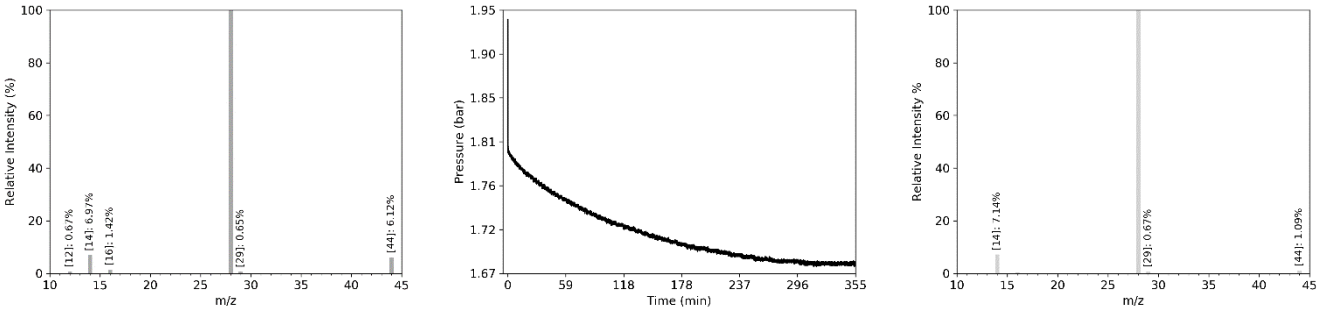

Figure A.7.11. 13X10CO2N2-2 Step 3.

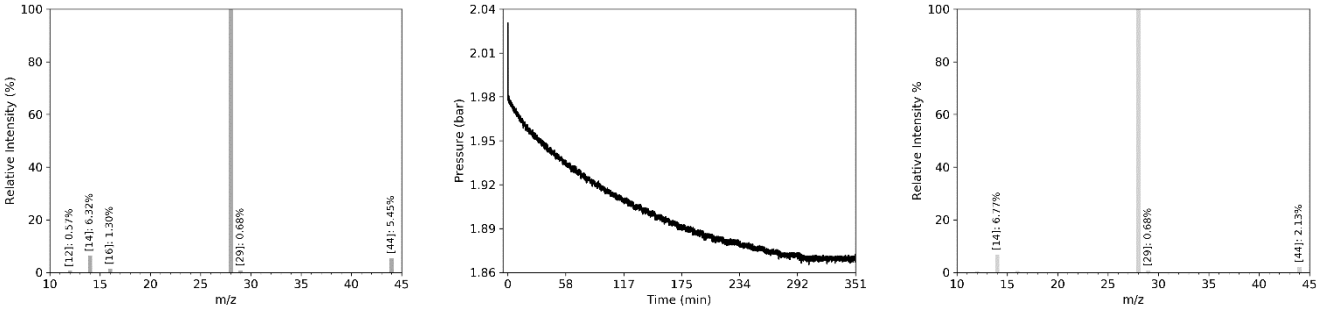

Figure A.7.12. 13X10CO2N2-2 Step 4.

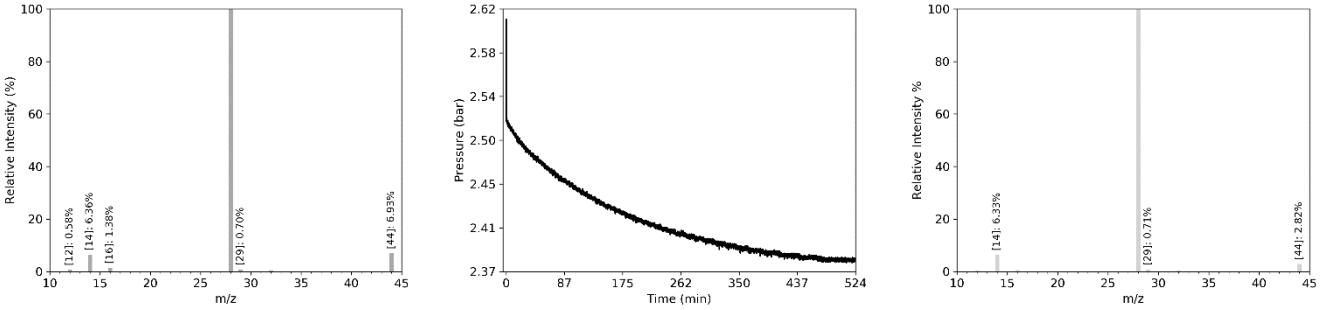

Figure A.7.13. 13X10CO2N2-2 Step 5.

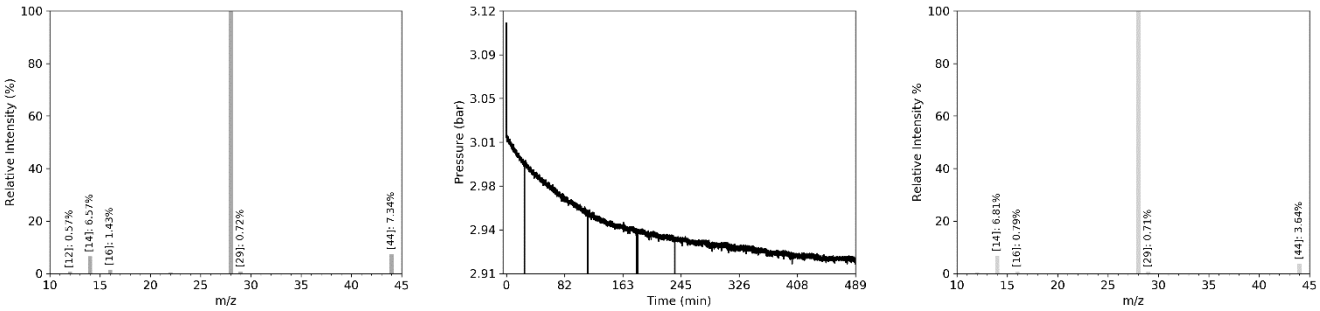

Figure A.7.14. 13X10CO2N2-2 Step 6.

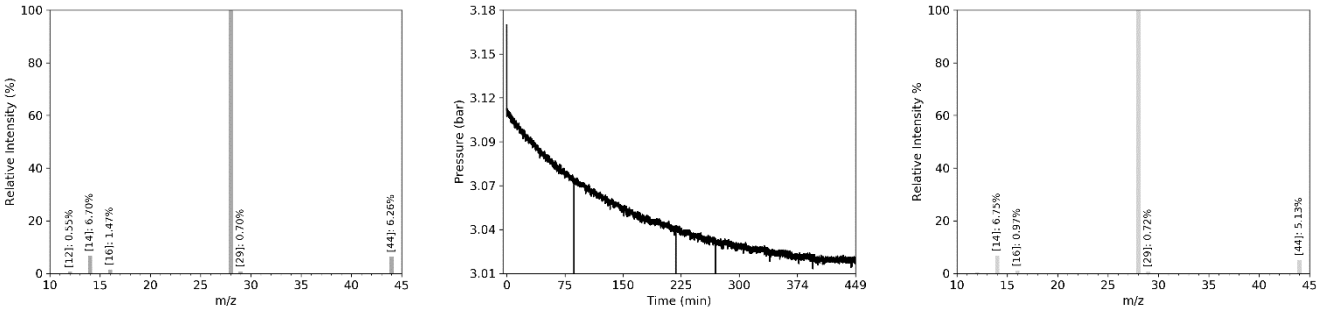

Figure A.7.15. 13X10CO2N2-2 Step 7.

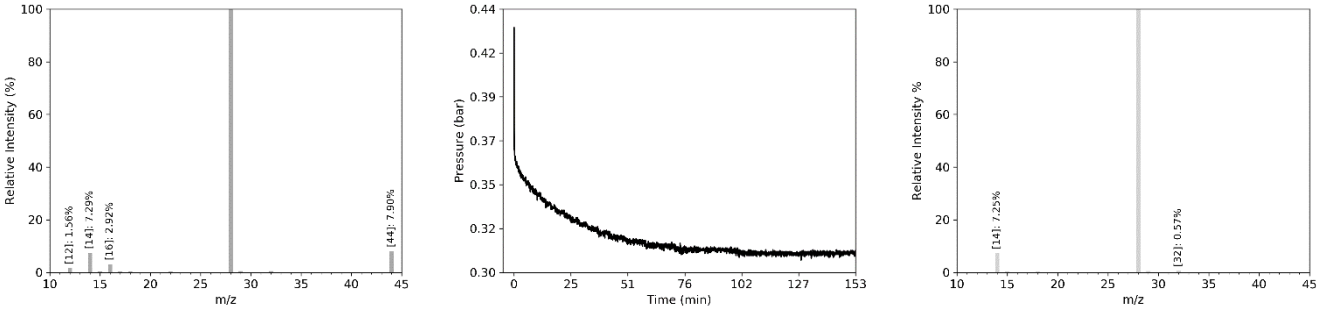

Figure A.7.16. 13X20CO2N2 Step 1.

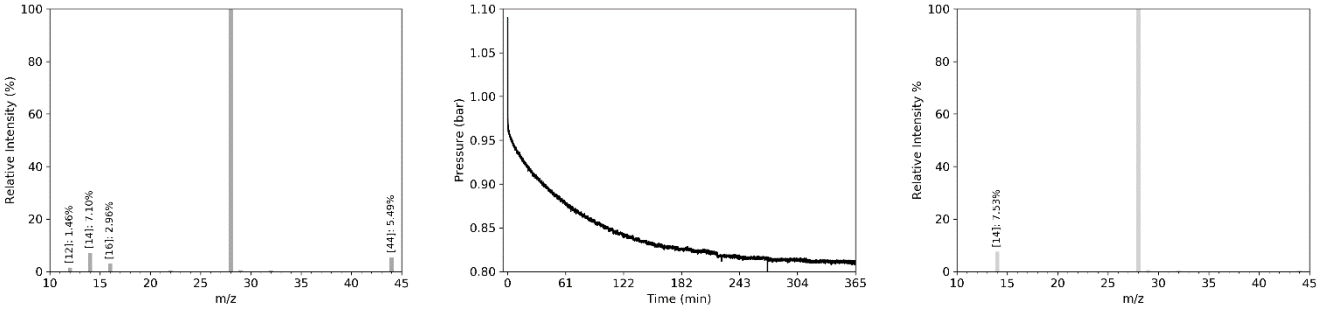

Figure A.7.17. 13X20CO2N2 Step 2.

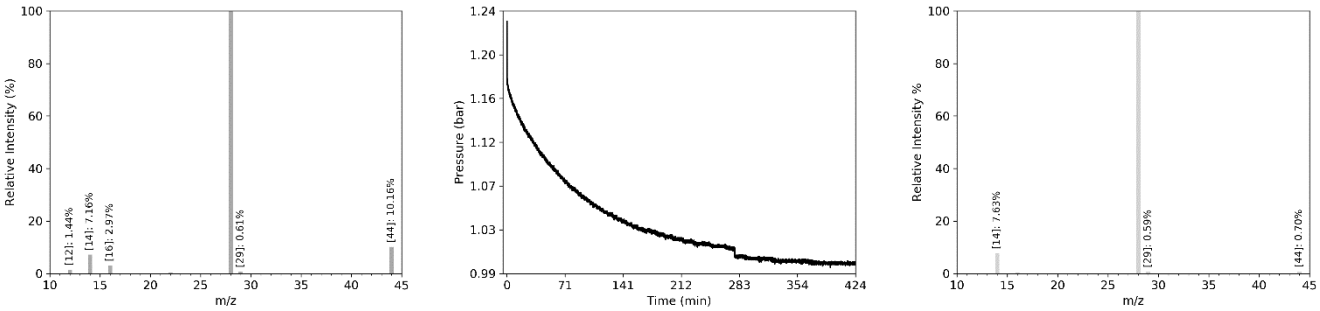

Figure A.7.18. 13X20CO2N2 Step 3.

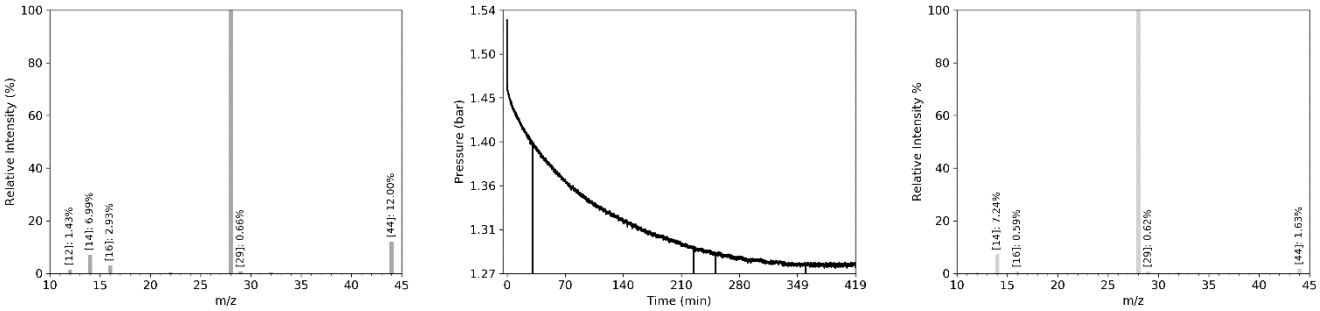

Figure A.7.19. 13X20CO2N2 Step 4.

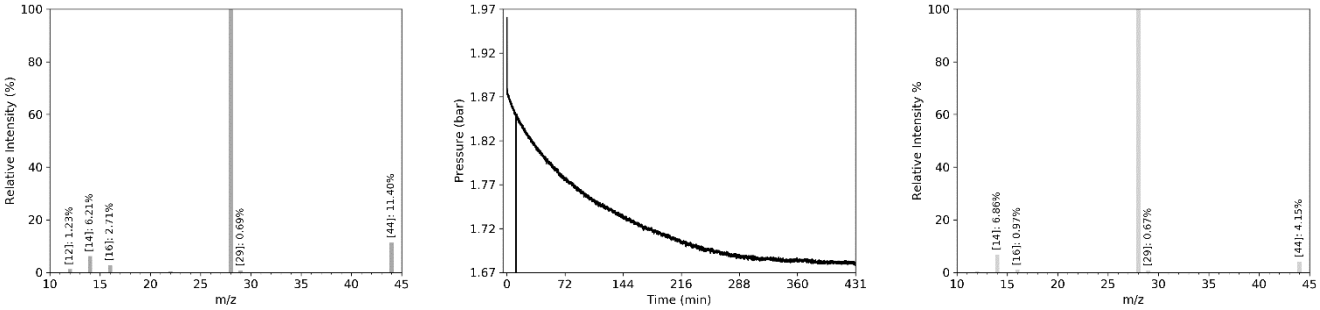

Figure A.7.20. 13X20CO2N2 Step 5.

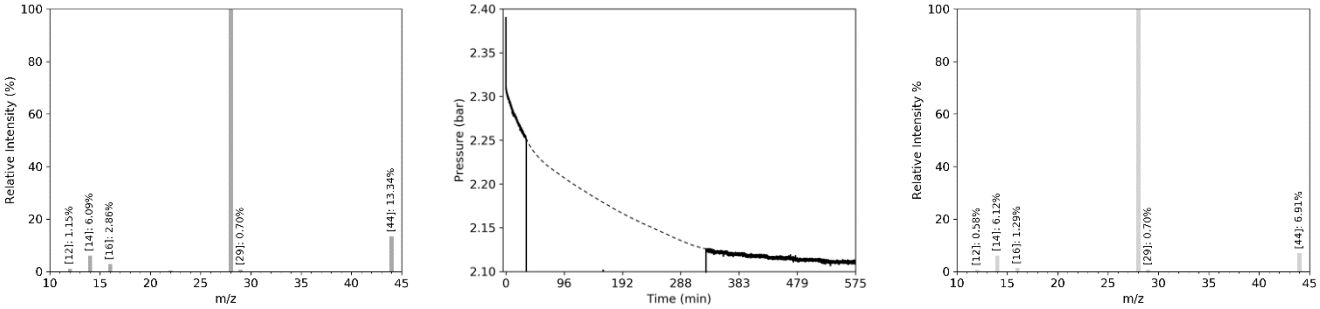

Figure A.7.21. 13X20CO2N2 Step 6.

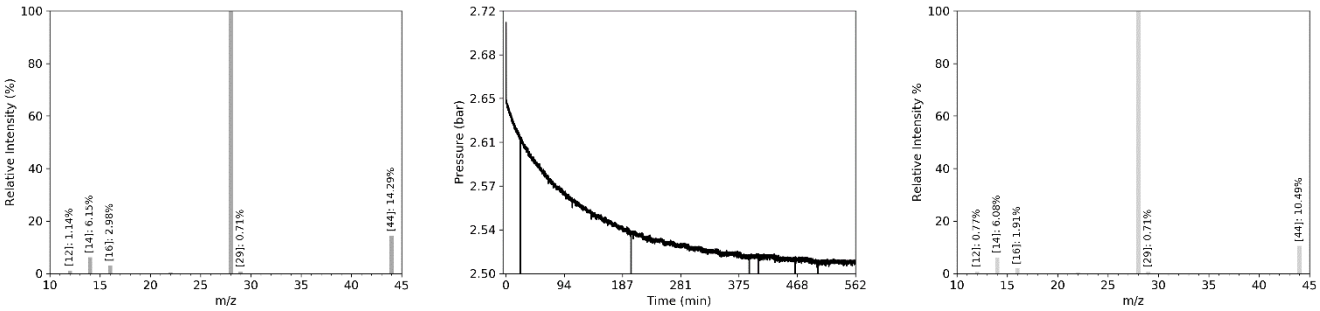

Figure A.7.22. 13X20CO2N2 Step 7.

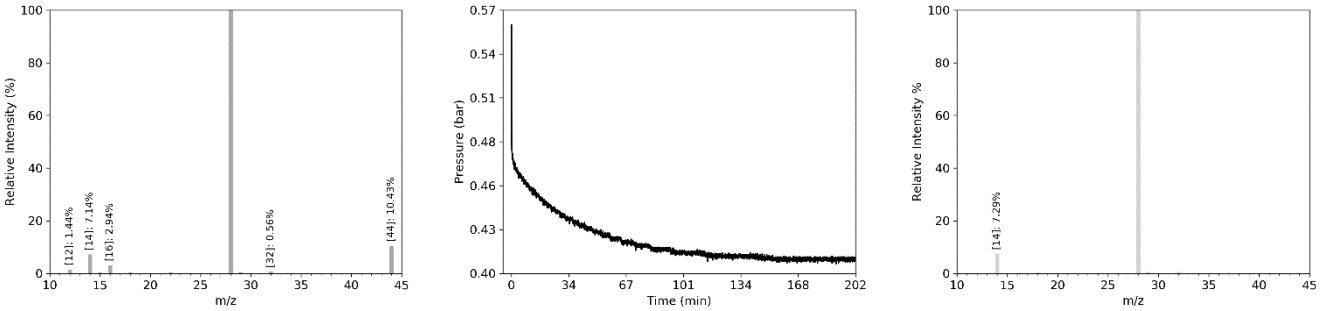

Figure A.7.23. 13X20CO2N2-2 Step 1.

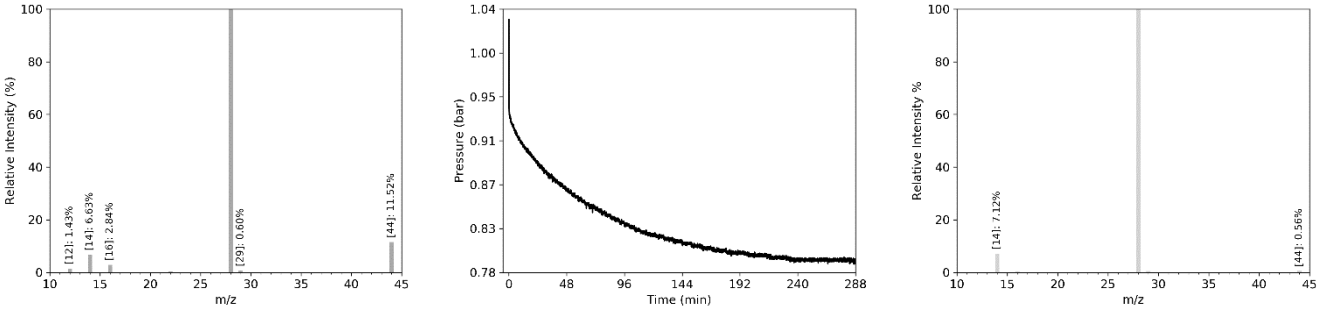

Figure A.7.24. 13X20CO2N2-2 Step 2.

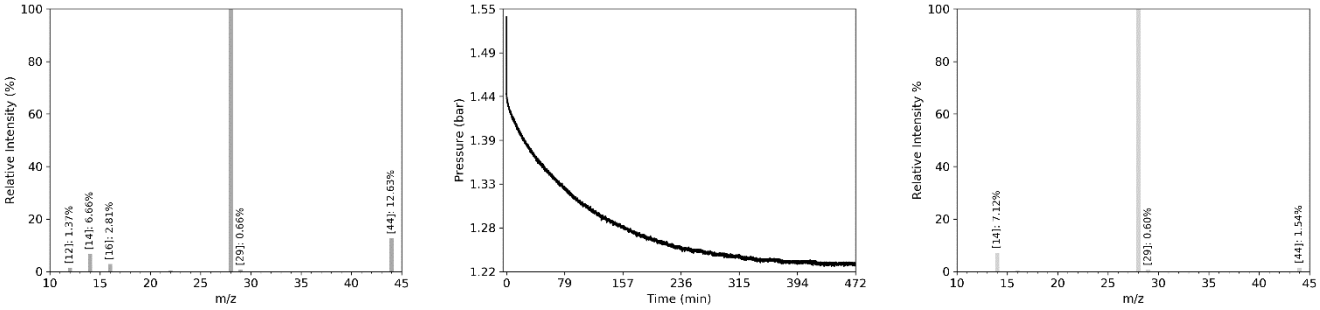

Figure A.7.25. 13X20CO2N2-2 Step 3.

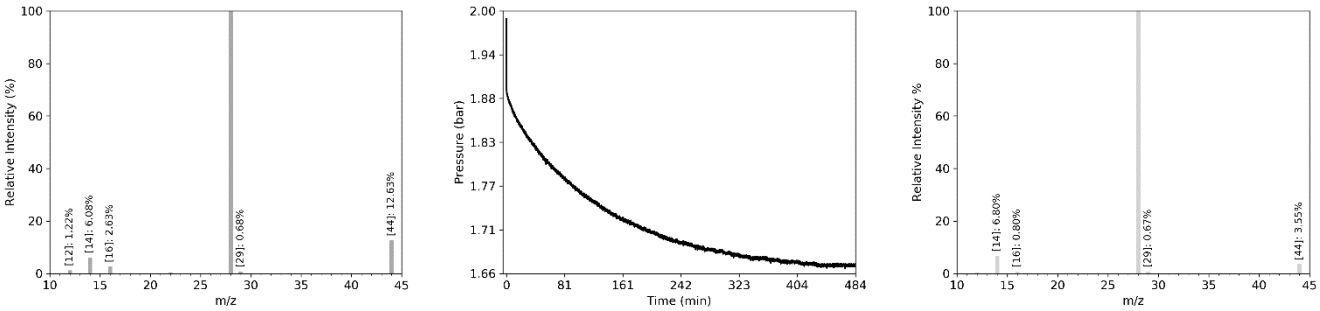

Figure A.7.26. 13X20CO2N2-2 Step 4.

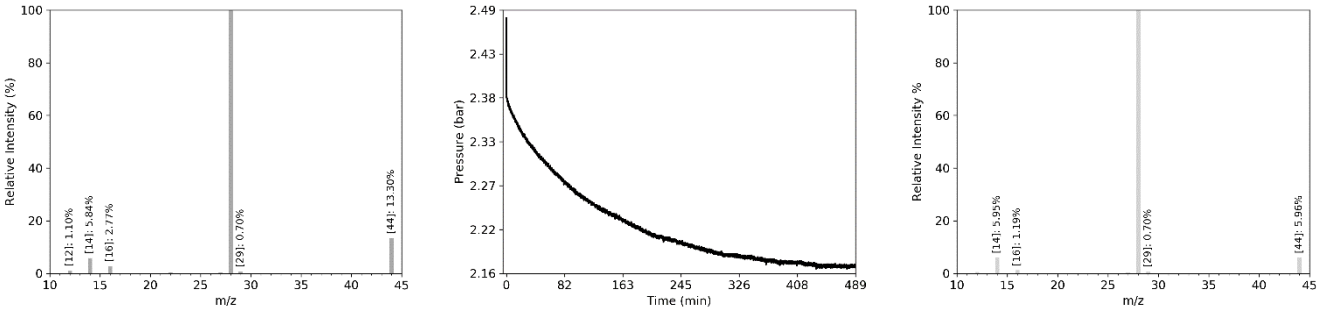

Figure A.7.27. 13X20CO2N2-2 Step 5.

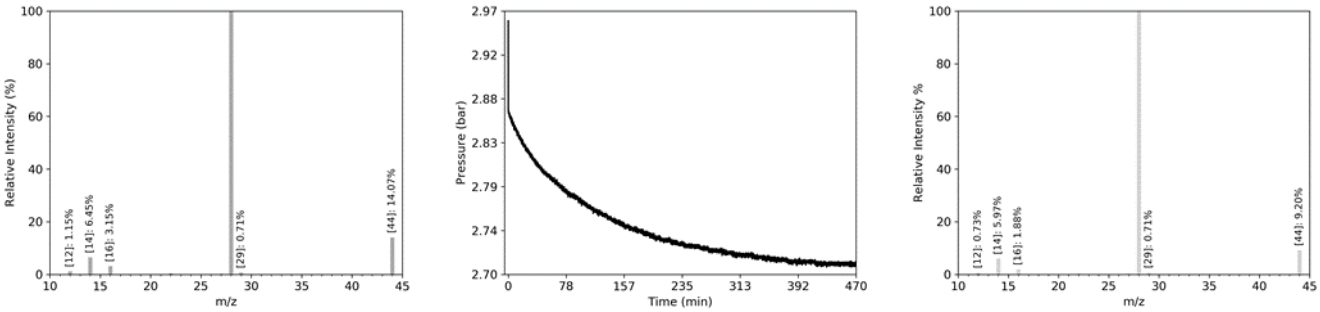

Figure A.7.28. 13X20CO2N2-2 Step 6.

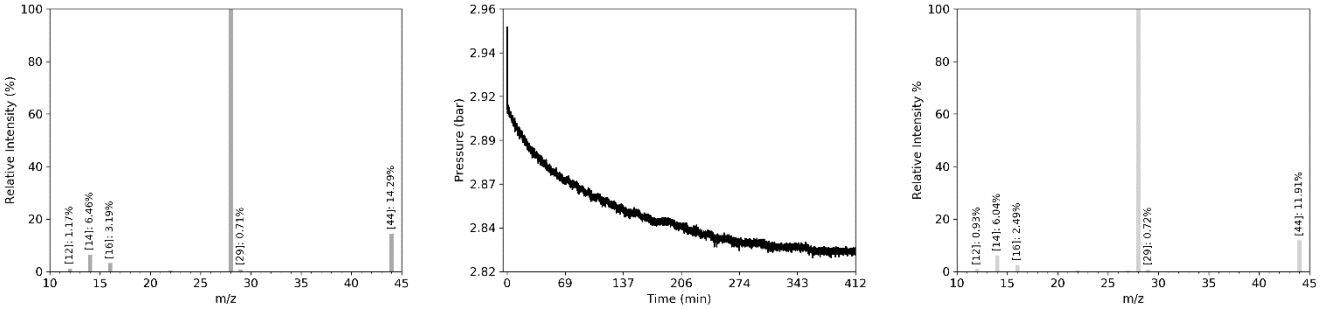

Figure A.7.29. 13X20CO2N2-2 Step 7.

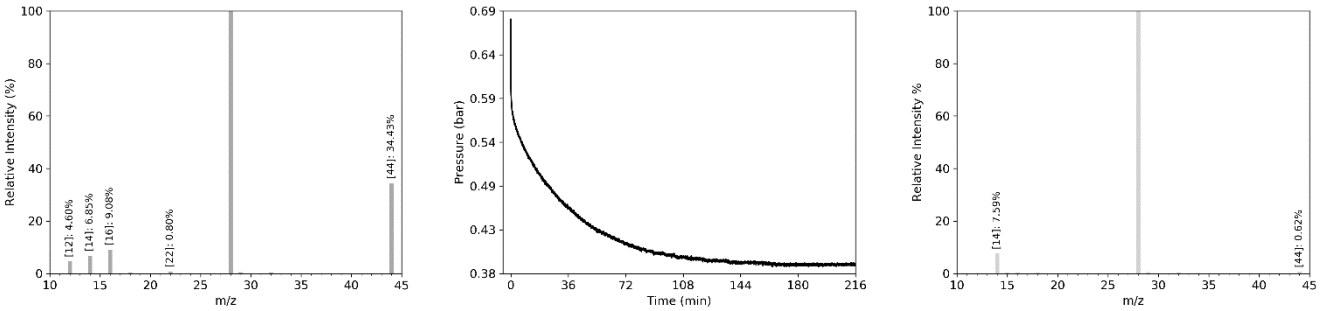

Figure A.7.30. 13X40CO2N2 Step 1.

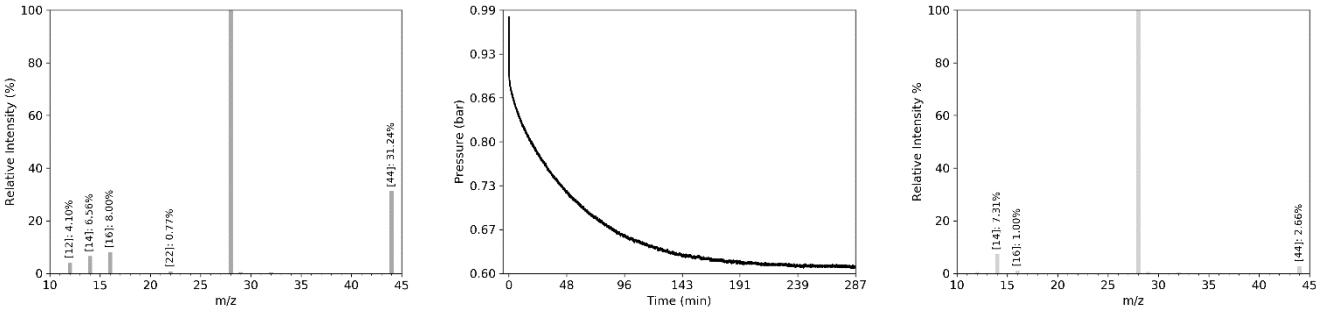

Figure A.7.31. 13X40CO2N2 Step 2.

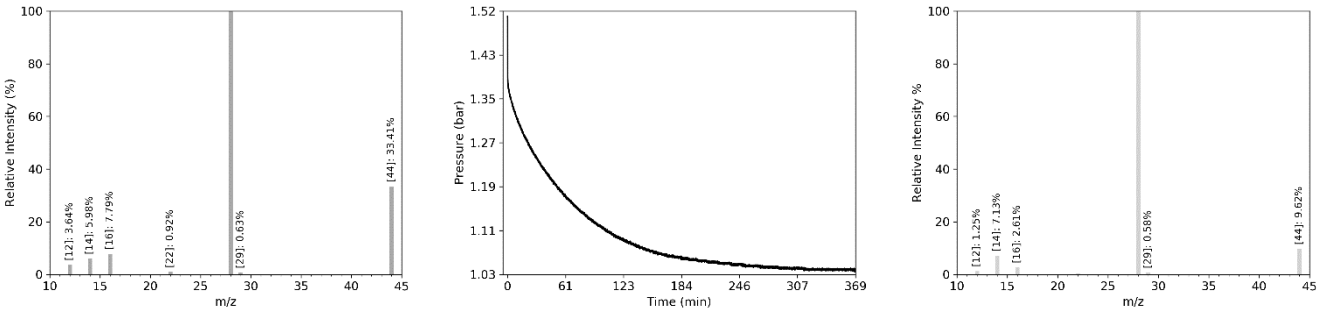

Figure A.7.32. 13X40CO2N2 Step 3.

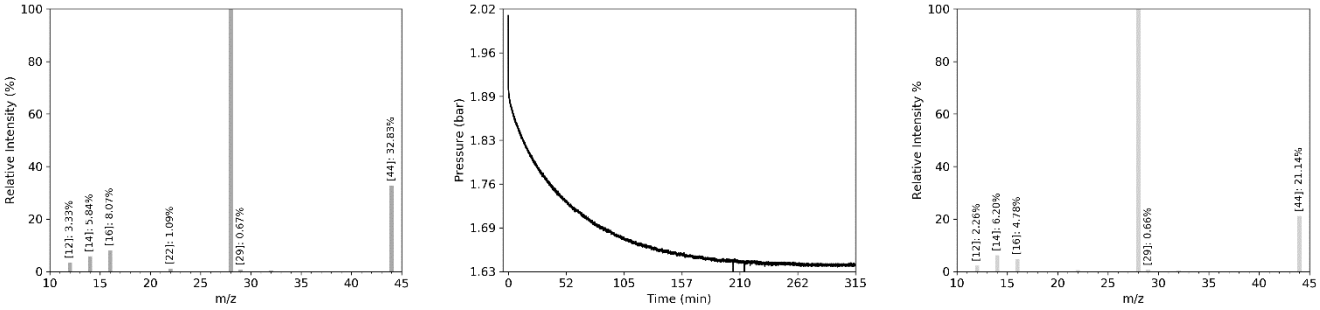

Figure A.7.33. 13X40CO2N2 Step 4.

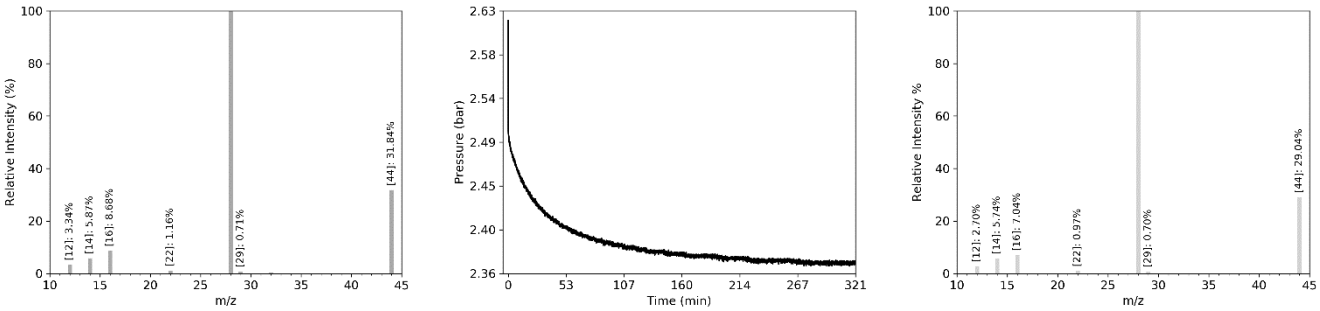

Figure A.7.34. 13X40CO2N2 Step 5.

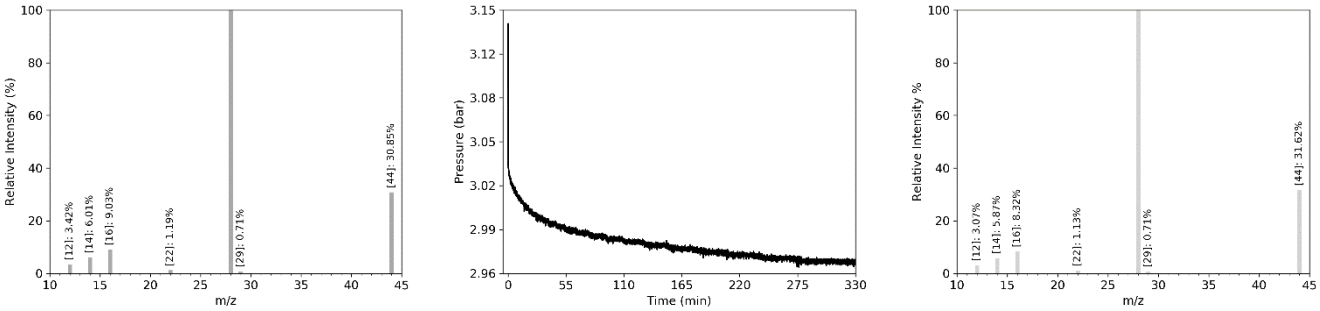

Figure A.7.35. 13X40CO2N2 Step 6.

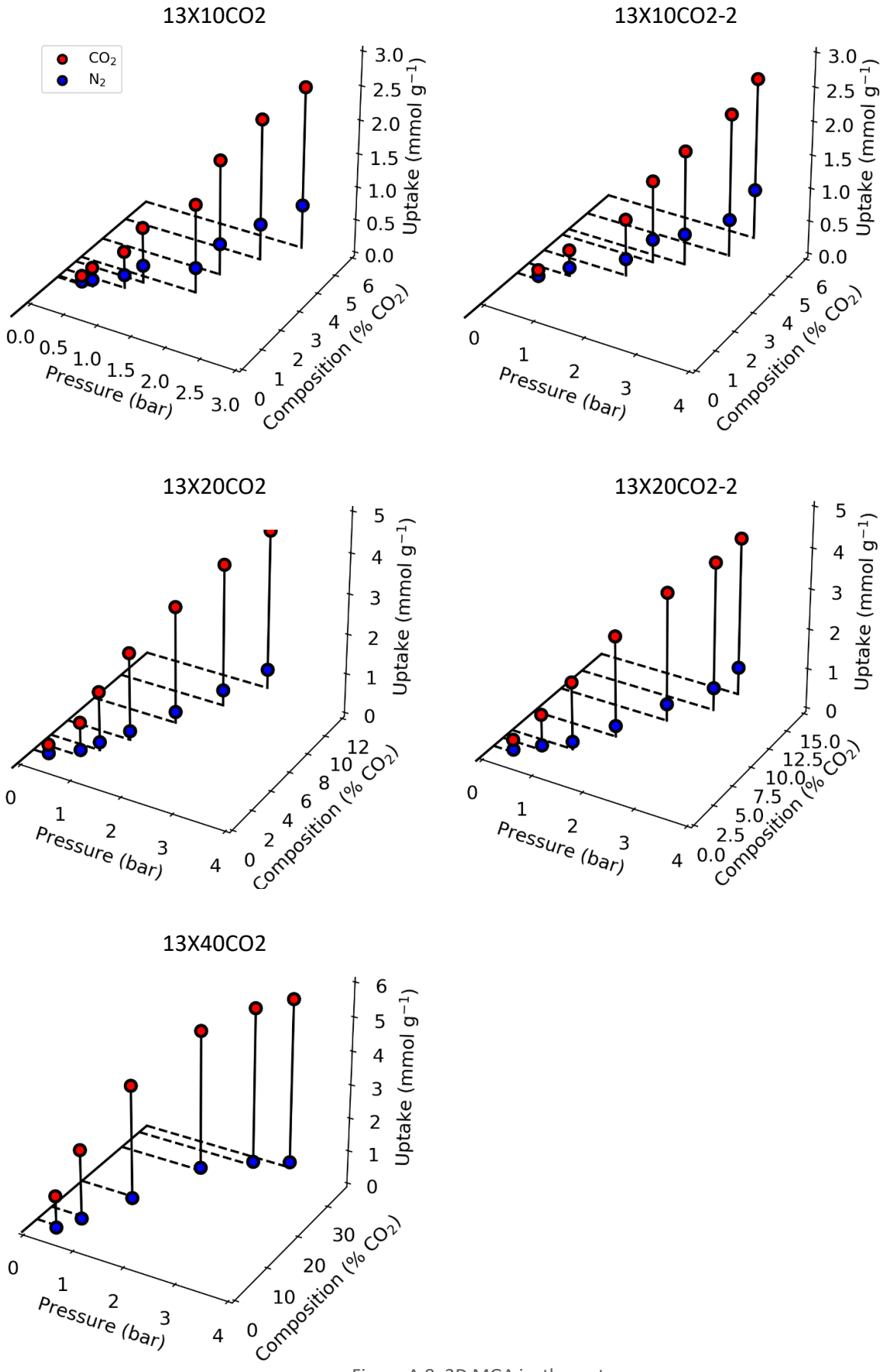

Figure A.8. 3D MGA isotherm traces.

A.3.7 Difference map (Experiment *vs* IAST)

Although there appears to be a loose agreement between experimental and IAST MGA isotherm morphologies, a difference map of $\Delta c = c_{IAST} - c_{EXP}$ versus pressure and composition illustrates the difference between the experimental results and IAST predictions (Figure A.9). With the limited SGA data measured in this study (Figure 2), IAST calculations are bound by the small demarcated region left of the 3.5 bar threshold. The smallest deviation is observed in this region, but the region itself is small in comparison to the measured region of the isotherms. The size of the predicted region can be increased by including high-pressure SGA isotherm data, such as those measured by Cavenati *et al*[11] left of the 45.7 bar threshold, but only by a small amount. In this extended region it becomes clear that IAST slightly overestimates CO_2 uptake and largely underestimates N_2 uptake.

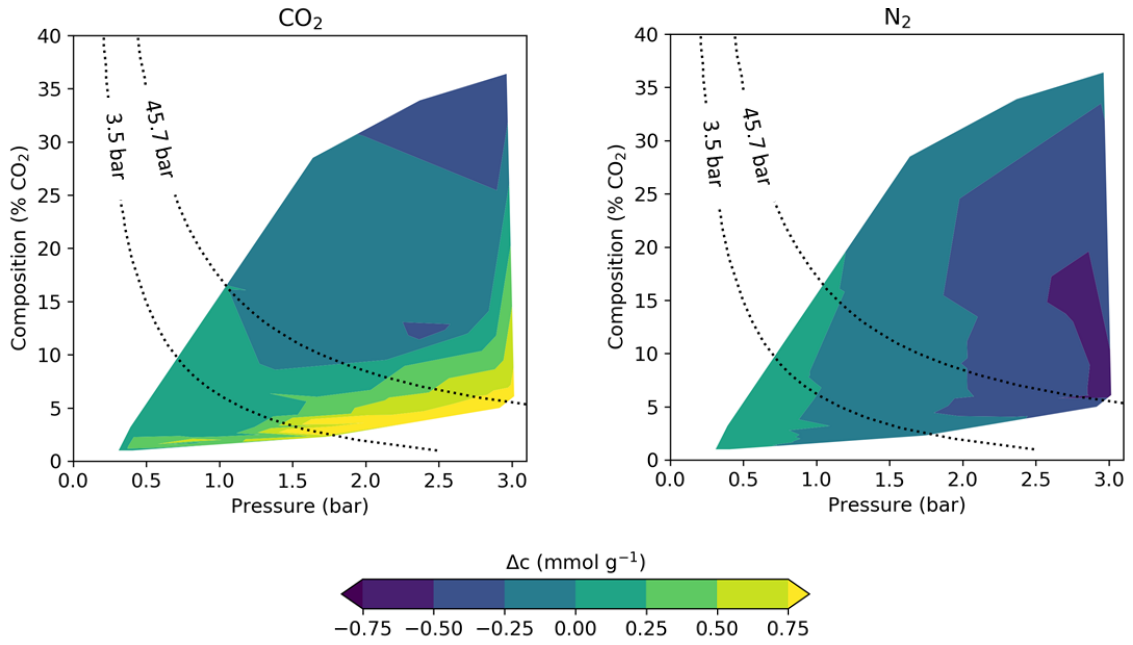

Figure A.9. Difference map of experimental results versus IAST results.

A.3.8 Extended Sips Isotherm

The Extended Sips[80] isotherm is an expanded version of the Sips[79] isotherm, much like the Extended Langmuir[81] isotherm is to the classical Langmuir[194] isotherm. The Extended Sips isotherm (Equation A6) is defined as

$$c_i = \frac{c_{m,i}\left(K_{S,i}\, y_i P\right)^{a_i}}{1 + \sum_j \left(K_{S,j} y_j P\right)^{a_j}} \qquad (A6)$$

where, exactly like the single-component Sips isotherm, c_i refers to the uptake, $c_{m,i}$ refers to the maximum uptake, P refers to the pressure, and a_i refers to the heterogeneity factor for pure component

i. The new only parameter that is introduced is the mole fraction of *i* in the gas phase. The parameters of the Extended Sips isotherm are calculated from SGA data; therefore, the Extended Sips isotherm can be calculated without MGA equilibrium data.

The measured, IAST, and Extended Sips MGA isotherms for CO_2 and N_2 on 13X are shown in Figure A.10. Among the three CO_2 isotherms, there is a visual agreement, while for the N_2 isotherms there is a loose agreement between the measured and the Extended Sips isotherms. The mean absolute error

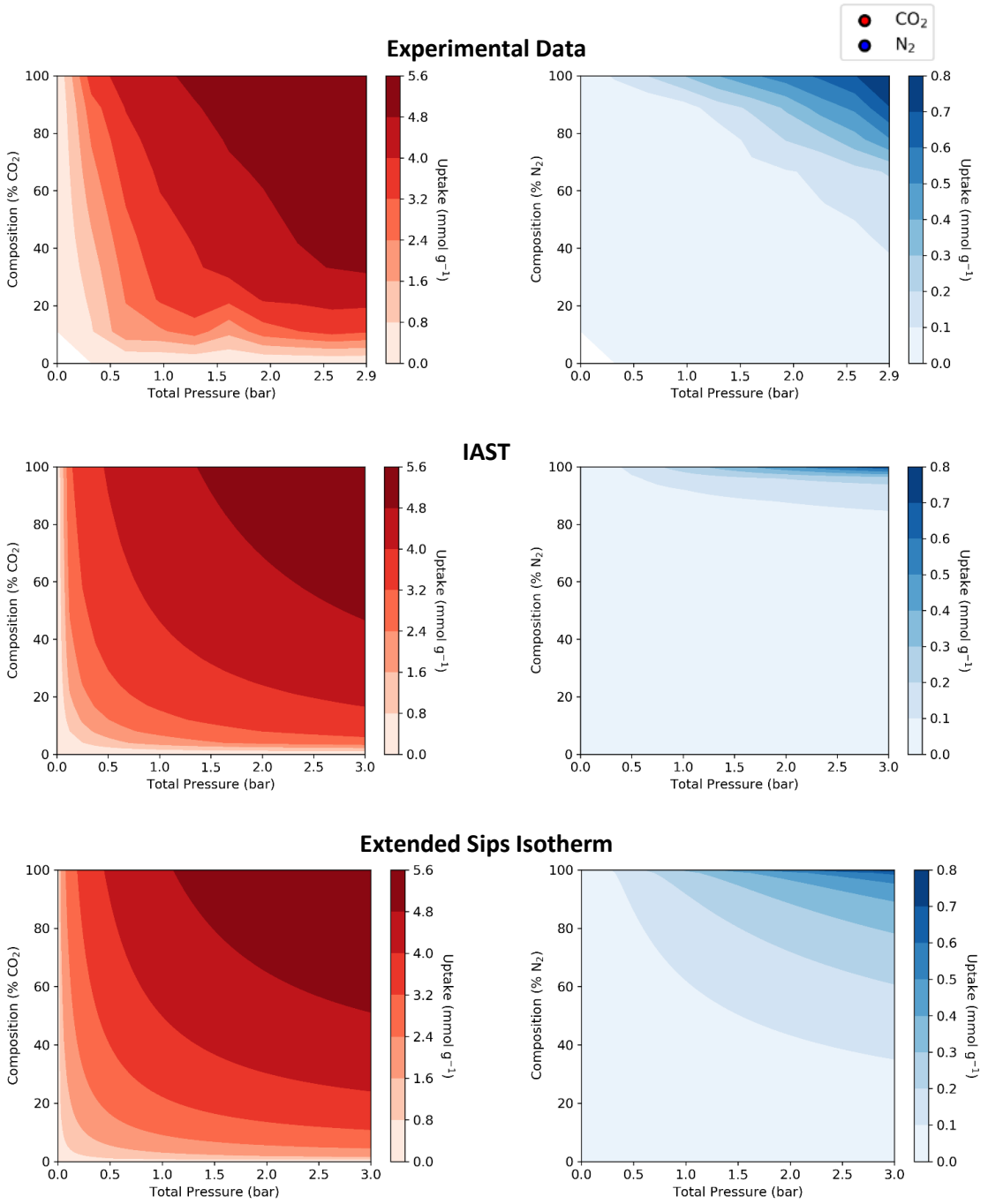

Figure A.10. Experimental, IAST, and Extended Sips isotherms for CO_2 and N_2.

and root mean squared errors were also calculated to get a clearer picture of the goodness of fit of IAST and the Extended Sips isotherm relative to the experimental results (see Table A.5).

Table A.5. Nonlinear Least-Squares Regression Parameters

Gas Species	Model	Mean Absolute Error (mmol g^{-1})	Root Mean Squared Error (mmol g^{-1})
CO2	IAST	3.60E-01	4.55E-01
	Extended Sips	4.28E-01	4.86E-01
N2	IAST	1.94E-01	2.69E-01
	Extended Sips	9.42E-02	1.19E-01

Appendix B. Supporting Information for Chapter 4

B.1 THEORETICAL BASIS

B.1.1 Single-Component Adsorption

Experimental single-component adsorption isotherm data were obtained from previously published studies for each material of interest. These were modeled according to the Sips isotherm, which is a robust 2-parameter isotherm model related to the Langmuir and Freundlich isotherms and is, therefore, sometimes called the Langmuir-Freundlich isotherm.[195] The Sips isotherm (Equation B1) is defined by

$$n_i(P) = \frac{n_i^{\infty}(b_i P)^{c_i}}{1 + (b_i P)^{c_i}} \qquad (B1)$$

where n_i is the amount of gas adsorbed, n_i^{∞} is the saturation capacity of the gas species, b_i is the Sips affinity coefficient, c_i is the heterogeneity parameter and P is the pressure. The Sips affinity coefficient is related to the equilibrium constant of the adsorption process. The heterogeneity parameter modifies the curvature of the Langmuir isotherm to account for deviations from the ideal uniform surface ($c_i = 1$) described in the Langmuir isotherm formulation.

B.1.2 Binary adsorption

The extended Sips isotherm is an empirical variant of the Sips isotherm that can be used to describe the simultaneous uptake of several gas species into the same adsorbent. The extended Sips isotherm (Equation B2) can be written as

$$n_{i,ext}(P, y) = \frac{{n_i}^{\infty}(b_i P_i)^{c_i}}{1 + \sum_{j=1}^{N_c}\left(b_j P_j\right)^{c_j}} \qquad (B2)$$

where $n_{i,ext}$ and P_i are the adsorbed amount and the partial pressure of component i, respectively, N_c is the number of adsorbates present in the system, P is the total pressure, and y is a vector containing the mole fractions of each of the gaseous components. The Sips affinity coefficient and heterogeneity factors are obtained from single-component adsorption isotherm data, implying that the extended Sips isotherm is a predictive model.

B.1.3 Adsorbed Solution Theory

Adsorbed Solution Theory (AST) is a thermodynamically-consistent model that utilizes the concepts of the Gibbs isotherm and vapor-liquid equilibria to describe the adsorption of gaseous species onto a rigid and inert surface.[39,196] AST is used to describe and, in special cases, predict the outcome of allowing an adsorbent to reach equilibrium with a multiple-component gas phase at a fixed pressure and composition. The limitations of AST are that the adsorbent may not chemically bind to the adsorbates or undergo any structural transformations. Additionally, AST is not necessarily an appropriate choice for describing the equilibrium between a gas phase and a porous material, owing to the vague description of the Gibbs dividing surface of a porous material. Nevertheless, AST has been used with great success over the years to describe the uptake of mixtures of gases by porous materials.[37]

The spreading pressure, often rewritten as the reduced surface potential, is one of the core concepts introduced in AST. The reduced surface potential (Equation B3), or reduced surface potential, of any adsorbate in equilibrium with the gas phase is defined as

$$\Pi_i = \frac{\pi_i A_i}{RT} \tag{B3}$$

where Π_i is the reduced surface potential, π_i is the spreading pressure, A_i is the specific surface area of component i, R is the gas constant and T is the temperature. The spreading pressure can be thought of as the two-dimensional pressure that is exerted by the adsorbate onto the surface of the adsorbent. Rigorous treatment of the specific surface area would limit the usage of AST to the ideal case where A_i tends to zero. However, in practice the parameter is ignored in favor of assuming that the ideal reduced surface potential is a reasonable approximation of the real reduced surface potential.

Myers and Prausnitz found that the reduced surface potential of any adsorbate is related to the pure-gas adsorption isotherm (Equation B4) *via* the integral

$$\Pi_i = \int_0^{P_i^0} \frac{n_i(P)}{P}\, dP \tag{B4}$$

where $n_i(P)$ is the fitted single-component adsorption isotherm of component i; P_i^0 is a special pressure which yields the same reduced surface potential as that of a mixture of adsorbate species. It can be shown for any multiple-component adsorption equilibrium that each set of partial pressures corresponds to a unique set of P_i^0 values. Owing to the lengthy description of the nameless P_i^0

parameter, and in recognition of the work by Professor Alan L. Myers on the thermodynamics of adsorption, it will henceforth be referred to as a Myers pressure in this study.

The criterion (Equation B5) used to calculate the correct set of Myers pressures for a multiple-component adsorption equilibrium is written as

$$\Pi_i = \Pi_{i+1} = \cdots = \Pi \tag{B5}$$

where Π is the reduced surface potential of the mixture and Π_i is the reduced surface potential of component i in isolation (see Equation B4).

The reduced surface potentials of two components in a mixture (Equation B6) as defined from Equation B4 and Equation B5 can be written as

$$\frac{n_1^{\infty} \ln(1 + (b_1 P_1^0)^{c_1})}{c_1} = \frac{n_2^{\infty} \ln(1 + (b_2 P_2^0)^{c_2})}{c_2} = \Pi \tag{B6}$$

(with subscripts 1 and 2 referring to the two components of the mixture) provided that the single-component adsorption equilibria of either species can be described by the Sips isotherm.

The equilibrium between the gas and adsorbed phase is defined by a relationship (Equation B7) analogous to Raoult's Law, with the exception that the equilibrium vapor pressure has been replaced by the Myers pressure of component i. This relationship between the partial pressure and the adsorbed fraction of component i is given as

$$P_i = \gamma_i x_i P_i^0(\Pi) \tag{B7}$$

where x_i is mole fraction and γ_i is the activity coefficient for component i. The mass balance (Equation B8) of adsorbate fractions can be written as

$$\sum_{i=1}^{N_c} x_i = 1 \tag{B8}$$

where N_c is the number of components present in the adsorbed phase.

The ideal case of AST ($\gamma_i = 1$), commonly referred to as IAST, can hence be solved. Specifically, for an ideal system that contains only two gas species, one would have four equations (originating from Equations B6, B7 and B8) and four variables (x_1, x_2, P_1^0, and P_2^0). This means that the adsorbed-phase mole fractions can be calculated exactly by only specifying the partial pressures of each component in the gas phase, provided that the pure-component adsorption isotherms of both species have been measured. Furthermore, the total amount of gas adsorbed (Equation B9) is related to the adsorbed-phase mole fraction and Myers pressure of each species *via*

$$\frac{1}{n_{tot}} = \sum_{i=1}^{N_c} x_i \left[\frac{1}{n_i \left(P_i^0(\Pi) \right)} + \frac{\partial \ln(\gamma_i)}{\partial \Pi} \right] \tag{B9}$$

where n_{tot} is the total amount adsorbed. The partial derivative terms are always omitted in IAST since the activity coefficients have a constant value of 1. However, in the non-ideal case of AST, they can be included depending on the activity coefficient model that is used.

B.1.4 Virial Activity Coefficient Model

Activity coefficients must therefore be calculated for the non-ideal case of AST. The most commonly-used methods for calculating the activity coefficients of the adsorbed-phase constituents are based on local composition theory (*i.e.* the Wilson equation[87] or the nonrandom two-liquid model).[197,198] We have chosen to avoid these models, as they were designed for describing the phase equilibria of nonionic liquid solutions. Instead, a simple empirical activity coefficient model inspired by the virial equation of state is introduced in this study. The case where two species are adsorbed yields Equation B12 upon rearranging Equation B7 and substituting x_j for $(1 - x_i)$, which can be written as

$$\gamma_j = \frac{P_j}{(1 - x_i) P_j^0(\Pi)} = A + B x_i + C x_i^2 + D x_i^3 + \cdots \tag{B12}$$

with empirical parameters A, B, C, and D. We will truncate our virial activity coefficient calculation at the cubic term of Equation B12. This power series is valid in the range where x_i lies strictly between 0 and 1. However, if the appropriate boundary conditions are invoked (*i.e.* $\gamma_j \to 1$ when $x_i \to 0$, and $\gamma_j \to \gamma_j^\infty$ when $x_i \to 1$)[199] then the first virial coefficient, A, can be replaced by 1. The mathematical relationship (Equation B13) between the remaining virial coefficients and the activity coefficient at infinite dilution after the substitution is

$$B + C + D + 1 = \gamma_j^\infty \tag{B13}$$

where γ_j^∞ is the activity coefficient of j at infinite dilution. This relationship provides some information regarding the constraints that must be imposed when the parameters are fitted to experimental data. Specifically, the activity coefficient at infinite dilution must be greater than zero. This constraint (Equation B14) can be expressed as

$$B + C + D > -1 \tag{B14}$$

and is obtained by substituting the lower bound of the activity coefficient at infinite dilution.

B.1.5 Working Capacity, Selectivity, and Working Selectivity

Two of the main measures[165] of the performance of an adsorbent under industrial conditions are the selectivity and the working capacity (W_i, Equation B15). Working capacity is the difference between the adsorbed amounts at two specified equilibria and it can be written as

$$W_i(P, y) = n_i(P, y) - n_{i,REF} \qquad (B15)$$

where y is the composition of the gas phase (see Equation B2), and $n_{i,REF}$ is the adsorbed amount of component i at the reference state. Pressure-swing adsorbers are usually cycled from atmospheric pressure to high pressure and back at a practically fixed gas-phase composition. Therefore the working capacity is used to determine how much of a component is adsorbed relative to the amount adsorbed at atmospheric pressure.

Selectivity[136] (S_{ij}, see Equation B16) is a measure of the ability of a material to adsorb one species over another. The selectivity ratio is written as

$$S_{ij} = \frac{x_i}{x_j}\frac{y_j}{y_i} \qquad (B16)$$

with x_i and x_j being the adsorbed-phase mole fractions of component i and j; y_i and y_j being the gas-phase mole fraction of component i and j.

We will also define our own version of selectivity that is more representative of the selectivity that one can expect from a real PSA cycle (Equation B17). This working selectivity, S_{ij}^{w}, is written as

$$S_{ij}^{w} = \frac{W_i(P,y)}{W_j(P,y)}\frac{y_j}{y_i} \qquad (B17)$$

with the adsorbed-phase mole fractions replaced by the working capacity of each component. The working selectivity can be defined as the selectivity of a multiple-component adsorption equilibrium relative to the reference state used to calculate the working capacity.

B.1.6 PRAST-S

Predictive RAST using the extended Sips isotherm (PRAST-S) is an algorithm that can be used to solve RAST equations without having multi-component gas adsorption data. The algorithm is outlined in Scheme B.1.

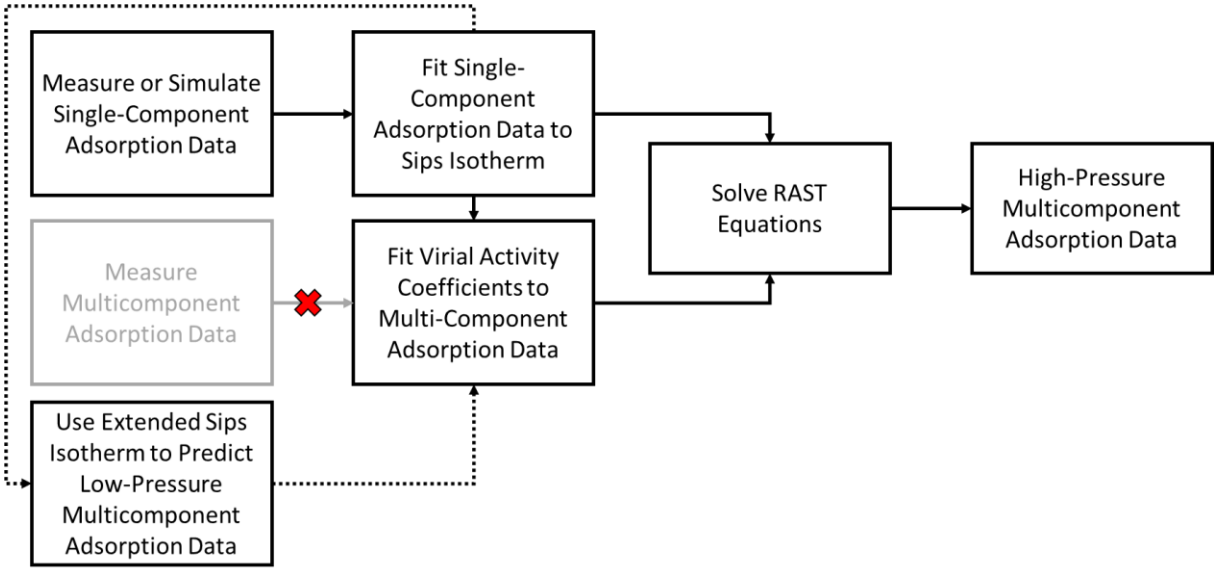

Scheme B.1. The PRAST-S method.

B.1.7 Predicted Isotherms

The predicted isotherms (IAST, extended Sips, and the predictive RAST method) for Cu-HKUST-1, MOF-14, UiO-66, and Mg-MOF-74 are contained in this section.

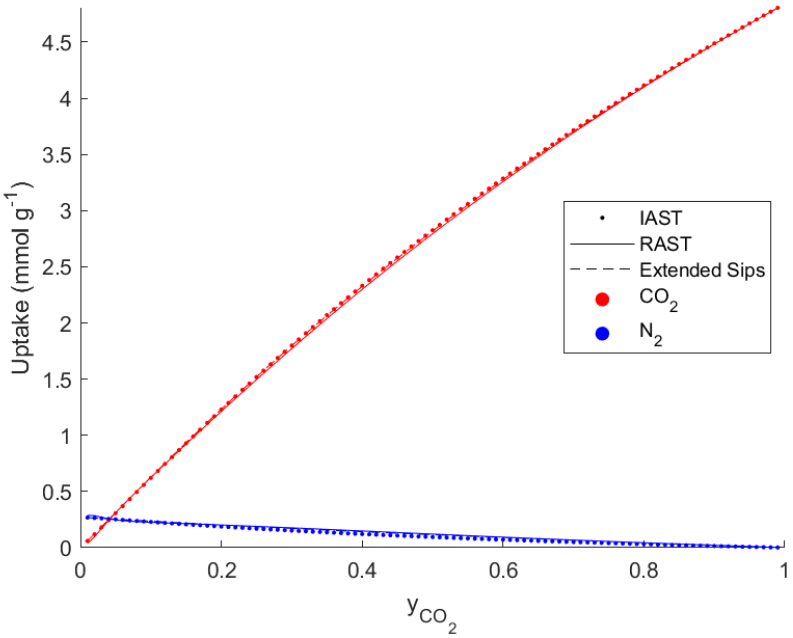

Figure B.1. Predicted multiple component adsorption isotherms for Cu-HKUST-1 @ 1 bar.

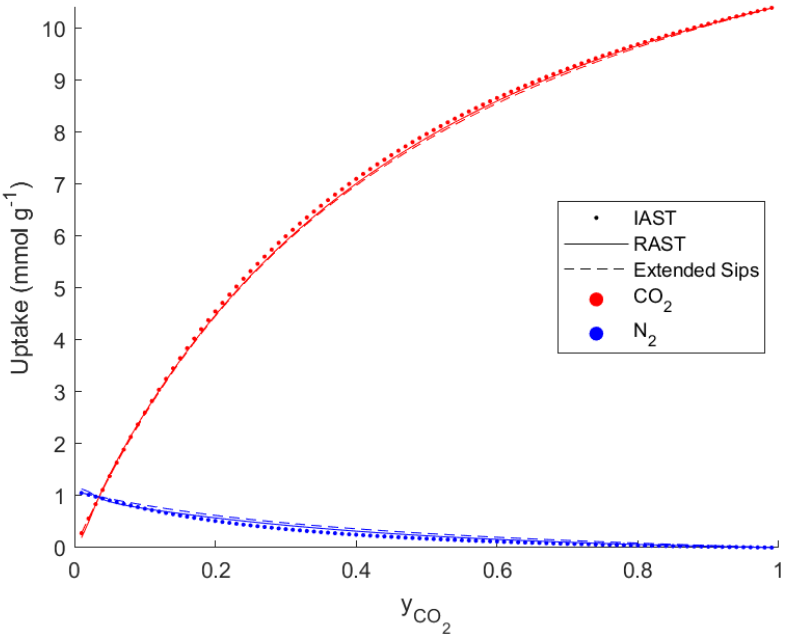

Figure B.2. Predicted multiple component adsorption isotherms for Cu-HKUST-1 @ 5 bar.

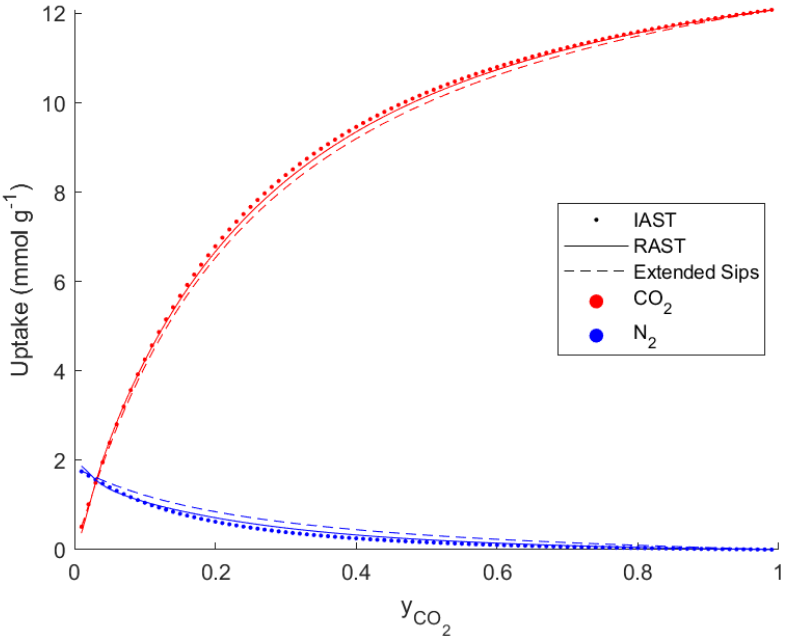

Figure B.3. Predicted multiple component adsorption isotherms for Cu-HKUST-1 @ 10 bar.

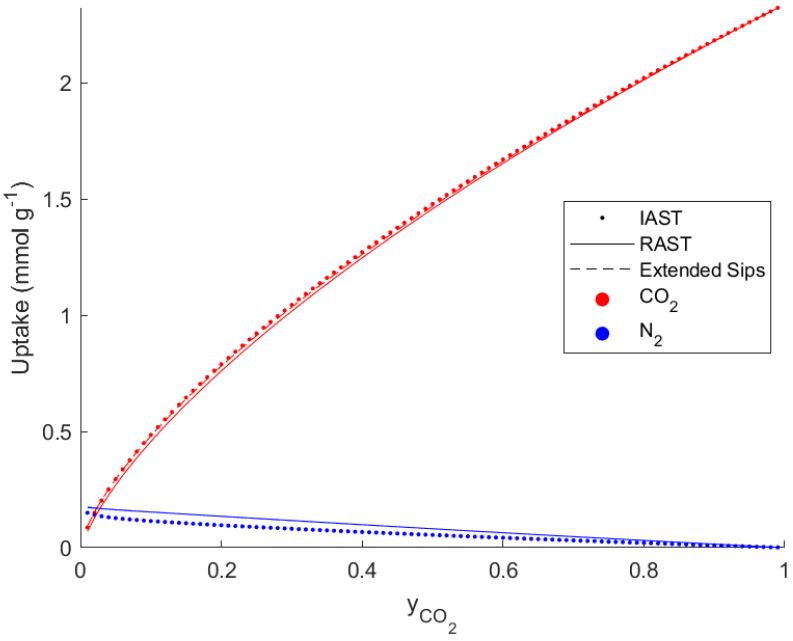

Figure B.4. Predicted multiple component adsorption isotherms for MOF-14 @ 1 bar.

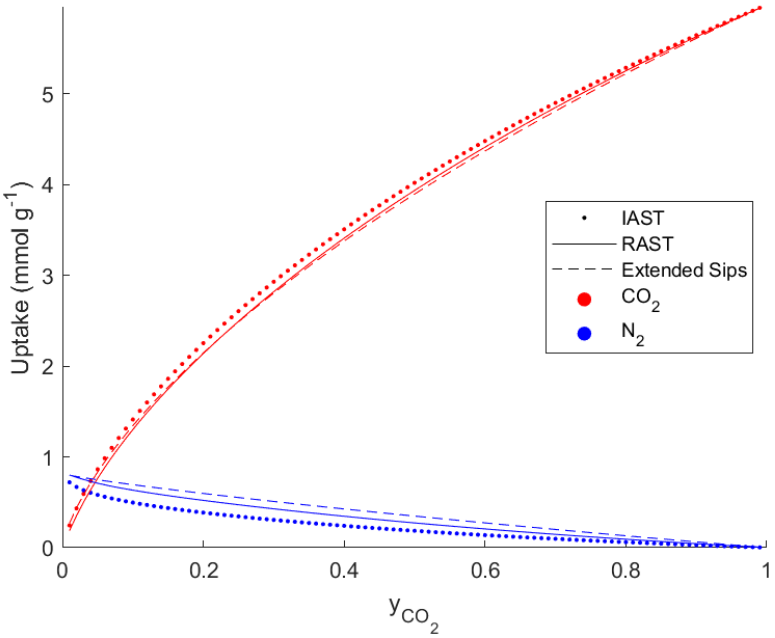

Figure B.5. Predicted multiple component adsorption isotherms for MOF-14 @ 5 bar.

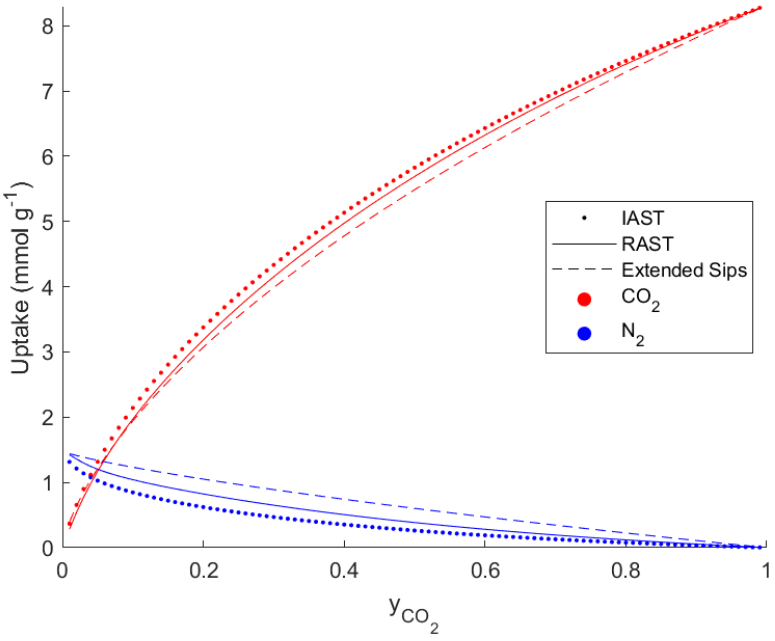

Figure B.6. Predicted multiple component adsorption isotherms for MOF-14 @ 10 bar.

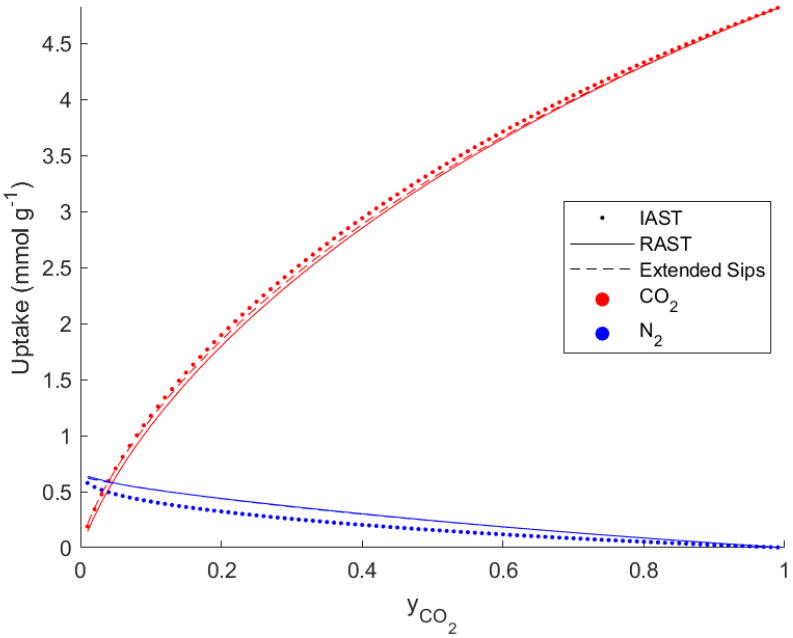

Figure B.7. Predicted multiple component adsorption isotherms for Mg-MOF-74 @ 1 bar.

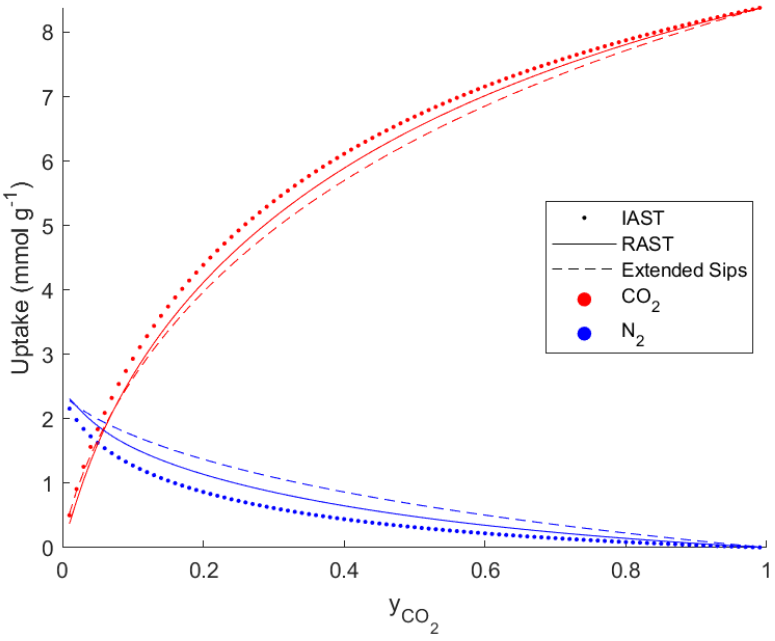

Figure B.8. Predicted multiple component adsorption isotherms for Mg-MOF-74 @ 5 bar.

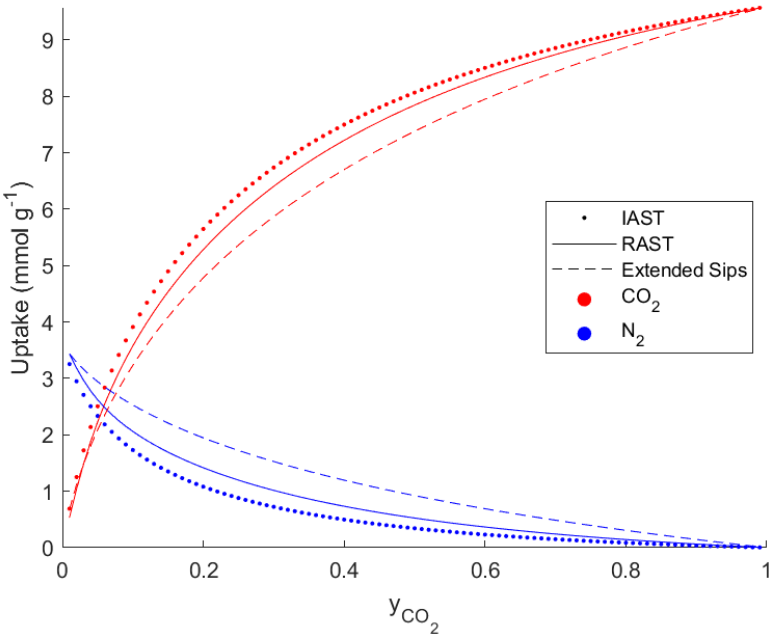

Figure B.9. Predicted multiple component adsorption isotherms for Mg-MOF-74 @ 10 bar.

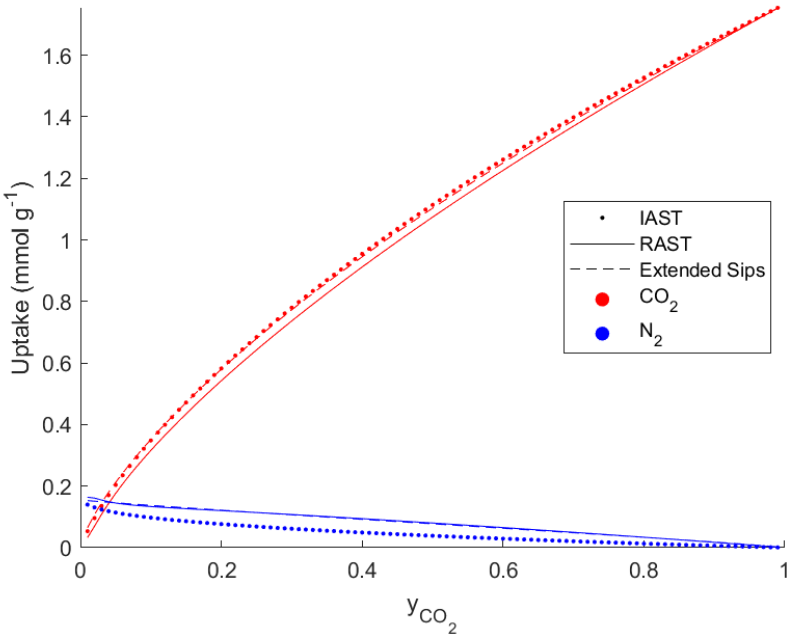

Figure B.10. Predicted multiple component adsorption isotherms for UiO-66 @ 1 bar.

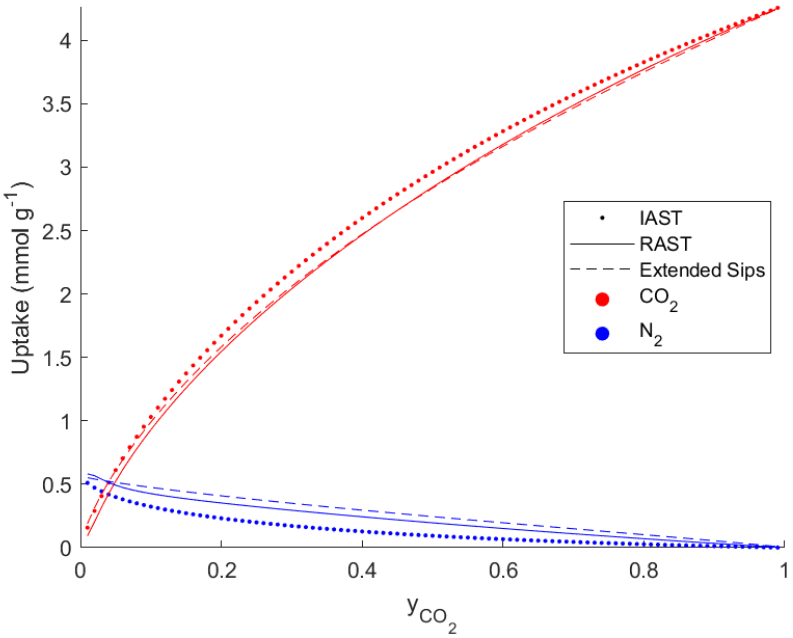

Figure B.11. Predicted multiple component adsorption isotherms for UiO-66 @ 5 bar.

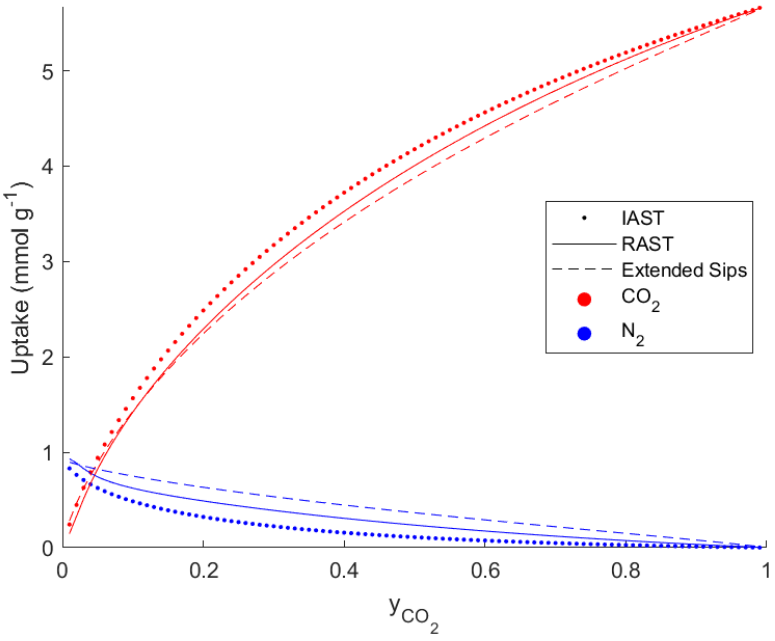

Figure B.12. Predicted multiple component adsorption isotherms for UiO-66 @ 10 bar.

B.2 EXPERIMENTAL DETAILS

B.2.1 Analytical gases

Analytical gases (He, CO_2, and N_2) with a minimum purity grade of 99.999% were purchased from *Afrox*. Gas mixtures of CO_2 and N_2 (20%, 40%, 60% and 80%) were also purchased from *Afrox*.

B.2.2 Powder X-Ray Diffraction

Powder X-Ray diffraction (PXRD) was performed on the *Bruker D2 Phaser* using a zero-background sample plate. The diffractometer is equipped with a Cu-K_α X-Ray source (λ = 1.54184 Å) and a *Lynxeye* 1-D detector. Data were recorded at atmospheric pressures and operational temperatures (T = 310 K) with an angular increment of 0.01617° in the scanning range of 5 - 30°.

The measured PXRD patterns for as-synthesized and activated (see Section B.2.4) Cu-HKUST-1 are shown in Figure B.13. The close agreement between the PXRD patterns are indicative that the activation method is appropriate for Cu-HKUST-1.

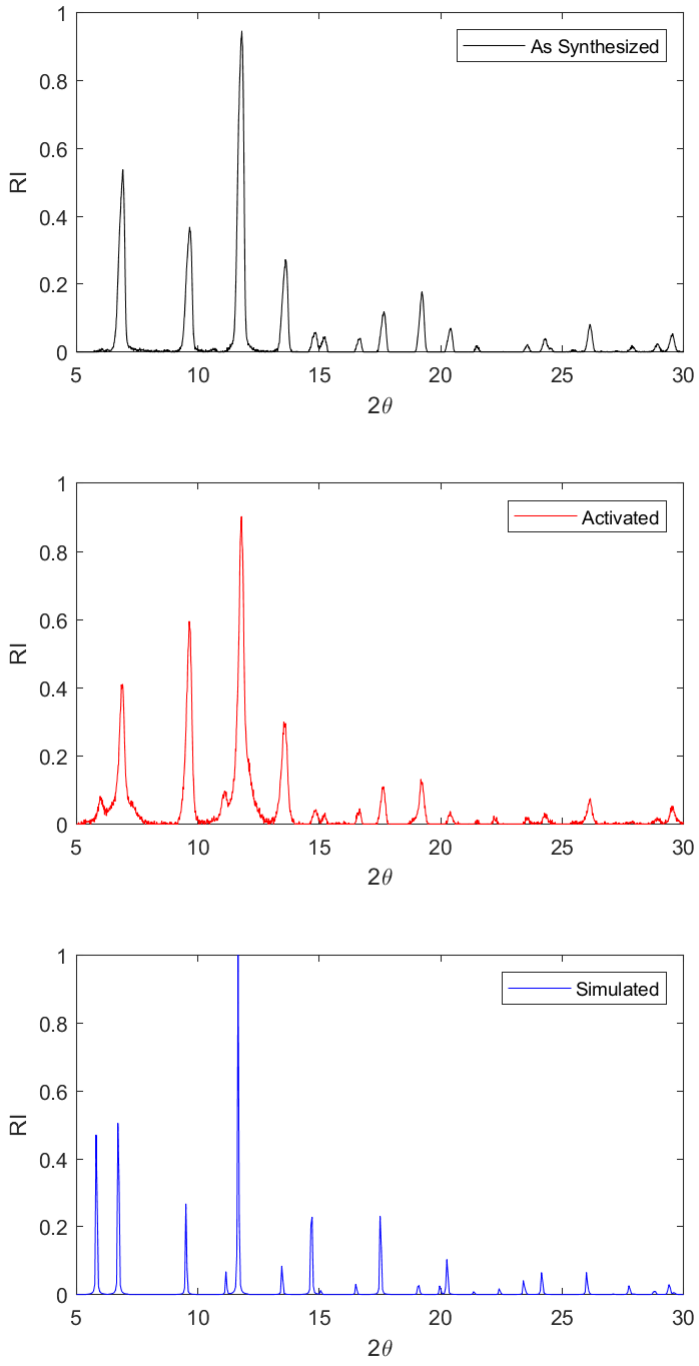

Figure B.13. Powder X-Ray diffraction data for Cu-HKUST-1.

B.2.3 Thermogravimetric Analysis

Thermogravimetric analysis (TGA) was performed on a *TA Instruments Q500* instrument. The sample was heated from room temperature to 873 K at a rate of 10 K min^{-1}, and weight loss was recorded under a constant flow of a purge stream of nitrogen at 50 mL min^{-1}. Thermogravimetric data were converted to a numerical format using the Universal Analysis 2000 software.

The thermograms of Cu-HKUST-1 (Figure B.14) shows that as-synthesized Cu-HKUST-1 contains a large amount of wet mass (~ 30%) that is expelled between room temperature and 373 K. The activated Cu-HKUST-1 also displays mass loss attributable to moisture adsorbed during transfer in this range. A small thermal event is observed in both cases between 373 K and 473 K, followed by a clear decomposition event at 573 K.

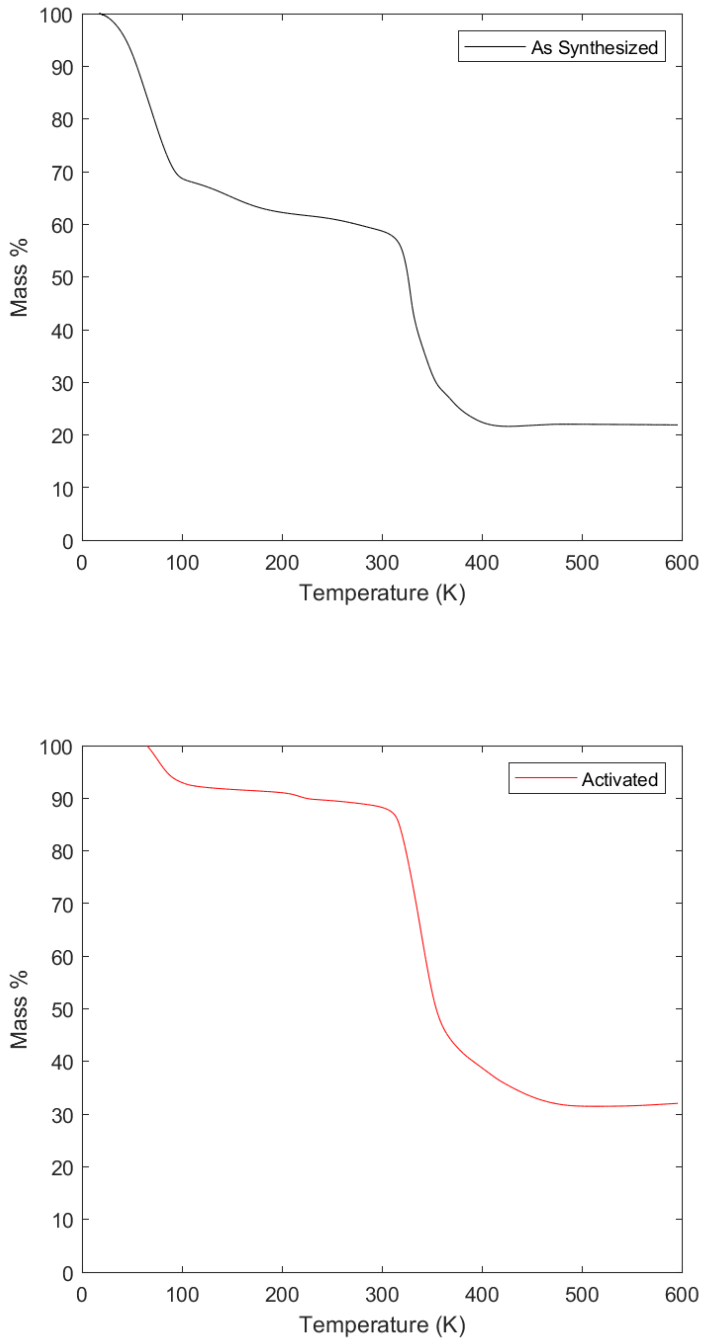

Figure B.14. Thermogravimetric analysis for the as-synthesized and activated forms of Cu-HKUST-1.

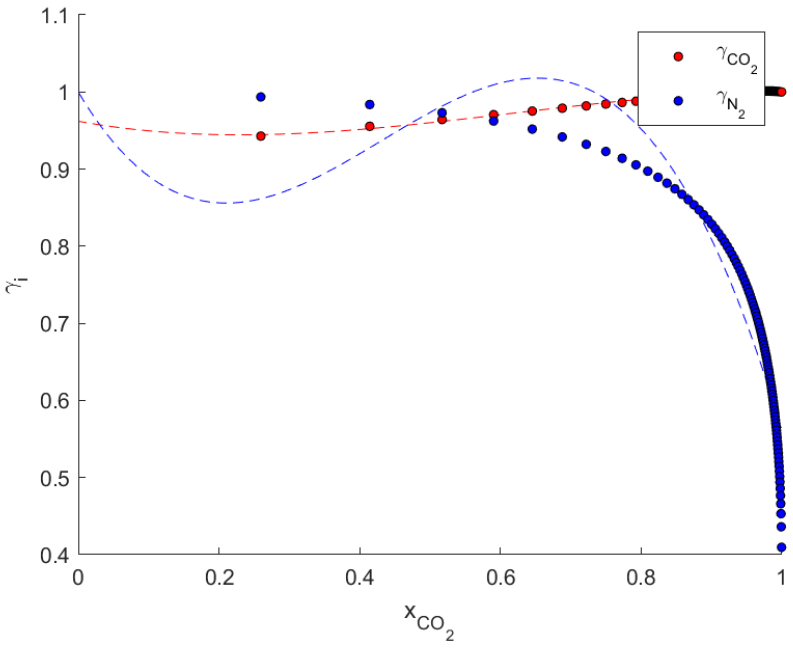

Figure B.15. Activity coefficient plot at 1 bar for Cu-HKUST-1.

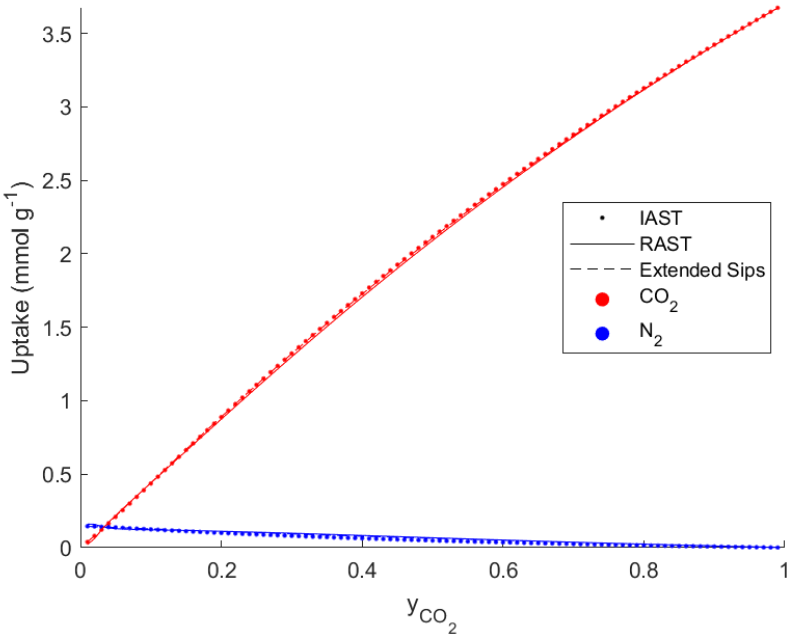

Figure B.16. Predicted multiple component adsorption isotherms for Cu-HKUST-1 @ 1 bar.

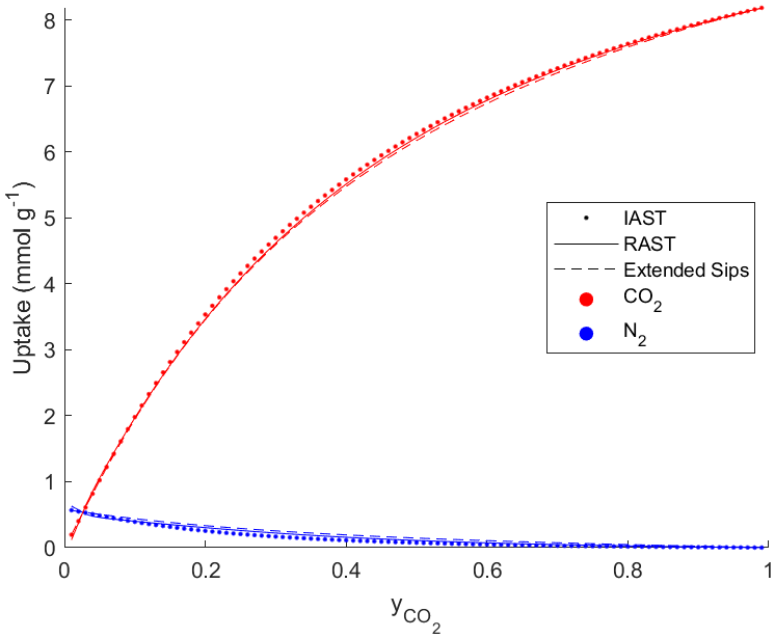

Figure B.17. Predicted multiple component adsorption isotherms for Cu-HKUST-1 @ 5 bar.

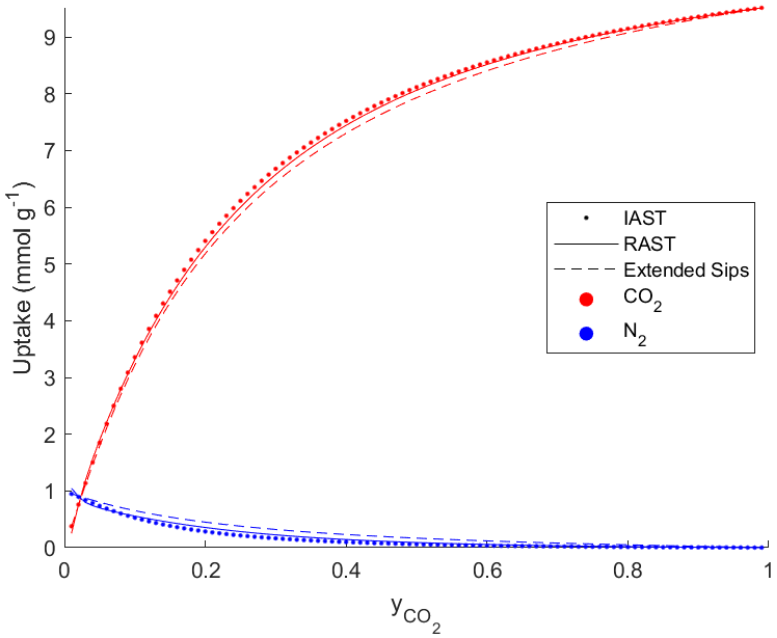

Figure B.18. Predicted multiple component adsorption isotherms for Cu-HKUST-1 @ 10 bar.

B.2.4 Multi-Component Gas Adsorption Experiments

Cu-HKUST-1 was activated ($T = 100\ °C$) under dynamic vacuum ($P = 1 \times 10^{-2}\ mbar$). A sample of 100 mg of Cu-HKUST-1 was transferred to a brass sample vessel after activation and attached to

the volumetric adsorption analyzer. The sample was then activated *in situ* for 3 hours at 50 °C before the adsorption experiment began.

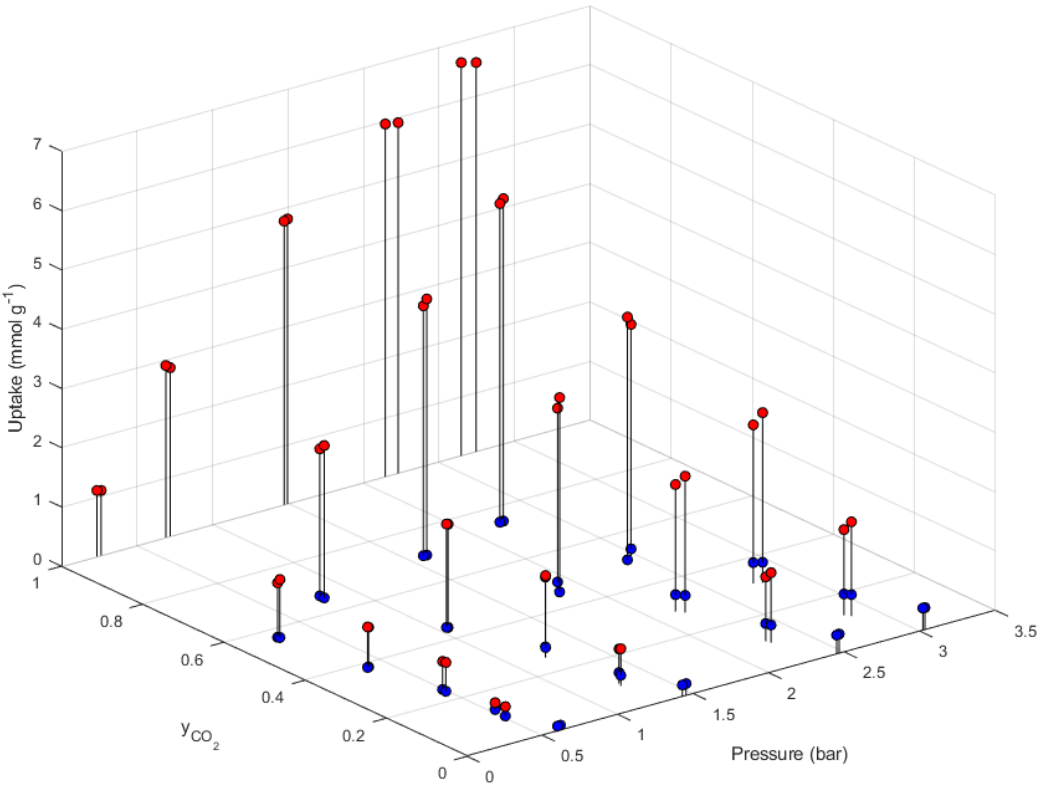

Figure B.19. Multiple-component adsorption data for Cu-HKUST-1 (Red circles indicate CO_2 adsorption, blue circles indicate N_2 adsorption).

Table B.5. Measured MGA data for Cu-HKUST-1

T (K)		*P* (bar)		*y* (% CO_2)		c_{CO2} (mmol g^{-1})		c_{N2} (mmol g^{-1})	
Mean	Std. Deviation	Mean	Std. Deviation	Mean	Std. Deviation	Mean	Std. Deviation	Mean	Std. Deviation
298.05	0.20	0.48	1.74E-04	8.38	0.40	0.23	0.01	0.08	0.01
298.07	0.19	1.27	2.19E-04	9.26	0.40	0.63	0.02	0.18	0.02
298.18	0.23	2.28	2.10E-04	9.83	0.40	1.18	0.04	0.30	0.04
298.19	0.20	2.85	2.17E-04	11.31	0.39	1.59	0.06	0.36	0.06
298.10	0.19	0.49	1.40E-04	11.40	0.39	0.19	0.01	0.08	0.01
298.31	0.19	1.28	1.77E-04	10.26	0.40	0.58	0.02	0.18	0.02
298.12	0.18	2.27	2.99E-04	10.79	0.40	1.09	0.04	0.30	0.04
298.33	0.20	2.82	1.94E-04	12.24	0.39	1.45	0.06	0.36	0.06
298.10	0.20	0.45	8.50E-05	22.05	0.37	0.56	0.01	0.07	0.01
298.15	0.14	1.20	2.28E-04	25.48	0.36	1.39	0.02	0.17	0.02
298.11	0.21	2.19	2.72E-04	27.65	0.36	2.30	0.05	0.29	0.05
298.10	0.15	2.77	2.13E-04	30.45	0.36	2.87	0.06	0.35	0.06
297.94	0.16	0.45	2.17E-04	22.94	0.37	0.55	0.01	0.07	0.01
298.03	0.24	1.21	2.34E-04	25.68	0.36	1.35	0.02	0.17	0.02
297.99	0.23	2.16	2.04E-04	28.86	0.36	2.14	0.04	0.29	0.04
298.10	0.17	2.73	1.13E-04	31.09	0.36	2.67	0.06	0.35	0.06
298.10	0.25	0.38	2.20E-04	38.28	0.35	0.75	0.01	0.02	0.01
298.17	0.19	1.03	5.41E-04	43.02	0.35	1.99	0.02	0.08	0.02
297.93	0.21	1.85	2.12E-04	45.91	0.35	3.61	0.03	0.04	0.03
298.19	0.19	2.40	2.05E-04	49.96	0.35	4.53	0.05	0.03	0.05
297.92	0.19	0.37	2.20E-04	38.27	0.35	0.76	0.01	0.01	0.01
298.18	0.19	1.02	4.61E-04	42.96	0.35	2.01	0.02	0.09	0.02
298.10	0.19	1.85	1.74E-04	46.41	0.35	3.40	0.03	0.17	0.03
298.27	0.26	2.43	1.54E-04	49.89	0.35	4.38	0.05	0.21	0.05
298.15	0.25	0.27	2.84E-04	56.71	0.35	0.92	0.01	0.01	0.01
298.12	0.23	0.81	4.42E-05	66.52	0.37	2.48	0.02	0.02	0.02
298.05	0.23	1.60	1.81E-04	70.34	0.38	4.22	0.03	0.04	0.03
297.99	0.19	2.22	1.48E-04	74.42	0.39	5.38	0.04	0.05	0.04
298.14	0.22	0.28	2.17E-04	56.41	0.35	0.98	0.01	0.01	0.01
298.04	0.23	0.81	1.53E-04	65.44	0.37	2.57	0.02	0.03	0.02
297.93	0.26	1.62	1.68E-04	70.24	0.38	4.32	0.03	0.04	0.03
297.94	0.19	2.24	1.97E-04	74.56	0.39	5.44	0.04	0.00	0.04

Appendix C. Supporting Information for Chapter 5

C.1 COMPUTATIONAL DETAILS

Forcefield definitions (COMPASSII)[97] were assigned to the atoms of the various porous frameworks; however, forcefield-assigned partial charges were not used. Instead, Density Functional Theory (DFT)[103–105,200–202] calculations were performed, using the *CASTEP*[115] software, to optimize the fractional coordinates and calculate the partial charges of the atoms in the porous frameworks. In these DFT calculations, the Generalized Gradient Approximation (GGA) level of theory was used, along with the Perdew-Burke-Ernzerhof (PBE) functional and the Grimme DFT-D3[116] dispersion correction. Furthermore, the core electrons were represented by ultrasoft pseudopotentials. Energy cut-off values of 598.7 eV and 571.4 eV were used for the plane-wave basis sets of 13X and Cu-HKUST-1, respectively. A k-point sampling of 1x1x1 was used with a 0.04 $Å^{-1}$ separation. The SCF convergence tolerance was set at 1×10^{-6} eV $atom^{-1}$. After the electronic description of the structures were optimized, partial charges were assigned to atoms using either the Mulliken population analysis (MPA) or Hirshfeld population analysis (HPA) charge schemes. Both the forcefield definitions and forcefield-assigned partial charges were used for adsorbate molecules.

Grand Canonical Monte Carlo (GCMC) simulations were performed with the optimized models of the microporous structures to test whether the models would yield accurate single-component gas adsorption isotherms. A GCMC simulation typically consisted of 20 pressure steps, each consisting of 10^5 equilibration steps and 10^6 production steps. Canonical Monte Carlo (CMC) simulations were performed with 10^5 equilibration steps and 10^6 production steps.

Molecular dynamics simulations of the canonical ensemble were performed with structures that were obtained from CMC simulations. The total duration of the simulations were 1000 ps with a time step of 5 fs (2×10^5 iterations). The internal coordinates of the guest molecules and the framework atoms were fixed for these simulations.

C.2 PRAST-S

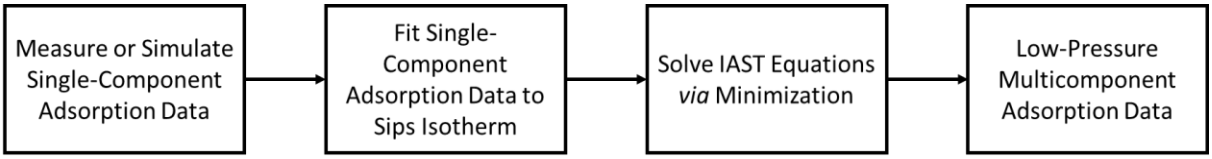

Figure C.1. Workflow used to calculate low-pressure binary adsorption equilibria via IAST.

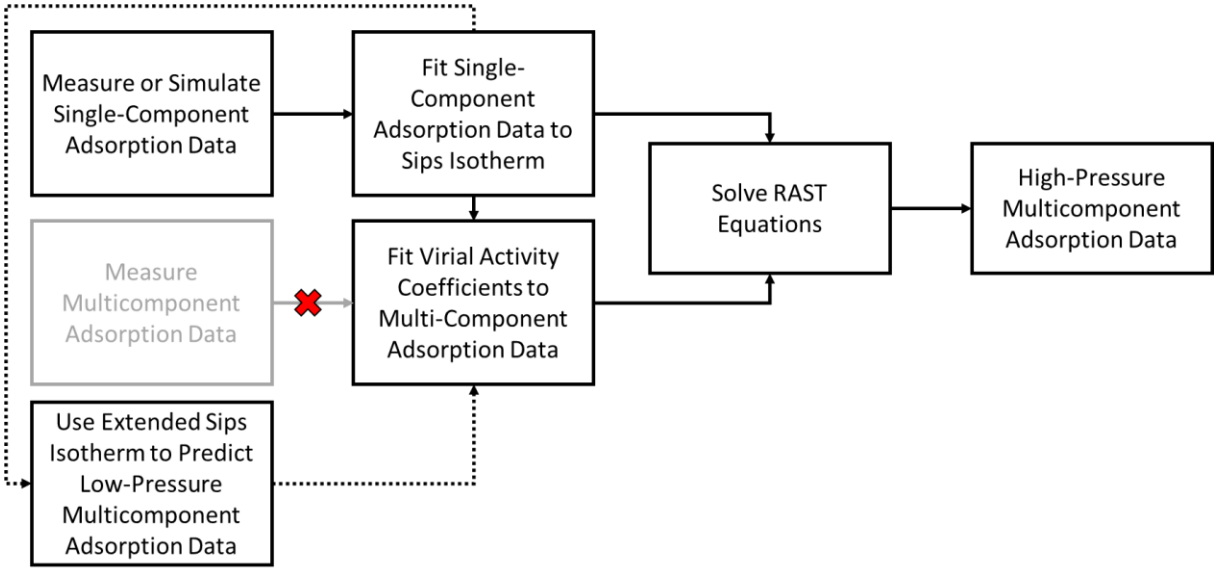

Figure C.2. Workflow used to calculate high-pressure multicomponent adsorption equilibria via PRAST-S.

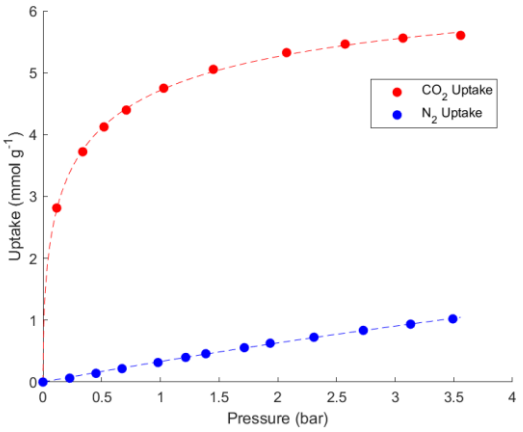

Figure C.3. Measured adsorption isotherm for CO_2 and N_2 with 13X fitted to the Sips isotherm.

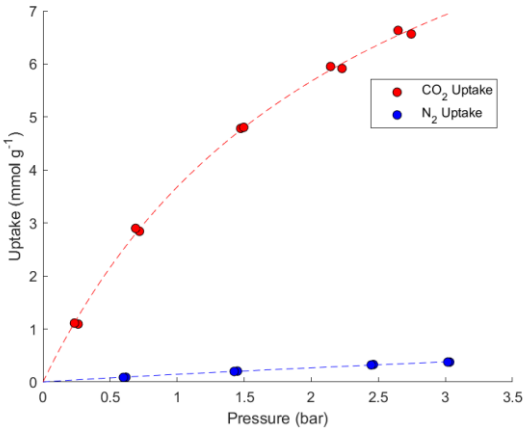

Figure C.4. Measured adsorption isotherm for CO_2 and N_2 with Cu-HKUST-1 fitted to the Sips isotherm.

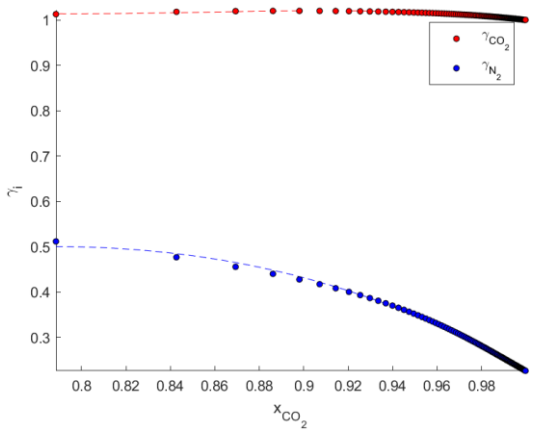

Figure C.5. Activity coefficients for the mixed adsorption of CO_2 and N_2 into 13X fitted to the virial activity coefficient function.

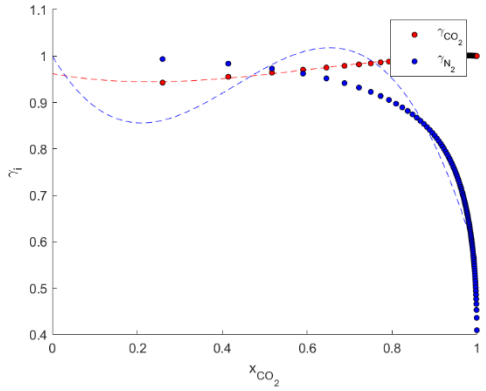

Figure C.6. Activity coefficients for the mixed adsorption of CO_2 and N_2 in Cu-HKUST-1 fitted to the virial activity coefficient function.

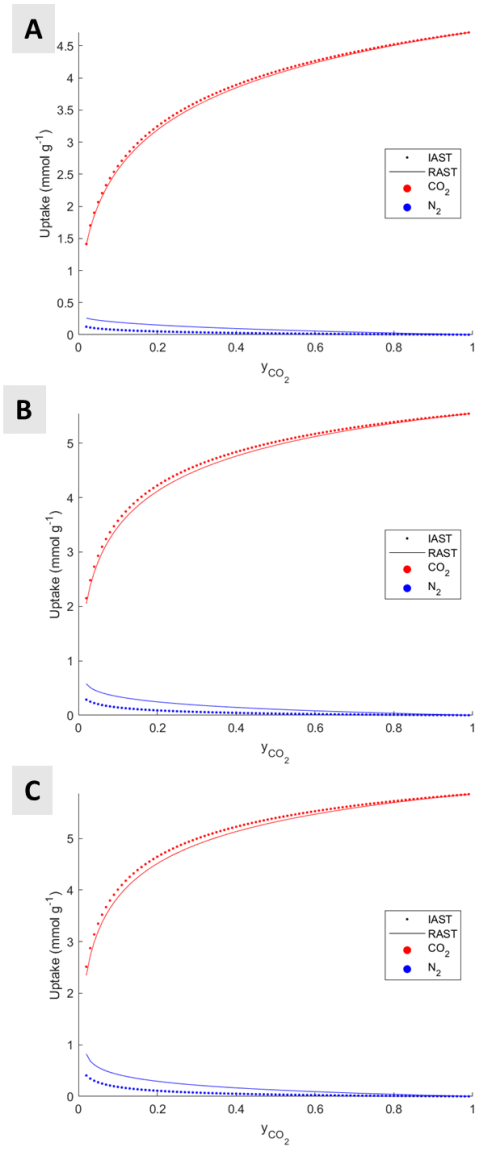

Figure C.7. Multi-component adsorption isotherms for CO_2 and N_2 at (A) 1, (B) 3, and (C) 5 bar total pressure when adsorbed into 13X.

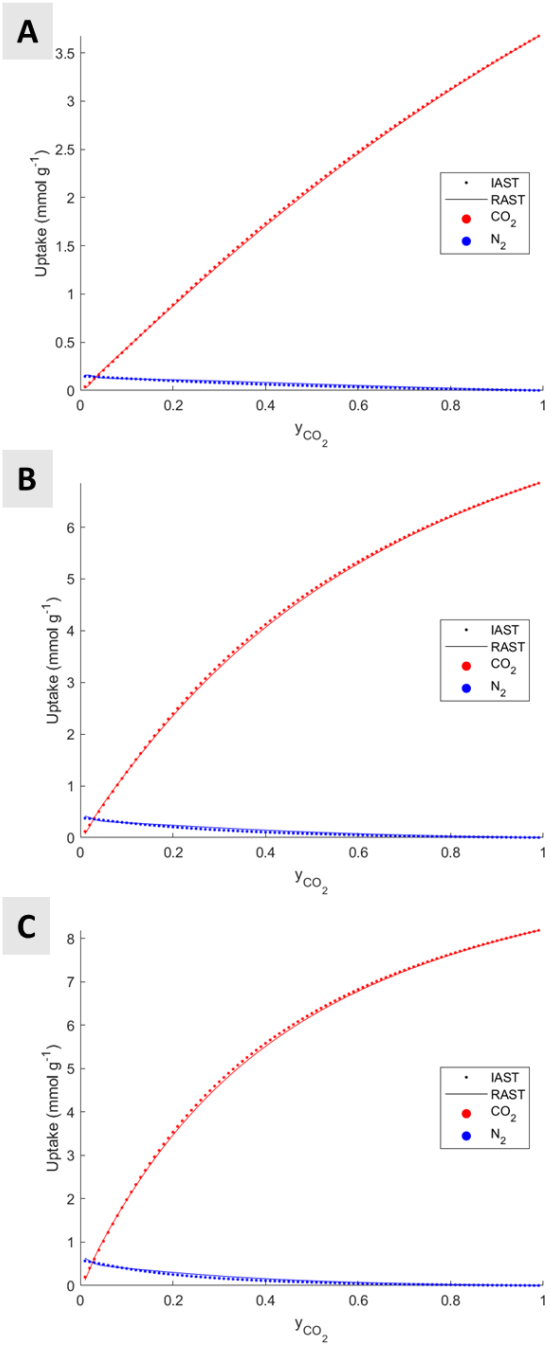

Figure C.8. Multi-component adsorption isotherms for CO_2 and N_2 at (A) 1, (B) 3, and (C) 5 bar total pressure when adsorbed into 13X.

C.3 ADDITIONAL INFORMATION

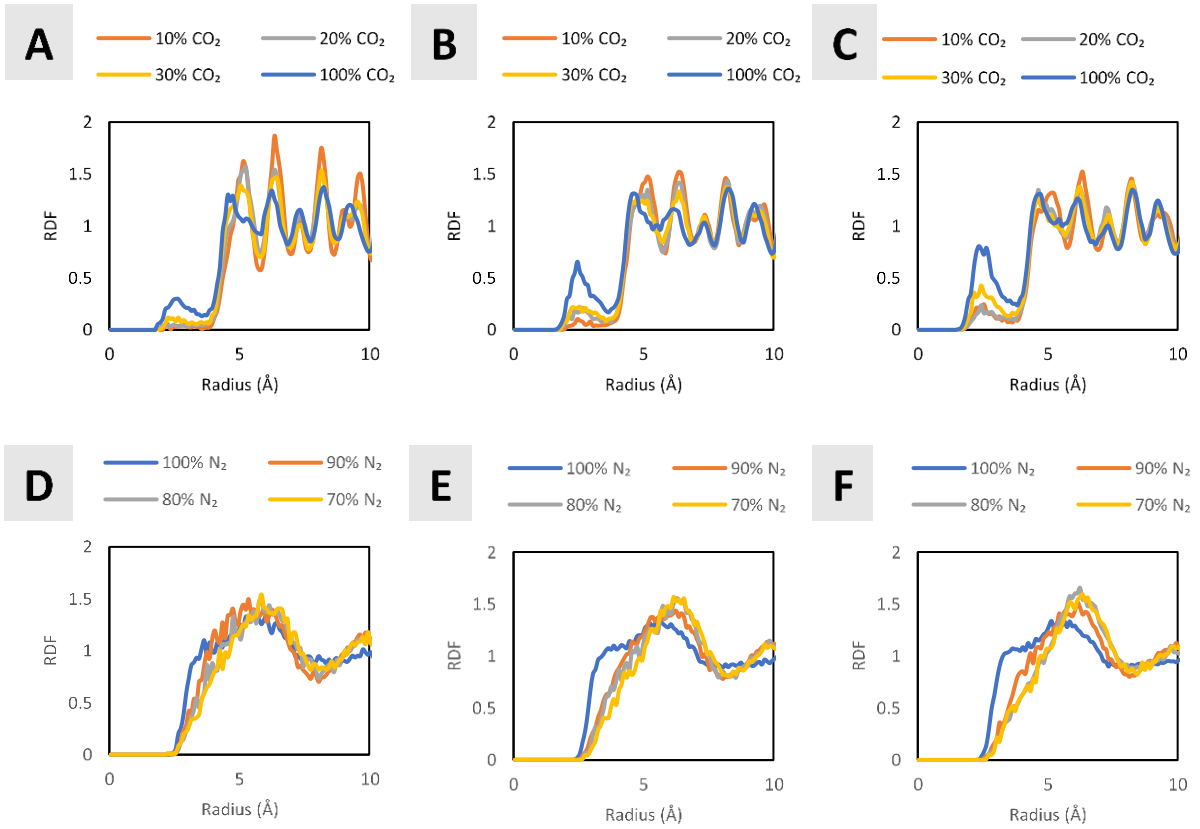

Figure C.9. Radial distribution functions of CO_2 around the unfilled Site III positions at (A) 1 bar, (B) 3 bar, and (C) 5 bar total pressure and N_2 around the Site II Na atoms at (C) 1 bar, (D) 3 bar, and (E) 5 bar total pressure.